Magnetic Detection of Microstructural Change in Power Plant Steels

Victoria Anne Yardley

Emmanuel College

This dissertation is submitted
for the degree of Doctor of Philosophy
at the University of Cambridge

PREFACE

This dissertation is submitted for the degree of Doctor of Philosophy at the University of Cambridge. The research described herein was conducted under the supervision of Professor H. K. D. H. Bhadeshia and Dr M. G. Blamire in the Department of Materials Science and Metallurgy, University of Cambridge, between October 1999 and April 2003.

Except where acknowledgement and reference are made to previous work, this work is, to the best of my knowledge, original. This dissertation is the result of my own work and includes nothing which is the outcome of work done in collaboration except where specifically indicated in the text. Neither this, nor any substantially similar dissertation has been, or is being, submitted for any other degree, diploma, or other qualification at any other university. This dissertation does not exceed 60,000 words in length.

Victoria Anne Yardley
May 2003

ACKNOWLEDGEMENTS

It is my pleasure to acknowledge all the PT-members, past and present, for their kindness, help and friendship and for many enjoyable times, in particular Daniel Gaude-Fugarolas, Ananth Marimuthu, Dominique Carrouge, Philippe Opdenacker, Yann de Carlan, Chang Hoon Lee, Professor Yanhong Wei, Carlos García Mateo, Thomas Sourmail, Mathew Peet, Gareth Hopkin, Miguel Yescas-Gonzalez, Pedro Rivera, Franck Tancret and Hiroshi Matsuda. My especial thanks go to Shingo, Michiko and Hiroki Yamasaki, for their warm friendship and hospitality, Japanese lessons and okonomiyaki.

Finally, I would like to thank my parents and friends for their love and support during the past three years.

In loving memory of
Edward and Mary Yardley

Contents

ABBREVIATIONS

b.c.c. Body-centred cubic

ppm Parts per million

ABBM Alessandro, Beatrice, Bertotti and Montorsi model

AQ As-quenched

BN Barkhausen noise

CSL Coincidence site lattice

EBSD Electron backscatter diffraction

FEG Field emission gun

FWHM Full width half maximum

IQ Image quality

MAE Magnetoacoustic Emission

NDT Nondestructive testing

ODS Oxide-dispersion strengthened

OIM Orientation imaging microscopy

PHD Pulse height distribution

RMS Root-mean-square

SEM Scanning electron microscope

TEM Transmission electron microscope

VSM Vibrating sample magnetometer

NOMENCLATURE

Note: Two SI systems for magnetics nomenclature exist, but the Sommerfeld system has been used throughout; equations not conforming to this system have been converted. A comparison table including the two SI systems and the cgs system can be found in Jiles (1998).

General

d Grain diameter

E Efficiency

M Magnification

M_f Martensite-finish temperature

M_s Martensite-start temperature

P Larson-Miller parameter

t Time

T Absolute temperature

T_1 Absolute heat source temperature

T_2 Absolute heat sink temperature

T_M Absolute melting temperature

Magnetics

$\mathbf{B}$ Magnetic induction

B_S Saturation induction

B_R Remanent induction

E_a Anisotropy energy

E_{area} Area reduction energy (Kersten model)

E_d Demagnetising energy

E_{demag} Inclusion demagnetising energy (Néel model)

E_{ex} Exchange energy

E_m Magnetostatic energy

E_{pin} Energy dissipated against pinning

E_{supp} Energy supplied

$\mathbf{H}$ Magnetic field

H_C Coercive field

H_d Demagnetising field

H_e Weiss mean field

H_{max} Maximum applied field

H_S Field at which $M = M_S$

K_1 Anisotropy constant

$\mathbf{M}$ Magnetisation

$\mathbf{m}$ Magnetic moment

M_R Remanent magnetisation

M_S Saturation magnetisation

N_d Demagnetising constant

P Barkhausen noise power

T_C Curie temperature

V Voltage

W_H Hysteresis energy loss

α Mean field constant

β Term characterising nearest-neighbour interactions

γ Domain wall energy

δ Domain wall thickness

λ_{UVW} Magnetostrictive strain along $< UVW >$

λ_{si} Ideal magnetostrictive strain

μ_0 Permeability of free space

μ' Differential permeability

μ'_{max} Maximum differential permeability

σ Electrical conductivity

χ'_{in} Initial differential susceptibility

χ'_{max} Maximum differential susceptibility

Φ Magnetic flux

$\omega*$ Surface pole density

$\mathcal{J}$ Term characterising nearest-neighbour interactions

Modelling: existing models

A, B Amplitude of fluctuations in ABBM

k pinning parameter

M_{an} Anhysteretic magnetisation

M_{JS} BN jump sum

M_{rev} Reversible magnetisation

$< M_{disc} >$ Average BN event size

v domain wall velocity

W noise term in ABBM

$< \epsilon_\pi >$ Pinning energy for 180° wall

$< \epsilon_{pin} >$ Pinning enrgy for wall at arbitrary angle

ξ Correlation length

Modelling: new model

A_i Total number pinning points of ith type per unit volume

$\mathbf{A}_w$ Wall surface area

C Constant

E Fitting error

E_0 Electric field amplitude

$\mathbf{l}_w$ Wall jump distance

$l\{H\}$ Distance between pinning sites at field H

$< l > \{H\}$ Domain wall mean free path

$N\{H\}$ Number of pinning sites of strength $\geq H$

$n\{S\}$ Number pinning sites of strength S

S Pinning site field strength

S_b Field at which unpinning first occurs

$< S >_i$ Mean value of S for ith type of pinning site

$V\{H\}$ BN voltage at field H

$V_r\{H\}$ Real $V\{H\}$

$V_p\{H\}$ Predicted $V\{H\}$

$<x>$ Mean value of $ln\{S\}$ for log-normal distribution

β Parameter depending on angle between adjacent domains

ΔS_i Standard deviation of S for ith type of pinning site

Δx Standard deviation of $ln\{S\}$ for log-normal distribution

Orientation Imaging Microscopy

$\mathbf{c}_c$ Crystal coordinate system

$\mathbf{c}_s$ Sample coordinate system

d Planar spacing

$\mathbf{G}$ Rotation matrix

$\mathbf{M}$ Misorientation matrix

$<UVW>$ Misorientation axis

ν_0 Brandon ratio proportionality constant

ν_m Maximum allowable deviation from ideal coincidence

λ Radiation wavelength

θ Misorientation angle

θ_B Bragg angle

ABSTRACT

Power plant components are expected to withstand service at high temperature and pressure for thirty years or more. One of the main failure mechanisms under these conditions is creep. The steel compositions and heat treatments for this application are chosen to confer microstructural stability and creep resistance. Nevertheless, gradual microstructural changes, which eventually degrade the creep properties, occur during the long service life. Conservative design lives are used in power plant, and it is often found that components can be used safely beyond the original design life. However, to benefit from this requires reliable monitoring methods. One such technique involves relating the microstructural state to measurable magnetic properties.

Magnetic domain walls interact energetically with microstructural features such as grain boundaries, carbides and dislocations, and are 'pinned' in place at these sites until a sufficiently large field is applied to free them. When this occurs, the sudden change in magnetisation as the walls move can be detected as a voltage signal (Barkhausen noise). Previous work has suggested that grain boundaries and carbide particles in power plant steels act as pinning sites with characteristic strengths and strength distributions.

In this study, the concept of pinning site strength distributions was used to develop a model for the variation of the Barkhausen noise signal with applied field. This gave a good fit to published data. The modelling parameters characterising pinning site strengths showed good correlations with grain and carbide particle sizes.

New Barkhausen noise data were obtained from tempered power plant steel samples for further model testing. The Orientation Imaging Microscopy (OIM) technique was used to investigate the grain orientations and grain boundary properties in the steel and their possible role in Barkhausen noise behaviour. The model again fitted the data well, and a clear relationship could be seen between the pinning strength parameter and the severity of tempering (as expressed by the Larson-Miller tempering parameter) to which the steel was subjected.

The experimental results suggest that the Barkhausen noise characteristics of the steels investigated depend strongly on the strain at grain boundaries. As tempering progresses and the grain boundary dislocation density falls, the pinning strength of the grain boundaries also decreases. A clear difference in Barkhausen noise response could be seen between a $2\frac{1}{4}$Cr1Mo traditional power-plant steel and an 11Cr1Mo steel designed for superior heat resistance.

A study of an oxide dispersion strengthened ferrous alloy, in which the microstructure undergoes dramatic coarsening on recrystallisation, was used to investigate further the effects of grain boundaries and particles on Barkhausen noise. The findings from these experiments supported the conclusion that grain boundary strain reduction gave large changes in the observed Barkhausen noise.

Chapter 1

Introduction

The aim of this work was to investigate the use of magnetic property measurements as a nondestructive tool for microstructural evaluation in power plant steels. A survey of the existing literature pointed to Barkhausen noise as a suitable property for investigation. A new model for Barkhausen noise from power plant steels was proposed and tested using previous published data. New data for further model testing were generated from $2\frac{1}{4}$Cr1Mo and 11Cr1Mo (wt. %) power plant steel samples. Detailed characterisation of the grain structures in these steels was carried out to study the role of grain boundaries in Barkhausen noise. Experiments on an oxide dispersion strengthened alloy, in which the grain size and oxide particle distribution could be varied separately, were used to give further clarification of this.

Power plant conditions and the physical metallurgy of power plant steels are discussed in Chapter 2, which also reviews some of the existing methods of nondestructive microstructural evaluation.

The concept of magnetic domains is essential for understanding the microstructural dependence of magnetic properties. The theory of domains is given in the first half of Chapter 3. Observations of the interactions between the domain structure and microstructural features appear in the second half.

Chapter 4 introduces the magnetic properties commonly used in microstructural characterisation, including magnetic hysteresis and Barkhausen noise. Previous work on the relationships between microstructural features and magnetic properties is reviewed, with particular emphasis on studies of

Barkhausen noise in tempered martensitic steels.

Insights from one of these studies were used as the basis for a new model of the microstructural dependence of the Barkhausen signal in tempered steels. Chapter 5 summarises existing models of hysteresis and Barkhausen noise, describes the derivation of the new model and gives details of model testing using published data from the literature.

Chapter 6 describes the preparation of power plant steel samples. Optical micrographs, hardness and coercive field data and estimates of the microstructural feature sizes are given in this chapter. A subset of the samples were selected for more detailed characterisation using the technique of Orientation Imaging Microscopy in the scanning electron microscope. Chapter 7 explains the basis of this technique and presents micrographs and analysis.

Barkhausen noise experiments on the power plant steel samples are described in Chapter 8. The data generated were used to fit the new model; the results are given in Chapter 9.

Chapter 10 gives details of experiments performed on an oxide dispersion strengthened alloy with the aim of understanding the role of grain boundaries and particle dispersions in hysteresis and Barkhausen noise.

Chapter 11 summarises the findings of this study and gives suggestions for future directions in which this work can be taken. The code of the model fitting program and a description of its operation are given in the Appendix.

Chapter 2

Microstructural Evolution in Power Plant Steels

2.1 Power plant operation

In power plant, heat energy from fuel combustion or nuclear fission is used to produce jets of steam. The kinetic energy of the steam is converted to electrical energy by a system of turbines and a generator. Figure 2.1 shows the route followed by the steam and water. Water is pumped into the boiler and converted to steam, then superheated. It is injected through nozzles onto the blades of the high pressure (HP) turbines. Following this, it is reheated and sent to the intermediate pressure (IP) turbines and then to the low pressure (LP) turbines. The rotary motion of the turbines is used to drive the generator to produce electrical power, and the exhaust steam is condensed and recirculated.

The Carnot efficiency E of such a cycle is given by:

$$E = \frac{T_1 - T_2}{T_1} \tag{2.1}$$

where T_1 and T_2 are the absolute temperatures of the heat source and heat sink respectively. It is therefore desirable from both economic and environmental points of view to use as high an operating temperature as possible. Progress in power-plant alloy design has allowed T_1 to be increased from 370°C in the 1920s to a current level of 600°C or higher, and there is a drive
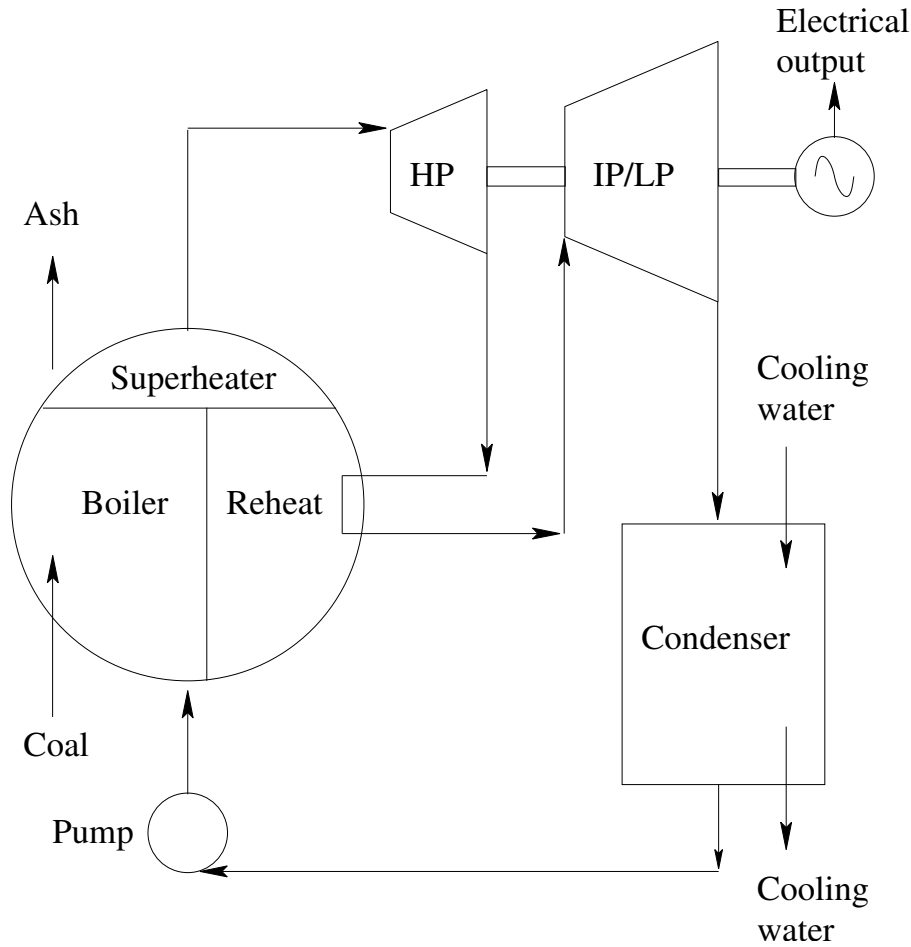
Figure 2.1: Schematic of a power plant steam cycle. After Cole, 2000.

towards further increases (Masuyama, 2001).

Steam turbines may be expected to withstand 28 or more years of continuous service (Berger *et al.*, 1993). These and many other components are exposed to conditions of 450–600°C and 15–100 MPa (Evans and Wilshire, 1985, Pickering, 1997).

Under such conditions, there are several life-limiting mechanisms, including corrosion, oxidation and fatigue, but one of the most important is creep, *i.e.* the progressive deformation of a component subjected to a high temperature and a stress which is lower than its yield strength. A typical tolerable creep strain rate for power plant is around 3×10^{-11} s^{-1}, which is equivalent

to 2% elongation over 30 years (Bhadeshia *et al.*, 1998).

Figure 2.2 shows a typical plot of strain against time in a sample subjected to a constant stress and a high temperature (Evans and Wilshire, 1993). The magnitude of the initial strain depends only on the stress. Usually the majority of the life is spent in the 'steady-state' regime, in which the strain rate is constant. The tertiary stage is characterised by an increase in creep rate, and ends with rupture.
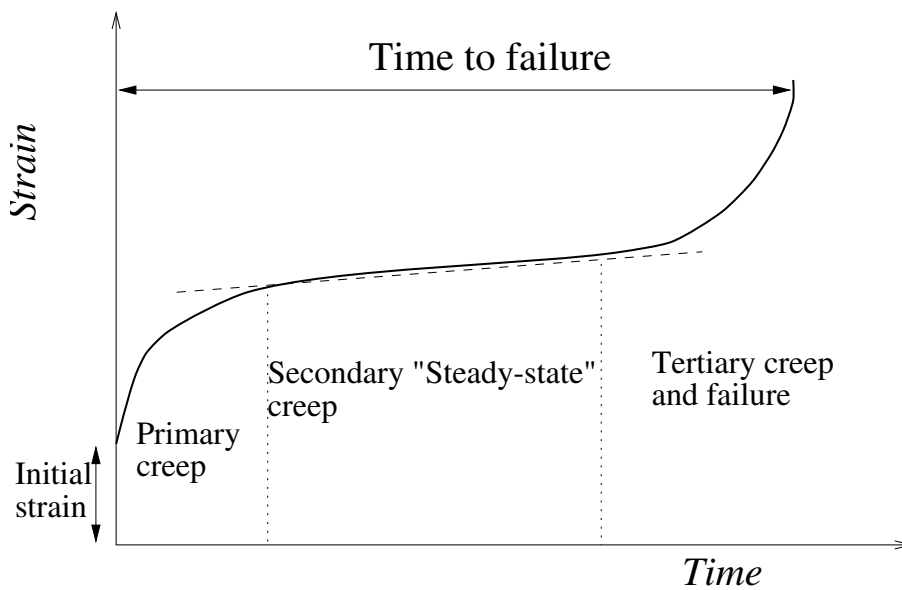
Figure 2.2: A typical strain-time curve showing the different regimes of creep (after Evans and Wilshire, 1993).

2.2   Creep mechanism

Creep only occurs to an appreciable extent when the temperature is above around $0.4T_M$, where T_M is the absolute melting temperature (Reed-Hill and Abbaschian, 1992). The predominant mechanism by which it occurs depends on temperature and stress. Deformation mechanism maps, in which the stress normalised against the shear modulus is plotted against the homologous temperature T/T_M, can be used to determine this (Frost and Ashby,

1982; Ashby and Jones, 1989). It is found that under typical power plant operating conditions, creep occurs by dislocation glide and climb, rather than by bulk diffusion.

Figure 2.3 shows how this occurs. The application of stress causes dislocations to move along slip planes until they encounter an obstacle, such as a second-phase particle. At room temperature, dislocations can only pass obstacles by cutting through them if they are coherent with the matrix, or by bowing out between them. However, at higher temperatures, the thermally activated diffusion of atoms to or away from the extra half-plane allows the dislocation to climb into a different, unobstructed slip plane, along which it can glide freely until it meets another obstacle and the process is repeated.
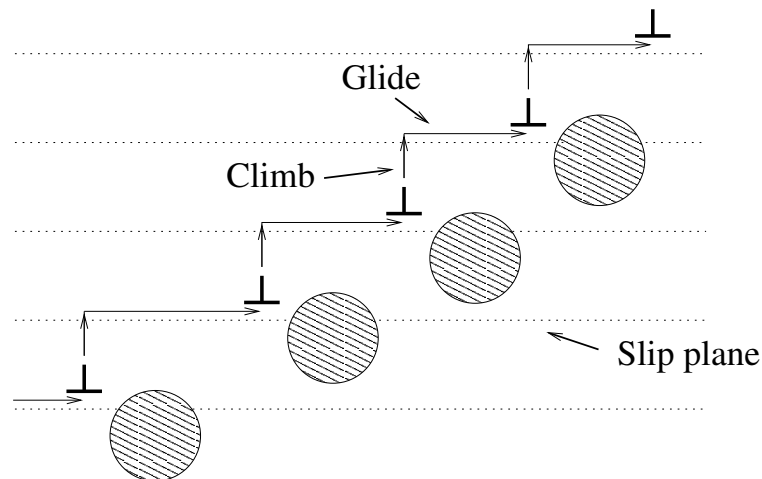
Figure 2.3: The processes of climb and glide.

2.3   Creep-resistant steels

Steels of the $2\frac{1}{4}$Cr1Mo type have been used in power plant for many decades, but recently 9–12Cr steels have been developed for use at higher operating temperatures. Both the compositions and the heat treatments of power-plant steels are chosen to give a fine, stable microstructure containing fine carbides. An austenitisation treatment to dissolve existing precipitates is

carried out above 1000°C, the exact temperature depending on the steel composition. The steel is then air-cooled. In $2\frac{1}{4}$Cr1Mo, this results in a predominantly bainitic microstructure, but 9–12 Cr steels are fully air-hardenable, and martensite is formed.

Tempering is then carried out, typically at around 700°C, to produce fine carbides and reduce the stored energy in the microstructure so that there is only a very small driving force for microstructural change during service. Bhadeshia *et al.* (1998) have calculated the stored energy of a power plant alloy in martensitic form is 1214 J mol^{-1} greater than that in its equilibrium state, whereas the post-tempering microstructure is only 63 J mol^{-1} above equilibrium.

Lower tempering temperatures give high creep rupture strength in the short term, but this decreases rapidly; tempering at a higher temperature gives better long-term creep properties (Yoshikawa *et al.*, 1986, Masuyama, 2001). This is believed to occur because the change from martensite to ferrite is complete after high-temperature tempering, but will occur during service if the tempering temperature is low.

2.3.1 Characteristics of martensitic steels

The transformation from austenite to martensite is diffusionless, occurring as a deformation of the parent lattice. On cooling sufficiently rapidly to suppress the diffusional ferrite and pearlite reactions and the intermediate bainite reaction, martensite formation begins at the martensite-start temperature M_s. The transformation is rapid and athermal. The M_f temperature marks the point at which transformation should be complete, but in practice, some retained austenite often remains. In plain carbon steels with <0.5 wt. % C, very little austenite is retained (2% or less) but higher carbon contents increase this proportion. Because the transformation from austenite is diffusionless, the martensite is supersaturated in carbon, and has a tetragonal crystal structure if the carbon content is sufficiently high.

2.3.2   Martensite morphology

Martensite forms in thin plates or laths on specific habit planes within the prior austenite grains. In order to accommodate the shape deformation of the transformation while maintaining a planar interface between the transformed and untransformed phases, the martensite slips or twins on a fine scale.

The dislocation density of ferrous martensites is of the order of 10^{11}–10^{12} cm^{-2}, similar to that achieved by severe cold work. In lower-carbon martensites (<0.5 wt. % C), only dislocations are usually present, but higher-carbon martensites also exhibit twinning, which is favoured by a higher yield stress.

Figure 2.4 illustrates schematically the structural levels in martensitic microstructures (Marder and Marder, 1969). The prior austenite grain boundary structure is preserved, and laths forming within the grains stop at these boundaries because the austenite grains do not, in general, have any special orientation relationship to one another. A packet is a region of laths with the same habit plane, and blocks are subunits of packets, in which the lath orientation is also the same. The combination of habit plane and orientation is known as a variant.

The sizes of both blocks and packets increased with increasing prior austenite grain size (Maki *et al.*, 1980). However, the clear block and packet structure in Figure 2.4 was only observed for carbon contents less than 0.5 wt. % in plain-carbon steels. Higher carbon contents gave a microstructure of irrationally arranged laths throughout the prior austenite grain.

In low-carbon martensitic steels (<0.5 wt. %C), the habit plane is $\{111\}_\gamma$, and the orientation relationship between the austenite γ and martensite α' is due to Kurdjumov and Sachs (1930):

$$
\begin{array}{ccc}
\{111\}_\gamma & \parallel & \{110\}'_\alpha \\
< 1\bar{1}0 >_\gamma & \parallel & < 1\bar{1}1 >'_\alpha
\end{array}
\tag{2.2}
$$

Intermediate carbon contents give rise to a habit plane close to $\{225\}_\gamma$ and the same Kurdjumov-Sachs relationship, but in high-carbon martensites (>1.4 wt. %) the habit plane is close to $\{229\}_\gamma$ and the orientation relation changes to Nishiyama-Wasserman (Wassermann, 1933; Nishiyama, 1934):
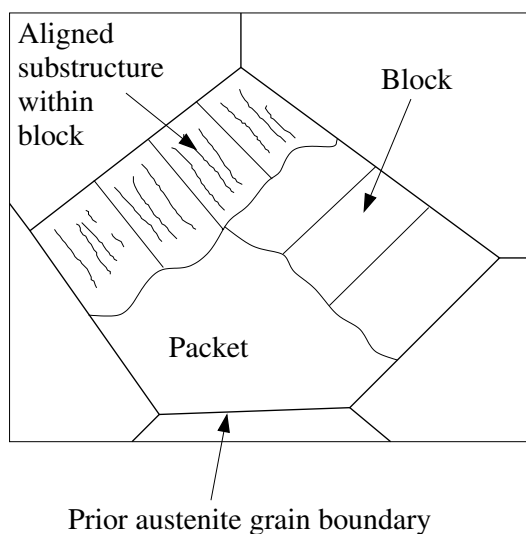
Figure 2.4: Levels of structure in martensite, (Marder and Marder, 1969).

$$
\begin{array}{ccc}
\{111\}_\gamma & \parallel & \{110\}'_\alpha \\
<11\bar{2}>_\gamma & \parallel & <1\bar{1}0>'_\alpha
\end{array}
\tag{2.3}
$$

2.3.3 Tempering of plain-carbon martensitic steels

The tempering of martensitic steels can be subdivided into four distinct stages (Balluffi *et al.*, 1951; Baker and Nutting, 1959: Honeycombe and Bhadeshia, 1995):

Stage 1: up to 250°C

Carbon in solution precipitates as laths or plates of ϵ-carbide, which has a definite orientation relationship with the matrix and is coherent with it in the early stages of precipitation. The tetragonality is reduced but not completely lost, and the matrix is still supersaturated in carbon.

Stage 2: 230–300°C

Retained austenite decomposes; it is believed to transform to bainitic ferrite and cementite.

Stage 3: 100–300°C

This overlaps with Stage 2. Cementite, Fe$_3$C, is precipitated as plates with a Widmanstätten distribution. It nucleates on ϵ-matrix interfaces or on twin, martensitic lath and prior austenite grain boundaries. The ϵ-carbides gradually dissolve as the cementite forms. Occurring concurrently with this is the loss of tetragonality of the martensite, which relaxes to ferrite as it loses its supersaturation.

Stage 4: 300–700°C (plain-carbon steels)

In plain-carbon steels, the final stage of tempering is the spheroidisation and coarsening of cementite particles. Coarsening begins between 300 and 400°C, but spheroidisation tends to occur at higher temperatures, up to 700°C. The driving force for these processes is the reduction in surface area, and hence in surface energy, of precipitates. Particles on lath boundaries or prior austenite grain boundaries are favoured for growth over those in the matrix since boundary sites allow easier diffusion and a source of vacancies to accommodate the less dense cementite. Recovery occurs between 300 and 600°C. Dislocations rearrange to form subgrains within the laths. Above 600°C, recrystallisation occurs, and equi-axed ferrite grains form at the expense of the original laths. Carbide particles retard grain growth by pinning grain boundaries, but eventually a microstructure of equi-axed grains and spheroidal carbides is produced. Further tempering causes a gradual coarsening of this structure.

Stage 4 in alloy steels

Chromium, molybdenum, vanadium, tungsten and titanium all form carbides which are thermodynamically more stable than cementite. Alloy carbide formation requires substitutional diffusion and therefore occurs more slowly than cementite precipitation, for which only interstitial carbon diffusion is necessary. Stages 1–3 occur in the same way as for a plain-carbon steel, and the cementite begins to grow, but it subsequently dissolves to be replaced by alloy carbide phases. Often, the new carbide is part of a precipitation

sequence of many phases, beginning with the most kinetically favoured and ending with the equilibrium phase. These changes may take place extremely slowly.

During the early stages of tempering, the precipitation of alloy carbides may increase the steel's strength above that of the as-quenched state (Figure 2.5). After this secondary hardening peak, the strength decreases monotonically with increasing tempering time.
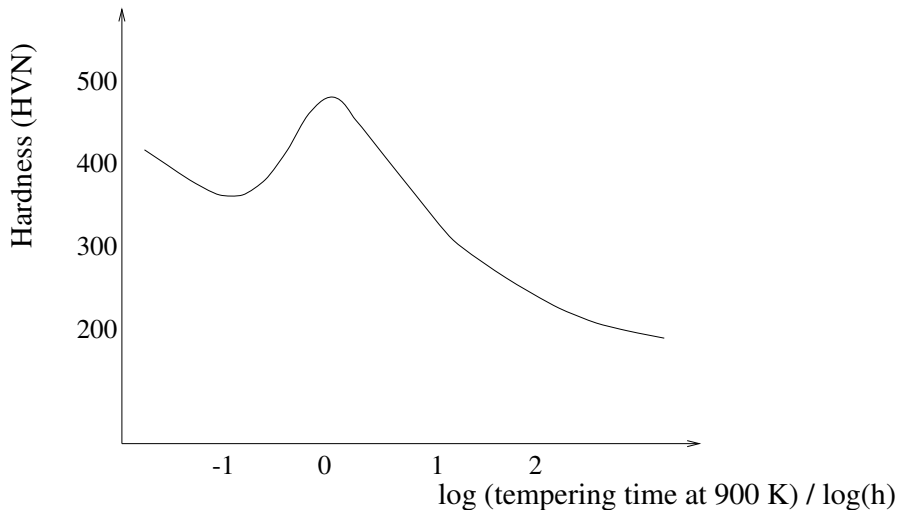
Figure 2.5: The secondary hardening effect in an alloy steel containing strong carbide formers (after Honeycombe and Bhadeshia, 1995).

2.3.4 Precipitation Sequences

The phases precipitating, and the order in which they form, depend on both the tempering temperature and the steel composition. Figure 2.6 maps the conditions for phase stability in $2\frac{1}{4}$Cr1Mo wt. % steel (Nutting, 1999). In alloy steels, carbides are described with a general formula M_xC_y or M_xX_y, where M signifies a metallic element and X a combination of carbon and nitrogen. In 9–12 wt. % Cr steels, precipitation sequences are similar, but occur at a much greater rate (*e.g.* Thomson, 1992).

Table 2.1 summarises the characteristics of precipitate phases found commonly in power-plant steels. Nucleation may occur in-situ, *i.e.* on the inter-
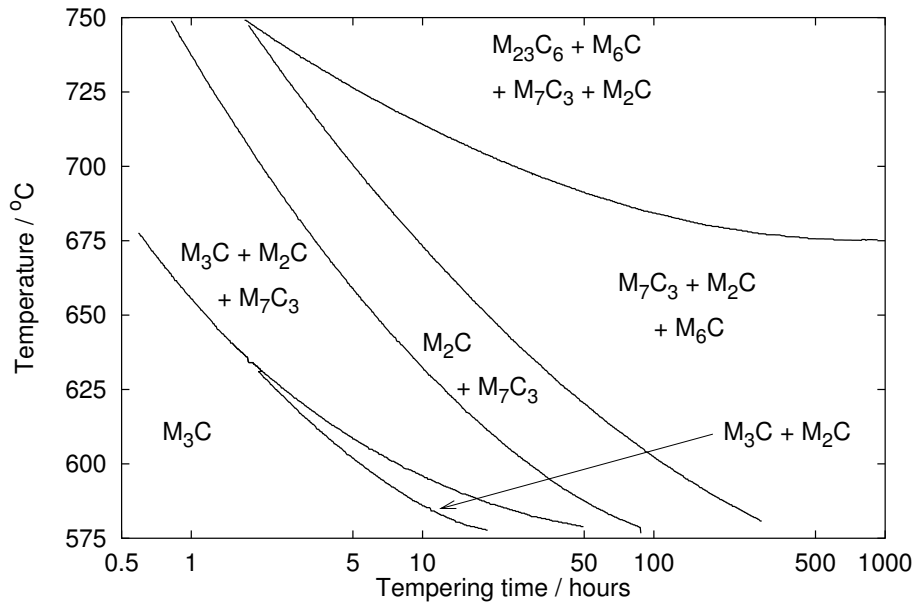
Figure 2.6: An updated version (1984) of the original Baker-Nutting carbide stability diagram (1959) for $2\frac{1}{4}$Cr1Mo steel, using new microanalytical techniques to identify phases (Nutting, 1999).

face between a pre-existing precipitate and the ferrite matrix. Alternatively, it may take place on intralath dislocations, lath boundaries, prior austenite grain boundaries or on the boundaries of subgrains formed during recovery of the dislocation structure. Such boundaries provide fast diffusion paths, enabling particles to coarsen more rapidly than they would if in the bulk.

M_3C

M_3C is the general formula for carbides with the same structure as cementite. Iron is in an approximately hexagonal close packed lattice, with distortions to accommodate the carbon atoms. The phase forms initially as Fe_3C, and then progressively enriches in substitutional solutes such as manganese and chromium (Woodhead and Quarrel, 1965). Its orientation relationship with the matrix is therefore the same as that of cementite. For example, Gingell *et al.* (1997) observed in 1Cr1Mo steels that M_3C occurred as elongated plates along $<111>_\alpha$.

Phase	Crystal structure	Nucleation site	Size	Shape	Benefits for creep?
M_3C	Orthorhombic	In-situ, MLB, PAGB	Coarse	Plates, then spheroidises	
M_2X	Hexagonal	D, MLB	Fine	Needle	Yes
M_7C_3	Trigonal	In-situ	Coarse	Spheroidal	No
$M_{23}C_6$	Cubic F	PAGB, MLB	Coarse	Spheroidal	No
M_6C	Cubic F	In-situ, PAGB, MLB	Coarse	Spheroidal	No
MX		Undissolved/ on MX	Fine	Spheroidal, platelike	Yes
Laves		PAGB, MLB, lath interior	Coarse	Spheroidal	Short-term?

Table 2.1: Data on common precipitates. D: dislocations, PAGB: prior austenite grain boundaries, MLB: martensitic lath boundaries. Crystal system data from Andrews *et al.*, 1967.

M_2X

The second phase to precipitate is commonly M_2X, which has a hexagonal structure (Andrews and Hughes, 1959). It commonly nucleates on dislocations and martensite lath boundaries (Raynor *et al.*, 1966), forming fine needles or rods. These have an orientation relationship with the matrix (Pitsch and Schrader, 1958):

$$
\begin{array}{ccc}
(0001)_{M_XC} & \parallel & (001)_\alpha \\
[11\bar{2}0]_{M_2X} & \parallel & [100]_\alpha
\end{array}
\qquad (2.4)
$$

It has also been seen growing perpendicular to austenite-ferrite interfaces (Edmonds and Honeycombe, 1973).

M_2X is very important to creep resistance in low-alloy steels, although it is only the carbides nucleating on dislocations which contribute significantly to this (Honeycombe and Bhadeshia, 1995). It dissolves rapidly in higher-chromium steels, but stabilising it in 12 wt. % Cr steel gave secondary hardening (Irvine *et al.*, 1960). However, the elements which favour its formation also promote the undesirable δ-ferrite phase.

M_7C_3

M_7C_3 only appears if the chromium content is sufficiently high compared to that of other alloying elements (Woodhead and Quarrell, 1965). If molybdenum is present, $M_{23}C_6$ may form instead. If M_7C_3 is observed, it forms after M_2X (Baker and Nutting, 1959) or after M_3C without the intermediate M_2X stage (Janovec *et al.*, 1994). It nucleates close to cementite, possibly at the cementite-ferrite interface (Kuo, 1953; Baker and Nutting, 1959). Darbyshire and Barford (1966) state that the nucleation can be in-situ or on fresh sites.

This phase coarsens rapidly (Sakuma *et al.*, 1981; Yong Wey *et al.*, 1981) and is not thought to be beneficial for creep resistance.

$M_{23}C_6$

This is rich in chromium (Woodhead and Quarrell, 1965) and is often an equilibrium phase in chromium-rich steels. It nucleates on prior austenite grain and martensite lath boundaries (Senior, 1989) and has also been identified adjacent to M_7C_3 (Nutting, 1999). It forms after either M_7C_3 or M_2X. The particles are large, and do not contribute to creep strength, but Bjärbo (1994) has suggested that it may retard microstructural coarsening by stabilising martensitic lath boundaries.

M_6C

M_6C is an equilibrium phase in molybdenum-rich, relatively chromium-poor steels (Edmonds and Honeycombe, 1973; Tillman and Edmonds, 1974). It can nucleate on prior austenite grain boundaries and martensitic lath boundaries. Kurdzylowski and Zielinski (1984) report that it also nucleates in-situ on M_2X- or $M_{23}C_6$-ferrite interfaces, but Nutting (1999) has suggested that it instead forms by diffusion. Its rapid coarsening rate, greater than that of $M_{23}C_6$, make it a particularly undesirable phase (Vodárek and Strang, 1997), especially since it forms at the expense of finer carbides.

MX

These carbonitrides occur in complex 9–12 wt. % Cr alloys. They often have a NaCl-type cubic F structure (Woodhead and Quarrell, 1965). Fine, spheroidal MX particles, which are believed to remain in the microstructure during austenitisation, have been observed in the as-quenched steel (Janovec *et al.*, 1994). On tempering, these act as nucleation sites for platelike MX which forms in a 'V-wing' shape (Nickel *et al.*, 1995). MX is thought to be beneficial to creep properties because of its fine distribution and stability.

Laves phase

This intermetallic phase has the formula Fe_2M, where M represents molybdenum, tungsten or a combination of the two. It is an equilibrium phase in Mo- and W-containing 9–12 wt. % Cr steels. The favoured nucleation sites are initially prior austenite grain boundaries, then lath boundaries, and at the longest heating times, within laths (Senior, 1989). A review by Robson (1996) concludes that Laves phase is undesirable because of its coarseness and its depletion of the matrix in Mo and W. However, work by Hald (1995) suggests that Laves phase precipitation gives a greater strengthening effect than W in solution. According to Ishii *et al.* (1998), its presence at prior austenite grain and martensite lath boundaries contributes to creep strength. The coarsening rates of both W- and Mo-containing Fe_2M are high (Kubon *et al.*, 1997) so any strengthening effect does not last into the long term.

Other long-term phases

Three further phases have recently been identified in power plant steels. Z-phase was found in 12CrMoVNb steels (Strang and Vodárek, 1996). It is a complex nitride and appears to form at the expense of the fine precipitates of MX and M_2X which confer creep resistance; it is therefore undesirable. Mann *et al.* (1995) found rod-shaped M_5C_2 in post-service $1Cr\frac{1}{2}Mo$ steels. This appeared to nucleate on M_2X. The intermetallic μ-phase (Fe_7W_6) is believed to improve high temperature creep strength (Igarashi and Sawaragi, 1997).

Figure 2.7 shows a typical tempered martensitic microstructure in 9–12 wt. % steel.
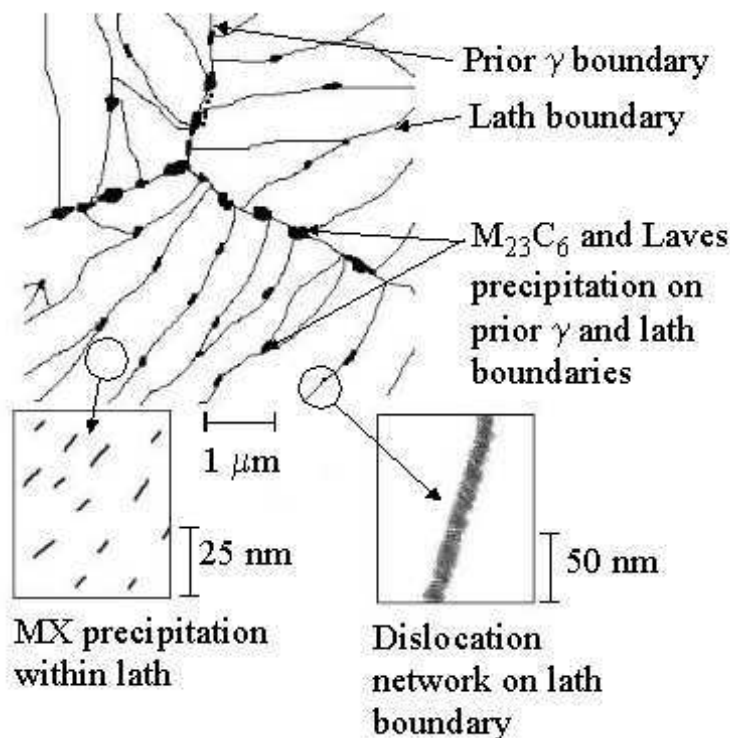
Figure 2.7: Typical microstructure of tempered martensitic 9–12 wt. % steel (after Masuyama, 2001).

2.4 Differences in bainitic microstructures

Bainite can occur in two forms (Honeycombe and Bhadeshia, 1995). 'Upper bainite' forms at a higher temperature (550-400°C) and consists of fine ferrite plates of length approximately 10 μm and thickness approximately 0.2 μm, growing in clusters (sheaves) in which all the plates are parallel and of the same crystallographic orientation, and separated by low-misorientation grain boundaries or by cementite precipitates. Lower bainite, which forms between 400 and 250°C, contains cementite precipitates within ferrite plates as well as between them.

Bainite is closer to equilibrium than martensite, being only slightly supersaturated in carbon. Cementite particles are already present and these tend to be larger than the cementite formed on tempering of martensite. The dislocation content is also smaller than that of martensite. In plain-carbon bainite, short-term tempering gives little change in microstructure, but a significant drop in strength is seen when the plate-like ferrite and cementite spheroidise to an equiaxed structure. The effect of alloying with carbide-forming elements is the same as for tempered martensite, but alloy carbides form on a longer timescale.

Baker and Nutting (1959) investigated the effect on tempering kinetics of using a martensitic rather than bainitic starting microstructure in $2\frac{1}{4}$Cr1Mo steel. Differences were observed, but they were very small, because the defect densities of the two starting microstructures were very similar. Bhadeshia (2000) raised the question of why the higher-Cr steel was martensitic, and concluded that this was a by-product of alloying to increase oxidation and corrosion resistance. However, he suggested that the fine plate-like microstructure in martensite may contribute to creep resistance by impeding dislocation motion. Yamada *et al.* (2002) found that in 9Cr3W3Co steels, water-quenching instead of air-cooling gave longer creep rupture lives. Quenching gave a better distribution of MX particles, suppressing complex MX phases and accelerating the formation of more beneficial VC.

2.5   Changes during service

In $2\frac{1}{4}$Cr1Mo steels, M_2X provides long-term creep resistance, but this phase dissolves rapidly when the chromium content is higher. A review of strengthening mechanisms in tempered high-Cr creep resistant steels by Maruyama *et al.* (2001) concludes that dislocations, solutes, intragranular particles (MX) and particles on boundaries all contribute to creep strength, but not in a simple additive manner.

During creep deformation, the dislocation substructure of the tempered steel, which is stable with respect to temperatures up to 650°C in the absence of stress, undergoes recovery into a subgrain structure (Nickel, 1995;

Iwanaga *et al.*, 1998; Cerjak *et al.*, 2000). The growth of these subgrains is accompanied by a reduction in dislocation density, and reduces the creep resistance.

2.5.1 Lath coarsening, recovery and recrystallisation

Martensite laths in 9Cr-W steels subjected to creep were found to coarsen concurrently with $M_{23}C_6$ particles (Abe, 1999). An increase in the tungsten content retarded the coarsening of both the $M_{23}C_6$ and the laths, while causing the precipitation of Laves phase. It was concluded from this that $M_{23}C_6$ particles are more effective than Laves phase for pinning lath boundaries. The lath coarsening observed by Abe occurred by lath boundary triple point migration (Figure 2.8).
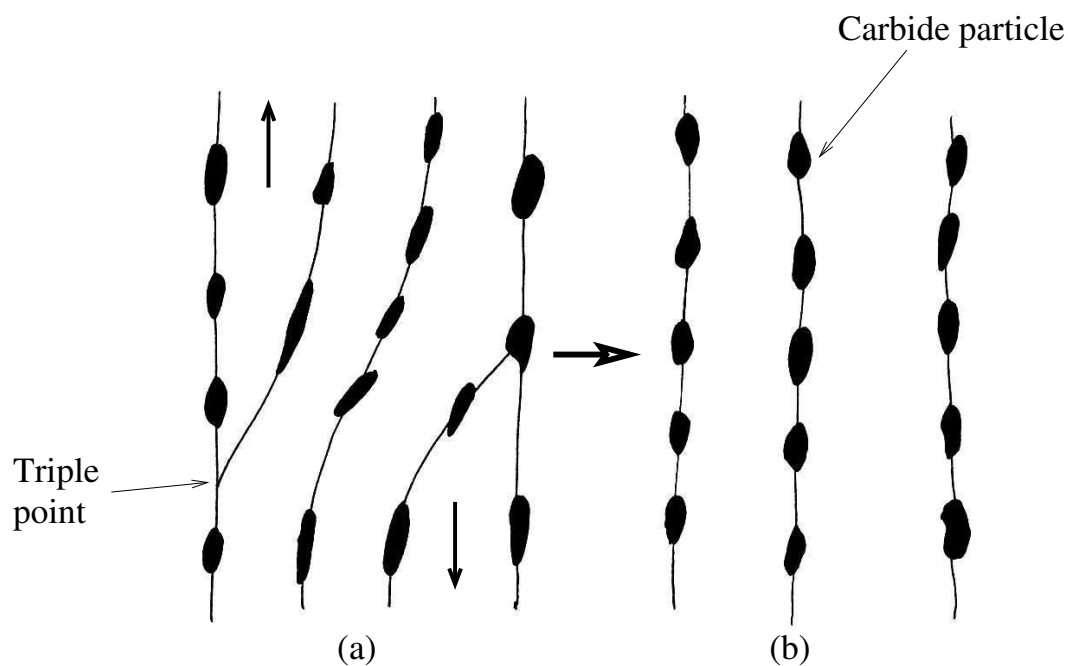
Figure 2.8: Lath coalescence: Triple points migrate and lath boundaries coalesce (a) to give a coarser structure (b). After Abe, 1999.

2.5.2 Cavitation and final failure

Creep rupture may occur in a more brittle or more ductile manner; cavities occur at smaller strains when the ductility is low (Beech *et al.*, 1984). Second-phase particles on grain boundaries can act as nucleation sites for voids (Martin, 1980). Grain boundary triple points also concentrate stress during grain boundary sliding in creep, resulting in cavitation (Watanabe, 1983).

In power-plant steels, failure can be promoted by preferential recovery at prior austenite grain boundaries (Kushima *et al.*, 1999; Abe, 2000). The large, rapidly coarsening particles on grain boundaries deplete the local matrix of solutes and fine particles, and the resulting recovered region acts as a strain concentrator and is able to crack easily.

2.6 Design life and remanent life estimation

Conservative component design lives are used to accommodate the effects of microstructural heterogeneity and variation in service conditions. The working stress is set at around 0.8 times the value of the lower bound of creep rupture stress at the intended life (Halmshaw, 1991). It has often been found that components reaching the end of their design lives are still in a safe condition for several more years of use. Bhadeshia *et al.* (1998) have reviewed the techniques available for the estimation of the remanent lives of such components. These subdivide into methods based on mechanical properties such as hardness and impact toughness, those involving microstructural observation, and those in which other properties, such as resistivity or density, are measured and used to infer the component condition. However, Bhadeshia *et al.* concluded that none of these techniques gave a sufficiently comprehensive characterisation to be used in isolation. Also, implementation often requires a plant shutdown, the expense of which contributes a great deal to the cost of life extension as opposed to component replacement at the end of the design life.

2.7   Scope for magnetic methods

It is clear that there is a need for additional microstructural monitoring techniques, especially those which can be used in-situ with minimal preparation, and which give a comprehensive characterisation of the component state.

Ferritic power plant steels are ferromagnetic, allowing the use of magnetic monitoring methods. Magnetic techniques are routinely in use for crack detection in ferromagnetic components, and appear promising for the measurement of stress effects. For example, a programme for the evaluation of structural materials in nuclear power plant after tensile and fatigue loading, which includes the measurement of several magnetic properties, is under development in Japan (Uesaka *et al.*, 2001).

The aim of this study is to investigate their usefulness as a method of microstructural evaluation for the purpose of remanent life estimation in power plant steels. This requires an understanding of the relationships between magnetic properties and the characteristics of microstructural features such as grain boundaries and carbides. Chapter 3 and Chapter 4 discuss the progress made so far in understanding these.

Chapter 3

Magnetic Domains

3.1 Ferromagnetism and domain theory

3.1.1 Atomic origin of ferromagnetism

Bulk magnetic behaviour arises from the magnetic moments of individual atoms. There are two contributions to the atomic magnetic moment from the momentum of electrons. Firstly, each electron has an intrinsic magnetic moment and an intrinsic angular momentum (spin). Secondly, electrons may also have a magnetic moment and an angular momentum as a result of their orbital motion in atoms.

The Pauli exclusion principle permits only one electron in an atom to have a particular combination of the four quantum numbers n, l, m_l and m_s. The first three numbers specify the electron energy state. The spin quantum number, m_s, can only take the values $\pm 1/2$. Each energy state may therefore contain up to two electrons. If only one electron is present, its spin moment contributes to the overall spin moment of the atom. A second electron is required to have an antiparallel spin to the first, and the two spins will cancel out, giving no net moment. Strong magnetic properties are associated with elements which have a large number of unpaired spins.

In solid materials, the orbital moments are strongly coupled to the crystal lattice and are therefore unable to change direction when a magnetic field is applied. Because of this 'orbital quenching', the magnetic moments in solids can be considered as due to the spins only. An atom with uncompensated

spins has a net magnetic moment in the absence of an applied field; solids composed of such atoms are termed 'paramagnetic'. In general, the atomic magnetic moments in paramagnets are randomly aligned when no field is present, and the magnetisation process consists of aligning them into the field direction. However, some paramagnetic materials undergo a transition on cooling to an ordered state in which there is local alignment of atomic moments. The ordered state is 'ferromagnetic' if adjacent atomic moments are aligned parallel to one another, and 'ferrimagnetic' if they are antiparallel but of different magnitude such that there is a local net magnetisation.

The temperature of the order/disorder transition is known as the Curie temperature (T_C) in ferromagnets. The degree of ordering increases with decreasing temperature. Iron in its body-centred cubic (b.c.c.) ferrite form is strongly ferromagnetic, as are many widely used steels. In the ferritic power plant steels discussed in Chapter 2, the austenitisation treatment takes the steel above its Curie temperature, and it becomes paramagnetic. Air-cooling or quenching to give bainite or martensite gives a b.c.c. or body-centred tetragonal structure which is ferromagnetic, and the ferromagnetism is retained on tempering.

3.1.2 Weiss domain theory

Weiss (1906, 1907) postulated that atoms in ferromagnetic materials had permanent magnetic moments which were aligned parallel to one another over extensive regions of a sample. This was later refined into a theory of 'domains' of parallel moments (Weiss, 1926). The overall magnetisation (magnetic moment per unit volume) of a block of material is the vector sum of the domain magnetisations. In the demagnetised state, this is zero. As a field is applied, changes in the domain configuration, for example in the relative widths of domains, allow a net magnetisation in the field direction. Weiss' hypothesis was later confirmed by direct observation (Bitter, 1931), and the concept of magnetostatic energy, which explained the formation of domains, was proposed by Landau and Lifshitz (1935).

3.1.3 Ideal domain structure

In a homogeneous, defect-free, single-crystal ferromagnet with cubic symmetry, the domain structure can be explained by a balance between four energy terms: exchange, magnetostatic, anisotropy and magnetoelastic (Kittel and Galt, 1956).

Exchange energy

Weiss extended an existing statistical thermodynamic theory for paramagnetism (Langevin, 1905), to describe the alignment of the atomic magnetic moments within domains. The Weiss 'mean field' $\mathbf{H}_e$ in the original theory was given by:

$$\mathbf{H}_e = \alpha \mathbf{M} \tag{3.1}$$

where $\mathbf{M}$ is the magnetisation, and α is the 'mean field constant'. The mean field approximation requires that all magnetic moments interact equally with all others. Although this is obviously a simplification of the true situation, it is nevertheless a useful concept for consideration of the atoms within domains, which usually extend over 10^{12} to 10^{18} atoms. The origin of the interaction was later identified by Heisenberg (1928) as a quantum-mechanical exchange effect due to overlapping wavefunctions of neighbouring atoms. If only nearest neighbours are considered, the exchange energy E_{ex} per unit volume associated with this interaction is:

$$E_{ex} = -2\beta \sum_i \sum_j \mathbf{m}_i \cdot \mathbf{m}_j \tag{3.2}$$

where β is a term characterising the strength of the interaction, and the summation is over all nearest-neighbour pairs i and j in a unit of volume. In ferromagnetic materials, β is positive, giving a minimum exchange energy when moments lie parallel. Complete alignment of all atomic moments in the sample (magnetic saturation) is therefore favoured by this term. An explanation is therefore needed of how the demagnetised state can arise; this is given by the magnetostatic energy term.

Magnetostatic energy

A body of magnetisation $\mathbf{M}$ in a magnetic field $\mathbf{H}$ has a magnetostatic energy E_m arising from the interaction of $\mathbf{M}$ with $\mathbf{H}$:

$$E_m = -\mu_0 \int \mathbf{H} \cdot \partial\mathbf{M} \tag{3.3}$$

where μ_0 is the permeability of free space. At any internal or external surface of a uniformly magnetised body, there is a discontinuous change in the component of $\mathbf{M}$ normal to the surface, which can be envisaged as a source of 'free poles'. These are magnetic (north or south) poles which are not compensated by poles of the opposite kind in the immediate vicinity. They produce a demagnetising field, which favours a change in the arrangement of magnetic moments such that the poles disappear. A finite body has free poles on its outer surfaces, resulting in a demagnetising field $\mathbf{H}_d$ antiparallel to the magnetisation $\mathbf{M}$; this tends to turn $\mathbf{M}$ so that it points parallel to the surfaces. This field is given by:

$$\mathbf{H}_d = N_d\mathbf{M} \tag{3.4}$$

where N_d is the demagnetising factor, which depends only on sample geometry. For a sample with magnetisation $\mathbf{M}$ but no applied field, the magnetostatic energy depends only on $\mathbf{M}$ and N_d, and can be obtained by substituting Equation 3.4 into Equation 3.3 to give:

$$E_d = \frac{\mu_0}{2}N_dM^2 \tag{3.5}$$

In the absence of an applied field, the magnetostatic energy is therefore a minimum when the magnetisation is zero, and subdivision into domains is favoured (Figure 3.1 (a), (b)). Reducing the domain width decreases the spatial extent of the field and hence the energy (c). If domains magnetised at 90° to the main domains can form, external free poles can be eliminated entirely, reducing the magnetostatic energy to zero (Figure 3.1 (d)).

Demagnetising factors can be determined exactly for ellipsoids of revolution only, but approximate values have been calculated for commonly used sample shapes, such as cylinders (Chen *et al.*, 1991).
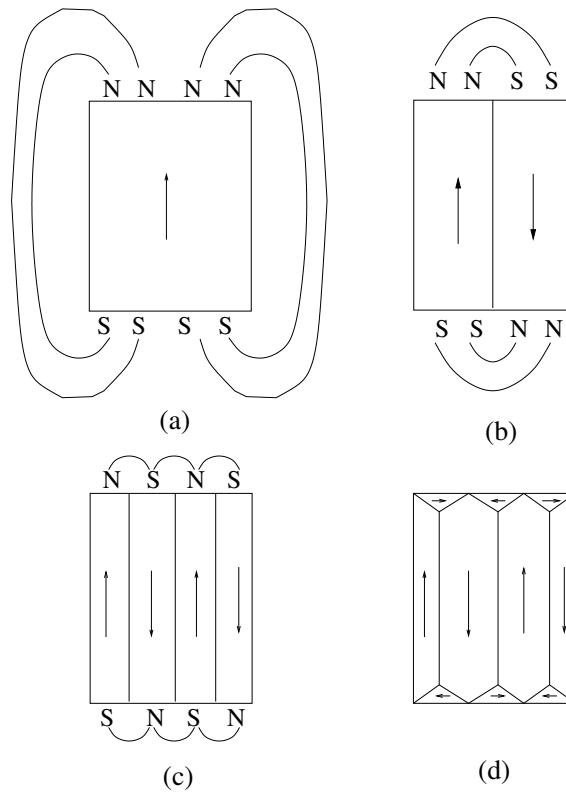
Figure 3.1: Subdivision into domains (cubic material with positive anisotropy). (a) a saturated sample, with high demagnetising energy E_d; (b) splitting into two reduces E_d; (c) more splitting reduces E_d further; (d) free poles eliminated by closure domains. After Kittel and Galt, 1956.

Crystalline anisotropy energy

Magnetocrystalline anisotropy is the preferential alignment of atomic magnetic moments along certain, 'easy' crystal directions. Other, 'hard' directions are particularly unfavourable. This arises from coupling between the spin and orbital moments (Brooks, 1940). The orbital moments are constrained in their directions by the crystal lattice, so the crystal symmetry influences the behaviour of the spins through this coupling.

To a first approximation, the anisotropy energy E_a per unit volume for a material with cubic symmetry is given by:

$$E_a = K_1(\alpha_1^2\alpha_2^2 + \alpha_2^2\alpha_3^2 + \alpha_3^2\alpha_1^2) \tag{3.6}$$

where K_1 is a constant of proportionality known as the anisotropy constant, and α_1, α_2 and α_3 are the cosines of the angles made by magnetisation vector with the crystal axes x, y and z. In b.c.c. iron, K_1 is positive, and the cube edges $< 100 >$ are the easy directions (Honda and Kaya, 1926). Antiparallel magnetisation directions are crystallographically equivalent, giving three distinct easy directions for positive-K_1 materials. This allows the formation of closure domains oriented at 90° to the main domains (Figure 3.1 (d)).

Magnetoelastic energy

If a cubic single crystal is magnetised to saturation in a direction defined by the direction cosines α_1, α_2 and α_3 with respect to the crystal axes x, y and z, a magnetostrictive strain λ_{si} is induced in a direction defined by the cosines β_1, β_2 and β_3:

$$\lambda_{si} = \lambda_{100}\left(\alpha_1^2\beta_1^2\alpha_2^2\beta_2^2\alpha_3^2\beta_3^2 - \frac{1}{3}\right) + 3\lambda_{111}(\alpha_1\alpha_2\beta_1\beta_2 + \alpha_2\alpha_3\beta_2\beta_3 + \alpha_3\alpha_1\beta_3\beta_1) \tag{3.7}$$

where λ_{100} and λ_{111} are the magnetostriction constants along $< 100 >$ and $< 111 >$ respectively. λ_{si} is the 'ideal' magnetic field-induced magnetostriction. This is defined by Cullity (1971) as the strain induced when a specimen is brought to technical saturation (§ 3.2.1) from the ideal demagnetised state, *i.e.* the state in which all of the domain orientations allowed by symmetry are present in equal volumes.

If magnetostriction is isotropic, *i.e.* $\lambda_{100} = \lambda_{111} = \lambda_{si}$, then Equation 3.7 may be simplified to:

$$\lambda_\theta = \frac{3}{2}\lambda_{si}\left(\cos^2\theta - \frac{1}{3}\right) \tag{3.8}$$

where λ is the magnetostriction measured at an angle θ to the magnetisation and the field.

In practice, however, the magnetostriction is not ideal, but depends on the magnetic history of the material and the thermomechanical treatment

to which it has been subjected. It is possible, for example, to produce a preferred orientation of magnetic domains by annealing in a magnetic field (*e.g.* review by Watanabe *et al.*, 2000).

If a domain is constrained by its neighbours, magnetostriction manifests itself as a strain energy rather than a dimensional change. Maintaining coherence between the closure domains and the main domains in Figure 3.1 (d) requires a strain energy proportional to the volume of the closure domains. This can be reduced, while maintaining the closure effect, by increasing the number both of closure domains and main domains. However, this requires more domain walls to be created; since, as will be discussed below, domain walls have a higher energy than the bulk, the equilibrium configuration is determined by a balance between domain wall and magnetoelastic energy contributions.

In polycrystals with no preferred orientation, the magnetostriction constant λ_{si} will be an average of the values of all the crystal orientations. To obtain an estimate for this average, assumptions must be made about the grain size and the transfer of stress or strain between grains. The expressions obtained depend on these assumptions unless the grains are elastically isotropic (Cullity, 1971).

3.1.4   Energy and width of domain walls

The transition region between domains magnetised in different directions was first studied by Bloch (1932). The change from one direction to the other is not discontinuous but occurs over a width determined by a balance between exchange and anisotropy energy. The energy and thickness of various types of domain walls have been calculated (Kittel and Galt, 1956).

The mean field approximation breaks down at domain walls, but the exchange energy per moment, E_{ex}, can be calculated by considering only nearest-neighbour interactions and neglecting others. For neighbouring moments $\mathbf{m}_i$ and $\mathbf{m}_j$, E_{ex} is given by:

$$E_{ex} = -\mu_0 z \mathcal{J} \mathbf{m}_i \cdot \mathbf{m}_j \qquad (3.9)$$

where $\mathcal{J}$ is a term characterising nearest-neighbour interactions and z is the number of nearest neighbours[1]. If the angle between $\mathbf{m}_i$ and $\mathbf{m}_j$ is ϕ,

$$E_{ex} = -\mu_0 z \mathcal{J} m^2 \cos\phi \qquad (3.10)$$

For a linear chain of moments, each has two nearest neighbours. Substituting the small-angle approximation $\cos\phi = 1 - \phi^2/2$ gives:

$$E_{ex} = \mu_0 \mathcal{J} m^2 (\phi^2 - 2) \qquad (3.11)$$

A wall separating domains magnetised at $180°$ to one another, and extending across n lattice parameters of size a, has an exchange energy per unit area $\frac{E_{ex}}{a^2}$:

$$\frac{E_{ex}}{a^2} = \frac{\mu_0 \mathcal{J} m^2 \phi^2 \pi^2}{na^2} \qquad (3.12)$$

E_{ex} is therefore lowest when n is large, favouring wide walls.

The anisotropy energy of the pth moment in a wall can be approximated as:

$$E_a = (K_1/4)\sin^2 2p\phi \qquad (3.13)$$

where K_1 is the anisotropy constant. Summing this over the domain wall width gives an anisotropy energy per unit area:

$$E_a = K_1 na \qquad (3.14)$$

where a is the lattice spacing and n the number of layers of atoms in the domain wall. E_a increases with n, favouring a narrow wall. The total wall energy per unit area $\gamma = E_{ex} + E_a$ is minimised by differentiating with respect to the wall width $\delta = na$ and setting the derivative to zero.

$$\frac{\partial\gamma}{\partial\delta} = \frac{-\mu_0 \mathcal{J} m^2 \pi^2}{\delta^2 a} + K_1 = 0 \qquad (3.15)$$

Hence,

---

[1]This is of a similar form to Equation 3.2 but in this case is expressed per moment.

$$\delta = \sqrt{\frac{\mu_0 \mathcal{J} m^2 \pi^2}{K_1 a}} \tag{3.16}$$

Using these expressions, Jiles (1998) has estimated the width of a wall separating antiparallel domains in iron as 40 nm, or 138 lattice parameters, and its energy as 3 x 10^{-3} J m^{-2}.

3.1.5 Determination of the equilibrium domain structure

To obtain the minimum-energy configuration of an assembly of domains so that the equilibrium structure can be found, a set of differential equations must be solved. These micromagnetics equations (Brown, 1963) assume continuously varying atomic moments, and are therefore difficult to solve for large-scale arrays of domains. In practice, a less complex 'domain theory' is applied, which treats each domain as uniformly magnetised to saturation, with variations in direction occurring only within domain walls (Hubert and Schäfer, 2000). It is assumed throughout the rest of this discussion that, far from domain walls, the domain magnetisation is M_S, which is known as 'saturation' or 'spontaneous' magnetisation.

3.2 Evolution of domain structure on application of a magnetic field

3.2.1 Ideal magnetisation and demagnetisation

When a magnetic field **H** is applied to a sample with no net magnetic moment, the energy balance previously existing is upset by the additional magnetostatic energy due to the field. The domain structure rearranges itself in order to minimise the energy under the new conditions.

In simple terms, at low H this occurs by the enlargement of domains with **M**$_S$ oriented approximately parallel to **H** at the expense of those oriented antiparallel (Kittel and Galt, 1956). As H increases, domain walls are swept out. Rotations of domain magnetisation vectors into easy directions near

that of **H** may also occur at intermediate fields. The resulting single domain has $\mathbf{M}_S$ parallel to the easy direction nearest the direction of **H**. At high field, $\mathbf{M}_S$ is rotated against the anisotropy to lie exactly parallel to **H**. This state is known as technical saturation. Further increases in the field give small increases in the magnetisation. Atomic moments deviate slightly from the applied field direction due to thermal activation,but higher applied fields reduce this deviation.

On reducing H, the domain magnetisation rotates into an easy direction, and the single domain subdivides by the nucleation of domains magnetised in the opposite direction to **M** ('reverse domains').

The balance between the energy terms varies from one material to another, and this influences the exact details of magnetisation and demagnetisation. Ferritic iron has a high anisotropy constant K_1, so rotation out of the easy directions is difficult, and all low-field magnetisation changes can be attributed to domain wall motion (Shilling and Houze, 1974).

3.2.2 Magnetic hysteresis

In real materials, the magnetisation behaviour is influenced by microstructural defects and inhomogeneities, such as grain boundaries, dislocations, solutes, precipitates, inclusions, voids and cracks. Cycling between negative and positive applied field directions gives a hysteresis loop, in which **M** takes different values depending on whether **H** is increasing or decreasing. Magnetic hysteresis, which was first noted in iron by Warburg (1881) and described and named by Ewing (1900), results from energy losses incurred in magnetisation and demagnetisation. These are due in part to energetic interactions between domain walls and defects, and in part to rotation against the anisotropy.

3.3 Theories of domain wall-defect interactions

3.3.1 Inclusions

Kersten inclusion theory

Since a domain wall has an energy per unit area (§ 3.1.4), this acts as a 'surface tension'. An inclusion, such as a void or second-phase particle, embedded in the wall, reduces the wall energy in proportion to the area embedded (Kersten, 1943). For a spherical inclusion, the energy is minimised when the wall bisects the inclusion; this gives an energy reduction:

$$E_{area} = \pi r^2 \gamma \qquad (3.17)$$

where r is the inclusion radius, and γ the wall energy per unit area (Figure 3.2). For rod- or plate-shaped inclusions, the energy reduction is greatest when the plane of largest area is parallel to the wall.
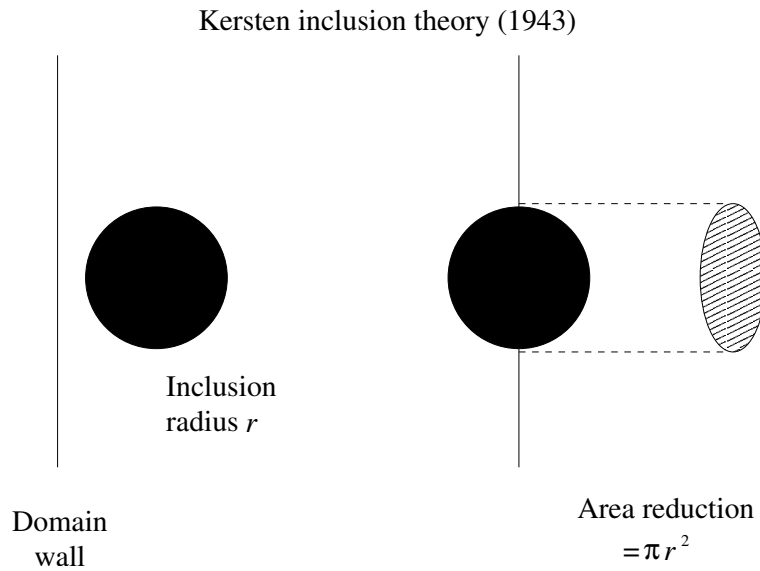
Figure 3.2: Energy reduction by intersection of inclusion with domain wall (Kersten, 1943).

Néel inclusion theory

Néel (1944) demonstrated that energetic interactions between domain walls and inclusions also arise from internal demagnetising fields. In general, an inclusion has different magnetic properties from the bulk. If the normal component of magnetisation is discontinuous across the inclusion/matrix interface, a distribution of free poles will be present, giving a demagnetising field (Figure 3.3 (a)).

For a spherical, nonmagnetic inclusion of radius r, the associated magnetostatic energy is:

$$E_{demag} = \frac{8\pi^2 M_S^2 r^3}{9} \tag{3.18}$$

where M_S is the saturation magnetisation of the matrix. Positioning the domain wall so that it bisects the inclusion redistributes the free poles, approximately halving the demagnetising energy (Figure 3.3 (b)). It is not necessary that inclusions be nonmagnetic to cause demagnetising effects; for example, Fe_3C is ferromagnetic at room temperature, but has a pronounced effect on the magnetic properties of ferritic iron (Dykstra, 1969). It still behaves as a magnetic inhomogeneity in ferritic steel because its magnetic properties are different from those of the bulk (Jiles, 1998).

The Néel demagnetising effect scales with r^3 (Equation 3.18), and therefore increases more rapidly than the Kersten area-reduction effect (Equation 3.17). However, for sufficiently large inclusions, it is energetically favourable to reduce the demagnetising energy of the inclusion by forming subsidiary domains around it, despite the additional domain wall energy involved. These thin, triangular 'spike' domains were predicted theoretically by Néel (1944) and subsequently observed by Williams (1947).

If an inclusion is bisected by a domain wall, closure domains can form, reducing the magnetostatic energy to zero (Cullity, 1972; Figure 3.4 (a)). When the main domain wall moves away from the inclusion under the action of an applied field, the subsidiary domain structure is drawn with it Figure 3.4 (b)) before becoming irreversibly detached and forming spike domains (c).

Craik and Tebble (1965) calculated that inclusions whose diameter was

Néel inclusion theory (1944)
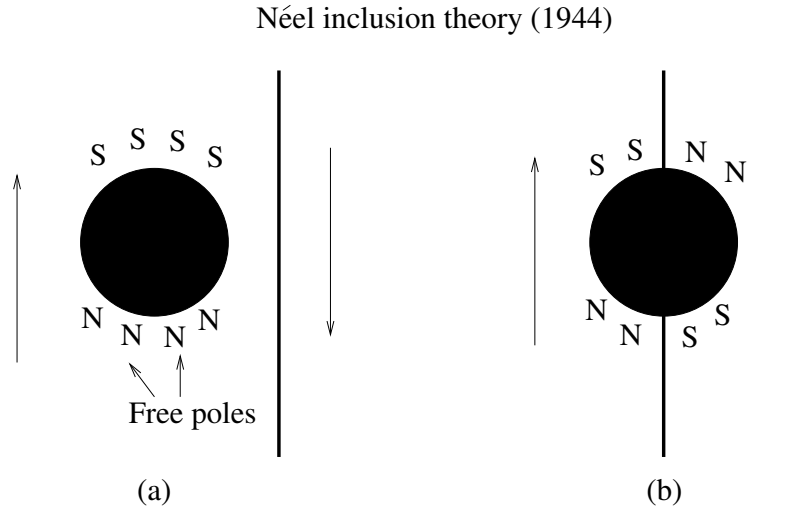
Figure 3.3: Distribution of free north (N) and south (S) poles around an inclusion (a) in the bulk (b) bisected by a domain wall (Néel, 1944).

equal to the domain wall width should be the most effective obstacles to domain wall motion.

For plate-like inclusions with magnetisation M_p having a planar interface with a matrix of magnetisation M_S, the free pole density at the interface ω_l* is given by:

$$\omega_l* = \mu_0(M_S \cos \alpha_s - M_p \cos \alpha_p) \tag{3.19}$$

where α_s and α_p are the angles made by the magnetisations M_S and M_p with the interface (Goodenough, 1954). Goodenough proposed that the angle α_p would adjust to minimise the total energy from free poles and the anisotropy of the inclusion.

3.3.2   Stress inhomogeneities

Stress affects the magnetic properties of a material via the converse of the magnetoelastic effect discussed above. The stress fields associated with vacancies, solute atoms and dislocations extend over a few atomic planes, but dislocations also interact with one another when sufficiently numerous, forming networks and tangles and creating a complex distribution of microstresses.
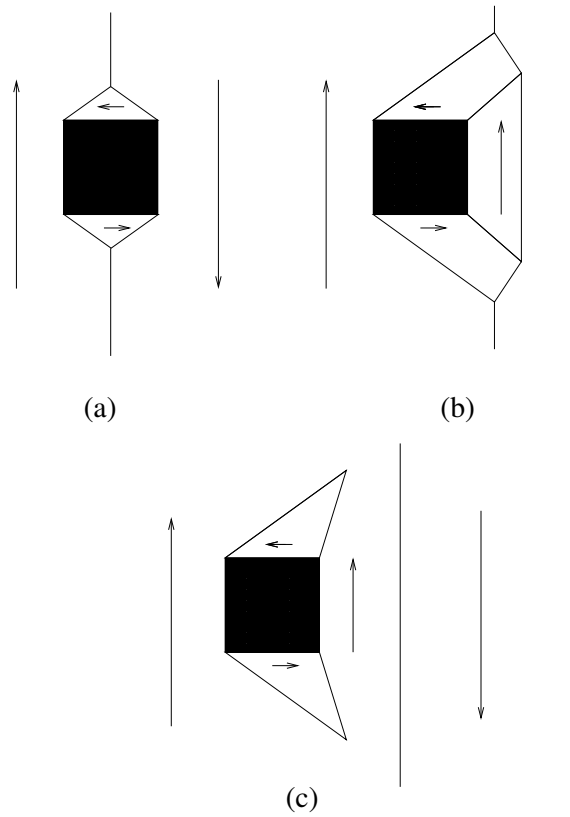
Figure 3.4: Interactions between domain wall and cubic inclusion with spikes (after Craik and Tebble, 1965): (a) domain wall at local energy minimum, (b) movement of main domain wall, (c) detachment of wall from inclusion.

The interaction between a domain wall and a stress field depends on the wall type (Träuble, 1969). 'Type-II' or '180°' walls are those separating domains whose magnetisation directions are antiparallel to each other. In this case, since the magnetostrictive strain is independent of the sense of the magnetisation, there is no strain difference between the domains. For other angles, domain wall motion will modify the local strain energy. Domain walls of this kind are known as 'Type-I' or 'non-180°' walls.[2]

It is therefore likely that Type-I walls interact more strongly with stress fields than do Type-II walls. The local stress state would determine both

---

[2]They are also sometimes called '90°' walls even in materials where the angle between the domains is not 90° .

the position and the energy of a Type-I wall, but the position of a Type-II wall would remain unchanged (Cullity, 1972). The longer-range interactions of Type-I walls with stress fields should make them less mobile, requiring a higher applied field before they will move (Träuble, 1969). As a result, magnetisation change at low applied fields is expected to occur predominantly by Type-II wall motion.

Calculations of the interaction force between domain walls and dislocations were made for several ideal cases by Träuble (1969). Scherpereel *et al.* (1970) calculated the energy of interaction of many different types of dislocations with Type-II and Type-I walls. On average, this was found to be higher for Type-II walls than for Type-I walls in iron, while the reverse was observed for nickel. This finding does not agree well with the model of Träuble. However, an experimental observation on an iron-based alloy appeared to support the Träuble interpretation (§ 3.4.2).

3.3.3   Grain boundaries

In general, two grains meeting at a grain boundary are at an arbitrary crystallographic orientation to one another, and their easy magnetisation directions are not parallel (Goodenough, 1954). If the applied field is not sufficient to rotate the grain magnetisations out of their easy directions, there will be a discontinuity in the component of the magnetisation normal to the grain boundary, and free poles will be present. If the angles made by the magnetisations $\mathbf{M}_S$ of the two grains with the normal to the grain boundary are θ_1 and θ_2, the surface pole density at the grain boundary is:

$$\omega* = \mu_0 M_S(\cos\theta_1 - \cos\theta_2) \tag{3.20}$$

Subsidiary domains may form at the boundary if the magnetostatic energy reduction achieved by this is larger than the domain wall energy required.

3.3.4   Models of domain wall dynamics

Two models of the 'pinning' of domain walls by microstructural defects have been proposed. The rigid-wall model considers an inflexible wall whose mo-

tion is retarded by statistical fluctuations in the density of defects, which modify the local potential energy. If defects are uniformly distributed on either side of the wall, the forces on it sum to zero, but otherwise a net force tends to move the wall to a more energetically favourable position.

The bowing-wall model, by contrast, allows the wall to bulge outwards between pinning points when a field is applied, before becoming detached when the wall area is too great. For some time, it was a subject of debate which of these models was correct (Hilzinger and Kronmüller, 1976).

Potential energy model

Kittel and Galt (1956) proposed that rigid-wall motion could be modelled by considering fluctuations of potential energy with position. This model has been widely used as a qualitative description of wall energetics and dynamics (*e.g.* Craik and Tebble, 1965; Astié *et al.*, 1982; Pardavi-Horvath, 1999). Defects, such as inclusions and dislocations, locally modify the 'constants' characterising the exchange interaction and magnetocrystalline anisotropy. The resulting potential energy wells act as pinning sites, holding the walls in place until sufficient energy is supplied to free them.

Using such a model, it is possible to estimate the magnetic properties of a material by making assumptions about its defect distribution (*e.g.* Jiles, 1998). Also, since the derivative of potential energy with respect to distance, $\partial E/\partial x$, is proportional to the magnetic field required to move the domain wall, the defect distribution can be related to the external applied field (Pardavi-Horvath, 1999; Figure 3.5). However, because of the demagnetising effect, the applied field necessary for unpinning is greater than the unpinning field value calculated from this model (Kawahara, personal communication). Also, the critical unpinning field depends on the magnetisation state of the surrounding domains as well as the properties of individual defects (Pardavi-Horvath, 1999).

A potential energy model should characterise the energy of the 'system', *i.e.* the wall and its surroundings, rather than the wall alone (Cullity, 1972). For example, the interaction between a domain wall and an inclusion involves reduction of the wall energy by decreasing its area, and reduction of the local

magnetostatic energy by free pole redistribution.
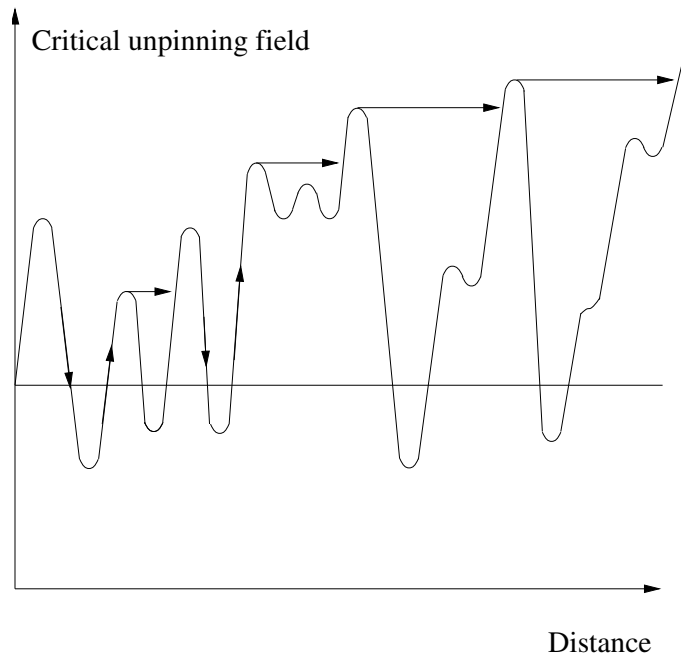
Figure 3.5: Field required for unpinning versus distance (adapted from Pardavi-Horvath, 1999). Arrows show the progress of a domain wall as the applied field increases. Once the field reaches a certain value, walls with critical unpinning fields less than this will not impede wall motion.

Certain microstructural features may act as potential energy maxima rather than wells (Pardavi-Horvath, 1999; Kawahara, personal communication). In this case, domain walls would be stopped, but not pinned, by the obstacle, and may lie close to, instead of directly on it. Some evidence of such behaviour has been observed by electron microscopy (Kawahara *et al.*, 2002).

Models including bowing

Hilzinger and Kronmüller (1976) extended existing theories of rigid wall motion in statistical defect distributions (Träuble, 1966; Pfeffer, 1967) by allowing wall bowing. Curvature may occur parallel or perpendicular to the magnetisation direction, but in the perpendicular case, stray fields will result

since the wall is no longer parallel to an easy direction.

A computer simulation, using randomly distributed defects and wall-defect interaction forces of varying magnitudes, demonstrated that wall-bowing would occur given sufficiently large interaction forces (Hilzinger and Kronmüller, 1976). The two cases of rigid and bowing walls could be described by a single theory with a limiting condition separating the two types of behaviour. Curvature perpendicular to the magnetisation direction was also predicted when the wall-defect interaction energy was sufficiently high (Hilzinger and Kronmüller, 1977). When bowing occurs, the wall position is no longer determined simply by potential energy fluctuations; it was suggested that motion could instead be modelled using a frictional force.

3.3.5 Correlated domain wall motion and avalanche effects

Porteseil and Vergne (1979) found that experimental results for the magnetisation curve in a Fe-Si single crystal (composition not specified) could be reproduced using a model of 'coupled' domain wall motion, *i.e.* that the movement of one domain wall could stimulate another to move. The coupling was attributed to the modification of the distribution of free poles when the first wall moved. Tiitto (1978) also discussed the same possibility from the point of view of steel microstructure. He considered two possible methods for coupling between domain wall motion events. Firstly, there is direct magnetostatic coupling between domain walls at either end of a domain, and secondly, changes in the effective magnetising field occur as a result of magnetisation changes nearby. The first of these mechanisms was considered to be the stronger, because it would occur over a shorter range. Tiitto proposed a model of magnetisation based on such correlated motion, and proposed a relationship between grain size and magnetic Barkhausen noise (one of the macroscopic magnetic properties), based on this.

3.3.6 Mechanism of magnetisation reversal

Goodenough (1954) assessed the possible mechanisms of reverse domain nucleation. Inclusions and grain boundaries, at which subsidiary domain structures are known to occur in non-saturated samples, were proposed as nucleation sites. If the spike domains on large spheroidal inclusions are to contribute to magnetisation reversal, their magnetisation must be rotated against the anisotropy energy to become antiparallel to the bulk magnetisation. Goodenough showed that, in materials with cubic symmetry, the applied field required to accomplish this is too large for it to be a viable reversal mechanism. Even in uniaxial materials, in which the energy of reverse domain formation is lower, a very large field is required to detach the domains so formed from their nucleating particles. Goodenough therefore considered that spike structures of this kind did not contribute to magnetisation reversal.

At grain boundaries or planar inclusions, by contrast, Goodenough calculated the reverse domain formation energy to be much lower. Reverse domains were modelled as prolate ellipsoids and assumed to be continuous across the grain boundary. Figure 3.6 is a schematic of such a layout, based on the description by Goodenough.

A further site for domain nucleation suggested by Goodenough is the material surface. Unless parallel to an easy direction, this has free poles, which may be compensated by domain formation.
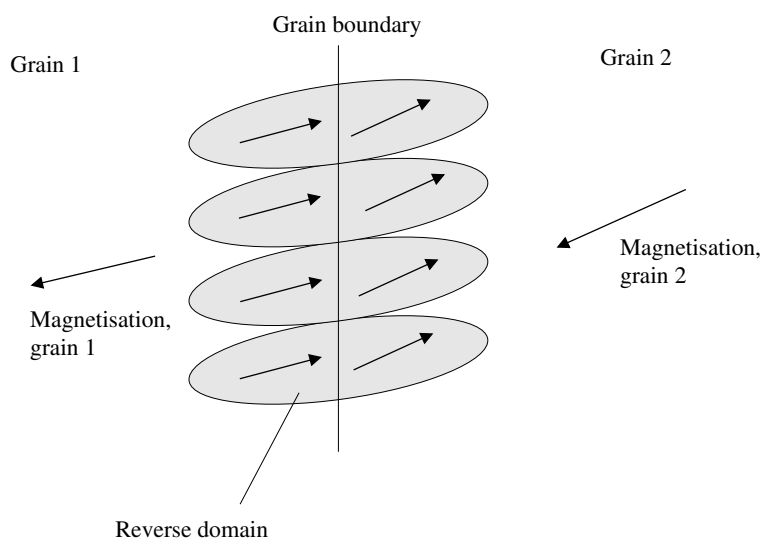
Figure 3.6: Reverse domain creation at a grain boundary (based on Goodenough, 1954).

3.4 Direct observation of domains and domain walls

Many of the predictions of domain theory have been confirmed by direct observations of domains and walls using magnetic contrast techniques. The earliest images were obtained using a very finely divided magnetic powder suspended in a liquid and spread over the sample surface (Bitter, 1931). At positions where domain walls intersect the surface, the resulting stray fields attract the particles more strongly than do the surrounding regions (Kittel, 1949).

Magneto-optical effects

In optical microscopy observations, the interaction between magnetic fields and polarised light is used to obtain contrast. The plane of polarisation of an incident beam is rotated if it is transmitted through, or reflected from, a magnetised material (Williams *et al.*, 1951; Fowler and Fryer, 1952; Fowler and Fryer, 1956). These phenomena are known as the Faraday and Kerr effects respectively. The rotation angle depends on the component of the

magnetisation in the direction of the incident beam, which depends in turn on the magnetisation direction of the domain on which the beam impinges. Domain contrast is obtained by setting an analyser in the extinction position for one of the sets of domains. The Faraday effect is of limited use for domain imaging since it requires an optically transparent medium, but Kerr microscopy is used extensively.

Electron microscopy

An electron beam incident on a magnetic domain is deflected in a direction determined by the domain magnetisation direction. In a transmission electron microscope (TEM), this can be used for magnetic contrast imaging ('Lorentz microscopy'). The beam deflection is extremely small, so no contrast is obtained using bright-field conditions, but by displacing the objective aperture so that only electrons deflected by certain sets of domains are allowed through, an image can be obtained in which some domains appear bright and others dark (Boersch and Raith, 1959). This is known as the Foucault method. Another technique, the Fresnel method, is used to observe domain walls. By going from an underfocused to an overfocused condition, domain walls change from bright to dark or *vice versa*. This enables domain walls to be distinguished from other features, such as dislocations, which do not show this behaviour (Hale *et al.*, 1959).

Scanning electron microscopy (SEM) techniques have also been developed. In highly anisotropic materials, in which the magnetisation has a component perpendicular to the surface, secondary electrons arising from a beam normally incident to the surface will be deflected in opposite directions by antiparallel domains. This gives rise to alternating light and dark bands in the secondary electron image (Type I contrast, Banbury and Nixon, 1969).

A method suitable for less anisotropic materials relies on the deflection of electrons after they enter the specimen (Type II contrast, Fathers *et al.*, 1973). The domain magnetisation direction governs whether deflection occurs towards or away from the surface, and hence determines the number of backscattered electrons emitted from that domain. This method requires a tilted specimen and a precise combination of electron beam parameters,

and has only successfully been applied in strongly magnetic materials such as Fe-3 wt. %Si (Jakubovics, 1994).

3.4.1 Surface domain structures

Subsidiary domain structures at sample surfaces, as predicted by Goodenough (1954) have been observed in practice. Figure 3.7 illustrates the dependence of domain structures on the orientation of the surface plane in Fe-3 wt. % Si with no preferred texture (Nogiwa, 2000). Simple, banded domain structures were found when the plane normal was close to {101}. Near {001}, arrowhead-shaped domains formed in addition to the bands. Between {101} and {001}, the domain walls were wavy, and small, pointed domains occurred within larger domains of the opposite type. When the surface plane was close to {111}, the domain structure was fine and complex, and individual domains were difficult to resolve.
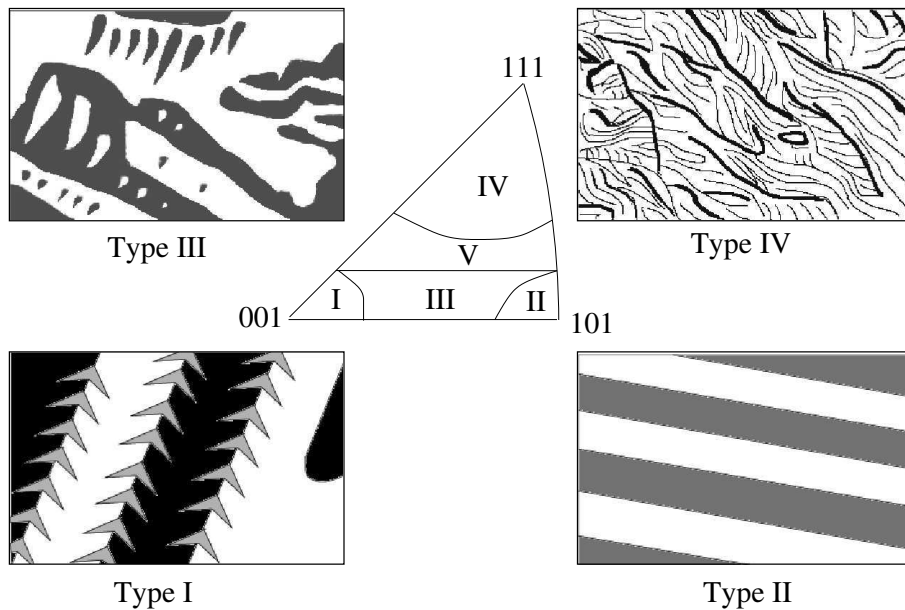
Figure 3.7: Effect of surface plane orientation on the domain structures observed in Fe-3 wt. % Si (Nogiwa, 2000)

The easy directions in Fe-3 wt. % Si are $< 100 >$. In order for at least one easy direction to lie in a plane, by the Weiss Zone Law, one of the indices

{*hkl*} of the plane must be zero, and for two perpendicular easy directions to be present, two of the indices must be zero. Hence, for {101} planes, only one pair of antiparallel easy directions lies in the plane, giving straight-sided domains (II). In {100} planes, the formation of domains magnetised at 90° to the main domains may occur (I). The {111} planes contain no easy directions so, in order to reduce the magnetostatic energy, a complex closure structure is generated on the surface (IV). The intermediate domain structure (III) occurs between {001} and {101}, so it should contain one easy direction. 90° walls are not allowed in this structure, so magnetostatic energy reduction occurs by the formation of small antiparallel domains within the main domains.

3.4.2   Magnetisation process in a single crystal

Figure 3.8 shows the evolution of the domain structure in annealed, single-crystal Fe-3.5 wt. % Si on increasing the applied field (Seeger *et al.*, 1969). The surface observed was parallel to the (100) plane, so that traces of 180° walls were parallel to $< 100 >$ directions, and traces of 90° walls were at 45° to $< 100 >$. At low fields, magnetisation change occurred solely by the movement of 180° walls, and only when this could no longer occur did other walls begin to move. The 90° walls bounding thin spikes in (b) become fully developed echelon domain structures at higher field (c).

3.4.3   Domain wall behaviour at grain boundaries

The domain structures at grain boundaries in thin iron foils were observed by Lorentz microscopy (Tobin and Paul, 1969). The crystallographic orientations of the grains were determined using electron diffraction. Five distinct types of structures were identified. In the no-interaction case, the wall passes straight through the boundary (a). The 'double spike' domain structure is continuous across the grain boundary and magnetised antiparallel to the bulk (b). The 'single spike' domain (c), by contrast, stops at the grain boundary, and its magnetisation direction is at 90° to that of the bulk. The echelon structure (d) is a series of domains at 90° to one another, separated
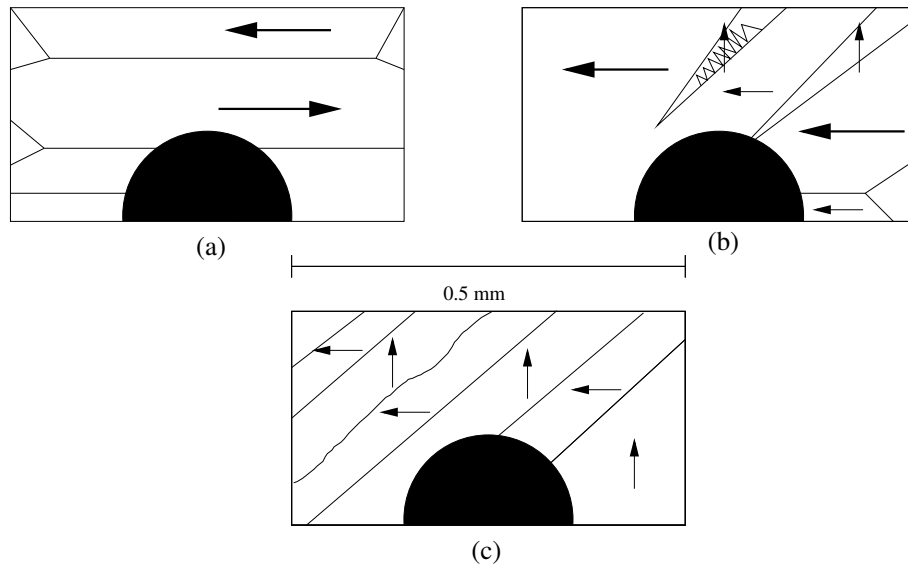
Figure 3.8: Domain structures in Fe-3.5 wt. % Si, observed by Bitter technique (Seeger *et al.* , 1969). (a) zero field; (b), (c) field increasing. The large black area is a dark area appearing on the original micrographs, perhaps due to surface damage.

from the bulk by a combination of 90° and 180° walls. The final case is the closure domain, in which the magnetisation direction is tangential to the grain boundary (e). Later observations by Degauque and Astié (1982) confirmed of the existence of echelon domains and single spikes in annealed high-purity iron using high-voltage TEM on thicker foils.

The free pole density at grain boundaries can be estimated using Equation 3.20 if the magnetisation directions of the domains are known. Tobin and Paul estimated these, assuming that domains were magnetised approximately in the easy directions of iron and that the domain arrangement was consistent with minimising anisotropy and magnetostatic energy. By further assuming that magnetisation vectors lay in the plane of the foil, the pole density was calculated. This last assumption is valid if the anisotropy energy required for the magnetisation to lie in a non-easy direction along the surface is less than the magnetostatic energy for $\mathbf{M}$ to have a component normal to the surface.
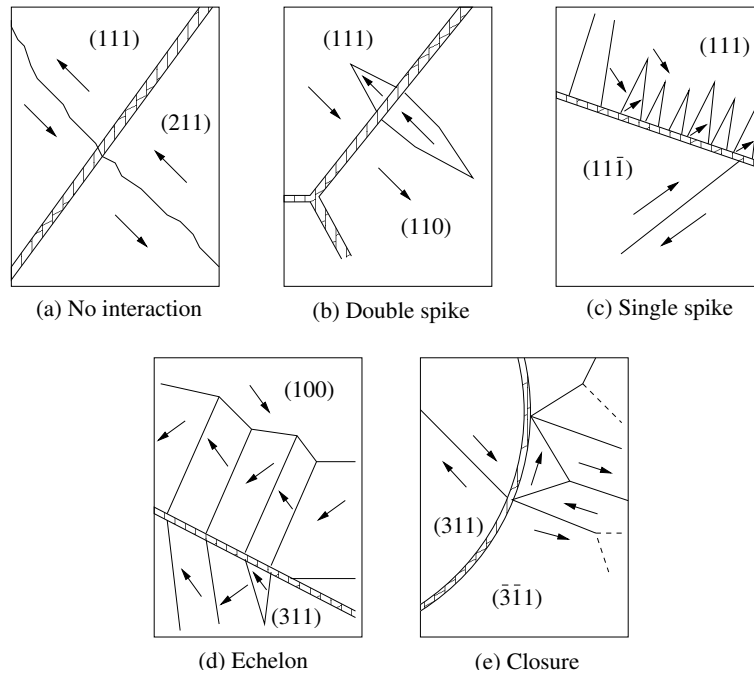
Figure 3.9: The five types of interaction between grain boundaries and domain walls, shown in order of increasing magnetic pole density at the grain boundary (Tobin and Paul, 1969).

The no-interaction and double-spike configurations were found to have the lowest pole densities, and closure domains the highest, with single-spike and echelon structures in the low-to-intermediate range. It is notable that $90°$ walls do not occur at low pole densities.

The observations of double spike domains are consistent with the theoretical analysis of Goodenough (1954), but he did not predict the existence of $90°$ closure walls at grain boundaries. It appears that if an easy direction occurs parallel to the wall, it is favourable to form such a closure domain. These domains, unlike the $180°$ reverse spike domains, are not expected to contribute to magnetisation reversal according to the arguments of Goodenough.

Lorentz microscopy observations of domain walls and grain boundaries during the magnetisation of spinel ferrites showed that if a domain wall was parallel to a grain boundary, the wall was stopped completely by the

boundary (Lin *et al.*, 1984)[3]. If the wall intercepted the grain boundary obliquely, its progress was retarded, with the least retardation occurring when the boundary and wall were normal to one another.

Closure domains were observed at grain boundaries in ferritic steel using Lorentz microscopy (Hetherington *et al.*, 1987). Domain walls were attached to triple junctions, and grains contained a substructure of domains which needed only a small applied field to move.

3.4.4 Effect of grain boundary misorientations

At a grain boundary, two differently oriented crystal lattices meet. One of the ways to characterise the geometry of grain boundaries is the coincidence site lattice (CSL) concept, which is discussed in more detail in Chapter 7. If the lattices from the two grains are superposed, with a common origin, then for certain pairs of grain orientations, a fraction of the lattice points of the two grains will coincide. The superlattice of coincident lattice points is a CSL, and is characterised by a parameter Σ, where 1 in Σ of the lattice points are coincidence sites. The Σ notation is applied to boundaries between grains whose lattices form, or nearly form, a CSL. Closer matching is expected at such boundaries than at those with no special orientational relationship, which are known as random boundaries. Low-angle boundaries are those in which the difference in orientation angle between the adjacent grains is $\leq 15°$. This misorientation is accommodated by a periodic array of dislocations.

Low-angle and random boundaries

Figure 3.10 (a) and (b) show schematically the domain arrangements observed at a low-angle grain boundary in Fe-3 wt. % Si using Kerr microscopy (Kawahara *et al.*, 2000). At one position, the domains were almost continuous across the boundary (a). In another region, the structure was disrupted, but the domains formed on the boundary were relatively large (b).

---

[3]Spinel ferrites are ferrimagnetic but, because they have a similar domain structure to ferromagnetic materials, these observations are still useful for understanding ferromagnetic domain wall behaviour.

At a random boundary the structure was in one region discontinuous (Figure 3.10 (c)), and in another continuous, with inclination of the bands (d).

The free pole density at a grain boundary depends not only on the angle between the magnetisation vectors in the adjacent grains, but also on the local orientation of the grain boundary with respect to these vectors (Shilling and Houze, 1974). It is very much reduced if the boundary approximately bisects the angle between the magnetisation vectors. This accounts for the difference between the domain structures in Figure 3.10 (c) and (d) (Kawahara *et al.*, 2000). In (c), the boundary is in an asymmetric position, resulting in a complex domain structure, but in (d), the symmetric arrangement allows simple banded domains to continue across the boundary.
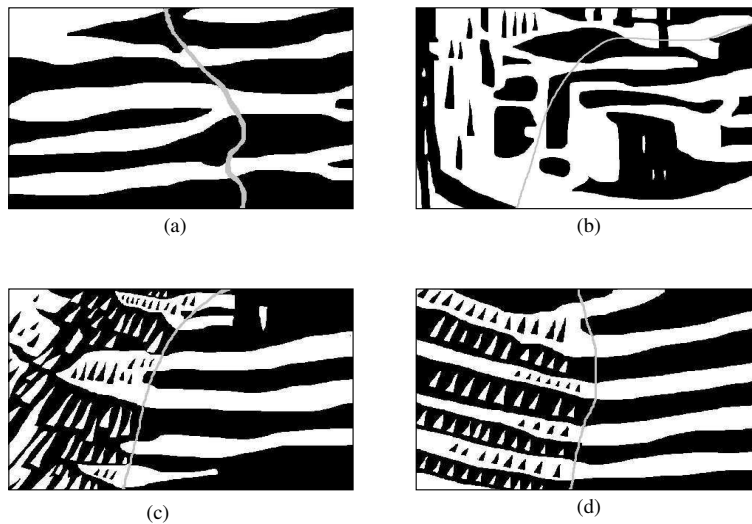
Figure 3.10: Domain structures observed at grain boundaries in Fe-3 wt. % Si by Kerr microscopy (schematic): (a), (b) low-angle boundary, (c), (d) random boundary (Kawahara *et al.*, 2000).

Significant differences were observed between low-angle and random boundary domain structures during magnetisation. At the low-angle boundary, only a small applied field was required to transform the arrangement in Figure 3.10 (b) into one of parallel-sided domains. As the field was increased, one set of domains gradually widened at the expense of the antiparallel set. The grain boundary appeared to act as a domain source, at which new do-

mains nucleated, and a sink into which they disappeared. At the random boundary, no abrupt changes were observed. Instead, one set of bands grew gradually at the expense of the other until the majority of the region was a single domain containing small antiparallel spikes.

Kawahara *et al.* discussed the possible influence of grain boundary stress fields, as well as free poles, on the domain structure. Because of the dislocation arrays at low-angle boundaries, the strain energy is expected to be higher than at random boundaries, where there is no periodic structure (Kawahara, personal communication). If magnetoelastic effects were the predominant source of domain wall-grain boundary interaction energy, this interaction would instead be stronger at low-angle boundaries, but since this is not so, it appears that magnetostatic energy from misorientation is more important.

Coincidence boundaries

Lorentz microscopy was used to study the interactions between domain walls and grain boundaries of different types (Kawahara *et al.*, 2002). Domain walls were observed lying directly on grain boundaries, in a ceramic ferrite sample. A triple junction between low-angle grain boundaries acted as a pinning site, holding in place five domain walls. A void also acted as a domain wall attractor, bending walls towards itself.

In a sample of pure nickel, domain walls were initially only observed on one side of a random boundary. On changing the applied field, the walls moved gradually towards the boundary but, as they approached closely, the domain configuration changed abruptly, and reverse domains appeared in the neighbouring grain. The domain wall moved so that part of its length lay along the boundary, before breaking away in another abrupt change.

Figure 3.11 is a schematic of another observation on pure nickel in which a similar combination of gradual and sudden processes was seen. The interactions between domain walls and grain boundaries depended on the angle of approach. Walls almost normal to a grain boundary were affected very little by it (a), but those approaching at a small angle were deflected to lie parallel to the boundary (b). This confirms the findings of Lin *et al.* (1984). However, low-angle boundaries were an exception, interacting only weakly
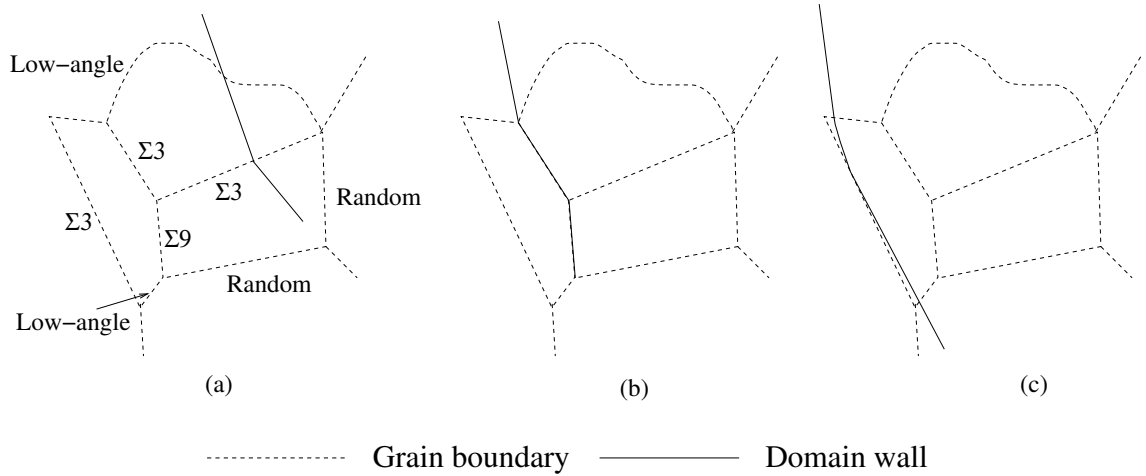
Figure 3.11: Interaction between a domain wall and grain boundaries of different types (schematic): (a) Domain wall interacts weakly with $\Sigma 3$ boundary because of almost perpendicular approach. Weak interaction between wall and low-angle boundary despite small impingement angle. (b) Domain wall jumps to lie parallel to $\Sigma 3$ boundary. (c) A jump to another $\Sigma 3$ boundary, but the wall appears to lie beside the boundary rather than on it (Kawahara *et al.*, 2002).

with domain walls even when approached at a small angle (Kawahara *et al.*, 2002).

On close inspection, domain walls appeared to lie just beside $\Sigma 3$ boundaries, but directly on random boundaries. Domain walls in potential energy wells would be found at the centre of the well, but walls impeded by potential energy maxima would be stopped some distance from the centre of the maximum. It was therefore suggested that random boundaries acted as wells, and $\Sigma 3$ boundaries as maxima.

3.4.5 Effect of grain size

In nanocrystalline nickel, with grain size < 1 μm, domain walls lay along grain boundaries for almost the whole of their length, only rarely passing into the grain interior (Kawahara *et al.*, 2002). This contrasts with the behaviour seen in Figure 3.11, in which the grain size was several tens of

μm. The greater concentration of grain boundaries in the nanocrystalline sample allows domain walls to lie on grain boundaries without significant deviation.

The domain width in Fe-3 wt. % Si increased with increasing grain size (Shilling and Houze, 1974). A grain boundary is more likely to be in an approximately symmetrical position between the magnetisation directions in adjacent grains when the misorientation angle between the grains is small. This becomes less likely with decreasing grain size. Larger demagnetising fields, and the consequent development of a finer domain structure, is therefore likely in finer-grained materials.

3.4.6   Effect of deformation

Heavy deformation of a Fe-3.5 wt. % Si single crystal produced a domain structure in which only one pair of antiparallel magnetisation directions was represented, even though directions perpendicular to these were permitted by symmetry (Seeger *et al.*, 1969). Deformation is believed to favour 180° over 90° wall motion because 90° walls interact more strongly with stress fields, becoming immobilised in a highly dislocated structure.

In-situ magnetising experiments on annealed, lightly deformed and heavily worked samples of pure iron demonstrated the pinning effect of dislocations on domain walls (Degauque and Astié, 1982a). The annealed material contained a few small tangles of dislocations, which acted as strong pinning sites, retarding the movement of the domain walls to which they were attached while other, unpinned domains moved more freely. Mixed dislocations in the lightly strained sample and long screw dislocations in the heavily worked sample also pinned domain walls. Work on macroscopic magnetic properties suggested that domain wall motion was more strongly pinned in the heavily worked sample (Astié *et al.*, 1981), but such differences were difficult to discern using TEM.

3.4.7   Second-phase particles and microstructural differences

Lath microstructures

Domain structures in bainitic and martensitic forms of the same carbon-manganese steel composition were compared (Beale *et al.*, 1992). In specimens with long, parallel laths, a regular structure of 180° walls, branching into 90° walls, was observed. In a sample in which only part of the structure contained laths, the domain walls were found to stretch across the laths, and to move parallel to them when the field was applied. Apart from this one study, domain arrangements in lath microstructures do not seem to have been studied extensively.

Ferritic-pearlitic steels

Hetherington *et al.* (1987) concluded that the domain wall arrangement in pearlitic steels depended on the orientation of the walls with respect to the cementite lamellae. If a wall lies parallel to a lamella, it is strongly pinned, whereas if it is perpendicular, it moves easily until it meets another grain in which the lamellae are oriented differently.

It is also believed that the lamellar spacing plays an important role in the domain layout (Lo *et al.*, 1997a). Small spacings gave small domains which were mainly bounded by Type-II walls following the ferrite/cementite interface. When the spacing was larger, domains extended across several lamellae, and Type-I walls were observed. Dynamic magnetisation experiments showed that in the finer pearlite, the nucleation and growth of reverse domains required a higher applied field, and individual domain wall jumps were smaller.

In both fully pearlitic and fully ferritic microstructures, domains of reverse magnetisation nucleated when the field was reduced from saturation, but the growth of domain walls across the grain occurred more rapidly in the ferritic sample (Lo and Scruby, 1999). In the pearlitic sample, it did not occur until the applied field direction had been reversed. These findings demonstrate the pinning strength of pearlite lamellae.

Lamellar and spheroidal cementite

The pinning effect of lamellar and spheroidised pearlitic microstructures were compared (Lo *et al.*, 1997b). In both cases, the cementite particles acted as domain wall pinning sites, but coarser domains were observed when the carbides were spheroidal. On reduction of the field from saturation, domain wall motion required a larger reverse field in lamellar than in spheroidised pearlite. Closure domains were observed on the carbide particles in the spheroidal microstructure, and these interacted with the 180° walls as they moved.

The results from experiments on pearlite show that lamellar particles are a more effective impediment to domain wall motion than spheroidal particles. This may be due to the flat, continuous nature of the particles, or to their parallel, regularly spaced arrangement, or to a combination of both. It does not appear that any observations have been made on needle- or plate-shaped particles such as M_2X in tempered steels. If the flat, elongated shape is the more important factor in pinning, these particles, too, would act as strong pinning sites. However, if parallelism is more important, then M_2X may only pin weakly since it tends to be small.

3.5   Conclusions

Experimental observations of domain structures in ferromagnetic materials show a remarkable agreement with the theory which, in some cases, pre-dated them by several decades. It has been shown that domains interact with grain boundaries, inclusions and dislocations. Some of the main findings from these studies are as follows:

- Cubic or spheroidal inclusions interact with domain walls by wall area reduction and by setting up demagnetising fields. Inclusions larger than a critical size have subsidiary spike domains.

- Lamellar precipitates in steel have a stronger pinning effect on domain walls than do spheroidal precipitates.

- Specimen surfaces nucleate fine domains to reduce magnetostatic energy if they are not parallel to crystallographic planes containing easy directions.

- It has been observed that at low values of applied field, magnetisation change occurs preferentially by 180° wall motion.

- Domain walls tend to be attracted towards voids and grain boundary triple (or multiple) junctions.

- The domain structure at grain boundaries depends on the misorientation between the adjacent grains, and on the angle made by the grain boundary plane with the grain magnetisations.

- The dynamic interaction between grain boundaries and domain walls depends on the angle at which the domain wall intercepts the grain boundary, and also on the grain boundary character. Low-angle boundaries exert a weaker pinning effect than boundaries of other types.

- The width of domains has been observed to increase with increasing grain size.

- In a material with finer grains, domain walls were observed to lie along grain boundaries for far more of their length than in coarser-grained material.

- It is predicted that reverse domains should nucleate on grain boundaries, surfaces and planar inclusions, but not on cubic or spheroidal inclusions.

Chapter 4

Magnetic Properties in Nondestructive Testing

It has been known for many years that the magnetic properties of steels depend on their composition and heat treatment. Mechanically harder steels have superior properties as permanent magnets than softer steels, hence the terminology of 'hard' and 'soft' magnetic materials. Curie (1898) found a relationship between magnetic behaviour and carbon content in permanent magnet steels, and Evershed (1925) observed a deterioration of magnet steel properties over time, which he related to slow metallurgical changes. Such relationships suggested that magnetic measurements could be used as a nondestructive testing (NDT) method to determine materials properties. In recent decades, many investigations have been carried out to develop such techniques; progress has been reviewed by Blitz (1991), Swartzendruber (1992), Devine (1992), Sipahi (1994), Sablik and Augustyniak (1999) and Ara (2002).

4.1   Hysteresis properties

4.1.1   The hysteresis loop

Figure 4.1 is a plot of magnetisation M against applied field H. On application of a field to a demagnetised sample, M increases with H, reaching the saturation magnetisation M_S if a sufficiently large field is applied. When H is reduced, and subsequently cycled between positive and negative directions,

M follows a hysteresis loop. A *major loop* (solid line) is one in which the saturation magnetisation M_S of the material is reached; if this is not the case, the curve is a *minor loop* (dashed line). The parameters most commonly used to characterise hysteresis are the field H_C required to reduce M to zero, the value M_R of M when $H = 0$, and the hysteresis energy loss W_H, which is determined from the area enclosed by the loop. H_{max} is the maximum applied field and H_S the field at which $M = M_S$.

The positions of greatest slope change are known as 'knees'; one of these is marked on Figure 4.1. The slope dM/dH of the initial magnetisation curve at $(H = 0, M = 0)$ is the initial differential susceptibility χ'_{in}, and that of the hysteresis loop at $H = H_C$ is the maximum differential susceptibility χ'_{max}. The terminology 'square' and 'sheared' is used to describe loops with large and small values of χ'_{max} respectively. The hysteresis parameters are in general regarded as independent, but in some materials, linear relationships have been found between, for example, W_H and H_C (Jiles, 1988a, b).
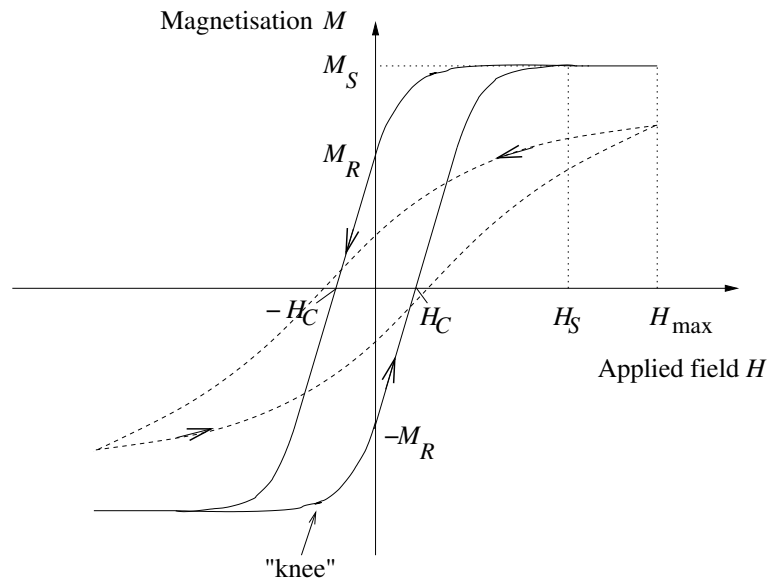
Figure 4.1: A major hysteresis loop (solid line), showing the coercive field H_C, remanence M_R and saturation magnetisation M_S, and a minor loop (dashed line). The arrows show the direction of magnetisation.

4.1.2 Alternative terminology

The magnetic induction $\mathbf{B} = \mu_0(\mathbf{H} + \mathbf{M})$ is sometimes used instead of $\mathbf{M}$. B-H and M-H loops contain the same information but different terminology is used: B_S and B_R instead of M_S and M_R, respectively. The slope of a B-H loop, $\mathrm{d}B/\mathrm{d}H$, is the differential permeability, μ'; the maximum value of this usually occurs at $H = H_C$ and is denoted $\mu'_{\max}$. The magnetic flux $\mathbf{\Phi}$ is the product of $\mathbf{B}$ and the sample cross-sectional area.

H_C is usually referred to as the coercive field, and B_R and M_R as the remanent induction and remanent magnetisation respectively. The alternative terms 'coercivity' and 'remanence' are also used, but an emerging convention (noted by Jiles, 1998) is to reserve these last two terms for major loops only[1].

Hysteresis experiments for use in NDT usually involve measurement of the $M - H$ or $B - H$ loop and extraction of a selection of the above parameters. An alternative approach, developed by Davis (1971) and Willcock and Tanner (1983a, b), is to express the loop in terms of Fourier coefficients. This method is used in industry for stress monitoring using magnetic hysteresis (Tanner, personal communication), and has the advantage that the entire data set is used, but it has not so far been adopted for microstructure-based investigations.

4.2 Magnetic noise

4.2.1 Barkhausen effect

Barkhausen (1919) discovered that, during the magnetisation of an iron bar, many short-lived voltage pulses were induced in a coil wound around the bar. These were detected as audible clicks in a loudspeaker. By electromagnetic induction, the voltage depends on the rate of change of magnetisation with time; discrete pulses imply abrupt changes in magnetisation. Even when care was taken to change the magnetising field smoothly, the discontinuities persisted, demonstrating that magnetisation was an intrinsically discrete pro-

---

[1]A distinction also exists between the *coercivity*, at which $B = 0$, and the *intrinsic coercivity*, at which $M = 0$, but this can be neglected for steels, in which H_C is small.

cess. Barkhausen used this observation to support the hypothesis of magnetic domains predicted theoretically by Weiss (1906, 1907). The characteristics of the Barkhausen noise (BN) signal depend on several factors, including microstructure.

4.2.2   Magnetoacoustic effect

The abrupt motion of Type-I domain walls is accompanied by a change in the magnetostrictive strain. This causes an acoustic wave, which travels through the material and can be picked up on the surface by a piezoelectric transducer (Lord, 1975). Since such magnetoacoustic emission (MAE) arises only from Type-I wall motion, but BN can be produced by any sudden change in the magnetisation state, measuring both properties gives complementary information.

4.2.3   Magnetic noise measurement

The basis of a BN measurement system is an electromagnetic yoke to produce an alternating field and a pickup coil to detect the noise pulses, but two variations exist. The sample may be positioned within the yoke, with the pickup coil surrounding the sample (Figure 4.2 (a)). This restricts the sample size and shape, and is therefore inconvenient for NDT. The alternative method uses a yoke placed onto a flat sample, and a pickup coil on or near the surface (Figure 4.2 (b)). MAE measurements are made using an arrangement similar to (b), but with a piezoelectric transducer bonded directly to the sample surface instead of a pickup coil.

Comparisons of magnetic noise literature reveal considerable differences in yoke geometry, experimental conditions and signal processing. In some cases, the influences of these factors on the signal have been investigated (§ 4.9), but such characterisations are not comprehensive.

4.2.4   Data analysis

The raw magnetic noise data are a series of voltage pulses, and their associated applied field values, obtained as a function of time (Figure 4.3 (a)).
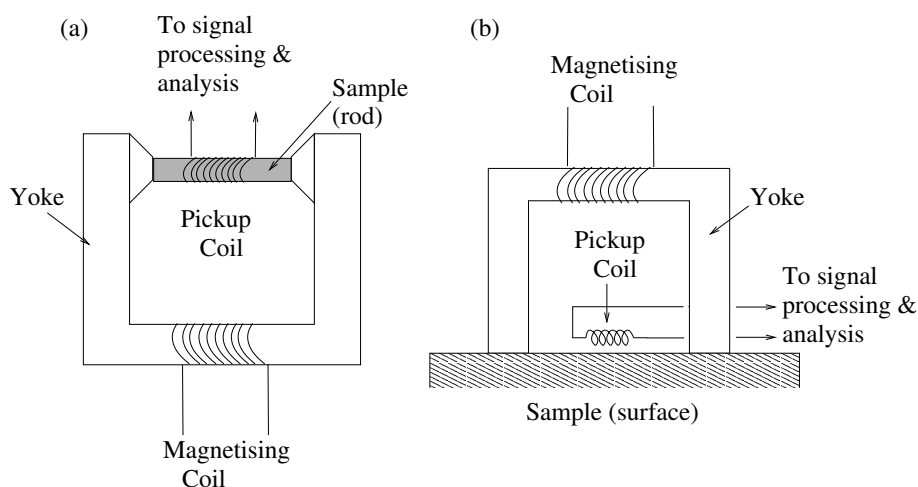
Figure 4.2: Typical measurement apparatus for magnetic noise: (a) magnetising yoke with rod-shaped specimen, (b) surface sensor.

The noise signal consists of a stochastic component superposed on a smooth variation with applied field. To obtain this variation, the root-mean-square (RMS) of the noise over several field cycles is obtained; a smoothing algorithm may also be applied. Figure 4.3 (b) shows the RMS noise in the increasing-field direction (solid line) and in the opposite direction (dotted line). These two curves are usually mirror images in $H = 0$, so only one direction is displayed. All subsequent diagrams and discussions will use increasing-field curves unless otherwise stated.

Fourier analysis can be used to study the noise frequency content (c). The square of the voltage is often referred to in the literature as the 'noise power', and a plot such as (c) as a frequency spectrum. Other plots frequently encountered in the literature are the size distribution of noise pulses ('pulse height distribution, PHD' (d)) and the number of pulses versus time or applied field (not shown, but of similar form to (b)). In addition, single parameters have been used to characterise the noise signal: the maximum pulse size, RMS pulse size, total number of pulses and the noise energy, calculated as the integral of the RMS noise signal over a whole cycle.

The large number of characterisation methods can lead to some difficulty in comparing the results of investigations, since the same quantities are not

always measured.
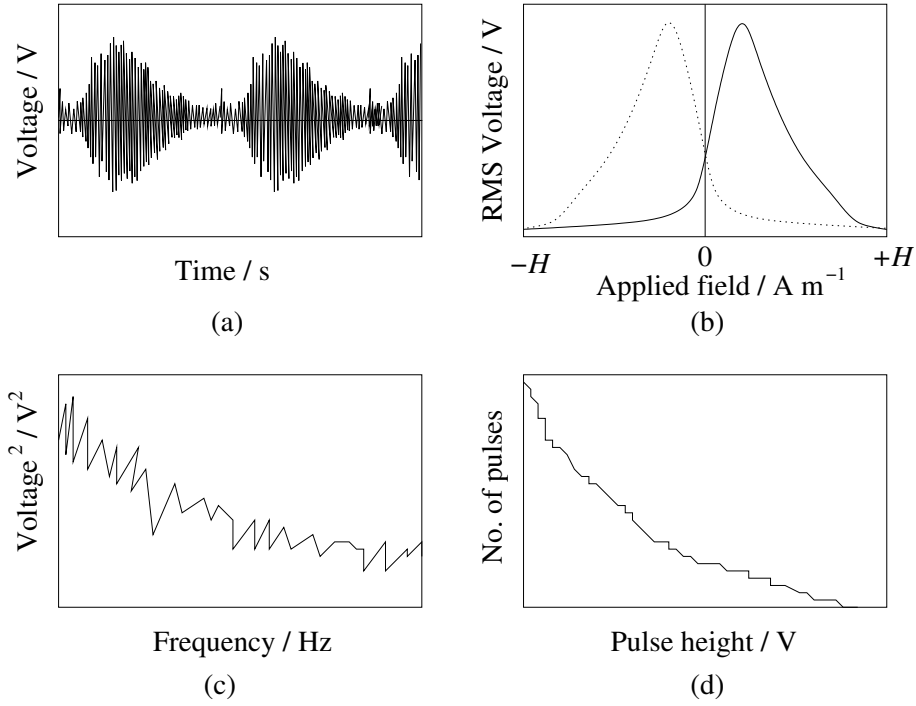
Figure 4.3: Magnetic noise plots: (a) Raw noise versus time. (b) Root-mean-square (RMS) noise versus applied field. (c) Noise voltage versus frequency (Fourier transform). (d) Pulse height distribution plot.

4.3 Applications of magnetic NDT

4.3.1 Microstructural type determination

Martensitic steels consistently have the greatest H_C, and ferrite-pearlite microstructures the least, with bainitic steels intermediate between these extremes (Jiles, 1988b; Mitra *et al.*, 1995, Saquet *et al.*, 1999). This should allow identification of the basic microstructural state with a simple magnetic measurement. BN measurements have also been used successfully to differentiate between microstructural states across the heat-affected zone of a weld (Moorthy *et al.*, 1997a).

4.3.2   Empirical correlations

Correlations for the determination of mechanical or microstructural properties using magnetic measurements have been found in many materials. Examples include extensive work in the former Soviet Union on monitoring the quality of heat-treatment and hardening in a variety of steels (Mikheev *et al.*, 1978; Kuznetsov *et al.*, 1982, Zatsepin *et al.*, 1983; Mikheev, 1983). Devine (1992) describes many more such results.

The important consideration for NDT is that there is a monotonic change in the magnetic property within the range of interest, as pointed out by Halmshaw (1991). Correlations are specific to particular microstructures and ranges of composition and temperature, and are liable to fail outside these limits. For example, in a pearlitic rail steel, the correlation between coercive field and hardness was poor at room temperature, but good at high temperatures (Bussière *et al.*, 1987). The suggested reason for this was that at high temperatures, the Fe_3C particles were above their Curie temperature T_C, and so acted as nonferromagnetic inhomogeneities.

Findings such as these have led to investigations of the effects of individual microstructural features, such as grain boundaries, dislocations and inclusions, on the magnetic properties.

4.4   Grain boundaries

4.4.1   Grain size effects

High-purity materials

Two distinct theoretical models predict that H_C should be proportional to $1/d$, where d is the average grain diameter, in materials where grain boundaries are the dominant obstacle to domain wall motion (Goodenough, 1954; Globus and Guyot, 1972). Degauque *et al.* (1982) found that this relationship was valid for annealed high-purity iron, although $d^{-1/2}$ also fitted the data satisfactorily. In commercial-purity nickel, too, the coercive field decreased with increasing grain size over a wide range from nanocrystalline to $\sim 10^2$ μm (Kawahara *et al.*, 2002).

The total number of pulses of both BN and MAE decreased with increasing grain size in nickel, following a $1/d$ dependence (Ranjan *et al.*, 1986, 1987a). In pure nickel, the RMS BN voltage was a minimum at an intermediate value of d (Hill *et al.*, 1991); an examination of the variation of noise voltage with applied field showed that the peak heights and positions changed with grain size in a complex way. It appears that using a single parameter to characterise the noise voltage is too simplistic in nickel. In pure iron, the RMS noise amplitude scaled with $d^{-1/2}$ (Yamaura *et al.*, 2001).

These results are collated in Table 4.1. The occurrence of both d^{-1} and $d^{-1/2}$ relationships may be due to experimental uncertainty allowing both to fit adequately (Degauque *et al.*, 1982). Since a d^{-1} relationship was predicted theoretically, this may have been the only fit attempted in some cases. Also, it has not been established theoretically that all the properties measured should depend on grain size in the same way. Further work on the interdependence of these properties would be useful.

Property	Pure Fe	Pure Ni	Mild steels
Coercive field	$\downarrow^{\text{D}}$ ($\propto d^{-1}$, $d^{-1/2}$)	$\downarrow^{\text{K}}$	$\uparrow^{\text{R}}$, $\downarrow^{\text{Yo}}$
BN: Total counts RMS voltage Max. voltage Peak height H of peak Integrated	 $\downarrow^{\text{Ya}}$ ($\propto d^{-1/2}$)	 $\downarrow^{\text{R}}$ ($\propto d^{-1}$) $\downarrow$(small d) $\uparrow$(large d)$^{\text{H}}$	 $\uparrow^{\text{R}}$ $\uparrow(\propto d)^{\text{R}}$ $\downarrow^{\text{A}}$ $\downarrow^{\text{S,G}}$ $\downarrow^{\text{G}}$
MAE: Total counts RMS voltage		 $\downarrow^{\text{R}}$ ($\propto d^{-1}$)	 $\uparrow^{\text{R}}$ $\uparrow^{\text{R}}(\propto d)$

Table 4.1: Variation of magnetic properties with increasing grain size: (A)nglada-Rivera *et al.*, 2001, (D)egauque *et al.*, 1982, (G)atelier-Rothéa *et al.*, 1992, (H)ill *et al.*, 1991 (K)awahara *et al.*, 2002, (R)anjan *et al.*, 1986, 1987a, b, (S)hibata and Sasaki, 1987, (Ya)maura *et al.*, 2001 (Yo)shino *et al.*, 1996.

Mild steels

The final column of Table 4.1 displays results from mild steels. In decarburised steel, all the properties show opposite trends to those in the purer metals; for example, the RMS noise voltages are directly proportional to d (Ranjan *et al.*, 1986, 1987a). This was explained by the presence of impurities – MnS particles within the grains and phosphorus on the grain boundaries – whose presence overwhelmed the intrinsic grain size effect (Ranjan *et al.*, 1987b). However, Yoshino *et al.* (1996) reported that in steels containing only ferrite, H_C was inversely proportional to the grain size.

The average BN amplitude in low carbon steel (composition not specified) varied as $\ln d/d_C$, where d_C is the extrapolated grain size for which the BN amplitude is zero, for small grain size d, and saturated at a critical value of d (Tiitto, 1978).

The variation of BN and MAE voltage with position in the magnetisation cycle for 0.1 wt. % C steel showed two peaks (Shibata and Sasaki, 1987). For BN, the first of these decreased in height with increasing grain size, while the second showed little variation. The first MAE peak occurred at a stronger applied field than the first BN peak, but the second peaks coincided. It was concluded that the first peak was due to domain wall motion, which occurred at a lower field for Type-II than for Type-I walls, while the second peak was attributed to discontinuous rotation of domains.

In Fe-0.013 wt. % C, a single BN peak, whose height decreased with increasing grain size, was seen (Gatelier-Rothéa *et al.*, 1992). Similarly, in 0.4 wt. % C steel, the maximum BN amplitude was largest in a fine-grained and smallest in a coarse-grained sample (Anglada-Rivera *et al.*, 2001). In both cases, these results were explained as due to a larger number of domain walls within fine-grained samples. The domain size was reported by Degauque *et al.* (1982) as proportional to the square root of grain size for grain diameters between 0.05 and 10 mm. Hence, both the the number of domain walls and the number of pinning sites per unit volume is greatest for small grains.

The BN peaks observed by Gatelier-Rothéa *et al.* (1992) were situated

just beyond $H = 0$. They moved closer to $H = 0$, corresponding to a decrease in pinning strength, with increasing grain size.

Complex microstructures

In the equiaxed, single-phase materials discussed above, grain boundaries are the only important microstructural feature. For NDT of more complex microstructures, the relative influence of grain boundaries and other features must be determined.

In pearlitic plain-carbon steels with a variety of carbon contents and fabrication histories, a linear trend was observed between H_C and d^{-1}, but the fit was not particularly good (Tanner *et al.*, 1988). However, much better agreement was obtained using the equation:

$$H_C = (c_1 V_P / d_P) + (c_2 V_F / d_F) \tag{4.1}$$

where V_P and V_F are the pearlite and ferrite volume fractions, and d_P and d_F the pearlite and ferrite grain sizes, respectively; c_1 and c_2 are constants.

Yoshino *et al.* (1996) found that the presence of pearlite did not significantly affect H_C at phase fractions < 0.17. When pearlite constituted more than 0.6 of the microstructure, H_C increased in proportion to the pearlite fraction and was no longer affected by the grain size. Similarly, in ferritic steels containing > 0.15 martensite, H_C was dominated by the martensite fraction rather than the ferrite grain size.

In austenitised, quenched and tempered plain-carbon and 12 wt. % Cr steel, the prior austenite grain size had a negligible effect on the hysteresis loop characteristics, which depended instead on hardness (Kwun and Burkhardt, 1987). It is clear that the formation of martensitic or bainitic microstructure, and the changes accompanying tempering, are the governing processes in quenched and tempered steels.

4.4.2   Grain boundary misorientation

In coarse-grained Fe-3 wt. % Si, the BN signal was measured on individual grain boundaries and within the grains adjacent to them (Yamaura *et al.*,

2001). The relative BN intensity at the boundary, $R_{\text{intensity}}$, was calculated from:

$$R_{\text{intensity}} = \frac{P_{\text{GB}} - P_{\text{AVG}}}{P_{\text{AVG}}} \qquad (4.2)$$

where P_{GB} and P_{AVG} are the noise power on the grain boundary and the average of the noise powers from the adjacent grains respectively. The increase of $R_{\text{intensity}}$ with boundary misorientation angle is shown in Figure 4.4. Only low-angle boundaries were found in the material.
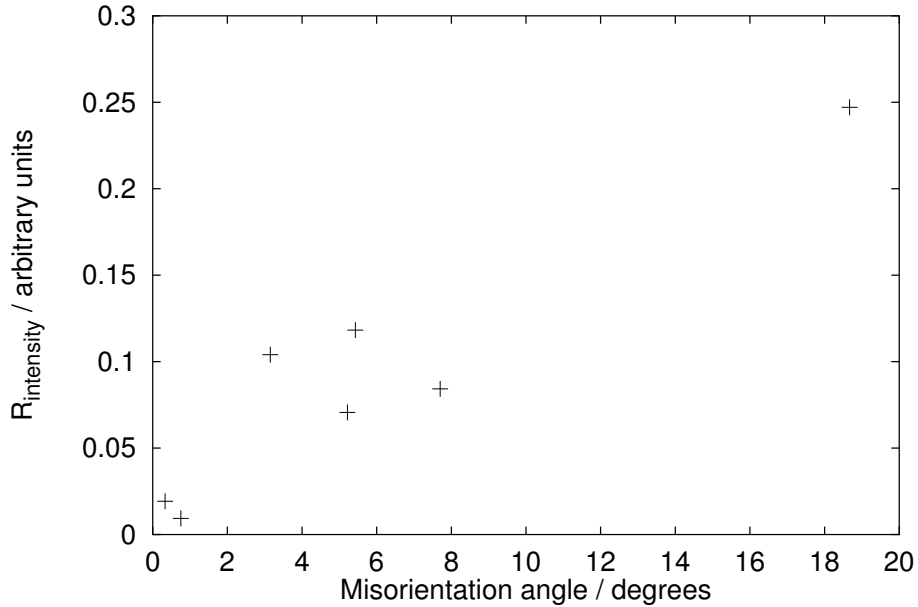
Figure 4.4: Dependence of $R_{\text{intensity}}$ on misorientation angle in Fe-3 wt. % Si (Yamaura *et al.*, 2001).

4.4.3 Grain size influence on BN frequency

In pure iron, the ratio of high-frequency to low-frequency components of the BN signal decreased as the grain size increased (Yamaura *et al.*, 2001). This was quantified using the parameter P_{60}/P_3, where P_{60} is the total noise with frequency 60 kHz and P_3 the noise with frequency 3 kHz; its variation with grain size is shown in Figure 4.5. The high-frequency noise was attributed

to emissions from defects such as dislocations and grain boundaries, which become less important as coarsening occurs, resulting in a decrease in P_{60}/P_3 (Yamaura *et al.*, 2001). Another interpretation is that the noise frequency is approximately the reciprocal of the time taken by a domain wall to move from one pinning site to the next, and this in turn is proportional to the distance between obstacles (Saquet *et al.*, 1999). Hence, in coarser microstructures, the proportion of high-frequency noise is lower.
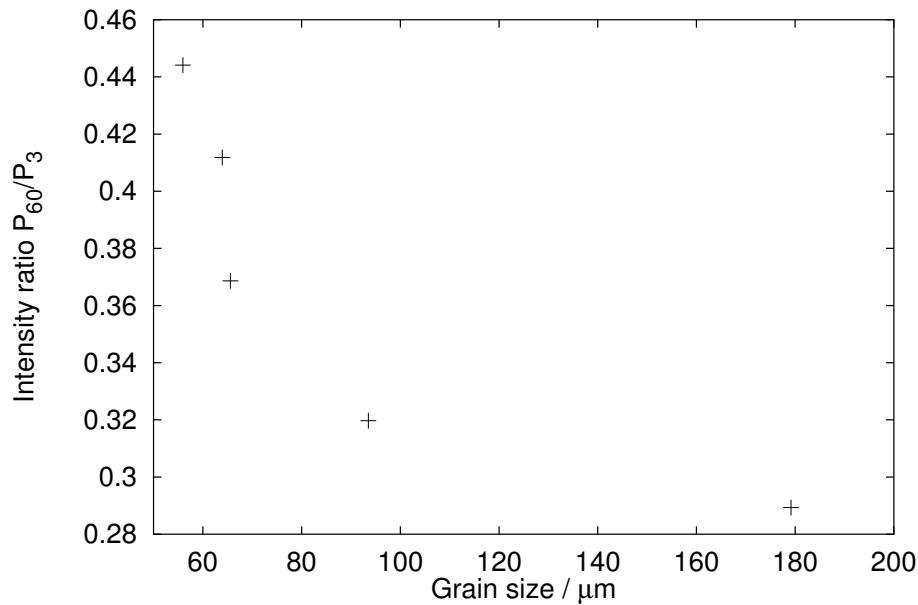
Figure 4.5: Relationship between frequency components of BN and grain size (Yamaura *et al.*, 2001).

4.4.4   Summary

In pure materials, relationships between grain size and magnetic properties are mostly simple, with decreases in coercive field and the level of BN and MAE as grain size increases. In mild steels, some inconsistencies have been found, but the general trend is also towards lower values of most properties as grain size increases. The opposing trends in peak height and average event size are not irreconcilable, since the noise peak height depends on both the number of events, which is smaller when there are fewer pinning sites and

moving walls, and the average event size, which is large when a domain wall can move a long distance without being pinned.

The pinning strength of grain boundaries was slightly greater for smaller grains. Finer-grained iron also gave a greater proportion of high-frequency noise; this can be related to a shorter domain wall time-of-flight between obstacles. At individual low-angle grain boundaries in Fe-3 wt. % Si, the ratio of the noise measured across the boundary to the noise from the adjacent grains increased with misorientation angle.

In steels with a second microstructural constituent, this tended to dominate magnetic behaviour when it was present in sufficient quantities. Similarly, in austenitised, quenched and tempered steels, the prior austenite grain size had no significant effect on hysteresis properties.

4.5   Dislocations and plastic strain

4.5.1   Deformation

At a low level of deformation in pure iron, isolated, homogeneously distributed dislocations appeared, but caused very little change in H_C compared to the undeformed state (Astié *et al.*, 1981). Further deformation produced dislocation tangles and a rapid increase in H_C with stress. At even higher strain, dislocations formed subgrain boundaries and the intragranular dislocation density decreased. H_C still increased with stress, but the rate of increase was smaller.

Jiles (1998b) investigated the effect of plastic compressive deformation on a high-chromium steel in three microstructural conditions: ferrite/pearlite, ferrite/bainite and tempered martensite. The coercive field was proportional to the hardness irrespective of the microstructure. However, some microstructural differences were evident. In ferrite/pearlite and ferrite/bainite, W_H and H_C increased with increasing plastic strain; this was attributed to the additional obstacles to domain wall motion provided by a greater dislocation density. In martensite, by contrast, H_C and W_H decreased with increasing plastic strain. It was suggested that this, in the same way as the

observations of Astié *et al.* (1981), was due to the formation of subgrains, between which the dislocation density would be relatively low.

4.5.2   Annealing of deformed materials

Previously deformed specimens of pure nickel were annealed at various temperatures, and the hardness and total BN and MAE counts determined (Ranjan *et al.*, 1987c; Figure 4.6). The hysteresis loss and MAE count number depended on temperature in the same way as the hardness, but the BN behaviour was more complex. It was suggested that this was due to a competition between the reduction in dislocation density, which reduces the number of domain wall pinning sites, and the nucleation of small recrystallised grains, which increases it. The lack of a similar trough in the MAE counts at 400°C was attributed to a smaller effect of grain size on MAE than on BN.

Plots of BN and MAE versus applied field both showed single peaks in deformed nickel. Prolonged annealing reduced the peak height by about 80%, demonstrating that it was due to pinning by dislocations (Buttle *et al.*, 1987a).
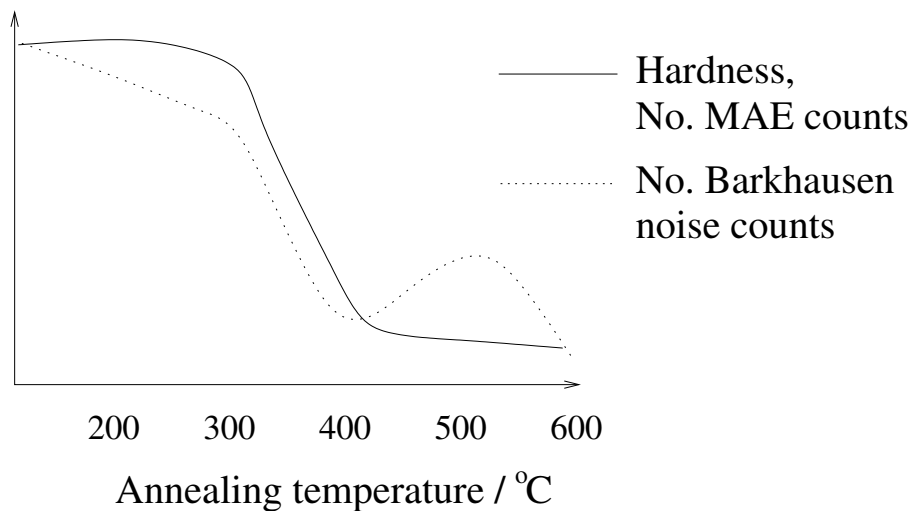
Figure 4.6: Effect of annealing temperature on mechanical and magnetic properties of deformed nickel (Ranjan *et al.*, 1987c).

Similarly, the BN and MAE properties of pure iron, plastically deformed

then annealed for 1 hour at a range of temperatures, were investigated (Buttle *et al.*, 1987a). The total event count and maximum event size for both BN and MAE depended on annealing temperature in a similar way to the MAE total count in nickel shown in Figure 4.6, but with a slight increase before the abrupt drop. The 'trough' observed by Ranjan *et al.* (1987c) in nickel was absent in iron.

Figure 4.7 shows the variation of BN and MAE voltage with applied field for a sample annealed below 550°C. The outer peaks of the BN signals, and the two peaks in the MAE, correspond to the 'knees' of the hysteresis loop. Up to 550°C, the BN peak at the negative knee grew, the central peak decreased slightly in height, and the two MAE peaks both grew, with increasing temperature. Above 550°C, all the peaks decreased rapidly to almost nothing.
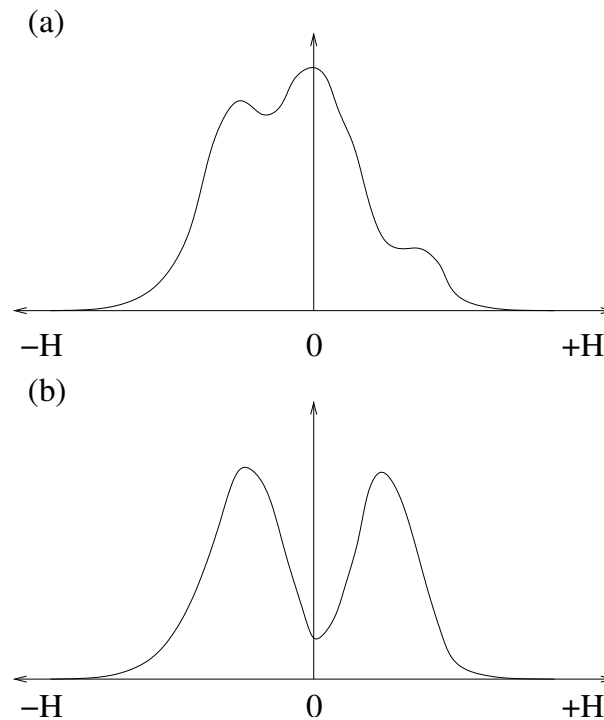
Figure 4.7: (a) BN signal from pure iron, cold-worked and annealed below 550°C; (b) MAE signal from the same sample (Buttle *et al.*, 1987a).

The BN and MAE peaks situated at the negative knee were attributed

to domain nucleation, and those at the positive knee to domain wall annihilation. The former are higher because a larger energy is required to nucleate domains, resulting in a smaller number of large-amplitude events. Annihilation, by contrast, may involve the sweeping out of only small volumes at a time, and hence the individual pulses need not be large. However, this argument makes the assumption that the peak height will be greater for a small number of large events than for a large number of small ones. It is not obvious whether this is indeed the case.

The BN peak close to $H = 0$ had no MAE equivalent. Since only Type-I domain wall motion produces MAE, Buttle *et al.* concluded only Type-II wall activity was occurring in this region. This behaviour was believed to be in agreement with the prediction of Scherpereel *et al.* (1970) that dislocations should interact more strongly with Type-II than with Type-I walls.

However, a more simple explanation could be that the difference in BN and MAE activity around $H = 0$ is related to the smaller number of Type-I walls present. A magnetoelastic energy penalty is involved in creating a domain at 90° to another (§ 3.1.3), so the preferred domain structure contains predominantly parallel, Type-II walls, with Type-I walls appearing only to provide flux closure at magnetic inhomogeneities. Secondly, if Type-II walls undergo stronger interactions with dislocations than do Type-I walls, the peak for the Type-II interaction should appear at a higher applied field than that for the Type-I, but there does not seem to be any evidence of this.

4.5.3   Deformation and saturation effects

Figure 4.8 shows the effect of deformation on the BN and hysteresis behaviour of a mild steel (Kim *et al.*, 1992). In the annealed, unstrained state, the hysteresis loop has straight, steep sides, and magnetisation change takes place over a small range of field. BN peaks are present at the knees. Straining causes a change to a sheared loop with a smaller saturation value, and a single, central BN peak coinciding with the peak in $\mathrm{d}B/\mathrm{d}t$.

Kim *et al.* also found that reducing H_{max} decreased the outer BN peak heights and increased the conformity between the BN curve and $\mathrm{d}B/\mathrm{d}t$ (Fig-
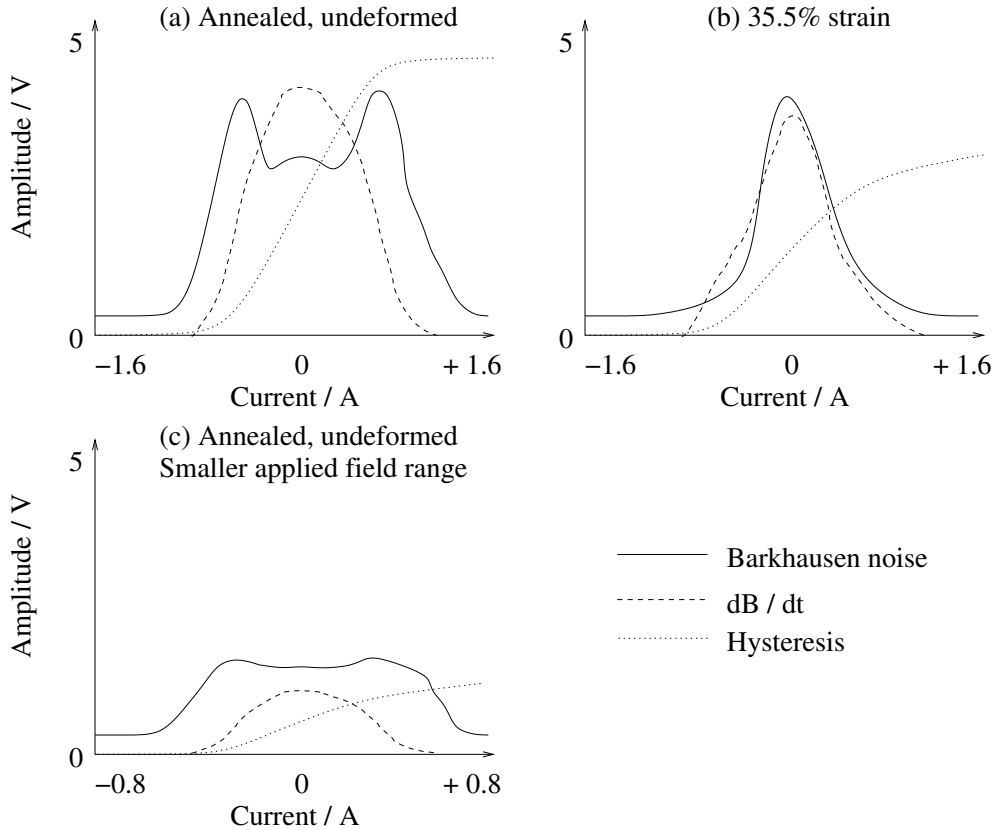
Figure 4.8: Effect of straining and changing the applied current range (and hence $H_{\max}$) on BN, hysteresis and $\mathrm{d}B/\mathrm{d}t$ curves (Kim *et al.*, 1992).

ure 4.8 (c)). The ability of both deformation and reduction of $H_{\max}$ to suppress the outer peaks led to the conclusion that domain nucleation and annihilation did not take place in many of the domains in the deformed material. The dramatic reduction in the value of M at $H_{\max}$ supports this; it is unlikely that the true M_S (which is generally viewed as a structure-insensitive property) could be changed to this extent by deformation. Instead, it seems that the highly dislocated material does not become fully saturated. The BN activity around zero field increases on deformation. It appears that in a relatively strain-free sample, it is easy for the structure to 'switch' from one state of near-saturation to another, but when many dislocations are present, domain walls must overcome these, with an associated emission of BN around

$H = 0$.

4.5.4   Summary

In many cases, there is a simple linear correlation between hardness and H_C, but when the dislocation density is very high, this relationship is altered by the formation of subgrain boundaries.

In pure iron and nickel, magnetic noise levels are high after deformation, but decrease to almost nothing after high-temperature annealing. By contrast, in mild steel, the large BN signal from annealed material was reduced by deformation. This was accompanied by a change from three peaks to only one. The outer peaks have been attributed to domain nucleation and annihilation and the central region to pinned domain wall motion. Heavy deformation increases the number of pinning sites and increases the difficulty of saturation so that the outer two peaks disappear.

4.6   Second-phase particles

4.6.1   Ideal systems

The study of particle effects on magnetic properties in steels is complicated by the inhomogeneous distribution of some precipitates, which nucleate preferentially on grain boundaries (§ 2.3.4) and by the ferromagnetic nature of Fe_3C and some other carbides below their Curie temperatures. To determine the essential features of particle effects, 'ideal' systems, which avoid these complexities, have been studied.

Magnetic precipitation hardening is an increase in H_C due to the formation of a precipitate phase on ageing. Shilling and Soffa (1978) found that this effect was linked to a periodic array of fine particles coherent with the matrix. Within this regime, H_C could be increased by increasing the volume fraction or size of particles. Overageing, *i.e.* reduction in H_C, was associated with a loss of periodicity. In the periodic alloy, the Kersten pinning theory (§ 3.3.1) was adequate for describing changes in H_C.

'Incoloy 904' nickel-based superalloy (33.8 Ni, 51.0 Fe, 14.0 Co,

1.2 Ti wt. %) was selected as an ideal system because the second phase is nonferromagnetic, nucleates homogeneously, is distributed evenly in the matrix and grows as spheres on ageing (Buttle *et al.*, 1987b). A monotonic increase in H_C with ageing time was observed, but the total BN event count showed a maximum at an intermediate time.

Domain wall-particle interactions were observed using Fresnel and Foucault microscopy (§ 3.4). Small particles deflected the walls slightly. As the applied field was increased, small wall displacements occurred in a quasi-continuous manner, passing through several inclusions at a time, up to a critical field at which a long-range domain wall jump occurred. When the particles were large, domain wall motion occurred in discrete jumps. The inclusions were surrounded by closure domains, which grew as the particles coarsened, to form an interacting network. This limited the domain wall jump size, since the wall was pinned by the networks rather than individual particles.

The maximum Barkhausen event size increased with ageing time in single-crystal Incoloy 904, but remained approximately constant in polycrystalline samples. This was attributed to the limitation of jump distances by grain boundaries. The maximum volume swept out in a single jump was calculated using BN data and found to be of similar magnitude to the grain size as observed by scanning electron microscopy.

As in the dislocation study (Buttle *et al.*, 1987a; § 4.5.2) the BN and MAE profiles both had peaks at the hysteresis loop knees, and an additional central peak was present in the BN signal. The BN peak heights increased up to an annealing time of 520 h, at which stage the inclusion diameter was about the same as the wall width, then decreased again after longer annealing. Buttle *et al.* (1987b) again attributed the outer peaks to domain nucleation and annihilation, and the central peak to domain wall motion, predominantly of Type-II walls. Very little noise activity occurred around $H = 0$ in unaged specimens; this was explained by the ease of domain wall motion in a matrix with few pinning points.

Buttle *et al.* suggested that the closure domains on large inclusions may persist at high fields, and regrow when the field is reduced, avoiding the

necessity for additional nucleation. This may explain why the outer BN peaks decrease in height after long ageing times.

4.6.2 Effect of carbon on hysteresis properties

On the basis of the Néel theory (§ 3.3.1), a maximum in H_C was predicted at the Curie temperature of Fe_3C in plain-carbon steels (Figure 4.9). This was sought unsuccessfully by Dijkstra and Wert (1950) and others, so it was concluded that Fe_3C behaved 'as if nonmagnetic'. However, English (1967) found such maxima in pearlitic Fe-0.8 wt. % C and 2Cr-1C wt. % steel. The temperatures at which they occurred were different for the two steels, and this was attributed to the modification of the carbide composition, and therefore its magnetic behaviour, by the presence of chromium in the carbide.

In coarse spheroidised pearlitic microstructures, no H_C anomaly was found. English suggested that this may have been due to interparticle interactions, such as the formation of a network of spike domains, which did not allow the particles to be considered in isolation.
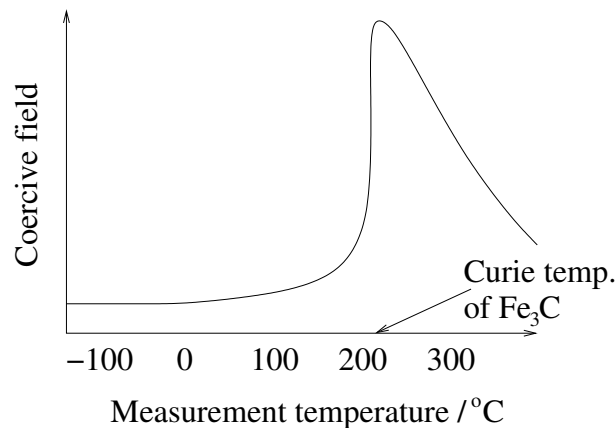
Figure 4.9: Anomaly in the coercive field predicted at the Curie temperature of Fe_3C (English, 1967).

In plain-carbon steels, H_C increased with carbon content in both pearlitic and spheroidal microstructures; this was a much stronger influence on H_C than that of grain size (Ranjan *et al.*, 1986, 1987; Jiles, 1988a). Monotonic

increases in H_C and W_H were observed for both microstructures, but the values of these properties were always higher in the pearlitic steels (Jiles, 1988a; Figure 4.10). This result was later confirmed by Lo *et al.* (1997b). The remanent magnetisation was independent of the carbon content, but affected by the carbide morphology, being higher in the spheroidal microstructures (Jiles, 1988a). H_C increased with hardness, irrespective of the microstructure (Jiles, 1988a; Tanner *et al.*, 1988) and varied linearly with the volume fraction of carbide (Jiles, 1988a). In this case, the proportionality constant depended on the carbide morphology. In addition, H_C depended on the volume fraction of pearlite grains.

Spike domains were again believed to be responsible for the difference in properties between spheroidal and lamellar structures, but in this case it was considered that the spikes on spheroids weakened domain wall-particle interactions compared to those in pearlite.
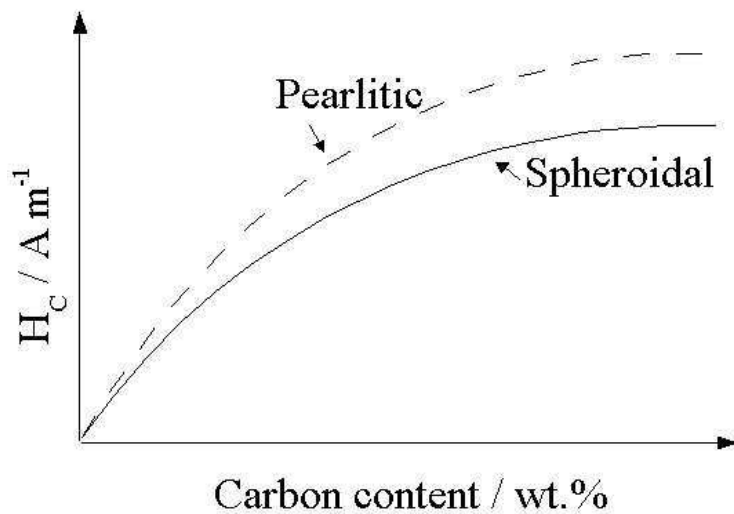
Figure 4.10: The effect of carbon content on coercive field in plain-carbon steel, for spheroidal and pearlitic microstructures (Jiles, 1988a).

Tanner *et al.* (1988) found that H_C increased with increasing carbon content in steels in which only the carbon content varied, but this relationship broke down in C-Mn steels. However, H_C was related to a weighted sum of carbon and manganese contributions:

$$H_C = 1.186(\text{ wt. } \% \text{ C}) + 0.237(\text{ wt. } \% \text{ Mn}) \tag{4.3}$$

This relationship is not general; in particular, it did not correctly predict H_C for manganese-free steels.

Fe-C alloys were prepared with carbon in solution (State A), as $\sim 0.5 \ \mu$m intragranular precipitates (B), and as larger carbides ($\sim 10 \ \mu$m) at grain boundaries (C) to compare their hysteresis properties (Lopez *et al.*, 1985). In C, islands of pearlite were also present when the carbon content was over 0.02 wt. %. H_C increased with increasing carbon content in all cases, but was much greater in State B samples (Figure 4.11). Plots of W_H and remanence against carbon content were similar to Figure 4.11. The interstitials in A, while exerting a dragging force, did not have a strong effect on large domain wall displacements. Grain-boundary precipitates, because of their wide spacing, also only weakly affected H_C. Fine particles, whose diameters were twice or three times the wall thickness, interacted strongly with domain walls. The carbon contents in this investigation were small (0.01–0.05 wt. %) so it is unlikely that closure domain networks were formed.
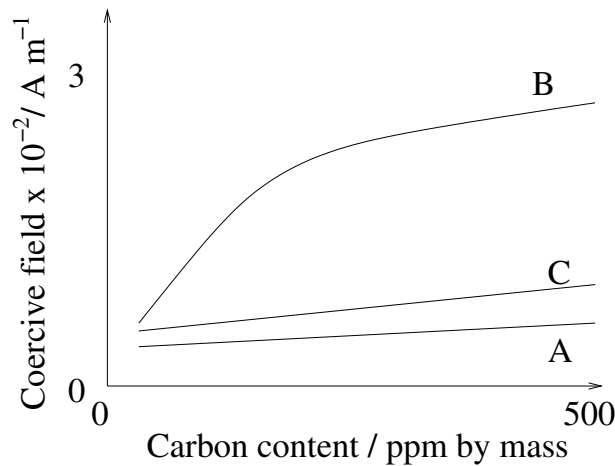
Figure 4.11: The effects of different precipitation states on the coercive field (A) carbon mostly in interstitial solution, (B) intragranular precipitates of around 0.5 μm diameter, (C) large carbides of around 10 μm diameter at grain boundaries (Lopez *et al.*, 1985).

4.6.3   Effect of carbon on BN and MAE

A single, very sharp RMS BN peak was observed in pure iron (Gatelier-Rothéa *et al.*, 1992). The presence of 0.013 wt. % carbon in the form of intergranular carbides reduced the peak height and increased the width. If the carbon was instead present in solution, the height decreased and the width increased further. This was attributed to the retarding force of interstitial carbon on domain walls.

On intragranular precipitation of ϵ-carbide from a solid solution, the BN maximum amplitude increased monotonically until precipitation was complete. When Fe_3C was instead precipitated, the amplitude increased at short ageing times, then subsequently decreased after precipitation was complete and coalescence of precipitates began to occur. At the longest times, the amplitude was approximately constant (Gatelier-Rothéa *et al.*, 1992). The variations were smaller from ϵ-carbide than from cementite, because ϵ is smaller, and no closure domains are generated; instead, the wall is bent by the precipitates. The areas under the peaks followed similar trends to the maximum amplitudes (Gatelier-Rothéa *et al.*, 1998). Intragranular precipitates affected BN behaviour more strongly than coarser, intergranular precipitates at the same carbon content.

In ferritic/pearlitic steels, the carbon content determines the proportion of the two components. The pulse height distribution extended to larger pulse sizes when the carbon content was greater (Clapham *et al.*, 1991). If individual domain wall displacement distances follow this distribution, this suggests that they are both larger and more varied in pearlite. However, another possible explanation is that the large event sizes are caused by many domain walls jumping together in an avalanche effect (§ 3.3.5).

Increasing the pearlite fraction decreased the MAE amplitude at $H = 0$ and changed the form of the RMS BN versus H plot from two peaks to only one (Lo and Scruby, 1999). This behaviour was attributed to a larger proportion of Type-I walls when the pearlite content was lower. Conflicting results were obtained by Ng *et al.* (2001); a single sharp peak occurring at a negative H in a ferrite-cementite sample broadened and extended to both

sides of $H = 0$ as the pearlite content was increased. Saquet *et al.* (1999) observed that the signal from ferrite-pearlite appeared to be a combination of the signals from the two components (Figure 4.12). However, the ratio of the heights of the two components of the curve is not the same as the volume ratio of ferrite to pearlite. The reasons suggested for this were the differences in carbon content in the two phases, or variations in correlation (avalanche) phenomena.
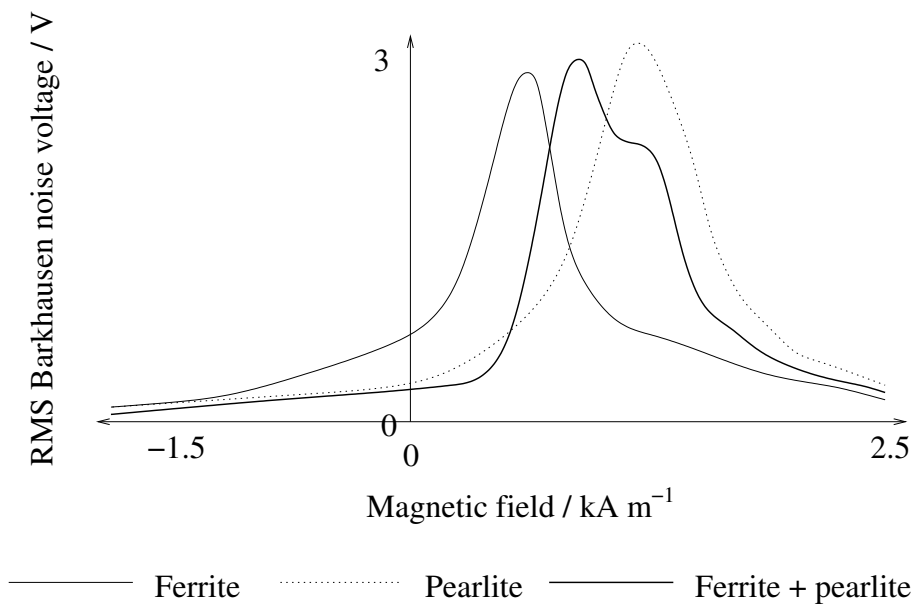
Figure 4.12: BN signals from ferritic, pearlitic and ferrite + pearlite microstructures in plain-carbon steel, showing two-component signal from the microstructure with two constituents (Saquet *et al.*, 1999).

4.6.4   Summary

Coherent or regularly spaced particles give higher H_C and W_H than spheroidal particles at the same bulk composition, whether or not the particles are ferromagnetic. In plain-carbon steels, H_C increases monotonically with carbon content, but this may be modified by the presence of other elements. In alloys containing particles, H_C shows a clear correlation with hardness, whatever the particle morphology and composition.

Carbon in solution is believed to exert a drag force on domain walls. Small intragranular particles bend the domain walls, which move in a quasi-continuous manner, with parts of the wall moving a short distance in an individual event. On coarsening, the motion transforms into large, discrete jumps. The formation of closure domains after prolonged coarsening, and their interaction to form a domain network, is thought to limit the jump size. In steels with only a small carbon content, particle coarsening reduces H_C and the BN amplitude because of the decreased number density of pinning sites.

Particles appear to outweigh grain boundaries in their influence on magnetic properties. However, the presence of grain boundaries limits the maximum domain wall jump size.

Experiments on the effect of carbide morphology on BN yielded inconsistent results. In one study, increasing the fraction of pearlite in a ferrite-pearlite steel caused a transformation from double- to single-peak behaviour. In another, an initial single peak was found to broaden. The reasons for this discrepancy are not clear. A third investigation showed that the two-component microstructure produced a peak which appeared to be a simple combination of the peak shapes of the constituents. This is an important result since it suggests that parts of the BN signal can be related rather straightforwardly to individual microstructural components.

4.7   Magnetic properties of tempered steels

4.7.1   Changes in hysteresis properties on tempering

Plain-carbon steels

The hardness and H_C of a plain-carbon steel at different stages of tempering are shown in Figure 4.13 (Kameda and Ranjan, 1987a). The hardness decreased smoothly with increasing temperature, but H_C changed most dramatically between 200 and 400°C. This corresponds to the precipitation of ϵ-carbide followed by fine needlelike Fe_3C. W_H followed the same dependence on temperature as H_C.
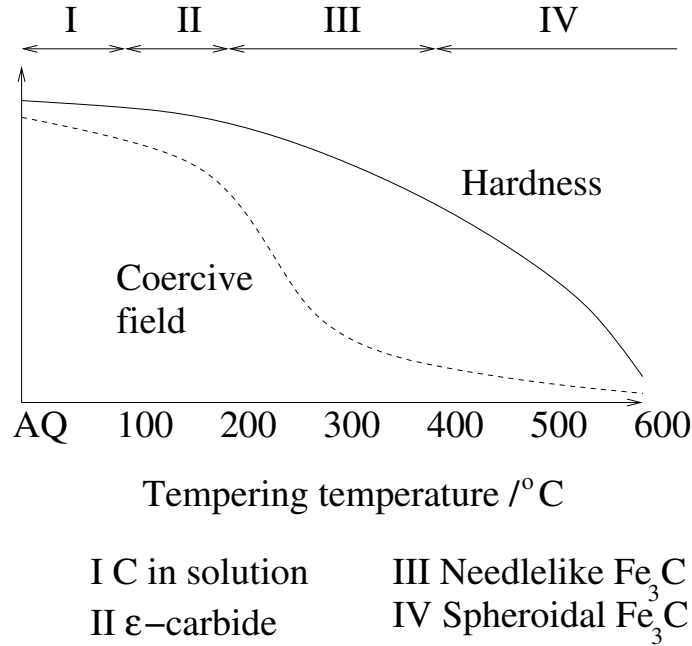
Figure 4.13: Changes in hardness and coercive field associated with different tempering times (Kameda and Ranjan, 1987a).

Under similar experimental conditions, Buttle *et al.* (1987c) observed a H_C curve shaped like the hardness curve in Figure 4.13, and a hardness curve similar to the H_C curve observed by Kameda and Ranjan. The difference in carbon content (0.17 wt. % for Kameda and Ranjan; 0.45–0.55 wt. % for Buttle *et al.*) could be responsible.

The hardness of a plain-carbon steel fell rapidly over the first hour of tempering at 600°C, then decreased more gradually at longer times (Moorthy *et al.*, 1998). H_C, after an initial decrease, peaked at 10 hours before decreasing smoothly. Peaks in B_R and the maximum induction B_{max} also occurred at this time, as did the onset of BN peak-splitting (§ 4.7.3).

Relationships between H_C and particle diameter $\bar{d}_p$ were presented by Kneller (1962) and Mager (1962):

$$H_C \sim \bar{d}_p^{3/2} \tag{4.4}$$

for $\bar{d}_p < \delta$, where δ is the domain wall thickness, and

$$H_C \sim \bar{d}_p^{-1/2} \qquad (4.5)$$

for $\bar{d}_p > \delta$.

A maximum was therefore expected at an intermediate time in plots of H_C against tempering time (Hildebrand, 1997). Instead, two peaks were seen in both plain-carbon and alloy steels. A greater tempering temperature caused accelerated kinetics, and increasing the carbon content gave higher H_C values. The first peak was attributed to the appearance on martensite packet boundaries of needlelike carbides and their spheroidisation and coarsening, and the second to precipitation and coarsening of spheroidal particles in the interior of the former packets. Given the timescale of the first peak ($\sim$ 10 minutes at 650°C), the carbides involved may well be ϵ, rather than Fe_3C as stated by Hildebrand. The second peak occurs at around 100 minutes and is more prominent the greater the carbon content. Further peak structures could be seen in a sample containing chromium, but it appears that the effects of different carbides often overlap, since the effects of MC and M_6C could not be separated.

Alloy steels

In 11Cr1Mo steel, H_C, B_R, W_H and hardness decreased rapidly with tempering time for periods up to 100 s (Yi *et al.*, 1994). Above this, the decrease became more gradual. B_S increased with tempering time, also with a slope change from rapid to gradual at 100 s. A monotonic decrease in H_C with increasing hardness was observed.

A secondary hardening peak was seen for $2\frac{1}{4}$Cr1Mo and 9Cr1Mo steels tempered at 650°C, and H_C also decreased rapidly, peaked at an intermediate time, then decreased gradually (Moorthy *et al.*, 1998, 2000).

The discrepancies between these results and those of Yi *et al.*, in which a secondary peak might also have been expected, may be reconciled by considering the wide range of timescales on which the H_C peaks were observed by Hildebrand (1997). In the lower-chromium steels, the second 'Hildebrand' peak may occur at a longer time than in the 11Cr1Mo sample so that it is

visible in $2\frac{1}{4}$Cr1Mo and 9Cr1Mo but occurs before the first measurement in 11Cr1Mo.

4.7.2   Effect of tempering on magnetic noise

Bulk noise properties

Quenched and tempered samples of 0.4C-5Cr-Mo-V steel were prepared with a range of prior austenite grain sizes and carbide sizes (Nakai *et al.*, 1989). The BN power increased linearly with the mean carbide diameter, and decreased with increasing number of carbide particles per unit area. There was a trend towards smaller BN power values as the prior austenite grain size increased but the correlation was less clear than those for the carbides.

Noise peak shapes

Kameda and Ranjan (1987a) observed an MAE peak at each of the hysteresis loop knees, but only a single BN peak. On decreasing the field from positive to negative, the largest MAE pulses occurred at the negative knee. This peak increased in height with tempering temperature; the greatest change occurred between 200 and 500°C. This range corresponds to the precipitation of fine ϵ and Fe$_3$C, and the beginning of Fe$_3$C spheroidisation. The position of this peak remained constant, but both the positive MAE peak and the BN peak moved further from $H = 0$ with increasing temperature. The BN peak height increased with tempering temperature in three distinct stages, corresponding to solid solution, precipitation of ϵ-carbon and needlelike Fe$_3$C, and spheroidisation of Fe$_3$C.

Analysis of the RMS noise signal revealed changes in the BN peak shape and a split into two peaks after high-temperature tempering (Figure 4.14; Buttle *et al.*, 1987c). The single, asymmetric peak from the as-quenched material increased in height with increasing temperature. A discernible 'shoulder' appeared at 500°C, and this grew into a second peak of similar height to the first. Broadening of the signal to a greater range of fields was also observed. The initial single BN peak was attributed to the martensitic structure, and the second to the precipitation of cementite at 500°C.
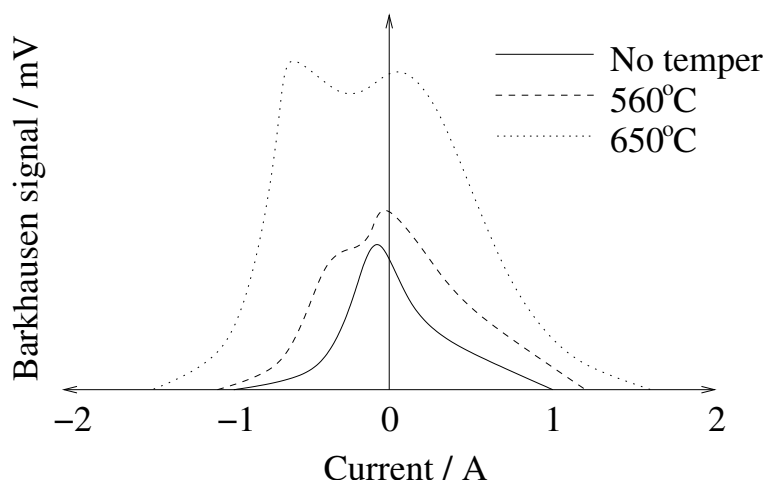
Figure 4.14: Changes in BN peak size and shape due to tempering (Buttle *et al.*, 1987c).

No observable MAE activity occurred at or below 350°C. This was attributed to the tetragonality of martensite, which favoured Type-II walls because of the unique easy axis. As the martensite relaxed to ferrite, this constraint was removed, and Type-I activity and hence MAE could occur. Two peaks appeared, one on either side of $H = 0$. These were larger the higher the tempering temperature. The initial peak, on the negative side of $H = 0$, was always the larger.

Figure 4.15 shows the change in RMS BN peak shape with tempering temperature observed in a very similar experiment (Saquet *et al.*, 1999). The peaks were narrower and higher, and occurred at smaller H, when the temperature was higher. This was accompanied by a change in the hysteresis loop shape, from broad and sheared to narrower, with straighter sides and a higher M_S. Single peaks were observed in MAE signals, at the same positions as the BN peaks; both occurred close to H_C as determined from the hysteresis loops.

In as-quenched steel, the noise was of a higher frequency ($\sim 100\,\text{kHz}$) than in the tempered samples ($\sim 10\,\text{kHz}$). The small amplitude of peaks from as-quenched steel was attributed to the greater attenuation by eddy currents of higher-frequency noise. This reduces the proportion of noise reaching the

pickup coil. Since the degree of attenuation, and the frequency filtering, may vary from one set of experimental apparatus to another, this could explain some of the discrepancies between the results of Saquet *et al.* and those of Buttle *et al.* (1987c).
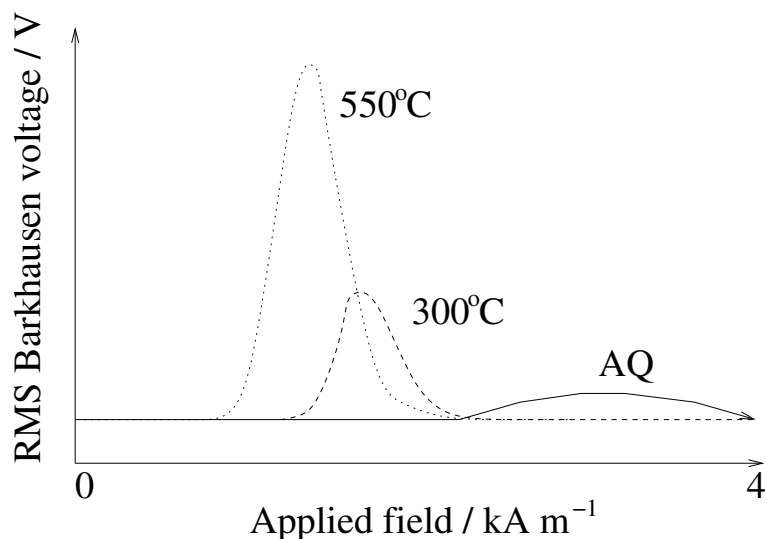
Figure 4.15: Change in the shape of the BN signal from as-quenched (AQ) state due to tempering for one hour at 300 and 550°C (Saquet *et al.*, 1999).

4.7.3   Changes in BN with tempering time

Samples of a plain-carbon steel were tempered at 600°C for times ranging from 0.5 to 100 hours (Moorthy *et al.*, 1997b). The average carbide size increased from 0.13 μm after 1 hour of tempering, to 0.46 μm after 100 hours. The carbide size distribution also broadened approximately fourfold. Equiaxed ferrite replaced the original martensitic structure, and coarsened as tempering progressed.

The as-quenched BN peak occurred at $H = 4$ kA m^{-1}, which is comparable with the value of 2.5–3 kA m^{-1} observed by Saquet *et al.*, given the difference in composition. Tempering for 0.5 hours shifted the peak to a smaller field and greatly increased its amplitude. This change was attributed to the increase in domain wall mobility and mean free path as the dislocation

density decreased. After 1 hour, the peak broadened and showed a change
in slope, which developed into a second distinct peak, clearly visible after
5 hours (Figure 4.16). Further tempering increased the separation of the
peaks and reduced the signal amplitude. The peak shapes were different
from those observed by Saquet *et al.* after 1 hour of tempering at 550°C; in
particular, the onset of noise activity occurred before $H = 0$ in the observa-
tions of Moorthy *et al.*, but well past $H = 0$ in those of Saquet *et al.*.
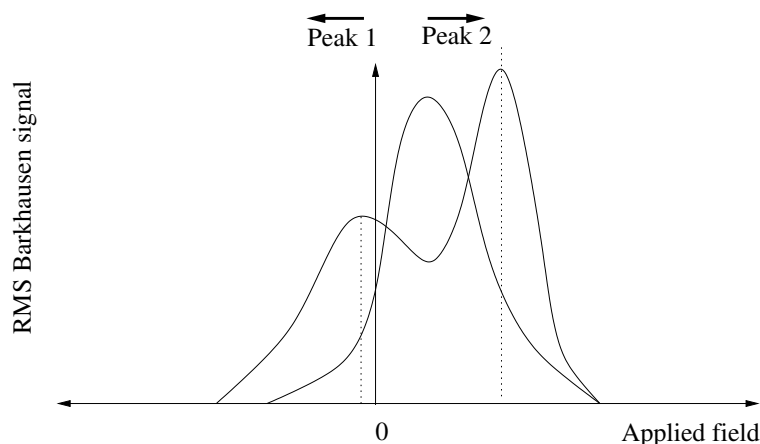
Figure 4.16: Development of two-peak behaviour with increasing tempering
time (Moorthy *et al.*, 1997b).

The peak-splitting was explained as follows: the BN was due mainly to
domain wall motion pinned by carbide particles and grain boundaries, rather
than to domain nucleation or annihilation. (It was considered that, since
ideal saturation was difficult to achieve in practice, domain nucleation would
not be likely since domains had not previously been annihilated. Dislocations
were believed to exert a general retarding effect rather than participating
in pinning.) The transformation of martensite to ferrite and carbides cre-
ates two distributions of domain wall pinning sites due respectively to grain
boundaries and precipitates. Prolonged tempering causes coarsening of both
carbides and grains. This increases the magnetostatic energy associated with
each particle (§ 3.3.1) but reduces the energy of grain boundaries by anni-
hilating boundary dislocations. Carbides therefore become stronger pinning

sites as grain boundaries become weaker. Peak 1, at the lower applied field, is due to grain boundary pinning, and Peak 2 to carbides.

Both types of sites were characterised as distributions of critical pinning fields H_{crit} with average critical pinning fields $\bar{H}_{\text{crit}}$ and ranges ΔH_{crit} characterising the width. At short tempering times, the $\bar{H}_{\text{crit}}$ values for the two distributions were similar and the ranges overlapped, giving a single peak. After a longer time, the distinct distributions could clearly be seen.

The position of Peak 1 on the H axis gave a good linear correlation with the average grain size (Moorthy *et al.*, 1998; Figure 4.17) and that of Peak 2 was even more clearly related to the average carbide size (Figure 4.18). This lends support to the suggested interpretation.

Peak heights were attributed to a combination of the number of domain wall events and the mean free path of walls. The Peak 1 height initially increased; this was explained by the coalescence of laths increasing the mean free path. Its subsequent decrease was attributed to the reduction in the number of domain walls as grains or laths coarsened. The height of Peak 2 was observed to be greatest for a narrow size distribution of carbides, and least when the distribution became broader on longer tempering.

Very similar peak-splitting was observed in $2\frac{1}{4}$Cr1Mo and 9Cr1Mo steels, but with delayed kinetics; an obvious double peak was only seen after 50 hours of tempering at 650°C, as opposed to 5 hours at 600°C in the plain-carbon steel (Moorthy *et al.*, 1998, 2000).

The height of Peak 1 dropped rapidly after 500 hours' tempering in the $2\frac{1}{4}$Cr1Mo steel, and after 200 hours in 9Cr1Mo. This was explained by the dissolution of fine, needlelike M_2X particles. These are too small to be efficient pinning sites in their own right, but their presence retards grain and lath coarsening and dislocation annihilation. On dissolution, grain sizes increase rapidly, giving a marked reduction in the number of domains, and hence in the peak height. Moorthy *et al.* suggested, on the basis of work by Goodenough (1954), that needles or plates of M_2X acted as domain nucleation sites, whereas spheroidal carbides such as M_7C_3 and $M_{23}C_6$ did not. Decreases in Peak 2 height were linked with the dissolution of M_2X and precipitation of spheroidal carbides. Since their diameter (~ 0.5 μm) is greater
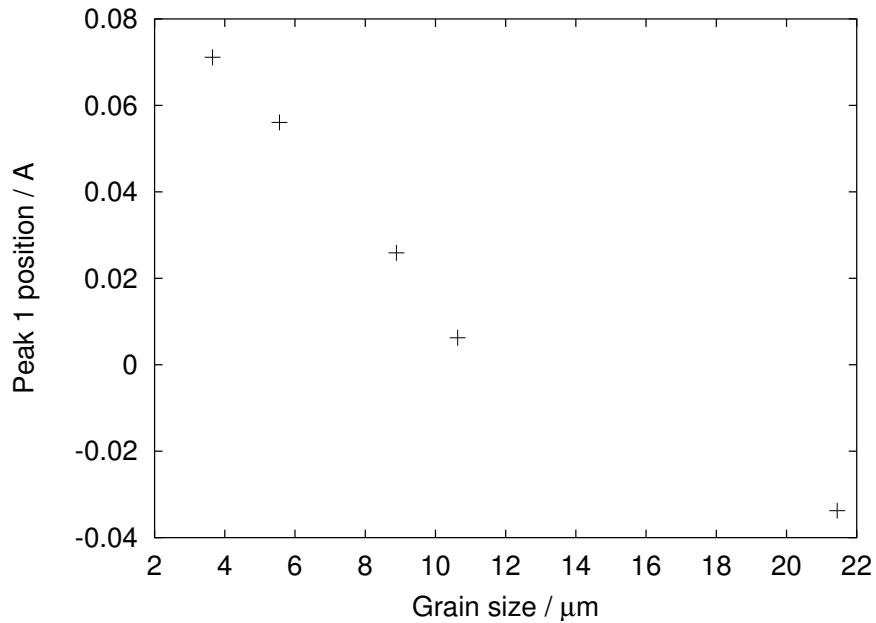
Figure 4.17: Relationship between Peak 1 applied field and grain size (Moorthy *et al.*, 1998).

than the critical value for spike domain formation (0.2 μm), it is likely that large carbides have associated spikes. Longer-range interaction is possible between domain walls and spikes than between walls and particles alone, giving a smaller domain wall mean free path.

11Cr1Mo steel was tempered at 650° for a range of times between 10 minutes and 80 hours, and the total number of BN counts and BN energy (defined as the integral of the square of the BN amplitude over one magnetisation cycle) were measured (Yi *et al.*, 1994). Both quantities displayed the same dependence on tempering time. An initial increase was followed by a plateau, a second more gradual increase, and a further plateau.

Based on microscopic observations, the initial increase was attributed to the precipitation of carbides from solid solution, releasing internal stresses, during the first hour of tempering. It was noted that noise pulses were large and tended to cluster together, with the jumping of one domain wall inducing the movement of a neighbour. The gradual increase in noise energy
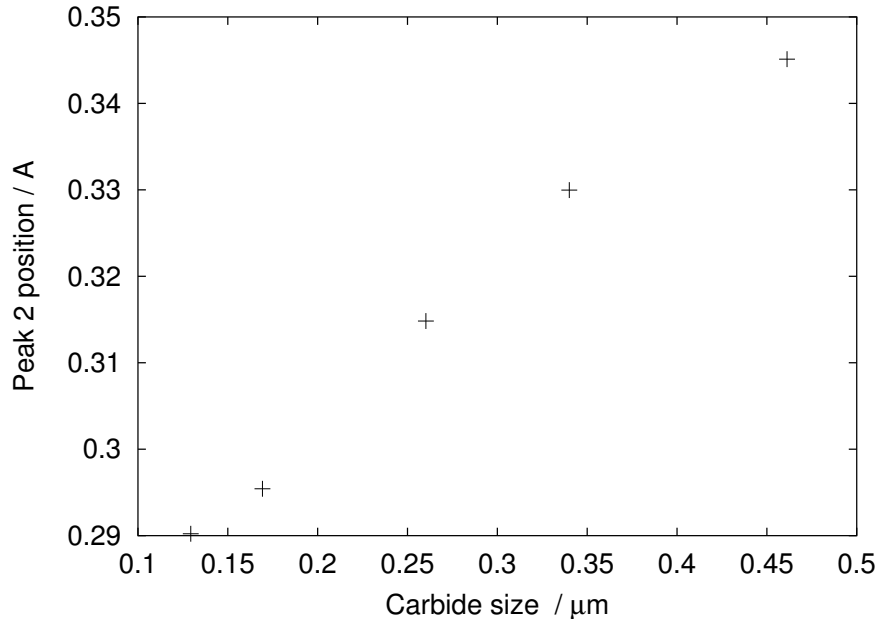
Figure 4.18: Relationship between Peak 2 applied field and carbide size (Moorthy *et al.*, 1998).

between 1 and 20 hours was attributed to the coarsening and reduction in number density of $M_{23}C_6$ particles; this increases the interparticle distance and hence the size of individual Barkhausen events. In the final stage, the observed abrupt change in noise energy was found to occur concurrently with a rapid decrease in dislocation density.

The measurements were made using a small range of applied field, such that only pinned domain wall motion should occur and nucleation and annihilation should be avoided. Within this regime, both the BN energy and the number of counts were linearly related to the hardness.

4.7.4   Summary

The most pronounced change in H_C on tempering in plain-carbon steel was associated with the precipitation of needlelike carbides from solution. During prolonged tempering at 600–650°C, maxima in hardness and H_C appeared in some cases but not in others. Measurements of H_C at very short tem-

pering times revealed two distinct peaks, the first of which occurred within ~ 10 minutes of the start of tempering. The timescale of the second varied; this may be the reason for the discrepancies seen in other studies. The simple relationships between H_C and hardness observed in other materials do not always hold in tempered steels.

In as-quenched samples, little or no MAE activity was seen, but peaks appeared at the 'knees' of the hysteresis curve after tempering, and grew in height with increasing tempering temperature. Although the precise characteristics of the BN peak shapes vary considerably from one experimental study to another, there is a trend towards higher peaks at lower H, signifying weaker pinning, with increasing tempering temperature. Prolonged, high-temperature tempering causes the peak to split into two parts, which separate and decrease in height with tempering time. Moorthy *et al.* (1997b, 1998, 2000) explained the peak shapes in terms of distributions of pinning sites from carbides and grain boundaries, and supported the interpretation with linear relationships between peak positions and microstructural feature dimensions.

4.8   Are the results inconsistent?

Concerns have been raised over discrepancies between magnetic noise results, for example variations in the number and shape of BN peaks in different studies on very similar materials (Moorthy *et al.*, 1997b; Saquet *et al.*, 1999, Sablik and Augustyniak, 1999). It has been suggested that inconsistencies in experimental apparatus and conditions are the cause.

It is true that conditions vary widely. As an illustration, Table 4.2 demonstrates the differences in applied field range, frequency and filtering used in experiments on tempered steels. It has been shown that changes in these parameters can alter the BN characteristics (§ 4.9.3, § 4.9.4) and even the number of peaks (Kim *et al.*, 1992). However, taking this into account, some conclusions can still be drawn (§ 4.10).

	Waveform	Frequency / Hz	Field range /kAm^{-1}	Filtering range / kHz
Kameda & R., 1987a	?	varied	± 14.3	1–300
Buttle *et al.*, 1987c	triangular	5×10^{-3}	± 21.6	3×10^{-4}–0.36
Saquet *et al.*, 1999	triangular	0.1 Hz	± 20	0.5–500
Moorthy *et al.*, 1998	triangular	0.1 Hz	± 12	0.1–100
Nakai *et al.*, 1989	triangular	1 Hz	?	10–700
Yi *et al.*, 1994	sine	0.1 Hz	± 2.4	1–150

Table 4.2: Experimental conditions used in BN and MAE measurements on tempered steels.

4.9 Effects of magnetising parameters

4.9.1 Surface condition

Because of attenuation by eddy currents, the penetration depth of the BN excitation field is small (~ 0.1 mm) and measurements may therefore be strongly influenced by surface condition, particularly strain.

Coarse grinding and fine polishing did not produce any noticeable difference in the BN signals of plain-carbon steel samples (Clapham *et al.*, 1991). However, in nickel, the influence of surface finish was pronounced, especially when the rate of change of field with time was high (Hill *et al.*, 1991). Vigorous grinding of steel, at feed rates up to 12.7 μm s^{-1}, caused changes in the measured RMS Barkhausen voltage compared to the signal measured at low feed rates (Parakka *et al.*, 1997). At such high rates, transformation to austenite can occur, leading to the formation of a martensitic layer when the surface is quenched with coolant.

Yoshino *et al.* (1996) found that the importance of the surface condition on H_C measurements depended on the magnetising frequency. The surface finish and the degree of oxidation were found to have little effect when magnetisation took place at a very low frequency (0.005 Hz), but to increase the measured H_C when a higher frequency (0.1 Hz) was used.

4.9.2   Magnetising field waveform

A number of different waveforms have been used for the alternating excitation field to obtain BN signals. The most common of these are triangular and sinusoidal, but square waves are also occasionally used. Sipahi *et al.* (1993) found that the noise frequency content was similar when obtained with the triangular or sinusoidal waveform, but was significantly altered by using a square wave. Square waves were more likely to introduce spurious data than either sinusoidal or triangular waves. It was therefore considered that sinusoidal or triangular waveforms should be preferred for BN studies.

4.9.3   Magnetising frequency

In a plain-carbon steel, the RMS BN voltage was higher, and larger peaks were observed, at higher magnetising frequencies (Dhar and Atherton, 1992). This result was true for a variety of applied field amplitudes. The suggested reason was that a greater number of domain walls participated in magnetisation at higher frequencies. However, it was admitted that the precise effect of frequency was difficult to determine.

Similarly, the maximum amplitude of both BN and MAE increased with frequency in a quenched and tempered plain-carbon steel (Kameda and Ranjan, 1987a).

In MAE, the integrated signal was found to be linearly related to magnetising frequency at higher frequencies, but to deviate from linearity at lower values, in both mild steel and nickel (Ng *et al.*, 1996). A model was suggested to explain this behaviour: the observed signal was attributed to a component from domain wall motion and a component from nucleation and annihilation. The different dependences of these on frequency were used to account for the shape of the curve.

A wide variety of magnetising frequency settings are found in the literature (*e.g.* Table 4.2). Work by Moorthy *et al.* (2001) has demonstrated, in addition, that variations in both the frequency and the filtering range can significantly affect the shape of a BN voltage peak, and even the number of peaks visible. It would therefore be advisable to introduce more consistency

into experimental design to ensure repeatability.

4.9.4   Magnetising field amplitude

It has been seen that modification of $H_{\max}$ can affect the number of BN peaks observed (Kim *et al.*, 1992; § 4.5.3).

In a plain-carbon steel, the RMS BN voltage increased smoothly to a maximum at an intermediate $H_{\max}$ value, then decreased at higher $H_{\max}$ (Dhar and Atherton, 1992). The increase was attributed to the greater capacity for overcoming pinning obstacles when the applied field was larger, and the decrease to the predominance of domain rotation over domain wall motion at very high fields. The same form of dependence of RMS voltage on $H_{\max}$ was seen for all frequencies investigated.

The dependence of RMS BN voltage on $H_{\max}$ is shown in Figure 4.19 for three microstructures with the same composition: bainitic, pearlitic and spheroidised pearlite (Mitra *et al.*, 1995). There is clearly a complex interdependence between magnetising frequency, $H_{\max}$ and microstructural state, and this may account for the discrepancies seen in BN results. It would be useful to conduct a systematic investigation of the dependence of peak shapes, RMS voltages, *etc.* for a wide range of compositions and microstructures to give a deeper understanding of these issues.

4.9.5   Demagnetising and stray fields

The demagnetising effect (§ 3.1.3) reduces the actual field experienced when a given field is applied. H_C should be independent of the demagnetising field (Swartzendruber, 1992) but in practice can have some shape-dependence (Blamire, personal communication). Other properties, including BN and MAE characteristics, are subject to demagnetising fields.

Stray fields are those which result from incomplete magnetic circuits, for example at air gaps between a magnetic yoke and a sample surface. In MAE experiments, nonmagnetic spacers are customarily used between the yoke and the surface to minimise extraneous noise. However, these spacers introduce demagnetising and stray fields. Ng *et al.* (1994) found that varying the spacer
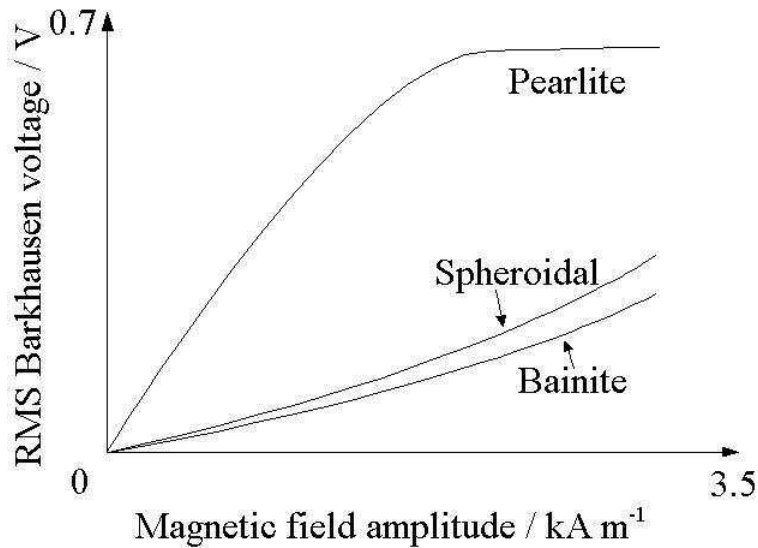
Figure 4.19: Dependence of the RMS BN voltage on applied field amplitude, after Mitra *et al.*, 1995

thickness caused significant changes to MAE peak shapes and even to the number of peaks observed. In nickel, increasing this thickness caused a single peak to split into three, and in mild steel the two peaks present moved apart and decreased in height. It is clear from these results that even small changes in the level of demagnetising or stray fields can have dramatic effects on the observed signal. This is another possible reason for observed discrepancies in results.

4.9.6   Stress

The magnetic behaviour of steels is influenced significantly by elastic stresses via the magnetoelastic effect, such that the evaluation of stress states by magnetic techniques is a large research field.

The BN voltage was measured as a function of the angle between the applied field direction and the axial direction of a steel pipe (Jagadish *et al.*, 1990). An applied tensile stress changed the angle of maximum BN voltage. This observation has important consequences for in-situ microstructural monitoring in stressed components.

4.9.7   Temperature

The transition between ferromagnetic and paramagnetic behaviour at the Curie temperatures of certain carbides can produce an anomaly in the measured H_C (English, 1967). From the two examples given by English, it appears that T_C can vary by at least 200°C depending on composition. Anomalies could cause confusing results if the temperature during NDT is close to T_C for any of the carbides present. However, it may also be possible, after a systematic study, to make use of the phenomenon for identification of phases and monitoring of their compositions.

A further temperature effect is thermal activation, which allows domain walls to overcome pinning sites more easily (Pardavi-Horvath, 1999) but this does not seem to have been investigated extensively.

4.9.8   Magnetic history

On repetition of an earlier measurement on a steel pipe, it was found that the direction in which the greatest BN voltage was observed had changed by 30° (Jagadish *et al.*, 1990). It appeared that the repeated magnetisation and demagnetisation during experiments had altered the magnetic properties of the sample. This effect does not appear to have been documented elsewhere, but it may present difficulties for NDT applications.

4.9.9   Solute segregation

Segregation of solutes, although it did not affect the hysteresis properties, was detectable by both BN and MAE measurement (Kameda and Ranjan, 1987b). For constant carbide morphology and hardness, the RMS and maximum MAE voltages increased as a greater proportion of solute segregated to grain boundaries. The maximum BN voltage was a minimum for an intermediate level of segregation. The results were the same for Sn, Sb and P dopants; this means that magnetic noise is not useful for monitoring grain boundary embrittlement, the degree of which depends on the chemistry of the segregant.

4.10   Summary and conclusions

Magnetic hysteresis and noise properties have been investigated for use in microstructural testing. Clear relationships between H_C and microstructural feature sizes, carbon content or hardness have often been found in simple systems such as equiaxed ferrite. However, these do not always hold in more complicated microstructures such as tempered martensite.

BN and magnetoacoustic emission signals can be difficult to interpret, and the discrepancies in results are well documented. Nonetheless, general results have emerged from this review. Magnetically hard materials, containing strong pinning sites, tend to produce a single BN peak, which can be attributed to pinned wall motion. Fine structure is sometimes seen on this peak if microstructural constituents have sufficiently different pinning strengths. In softer materials, by contrast, two peaks positioned at the 'knees' of the hysteresis curve are present in addition to, or in place of, the single peak. These, because of their position, are believed to arise from domain nucleation and annihilation. Reducing the applied field range in these samples, so that the material is only cycled through a minor loop, suppresses the outer peaks. It is suggested that increasing the level of pinning has a similar effect, preventing domain nucleation and annihilation.

Single-value BN or MAE parameters such as the total number of counts or maximum noise amplitude can be related to microstructural data in simple systems, but may not always be useful when more than one microstructural feature is changing. Analyses of the entire signal contain more information and, in particular, allow the variation in pinning field strength to be followed.

Experimental conditions, such as the magnetising frequency and $H_{\max}$, can significantly affect the measured noise signals. Because of this, it would be advisable to adopt a standard set of experimental practices, or to conduct systematic studies of the effects of magnetising conditions on the material of interest before using magnetic methods for NDT.

Chapter 5

Barkhausen Noise Modelling

5.1 Existing models of hysteresis and Barkhausen noise

5.1.1 Jiles-Atherton model

Jiles and Atherton (1983) used an energy balance to model magnetic hysteresis. The energy supplied to the material by a change in applied field can be dissipated either as a change in magnetostatic energy, or as hysteresis loss.

In the absence of hysteresis, all the energy supplied would go toward modifying the magnetostatic energy. In such a case, the magnetisation would be a reversible, single-valued function of the applied field. This anhysteretic magnetisation M_{an} can be modelled as:

$$M_{an} = M_S f\{H_e\} \tag{5.1}$$

where M_S is the saturation magnetisation, $H_e = H + \alpha M$ is the Weiss mean field (Equation 3.1) and f is an arbitrary function with the properties:

$$\begin{array}{llll} f = 0 & \text{when} & H_e = 0 \\ f \to 1 & \text{when} & H_e \to \infty \end{array} \tag{5.2}$$

A modified Langevin expression (Langevin, 1905) was used to model M_{an}:

$$M_{an}\{H_e\} = M_S \left[\coth\left\{ \frac{H_e}{a} \right\} - \left(\frac{a}{H_e} \right) \right] \tag{5.3}$$

where a is a parameter with units of field.

The energy supplied E_{supp} can therefore be expressed in terms of M_{an}:

$$E_{supp} = \mu_0 \int M_{an}\{H\}\mathrm{d}H \tag{5.4}$$

Hysteresis loss was attributed to domain wall pinning by sites distributed at random, all of which had the same pinning energy for 180° walls, $< \varepsilon_\pi >$. For other domain wall angles θ, the pinning energy $< \varepsilon_{pin} >$ is:

$$< \varepsilon_{pin} >= \frac{1}{2} < \varepsilon_\pi > (1 - \cos\theta) \tag{5.5}$$

For an average pinning site density per unit volume n, the total energy dissipated against pinning E_{pin} when a domain wall of area A sweeps out a distance x between domains at an angle θ to one another is:

$$E_{pin}\{x\} = \int_0^x \frac{n < \varepsilon_{pin} >}{2m}(1 - \cos\theta)A\mathrm{d}x \tag{5.6}$$

where m is the magnetic moment of a typical domain. This gives a net change in magnetisation $\mathrm{d}M$:

$$\mathrm{d}M = m(1 - \cos\theta)A\mathrm{d}x \tag{5.7}$$

Hence E_{pin} can be expressed in terms of M:

$$E_{pin}\{M\} = \frac{n < \varepsilon_{pin} >}{2m} \int_0^M \mathrm{d}M \tag{5.8}$$

The constant $n < \varepsilon_{pin} > /2m$ was termed the pinning parameter k. Equating E_{supp} with the sum of E_{pin} and the magnetostatic energy due to the change in magnetisation $\mathrm{d}M$ gives:

$$\frac{\mathrm{d}M}{\mathrm{d}H} = \frac{M_{an}\{H\} - M\{H\}}{k} \tag{5.9}$$

A subsequent modification allowed for reversible magnetisation M_{rev}, assuming wall-bowing in the direction tending to reduce the difference between the actual magnetisation M and M_{an}:

$$M_{rev} = c(M_{an} - M) \tag{5.10}$$

where c is a constant. The final equation is then given by:

$$\frac{\mathrm{d}M}{\mathrm{d}H} = \frac{M_{an}(H) - M_{irr}(H)}{(k\delta/\mu_0) - \alpha(M_{an}(H) - M_{irr}(H))} + c\left(\frac{\mathrm{d}M_{an}}{\mathrm{d}H} - \frac{\mathrm{d}M}{\mathrm{d}H}\right) \qquad (5.11)$$

where M_{irr} is the irreversible component of magnetisation and δ is a parameter inserted to account for the direction of field increase:

$$\begin{aligned} \delta &= +1 \text{ for } \mathrm{d}H/\mathrm{d}t > 0 \\ \delta &= -1 \text{ for } \mathrm{d}H/\mathrm{d}t < 0 \end{aligned} \qquad (5.12)$$

Hysteresis can therefore be expressed in terms of five constants: α, a, M_S, c and k. Jiles and Atherton later modified k so that it had the same dimensions as H_C:

$$k = \frac{n < \varepsilon_{pin} >}{2m\mu_0} \qquad (5.13)$$

Extensions have been made to this model to allow the modelling of minor loops (Jiles and Atherton, 1984; Carpenter, 1991), and the effects of magnetocrystalline anisotropy (Ramesh *et al.*, 1996, 1997) and crystal texture (Shi *et al.*, 1998). Methodologies for the extraction of modelling parameters from experimental data have also been developed (*e.g.* Jiles *et al.*, 1992; Del Moral Hernandez *et al.*, 2000).

5.1.2   Preisach model

An earlier model by Preisach (1935) considered a magnetic material as an assemblage of particles, each of which could be in one of two magnetisation states. The particle switches between these states at particular field values. If the particle were isolated, its hysteresis loop would be symmetrical, but interactions with other particles with different switching fields shifts the loop along the H axis. The overall behaviour of the material is modelled using a Preisach distribution function, which is a statistical representation of the number of domains switching their states as the applied field is changed. This model is widely used for the magnetic properties of recording media (Jiles, 1998) and has been the subject of many developments and modifications since its introduction.

5.1.3   Equivalence of models and relationship to microstructure

Dupré *et al.* (1999) identified the relationships between modelling parameters in the Jiles-Atherton and Preisach models. Pasquale *et al.* (1999) also demonstrated that the two formulations were equivalent and found simple relationships between the Jiles-Atherton parameter k and the grain size in nonoriented silicon steel, and between k and other material parameters in a metallic glass. Further work has demonstrated that the Jiles-Atherton parameters k and a are affected by the grain diameter d_g and dislocation density ρ_d:

$$
\begin{aligned}
k &= k_0 \left(G_1 + \tfrac{G_2}{d_g} \right) \sqrt{\rho_d} \\
a &= a_0 \left(G_1 + \tfrac{G_2}{d_g} \right) \sqrt{\rho_d}
\end{aligned}
\tag{5.14}
$$

where k_0, a_0, G_1 and G_2 are constants (Sablik, 2001). The rationale behind this formulation was that k, being a measure of the hysteresis loop width, was proportional to the coercive field, which was found from a survey of previous work to depend on the reciprocal of the grain size and the square root of dislocation density. The parameter a was found by Sablik and Jiles (1993) to be proportional to the domain density in the demagnetised state, which should be proportional to the pinning site density and hence to k. Numerical experiments, using values obtained from previous experimental work and the dependencies in Equation 5.14, were performed by Dupré *et al.* (2002) to investigate the variation of the Preisach model parameters on dislocation density and grain size. It appears that, so far, there has been no work on the effects of particles on modelling parameters.

5.1.4   Alessandro, Beatrice, Bertotti and Montorsi (ABBM) model

Alessandro *et al.* (1990a) developed a model for BN based on stochastic fluctuations in the coercivity, initially considering a single, planar 180° domain wall. Williams, Shockley and Kittel (1950) showed that, for macroscopic domain wall movement, the wall velocity v was proportional to the difference

between the field acting on the wall H and the coercive field H_C:

$$kv = H - H_C \qquad (5.15)$$

where k is a constant characterising eddy current damping. Alessandro *et al.* assumed that this relationship was also valid for local fluctuations of H_C on a microstructural scale.

The rate of change of magnetic flux $\dot{\Phi}$ is related to the domain wall velocity v by the equation:

$$\dot{\Phi} = 2\mu_0 M_S \mathrm{d}v \qquad (5.16)$$

where M_S is the saturation magnetisation. Thus,

$$\sigma G \dot{\Phi} = H - H_C \qquad (5.17)$$

where σ is the electrical conductivity and G is a dimensionless coefficient.

The correlation length ξ characterises the range over which a domain wall interacts with a perturbation. The H_C fluctuations were modelled by considering H_C as a random function of domain wall position, and hence of Φ:

$$\frac{\mathrm{d}H_C}{\mathrm{d}\Phi} + \frac{H_C - <H_C>}{\xi} = \frac{\mathrm{d}W}{\mathrm{d}\Phi} \qquad (5.18)$$

where

$$<\mathrm{d}W> = 0, <|\mathrm{d}W|^2> = 2A\mathrm{d}\Phi \qquad (5.19)$$

and A is an unknown constant. The term W represents noise, leading to stochastic fluctuations in H_C, and A characterises the amplitude of these fluctuations.

The magnetic field H experienced by the domain wall depends on both the applied field and the demagnetising field H_d. Because of the difficulty of determining H_d exactly, Alessandro *et al.* restricted the model to regions in which the differential permeability was constant.

Using this basis, models for the pulse amplitude distribution and the power spectrum (*i.e.* Fourier transform) of BN were obtained by applying the theory developed for a single domain wall to the movement of an assemblage of walls. These models agreed reasonably well with experimental measurements of BN from nonoriented Fe-3 wt. % Si within the constant differential permeability regime (Alessandro *et al.*, 1990b).

5.1.5   Extensions to ABBM

Potential energy model

McMichael *et al.* (1993) used ABBM concepts in a BN model for the whole hysteresis loop. Domain walls were assumed to be rigid and planar. The energy per unit area E of a domain wall element under an applied field H is given by:

$$E = -2M_S Hx + E_{dw}\{x\} \qquad (5.20)$$

where x is the domain wall position measured normal to the wall area, M_S is the saturation magnetisation, and $E_{dw}\{x\}$ is the domain wall energy per unit area as a function of its position. The force F on the wall is the derivative of its energy with respect to position:

$$F = \frac{\partial E}{\partial x} = 2M_S H - \frac{\partial E_{dw}\{x\}}{\partial x} \qquad (5.21)$$

Normalised variables $f = F/2M_S$ and $H_C\{x\} = (1/2M_S)(\partial E_{dw}\{x\}/\partial x)$ were used, and the domain wall was considered to move in a positive direction for $f > 0$ $[H > H_C\{x\}]$ and in a negative direction for $f < 0$ $[H < H_C\{x\}]$. For $f = 0$ the wall was in a position of equilibrium, but this was only stable for $dH_C/dx > 0$, *i.e.* a minimum-energy position.

The combined effect of movements of N domain walls contributes to the magnetisation M:

$$M = \frac{1}{N} \sum_{i=1}^{N} A_i x_i \qquad (5.22)$$

where A_i and x_i are the area and position of the ith wall element.

The fluctuations in $h_{ci}\{x_i\}$ are modelled in a similar form to the ABBM model (Equation 5.18):

$$\frac{\mathrm{d}h_{ci}}{\mathrm{d}x_i} = \frac{h_{ci}}{\xi} + \frac{\mathrm{d}W}{\mathrm{d}x_i} \tag{5.23}$$

where, as in Equation 5.18, ξ represents a correlation length and W a noise term with $< \mathrm{d}W_i > = 0, < |\mathrm{d}W_i|^2 > = 2B\mathrm{d}x_i$, B characterising the size of fluctuations in h_{ci}. In this model, the field H is obtained from:

$$H = H_a - N_d M \tag{5.24}$$

where M is magnetisation given by Equation 5.22, H_a is the applied field and N_d is the demagnetising factor.

Combination with Jiles-Atherton

Jiles *et al.* (1993) started, instead, from the rate of change of magnetisation $\dot{M}$, which was kept constant in the original ABBM model:

$$\dot{M} = \left(\frac{\mathrm{d}M}{\mathrm{d}H}\right)\left(\frac{\mathrm{d}H}{\mathrm{d}t}\right) = \chi' \dot{H} \tag{5.25}$$

where χ' is the differential susceptibility.

The BN jump sum M_{JS} is the product of the number of BN events N and average event size $< M_{disc} >$. The rate of change of M_{JS} with time was assumed to be proportional to $\dot{M}$:

$$\frac{\mathrm{d}M_{JS}}{\mathrm{d}t} \propto \chi' \dot{H} \tag{5.26}$$

Assuming that the average BN jump size $< M_{disc} >$ remains constant throughout, and expressing the number of events per unit change of magnetisation as $N'\{t_n\} = \mathrm{d}N\{t_n\}/\mathrm{d}M$, the rate of change of M_{JS} with time was modelled as:

$$\frac{\mathrm{d}M_{JS}\{t_n\}}{\mathrm{d}t} \propto \chi' \left[N'\{t_{n-1}\} + \delta_{rand}\sqrt{N'\{t_{n-1}\}} \right] \tag{5.27}$$

where δ_{rand} is a random number between -1 and $+1$. Predictions of BN signals were made by combining this model with the Jiles-Atherton model

predictions of χ'. In a later modification, Lee *et al.* (2001) proposed that the anhysteretic differential susceptibility $\mathrm{d}M_{an}/\mathrm{d}H$ should be used instead of $\mathrm{d}M/\mathrm{d}H$.

Variations in average coercive field

In Equation 5.18, the average coercive field $< H_C >$ is constant. Clatterbuck *et al.* (2000) proposed that the restriction of ABBM to constant applied fields could be relieved by varying this average as a function of position on the hysteresis loop. The magnetisation then sweeps out a hysteresis loop whose behaviour, over a large number of cycles, is close to the average behaviour, but whose fine structure varies from one cycle to the next because of the random noise component. By varying the parameters ξ and A, this model could be fitted well to experimental BN data from nickel.

5.1.6 Relationships between ABBM parameters and real data

Recent work has investigated relationships between fitting parameters and microstructural data. Lee *et al.* (2001) measured hysteresis loops and BN from Fe-0.05 wt. % C. The Jiles-Atherton model parameters were obtained by fitting the hysteresis loop, and substituted into an ABBM-type model. This allowed good replication of the noise peak position by the model.

Ferritic-pearlitic steels with a variety of carbon contents have also been investigated in the same way (Lo *et al.*, 2002). By adjusting the model parameters ξ and A, it was found that ξ had a strong effect on the simulated pulse height distributions, while A influenced them only weakly. A was held constant and ξ fitted to the experimental data, giving a relationship:

$$\xi = C_1 V_F d_F + C_2 V_P d_P \tag{5.28}$$

where V_F and V_P are the volume fractions of ferrite and pearlite, and D_F and D_P the ferrite and pearlite grain sizes, respectively, and C_1 and C_2 are constants. This simple combination of ferrite and pearlite effects is similar to Equation 4.1.

According to this relationship, the range ξ over which a domain wall interacts with a pinning site depends on the sizes of the grains. Lo *et al.* state that the interaction range is related to the displacement of the wall between pinning sites. There seems to have been a subtle change in the meaning of the term ξ since the original paper by Alessandro *et al.* (1990a); it was then regarded as the range of influence of a pinning site, but Lo *et al.* consider it more as a 'mean free path' between sites. These differences can be reconciled if it is considered that the wall is always within the range of influence of one site or another. This may well be the case in a material with a high defect density such as ferritic-pearlitic steel.

5.1.7   Microstructure-based modelling

Sakamoto *et al.* (1987) modelled the effect of grain size and particle distributions on the RMS Barkhausen noise. It was assumed that all BN pulses had the same duration 2σ and that the time interval between successive pulses τ was also constant. The RMS noise was modelled as:

$$\text{RMS} = C_R \cdot \frac{\tau^2}{\sigma^2} \tag{5.29}$$

where

$$C_R = \frac{1}{8\sqrt{2\pi}H_{max}} \left(\frac{\mathrm{d}H}{\mathrm{d}t}\right)(N \cdot \Delta\Phi) \tag{5.30}$$

and H_{max}, $\mathrm{d}H/\mathrm{d}t$, N and $\Delta\Phi$ are the maximum applied field, the rate of change of field, the number of pulses per unit cross-sectional area and the magnetic flux change respectively.

Expressions for the RMS noise in terms of the microstructure were derived by assuming that the majority of noise originated from domain nucleation and growth.

Grain boundaries

Assuming that the nucleation of a domain wall at a grain boundary, and its propagation across to the opposite side of the grain, produced a single noise pulse of duration 2σ,

$$\sigma = d_g/2\bar{v} \tag{5.31}$$

where d_g is the grain diameter and $\bar{v}$ the average wall velocity.

By combining previous results from Döring (1938), Williams (1950), Nagashima (1959), Bloor and Martin (1959) and Carey (1960), an expression for the RMS voltage was derived in terms of grain size d_g and a grain-size-independent term C_g:

$$\text{RMS} = C_g d_g^{-1/2} \tag{5.32}$$

Particle distributions

In the case of a ferrite microstructure containing cementite particles, after nucleating at the grain boundaries, the domain walls would encounter the particles and be pinned. For a pulse of duration 2σ, in this case:

$$\sigma = \frac{\bar{s}}{2C_v H_p} \tag{5.33}$$

where $\bar{s}$ is the domain wall mean free path, C_v is a proportionality constant and H_p is the pinning field. $\bar{s}$ was approximated to $d_p/\alpha^{1/3}$, where d_p is the cementite particle diameter and α the volume fraction of particles. H_p was obtained from an expression due to Kersten (1943):

$$H_p = 2.5 \left(\frac{K}{\mu_0 M_S} \right) \left(\frac{\delta}{d_p} \right) \alpha^{2/3} \tag{5.34}$$

where δ is the domain wall width and K the anisotropy constant.

The number of pulses N was equated to the number of cementite particles per unit area, $6\alpha/\pi d_p^3$, giving a value for τ:

$$\tau = \frac{\pi t_{total}}{6} \frac{d_p^3}{\alpha} \tag{5.35}$$

so that the RMS voltage is given by:

$$\text{RMS} = C_p d_p^2 \tag{5.36}$$

where, as above, the term C_p is independent of the particle diameter d_p.

Good agreement with experiment was obtained for the dependence of the RMS noise on d_g in ferrite without cementite. In an alloy containing particles, the experimental data agreed with Equation 5.36 for particles smaller than 1 μm in diameter, but broke down when they were larger than this. It is likely that this is due to the dominance of the magnetostatic pinning effect and the formation of spikes when particles are larger (§ 3.3.1).

5.1.8   Models for power plant steels

Domain nucleation and growth

Kameda and Ranjan (1987a) considered that the magnetic BN signal intensity was proportional to dB/dt and the effective surface skin area A from which noise originated. B was expressed as:

$$B = \lambda \left[\beta_n N_n + \left(\frac{\bar{s}}{\delta_w} \right) N_g \right] \tag{5.37}$$

where λ is a coefficient related to the atomic magnetic moment, β_n a coefficient related to the spike shape of nucleated domains, N_n the density of nucleated walls, $\bar{s}$ the average displacement of growing domains, δ_w the domain wall thickness and N_g the density of propagating domain walls. The first term describes domain nucleation, and the second, domain growth.

Kameda and Ranjan predicted that dN_n/dH would be a maximum as the field was reduced from saturation and the nucleation of domains allowed a reduction in magnetostatic energy. dN_g/dH was believed to have a more complex form, with two maxima and two minima, and a smaller maximum amplitude than dN_n/dH. They considered that the BN behaviour would be dominated by nucleation when the number of defects was large, for example in a power plant steel after quenching. Reducing the density of defects would give a larger mean free path $\bar{s}$, allowing domain growth to become significant. This interpretation was used to explain the change from a single to a double peak on tempering martensitic steel.

Moorthy *et al.* interpretation

The alternative interpretation of power plant steel BN data, by Moorthy *et al.* (1997b, 1998, 2000) was introduced in § 4.7.3. Pinning sites due to grain boundaries were considered to have a distribution of strengths with a width ΔH_{gb} and average value $\bar{H}_{gb}$, and pinning sites due to carbide particles could likewise be described by ΔH_{cp} and $\bar{H}_{cp}$. Magnetisation was described as a two-stage process: firstly, the domain walls nucleated at, and became unpinned from, the grain boundaries and were pinned by the carbides, and secondly, they were unpinned from the carbides. The two sets of unpinning events were each associated with a peak in BN emission.

5.1.9   Summary

It has been seen that there are several modelling strategies for magnetic hysteresis and BN:

1. Use of an energy balance to model hysteresis, with a single parameter to characterise pinning strength.

2. Preisach-type models using distributions of subunits, each of which can adopt one of two states.

3. Models based on stochastic fluctuations in local coercive field, characterised by their amplitude and interaction range.

4. Quantitative microstructural interpretations based on the effect of feature spacing on jump sizes.

5. Considerations of the probability of domain nucleation and growth.

6. Qualitative microstructural interpretations based on distributions of pinning site strengths due to grain boundaries and carbides.

If, as is suggested by Moorthy *et al.*, both grain boundary and carbide particle pinning sites play a part in the overall BN behaviour, it is possible that models of types 1 and 3 will not be able to accommodate the complexity

of the problem without the introduction of, for example, a second k parameter in the Jiles-Atherton model or two distributions of H_C fluctuations in ABBM-type models. The Sakamoto *et al.* model (4) considers both kinds of sites, but these were used to model the overall RMS noise rather than the variation of the BN voltage with H. Kameda and Ranjan (5) considered the effect of pinning site densities on mean free path, and Moorthy *et al.* (6) introduced the idea of distributions of pinning site strengths. These two concepts were used to develop a new model of the dependence of BN voltage on H in a steel containing two types of pinning sites.

5.2   A new model for BN in power plant steels

This model considers statistical distributions of pinning site strengths from two types of microstructural features, and their combined effect on the number of BN events and the domain wall mean free path as H varies.

Initially, domain walls are pinned in place by both grain boundaries and carbides. At a certain value of applied field, those pinned by grain boundaries are released, but the carbide-pinned domain walls remain in place until the field has increased sufficiently for them to escape. This model is slightly different from that of Moorthy *et al.*, in which the walls are initially considered to be pinned only by grain boundaries.

The distance moved by a domain wall after unpinning, and the resulting change in magnetisation, depend on the spacing of domain wall obstacles. Pinning sites which act as obstacles at low applied fields may easily be bypassed at higher fields, so that they would no longer act as effective pinning sites. This new model therefore considers the domain wall mean free path as a function of applied field, rather than adopting a constant value as has been used in most previous interpretations apart from the work of Kameda and Ranjan (1987a).

5.3   Assumptions

It is assumed that all domain walls are planar and of Type-II character. BN events are due solely to domain wall motion, and the number of domain walls remains constant, within the applied field range of interest. The domain wall surface area also remains the same throughout, and domain walls do not interact with one another. In essence, it is assumed, as in the ABBM model, that the ensemble of domain walls behaves in exactly the same way as would a single wall. The domain walls are assumed always to move in discrete jumps rather than continuously. Their motion is assumed to be rapid compared to the rate of change of field with time.

Fluctuations in the coercive field or potential energy originate only from microstructural features, which are distributed evenly in space. The strength

of these pinning sites is characterised not by a constant but by a statistical distribution. It is assumed for the sake of simplicity that there is no energetic interaction between pinning sites.

Based on previous experimental observations, it is proposed that the number and type of pinning sites which are actively able to obstruct domain walls varies with the applied field. The field required to overcome a pinning site is determined by the local coercive, or pinning, field. If the field experienced by the domain walls is H, pinning sites with $H_C < H$ can be overcome, and only those with $H_C \geq H$ will resist wall motion.

The actual field experienced by the domain wall differs from the applied field by an amount depending on the magnetisation and the demagnetising factor. Many previous models have relied on the assumption that the BN signal amplitude is proportional to the rate of change of magnetisation $\mathrm{d}M/\mathrm{d}t$ or induction $\mathrm{d}B/\mathrm{d}t$. If this relationship were to be used here then it would be possible to estimate the demagnetising field. However, it has been shown experimentally that this proportionality does not always hold (Kim *et al.*, 1992) and that the regime of its applicability is complex, depending on the microstructural condition and the applied field amplitude. It was therefore decided to avoid using this relationship.

A possible solution to this problem of demagnetising fields would be to obtain the magnetisation as a function of applied field from the Jiles-Atherton or Preisach model, as used when fitting ABBM-type models, and use this to modify the field value for the new model. However, the published data sets used for the fitting did not include hysteresis measurements.

It was considered that, for the initial development of the model, demagnetising fields should be assumed not to have a significant effect on the behaviour of the domain walls. Since BN measurement geometry is designed to minimise demagnetising and stray fields, this assumption may be reasonable. Modifications to include a demagnetising factor could be made if the model showed promise.

5.4 Origin of the noise

A domain wall of surface area $\mathbf{A}_w$, moving a distance $\mathbf{l_w}$ and sweeping out a volume $(\mathbf{A}_w.\delta\mathbf{l_w})$, causes a change in magnetisation $\delta\mathbf{m}$:

$$\delta\mathbf{m} = \beta(\mathbf{A}_w.\delta\mathbf{l_w}) \tag{5.38}$$

where β depends on the angle between the magnetisation of adjacent domains and the atomic magnetic moment (Saquet *et al.*, 1999). If it is assumed that the domain walls always move in a direction parallel to the normal of the domain wall plane, then the expression $(\mathbf{S}.\delta\mathbf{l})$ reduces to $S \cdot \delta l$. The total change in magnetisation $\delta M\{H\}$ at a certain field H is given by the product of the number of domain wall movement events at field H, $N\{H\}$ and the vector sum of all the individual changes $\delta\mathbf{m}$. Assuming that all the domain walls involved are Type-II (180°), β is constant, and Equation 5.38 reduces to:

$$\delta M\{H\} \propto N\{H\} < l > \{H\} \tag{5.39}$$

where $< l > \{H\}$ is the average domain wall displacement (mean free path) at field H.

The electric field amplitude E_0 induced by this change in magnetisation is given by the rate of change of magnetisation with time. For a discrete change in magnetisation, this is given by:

$$E_0 = \frac{\delta M}{\delta t} \tag{5.40}$$

where δt is the time interval over which the change occurs. As mentioned above, it is assumed that the domain walls move rapidly enough that the change in magnetisation $\delta M\{H\}$ occurs immediately the field is changed, and does not depend on the rate of change of field.

The noise voltage V measured by the pickup coil depends on the noise frequency, with higher-frequency noise experiencing more signal attenuation (Saquet *et al.*, 1999). However, for low-frequency noise, the measured voltage can be considered to be proportional to E_0. For simplicity, therefore, it is

assumed that the frequency f is low enough to avoid attenuation and to allow a simple proportionality between the change of magnetisation and the measured pulse size:

$$V \propto N\{H\} < l > \{H\} \tag{5.41}$$

This is the simple relationship 'Noise amplitude = number of events $\times$ mean free path' which is sometimes used to interpret BN signals in the literature, but it is only truly valid in a limited range of circumstances.

5.5   Construction of the statistical model

5.5.1   Distribution of pinning sites

Initially, it was assumed that the number of pinning sites per unit volume with pinning strength S, $n\{S\}$, follows a normal distribution with mean value $< S >$ and standard deviation ΔS. The total number of pinning points per unit volume was A. Thus:

$$n\{S\} = \frac{A}{\Delta S\sqrt{2\pi}} \cdot \exp\left\{-\frac{1}{2}\left(\frac{S - <S>}{\Delta S}\right)^2\right\} \tag{5.42}$$

5.5.2   Impediments to domain wall motion

When the material experiences a magnetic field H, pinning sites with pinning strength $S \geq H$ are able to impede domain wall motion. These sites will be referred to as 'active sites'.

The number of active sites per unit volume $N\{H\}$ is given by the integral of $n\{S\}$ with respect to S from H to infinity:

$$N\{H\} = \int_H^\infty n\{S\}\mathrm{d}S \tag{5.43}$$

Thus:

$$N\{H\} = \frac{A}{2}\,\mathrm{erfc}\left\{\frac{H - <S>}{\Delta S\sqrt{2}}\right\} \tag{5.44}$$

5.5.3 Mean free path of domain walls

In order to estimate the mean free path, it is necessary to make an assumption about the arrangement of the active pinning sites. A suitably basic first approximation is to consider all the pinning sites as points arranged in a simple cubic lattice, with one site per cube of side l, where $l = l\{H\}$:

$$l\{H\} = \left(\frac{1}{N\{H\}}\right)^{\frac{1}{3}} \tag{5.45}$$

The mean free path of domain walls travelling through the material can be approximated to $l\{H\}$:

$$< l > \{H\} = l\{H\} \tag{5.46}$$

The assumptions made to derive this expression are crude, taking no account of the planar nature of grain boundaries, variations in carbide diameter, or phenomena such as the preferential nucleation of carbides at grain boundaries, but subsequent refinements could be made if the model showed promise.

5.5.4 Number of Barkhausen events occurring

Assuming for simplicity that there are no demagnetising fields, the field H experienced by the material is equal to the applied field. The number of Barkhausen events occurring due to domain wall unpinning at applied field H is equal to the number of pinning sites of strength $S = H$.

This is obtained from Equation 5.42:

$$n\{H\} = \frac{A}{\Delta S \sqrt{2\pi}} \cdot \exp\left\{-\frac{1}{2}\left(\frac{H - < S >}{\Delta S}\right)^2\right\} \tag{5.47}$$

5.5.5 Barkhausen amplitude

Adopting the assumption that the RMS voltage $V\{H\}$ at field H is proportional to the number of Barkhausen events $n\{H\}$ multiplied by the mean free path $< l > \{H\}$:

$$V\{H\} = C \cdot n\{H\} \cdot < l > \{H\} \tag{5.48}$$

where C is a constant, gives:

$$V\{H\} = C \cdot \frac{A}{\Delta S \sqrt{2\pi}} \cdot \exp\left\{-\frac{1}{2}\left(\frac{H- < S >}{\Delta S}\right)^2\right\} \cdot \left[\frac{A}{2}\ \text{erfc}\left\{\frac{H- < S >}{\Delta S \sqrt{2}}\right\}\right]^{-\frac{1}{3}} \tag{5.49}$$

5.5.6 Multiple distributions of pinning points

Different types of pinning site can be modelled by introducing more than one distribution, with different constant terms for each:

$$n_i\{S\} = A_i \cdot \exp\left\{-\left(\frac{S- < S >_i}{(\Delta S)_i}\right)^2\right\} \tag{5.50}$$

The overall number of pinning sites with a pinning strength greater than H is now given by:

$$N\{H\} = \sum_{i=1}^{m} \int_{H}^{\infty} n_i\{S\} \mathrm{d}S \tag{5.51}$$

where m is the total number of pinning site distributions.

Thus:

$$N\{H\} = \sum_{i=1}^{m} \frac{A_i \sqrt{\pi}}{2(\Delta S)_i} \cdot \text{erfc}\left\{\frac{H- < S >_i}{(\Delta S)_i}\right\} \tag{5.52}$$

The relation $V\{H\} = C \cdot n\{H\} \cdot < l > \{H\}$ (Equation 5.48) should still apply as long as there are no preferential orientations of particular types of sites; hence:

$$V\{H\} = C \cdot \sum_{i=1}^{m} \frac{A_i \sqrt{\pi}}{2(\Delta S)_i} \cdot \text{erfc}\left\{\frac{H- < S >_i}{(\Delta S)_i}\right\} \tag{5.53}$$

Plots of this function for $m = 2$ were able to replicate single-peak, shoulder and double-peak behaviour when appropriate values of the parameters A_i, $< S >_i$ and ΔS_i were selected. An example is shown in Figure 5.1. This

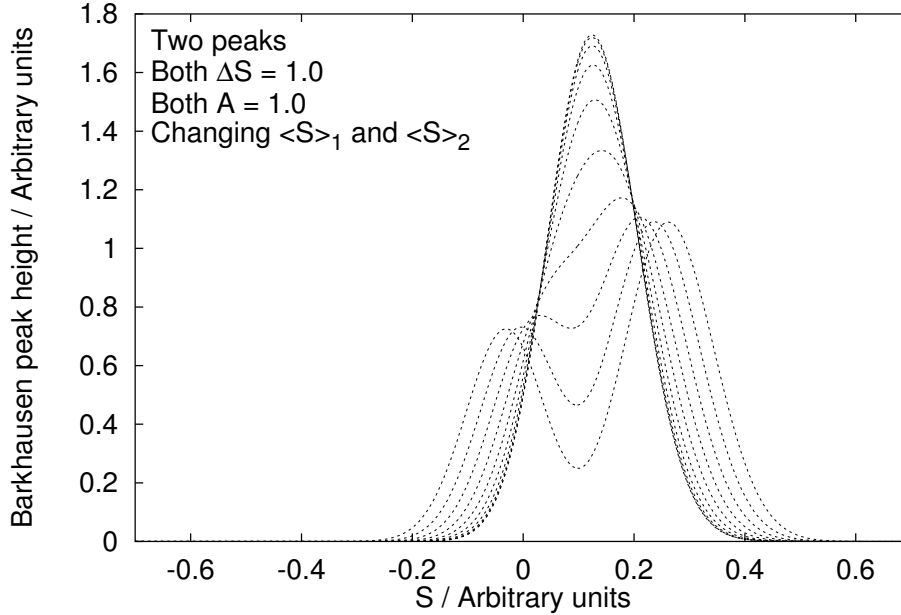first attempt at modelling, using two normal distributions, is referred to as Model 1.

Figure 5.1: Transition between single- and double-peak behaviour

5.6 Log-normal model

In the real experimental data sets shown in Figure 5.2, the lower-field peak appears asymmetric. A modified model, in which the pinning site strengths contributing to this peak follow a log-normal distribution (Mihram, 1972), was therefore proposed:

$$n\{S\} = \begin{cases} \frac{A}{S\Delta x\sqrt{2\pi}} \cdot \exp\left\{-\frac{1}{2}\left(\frac{\ln(S-S_b)-<x>}{\Delta x}\right)^2\right\} & S > 0 \\ 0 & S \leq 0 \end{cases} \tag{5.54}$$

where $<x>$ and Δx are the mean value and the standard deviation of $\ln(S-S_b)$ respectively, and S_b is the field at which the first unpinning events due to this distribution occur.

This gives an integrated value from H to infinity of:

– 114 –

$$N\{H\} = \begin{cases} \frac{A}{2} \cdot \mathrm{erfc}\left\{\frac{\ln(H - S_b) - <x>}{\Delta x \sqrt{2}}\right\} & S > 0 \\ 0 & S \leq 0 \end{cases} \tag{5.55}$$

If, as suggested by Moorthy *et al.*, the pinning strengths contributing to the first peak are related to grain size, a log-normal distribution would be a reasonable assumption, since this is the approximate distribution found in experiment (Okazaki and Conrad, 1972; Rhines and Patterson, 1982; Pande, 1987, reported in Krill and Chen, 2002).

The second peak, as before, is modelled as a normal distribution. The overall model is constructed in the same way as above, and referred to as Model 2.

5.7 Summary of model equations

Model 1

$$\begin{aligned} n_1\{S\} &= A_1 \cdot \exp\left\{-\left(\frac{S - <S>_1}{(\Delta S)_1}\right)^2\right\} \\ n_2\{S\} &= A_2 \cdot \exp\left\{-\left(\frac{S - <S>_2}{(\Delta S)_2}\right)^2\right\} \end{aligned} \tag{5.56}$$

Model 2

$$\begin{aligned} n_1\{S\} &= \begin{cases} \frac{A_1}{S \Delta x \sqrt{2\pi}} \cdot \exp\left\{-\frac{1}{2}\left(\frac{\ln(S - S_b) - <x>}{\Delta x}\right)^2\right\} & S > 0 \\ 0 & S \leq 0 \end{cases} \\ n_2\{S\} &= A_2 \cdot \exp\left\{-\left(\frac{S - <S>_2}{(\Delta S)_2}\right)^2\right\} \end{aligned} \tag{5.57}$$

Both models

$$N\{H\} = \int_H^\infty (n_1\{S\} + n_2\{S\})\mathrm{d}S \tag{5.58}$$

$$V\{H\} = C \cdot (n_1\{H\} + n_2\{H\}) \cdot \left(\frac{1}{N\{H\}}\right)^{\frac{1}{3}} \tag{5.59}$$

5.8 Comparison with experimental data

Models 1 and 2 were tested against experimental data from Moorthy *et al.* (1998) on a 0.22 C 0.12 Mn wt. % steel, quenched and tempered at 600°C

for a range of times between 0.5 and 100 hours (Figure 5.2). These data were chosen because, after the earliest stages of tempering, there was only one type of carbide present: Fe_3C. Also, published data on the average grain and carbide sizes in these steels were available. Data were acquired using the program 'DataThief', which converts images into digital data.
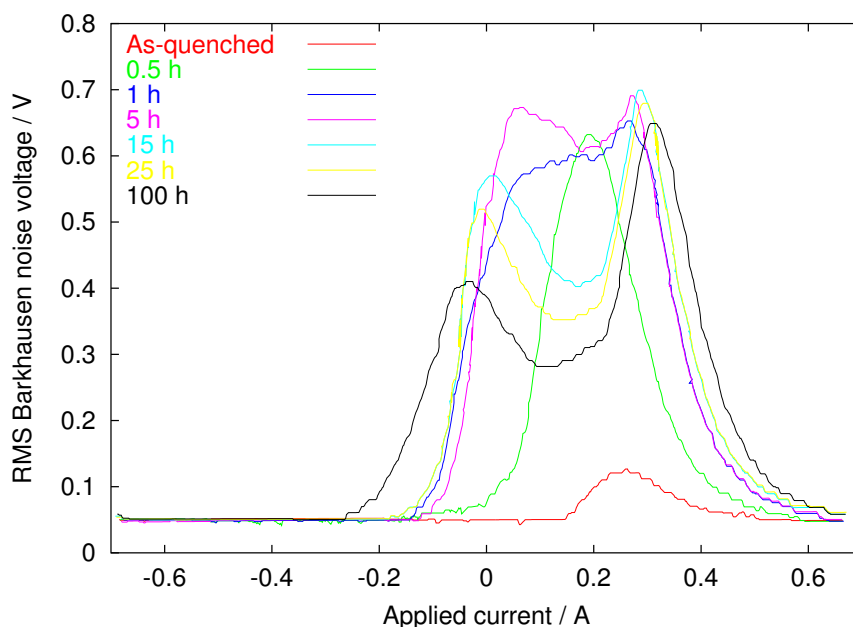

Figure 5.2: Real BN data from tempered 0.22 C 0.12 Mn wt. % steel. Data from Moorthy *et al.*, 1998.

Programs were written to fit Models 1 and 2 to the experimental data. The Fortran 77 code for the Model 2 program, and details of the fitting methodology, are given in the Appendix.

The fitted BN curves are shown in Figure 5.3–Figure 5.8. The horizontal scales on these diagrams are in units of magnetising current rather than applied field, but the field is proportional to the current so the shape of the curve is not affected by this. It can be seen that single peaks can be fitted very well using both models (Figure 5.3). Model 2 is better at fitting shoulder behaviour (Figure 5.4) and two-peak behaviour (Figure 5.8). The region between the peaks is the most problematic for both models; the real

V value is higher than the modelled value, causing the fitted peaks to move closer together than the real peaks. The noise in this central area may be due to pinning by intragranular dislocations, which have not been considered in either model.

The 'error' figure quoted to quantify the goodness of fit is calculated using:

$$E = \left[\frac{\sum (V_r\{H\} - V_p\{H\})^2}{\sum (V_r\{H\})^2} \right]^{-\frac{1}{2}} \cdot 100\% \tag{5.60}$$

where $V_r\{H\}$ is the real value and $V_p\{H\}$ the predicted value of the RMS Barkhausen voltage *V* at field *H*.

Barkhausen two-peak data may also be analysed by fitting a normal distribution to each peak. The total amplitude is given by the sum of two expressions of the form of n_1 and n_2 in Equation 5.56 (but since Equation 5.58 and Equation 5.59 are not considered, the parameters in the normal distribution expressions have different meanings from those in Equation 5.56). The error due to fitting using this method was compared with the errors due to the two models. The results in Table 5.1 show that, while the peak-fitting method sometimes produces a fit comparable with that of Model 1, Model 2 performs consistently better, especially at longer tempering times when the double-peak behaviour is well developed.
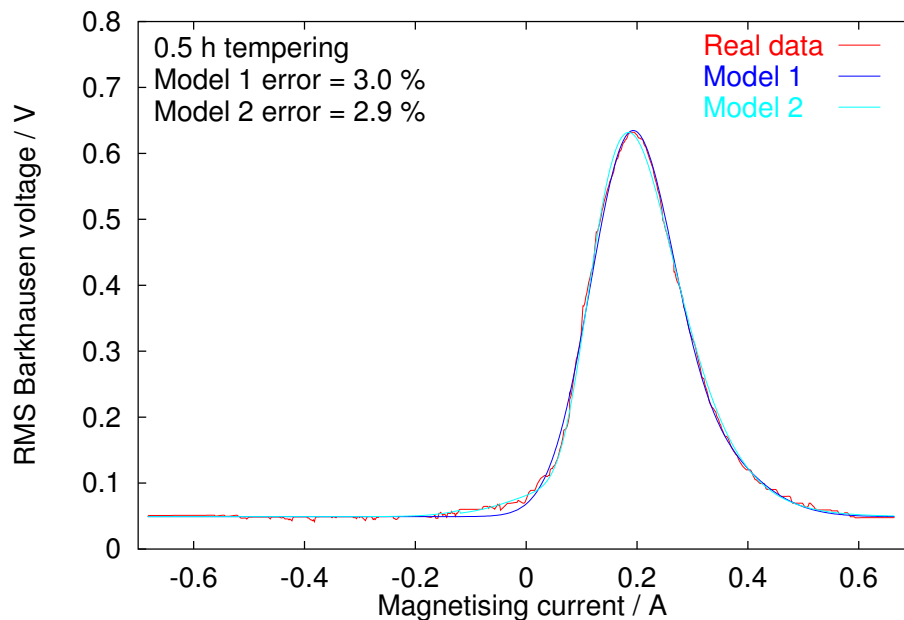
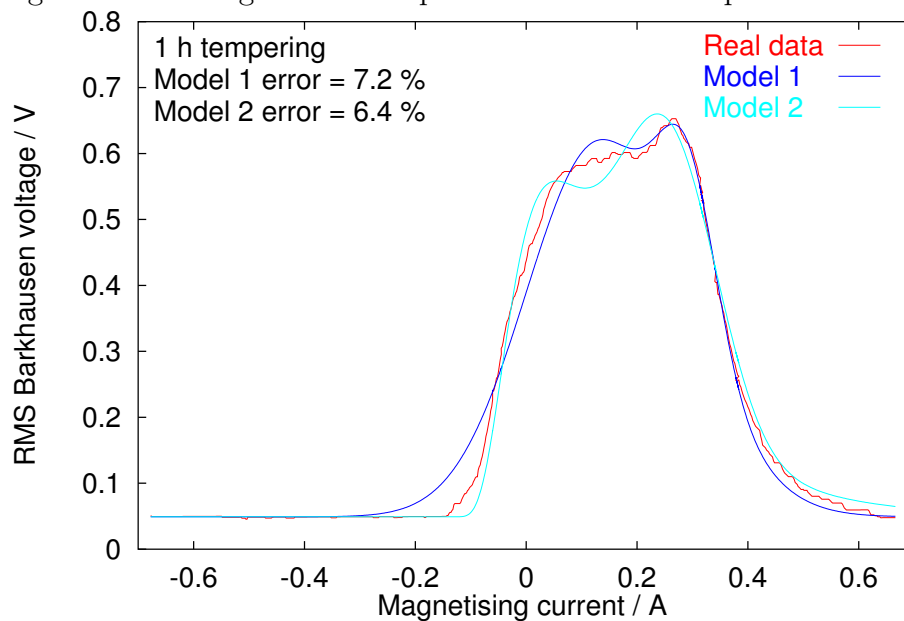Figure 5.3: Fitting of data for plain-carbon steel tempered for 0.5 h.

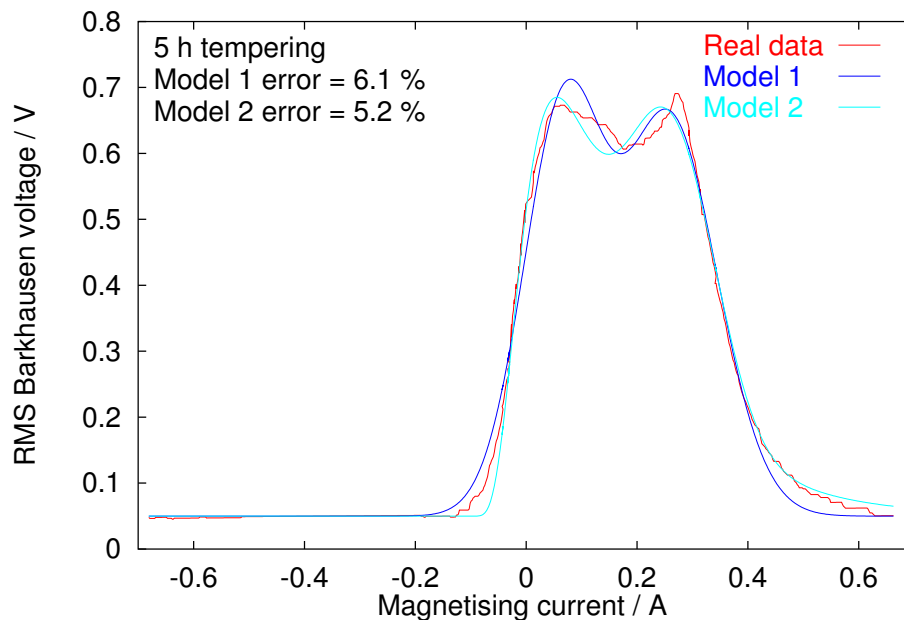Figure 5.4: Fitting of data for plain-carbon steel tempered for 1 h.

Figure 5.5: Fitting of data for plain-carbon steel tempered for 5 h.
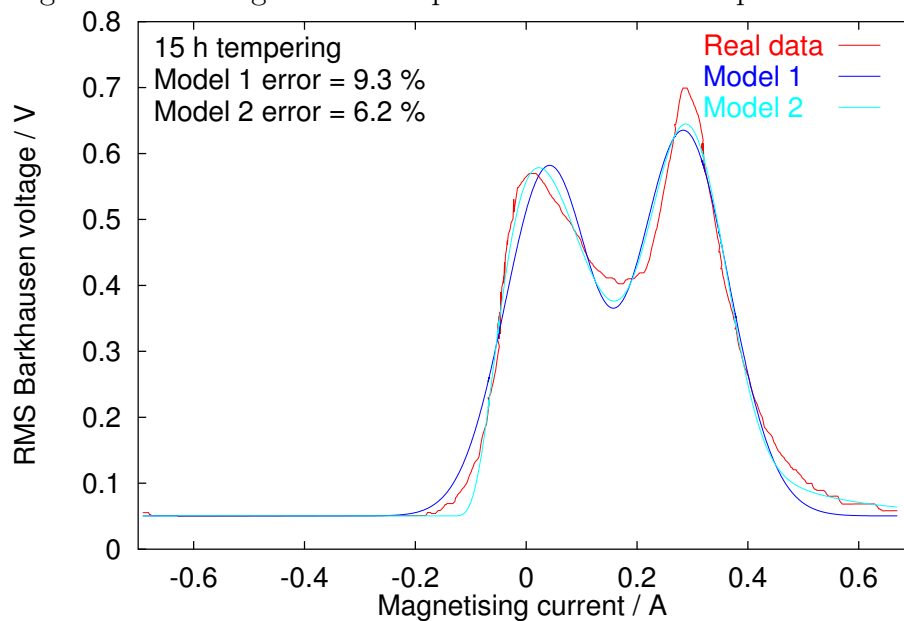

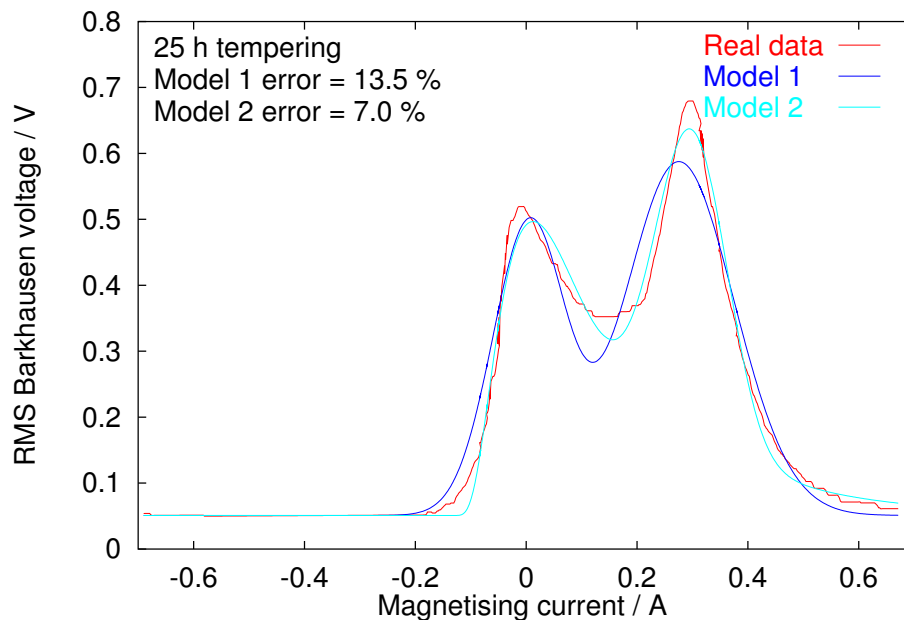Figure 5.6: Fitting of data for plain-carbon steel tempered for 15 h.

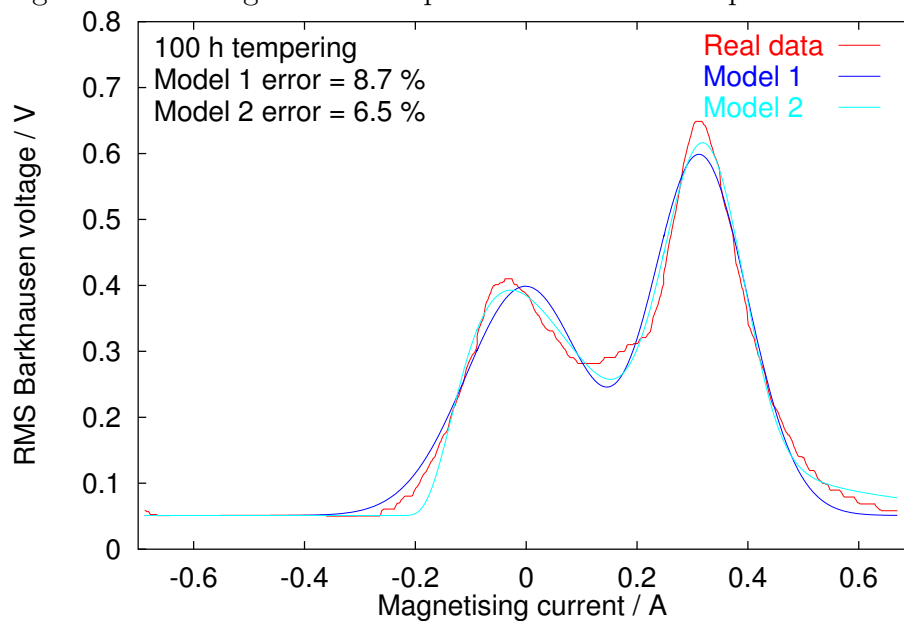Figure 5.7: Fitting of data for plain-carbon steel tempered for 25 h.

Figure 5.8: Fitting of data for plain-carbon steel tempered for 100 h.

Time	Error (%)		
	Peak-fitting	Model 1	Model 2
0	3.58	3.60	3.14
0.5	2.98	3.03	2.85
1	13.1	7.18	6.44
5	6.16	6.05	5.20
15	9.01	9.31	6.23
25	13.9	13.5	6.96
100	8.44	8.69	6.53
Mean	**8.17**	**7.34**	**5.34**

Table 5.1: Fitting errors of arbitrary peak-fitting, Model 1 and Model 2.

5.9 Relationship between fitting parameters and metallographic data

5.9.1 Pinning strength relationships to grain and carbide sizes

In order to test whether the model has any physical basis, the fitting parameters obtained were compared with grain and carbide size data from the work of Moorthy *et al.*

In Model 1, the parameters $< S >_1$ and $< S >_2$ represent the average pinning strengths of the two distributions. Figure 5.9 shows a decrease in $< S >_1$ with increasing grain size, but an indeterminate relationship between $< S >_2$ and carbide size.

In Model 2, the average pinning strength of the log-normal distribution is given by $e^{<x>} + S_b$ (Equation 5.54). Figure 5.10 shows a clear decrease in $e^{<x>} + S_b$ with increasing grain size, and an increase in $< S >_2$ with increasing carbide size. These trends correspond well with the expected pinning strength behaviour of grain boundaries and carbides in tempered steels. It is therefore likely that Model 2 has a more reliable physical basis than Model 1. Since the relationships between the modelling parameters and the microstructural measurements are approximately linear, it should

Time	Grain size / μm	Carbide size / μm	Fitting error / %
1	3.7	0.13	9.29
5	5.6	0.17	5.63
15	8.9	0.26	8.00
25	10.7	0.34	7.05
100	21.5	0.46	6.82

Table 5.2: Fitting errors for model with values of $e^{<x>} + S_b$ and $< S >_2$ calculated from microstructural data.

be possible to estimate grain and carbide sizes within this range by fitting the Barkhausen profile using this model.

5.9.2 Fitting of model to microstructural data

Linear regression was applied to obtain the slopes of the straight lines on Figure 5.10. Using these slopes, values of $e^{<x>} + S_b$ and $< S >_2$ calculated from the grain and carbide sizes respectively were substituted into the model and the other parameters fitted as before. Table 5.2 shows the errors generated by this fitting. They are larger than those for Model 2 in Table 5.1, but still lower than for peak-fitting, and for Model 1 in all cases but one. As before, the superiority of Model 2 is more evident at longer tempering times.

5.9.3 Tests of the model on other data sets

Three further data sets were available, from a 0.22 C, 0.02 Mn wt. % steel, a $2\frac{1}{4}$Cr1Mo and a 9Cr1Mo steel (Moorthy *et al.*, 1997b, 1998, 2000). Model 2 was fitted to these data sets, and the variation of the fitting parameters with tempering time was studied.

Carbon-manganese steels

Comparisons between the Model 2 fitting parameters from the two C-Mn steel data sets are shown in Figure 5.11–Figure 5.14. Fitting of the 5 hour data set gave a ΔS_2 value several orders of magnitude greater than those of the other data sets. This was clearly an unphysical solution, and an indication

that the fitting program must be modified to avoid even infrequent failures of this sort. This point was removed from the plots so that trends in the other values could be seen. Figure 5.11 shows the variation of $e^{<x>} + S_b$, with tempering time. It initially drops very rapidly, then decreases more slowly at longer times. This corresponds well with the expected changes in grain boundary pinning strength, with an initial rapid decrease as the dislocation density reduces, followed by a more gradual change as coarsening and recrystallisation take place. The peak at 5 hours in the blue curve is from the same set of parameters as the unrealistic ΔS_2 value was found, so the $e^{<x>} + S_b$ value here may also be unreliable.

$< S >_2$ increases rapidly at short tempering times, then begins to level off at longer times (Figure 5.12). This may be due to the pinning site strength increasing as the carbides coarsen, then reaching the critical size for spike domain formation at longer times.

The relationship betwen Δx and the tempering time is less clear (Figure 5.13), but the variation of ΔS_2 with tempering time is consistent between the two steels. However, ΔS_2 does not correspond to the widths of the carbide size distributions published by Moorthy *et al.* (1997b), which increase monotonically with tempering time.

Power plant steels

Figure 5.15 and Figure 5.16 show experimental data from $2\frac{1}{4}$Cr1Mo and 9Cr1Mo steels respectively. The variations of $e^{<x>} + S_b$ and $< S >_2$ with tempering time for these data are plotted in Figure 5.17 ($2\frac{1}{4}$Cr1Mo) and Figure 5.18 (9Cr1Mo). In both cases, $e^{<x>} + S_b$ decreases rapidly in the very early stages of tempering, before increasing slightly at longer times. $< S >_2$ peaks at an intermediate tempering time in the $2\frac{1}{4}$Cr1Mo steel, but not in the 9Cr1Mo steel. This may be related to a real phenomenon involving carbide precipitation sequences, or to errors in fitting. It is difficult to know which is the case without carbide size data for these steels.
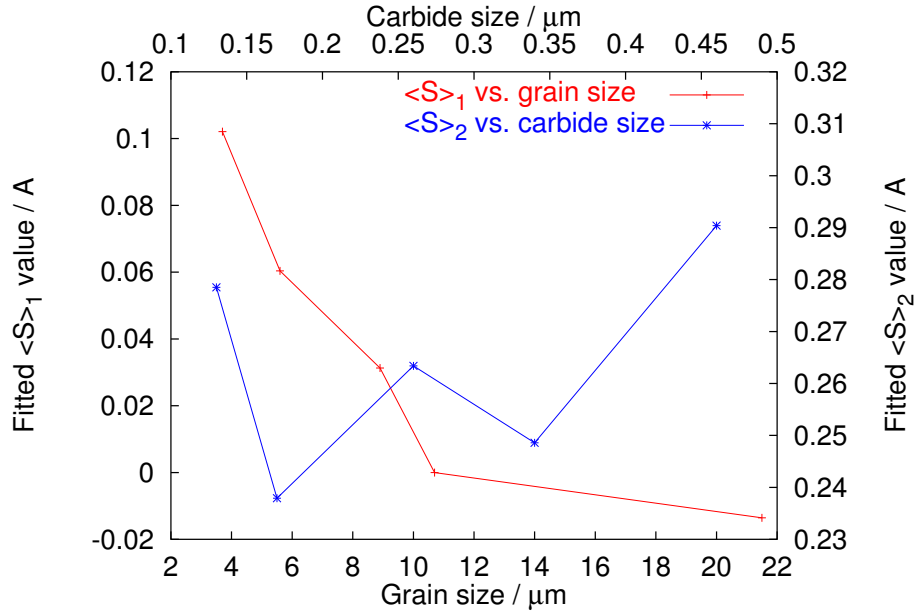
Figure 5.9: Fitting parameters $< S >_1$ versus grain size and $< S >_2$ versus carbide size for Model 1.
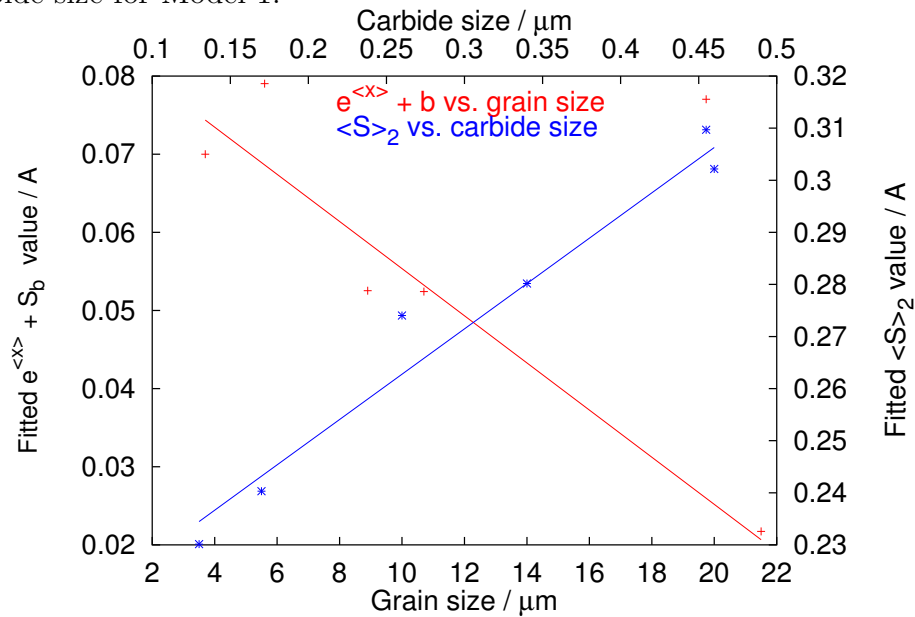

Figure 5.10: Fitting parameters $e^{<x>} + S_b$ versus grain size and $< S >_2$ versus carbide size for Model 2.
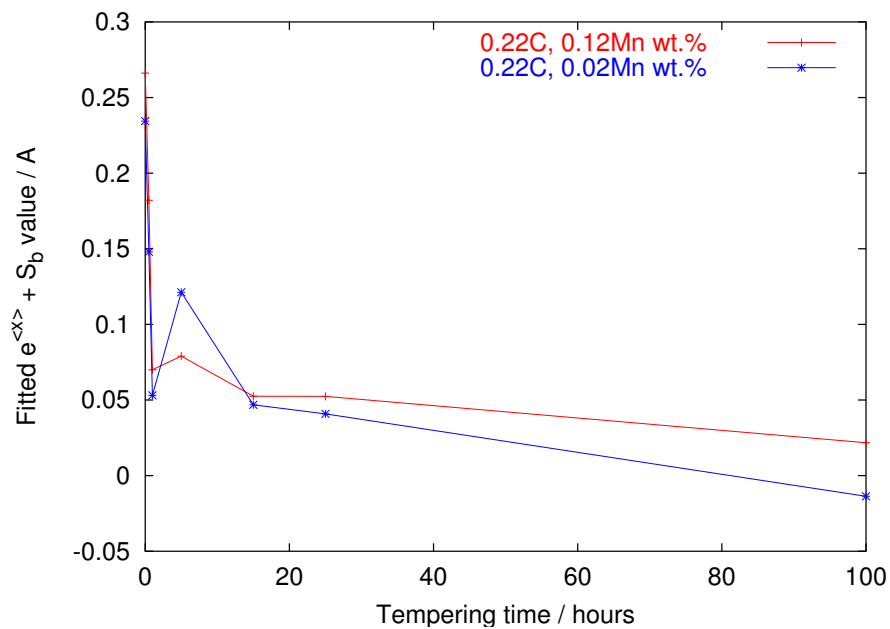
Figure 5.11: Relationship of Model 2 fitting parameters $e^{<x>} + S_b$ with tempering time for two steels of similar composition.
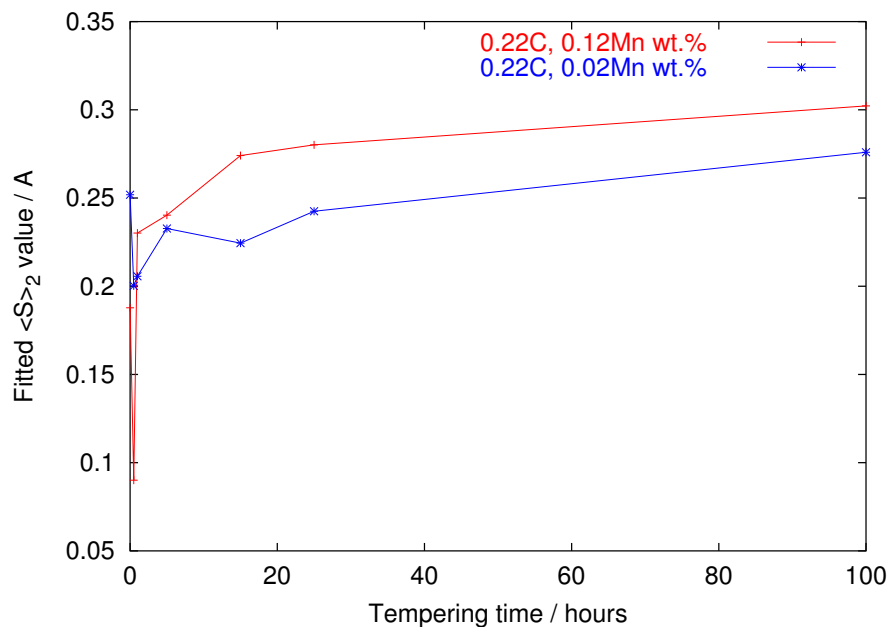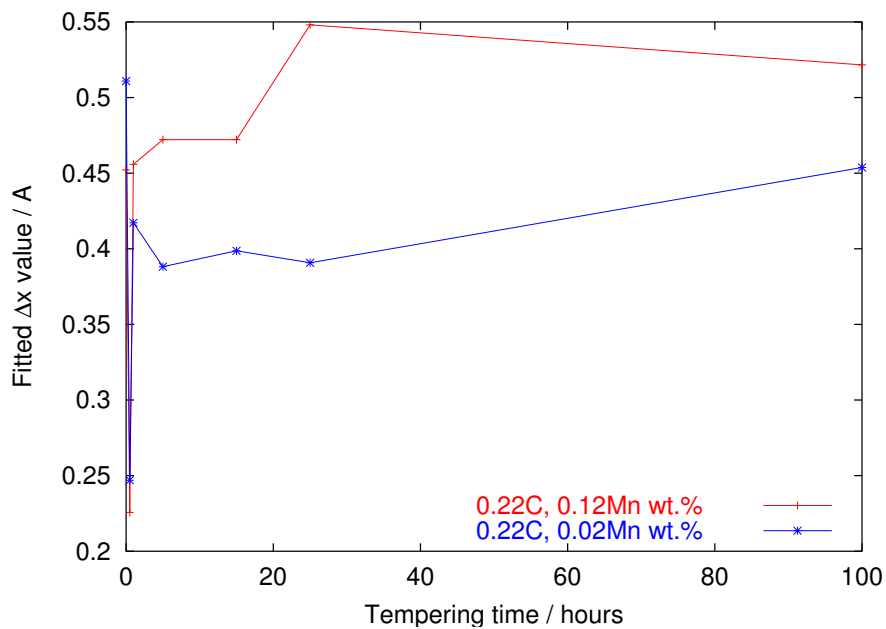

Figure 5.12: Relationship of Model 2 fitting parameter $< S >_2$ with tempering time for two steels of similar composition.
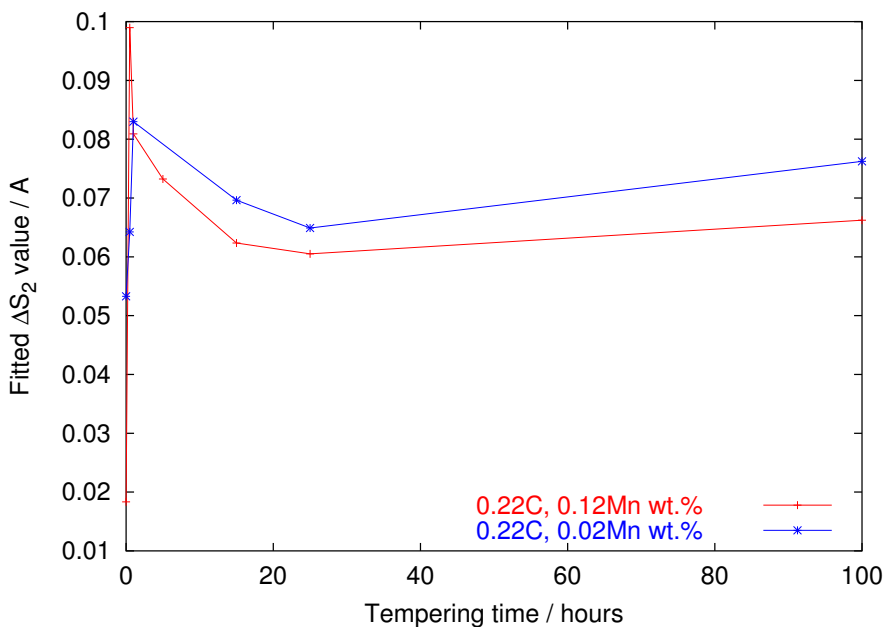
Figure 5.13: Relationship of Model 2 fitting parameter Δx with tempering time for two steels of similar composition.

Figure 5.14: Relationship of Model 2 fitting parameters ΔS_2 with tempering time for two steels of similar composition.
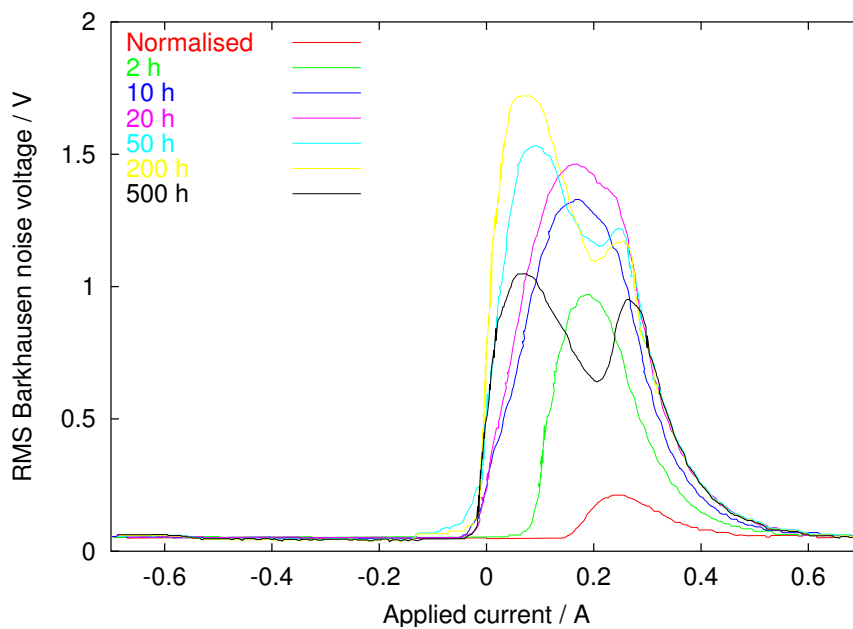
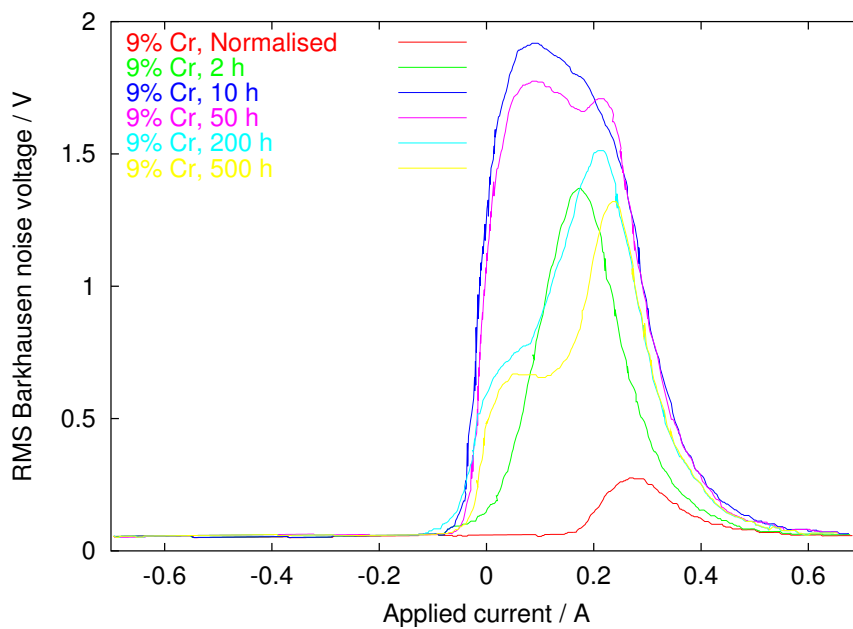Figure 5.15: Real BN data from tempered $2\frac{1}{4}$Cr1Mo power plant steel. Data from Moorthy *et al.*, 1998.

Figure 5.16: Real BN data from tempered 9Cr1Mo power plant steel. Data from Moorthy *et al.*, 1998.
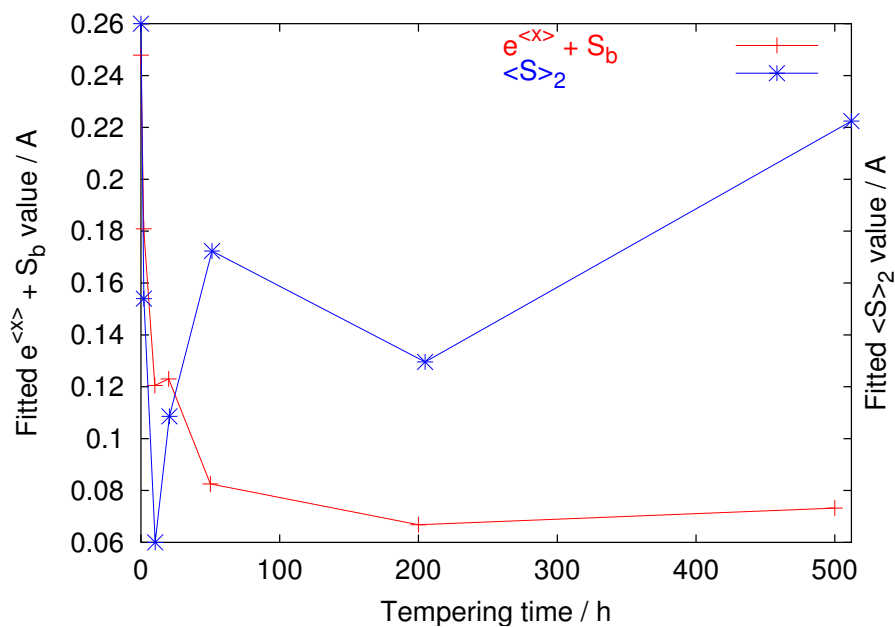
Figure 5.17: Model 2 fitting parameters $e^{<x>} + S_b$ and $< S >_2$ versus time for $2\frac{1}{4}$Cr1Mo steel.
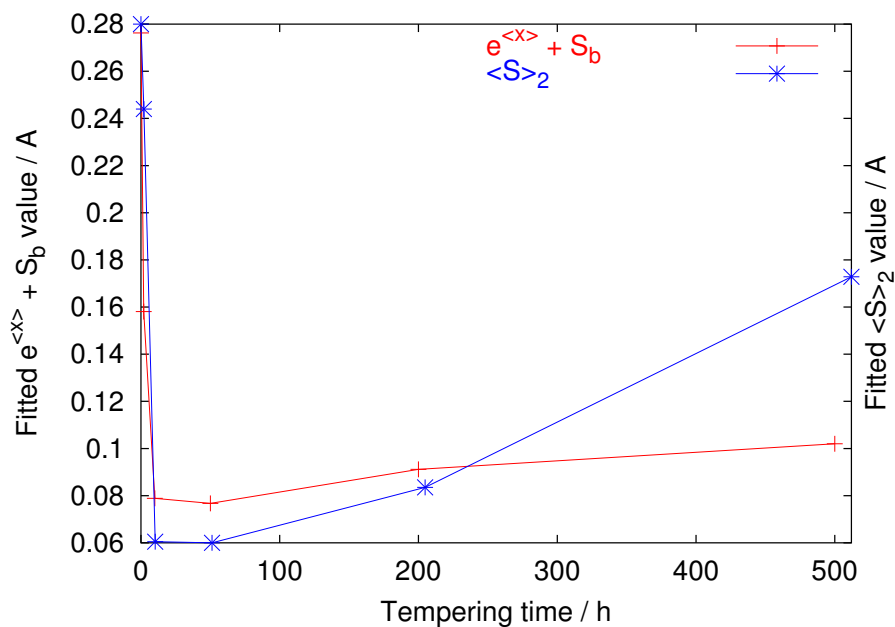

Figure 5.18: Model 2 fitting parameters $e^{<x>} + S_b$ and $< S >_2$ versus time for 9Cr1Mo steel.

5.10 Discussion

Model 2 fits experimental data well in most cases, and it is therefore likely that its physical basis is better than that of Model 1. In order to test the model further and to understand the relationships of its modelling parameters with microstructural data, it is necessary to obtain BN data sets from a wide range of samples with well characterised microstructures. The following four chapters describe the microstructural characterisation, BN experiments and model-fitting carried out for this purpose.

It appears that, despite extensive testing before use, the fitting program cannot always be relied upon to produce reliable parameters. It may be useful to modify the program to limit the range in which the solutions can lie, or to apply other constraints on the basis of experience. Δx and ΔS seem to be the parameters presenting the greatest problems for fitting, possibly because both A and ΔS affect the peak heights, so that it is difficult to determine correctly the effect of these two parameters on a peak.

5.11 Conclusion

Two models have been proposed to interpret BN data obtained from tempered steel. A model using a log-normal distribution of pinning site strengths for the lower-field peak, and a normal distribution for the higher-field peak, gave good agreement with real data. Clear relationships were found between the fitting parameters characterising the centres of the distributions, and measured grain and carbide dimensions. It therefore appears that this model both supports the interpretation of Moorthy *et al.* that two-peak BN signals are due to the separate effects of pinning by grain boundaries and carbides, and provides a basis for microstructural estimation from Barkhausen data. However, it will be necessary to test the model against more experimental data to confirm this relationship, and to improve the fitting method so that it always produces physically realistic model parameters.

Chapter 6

Sample Preparation and Characterisation

6.1 Sample preparation

$2\frac{1}{4}$Cr1Mo steel

A section of a $2\frac{1}{4}$Cr1Mo power plant steel from Drax Power Station was supplied by National Power plc. The composition is given in Table 6.1.

A piece of this steel of approximate dimensions $100 \times 100 \times 12$ mm was placed in a furnace at 500°C. The temperature was increased to 1000°C and held for 30 minutes to transform the steel to austenite. The sample was then quenched directly into water. During quenching, it was agitated to prevent the buildup of a layer of bubbles which would provide insulation and reduce the cooling rate.

Using a spark-cutter, square plates of the material of side 10 mm and approximate depth 1 mm were cut from the large piece, taking care to discard

C	Si	Mn	P	S	Cr	Mo	Ni	Al	As
0.12	0.29	0.51	0.021	0.021	2.22	0.97	0.21	0.008	0.030
Co	Cu	Nb	Pb	Sn	Ti	V	W	Sb	
0.027	0.23	<0.005	0.009	0.022	<0.005	0.017	0.019	0.015	

Table 6.1: Composition of $2\frac{1}{4}$Cr1Mo steel; all quantities in wt. %. Data supplied by Bodycote Materials Testing Ltd., Bridgwater, Somerset.

the decarburised layer on the outside. The thickness of this layer was esti-
mated at 0.05 mm using the constant-concentration solution to Fick's second
law, but 2 mm was cut from each edge to be sure of excluding decarburised
material.

In order to prevent decarburisation and oxidation during tempering, the
square plates were sealed into silica tubes which were evacuated and back-
filled with a small partial pressure of argon to provide an inert atmosphere.
Two plates were placed into each tube so that the samples for Barkhausen
analysis and for electron microscopy would receive exactly the same heat
treatment.

The samples were subjected to tempering heat treatments of between
1 hour and 512 hours at 500°C and at 600°C, and between 1 hour and
8 hours at 700°C. This last series was intended to replicate the microstruc-
tural changes during the pre-service tempering treatment of power-plant
steels (Morris, personal communication). As-quenched (AQ) samples were
retained for comparison with the tempered steels.

After tempering, the samples were allowed to air-cool while remaining
within the silica tubes. The tubes were then broken, and the samples were
hot-mounted in Bakelite, ground using 2500 grit silicon carbide paper and
polished to 1 μm using diamond paste. Finally, the surfaces were etched
using 2% nital to remove the strained layer and reveal the microstructure for
observation using an optical microscope and a Hitachi S-4200 Field Emission
Gun SEM.

Long-term specimens

Specimens of 11Cr1Mo wt. % steel which had been heated for several thou-
sands of hours at 550°C were supplied by Corus RD&T. These were from
creep tests, and comprised a screw-thread, which was used to hold the speci-
men in place, and a gauge length tapering to a fracture surface (Figure 6.1).
In order to study only the effects of prolonged exposure to high tempera-
ture, samples for BN testing and microscopy were cut from the threaded
area, which was not subjected to stress, using a Struers Accutom lubricated
rotary cutter.

C	Si	Mn	P	S	Cr
0.205	0.36	0.49	0.011	0.009	11.15
Mo	Ni	Nb	V	W	
0.85	0.34	0.01	0.28	0.02	

Table 6.2: Composition of creep-tested steel; all quantities in wt. %. Data supplied by Corus RD&T.

The steel composition is given in Table 6.2 and details of the heat treatment in Table 6.3. The surfaces were prepared in the same way as those of the power plant steels, except that Kalling's No. 2 reagent (2 g $CuCl_2$, 40 ml HCl, and 40-80 ml ethanol; Vander Voort, 1984) was used as an etchant since 2% nital would not etch this steel.
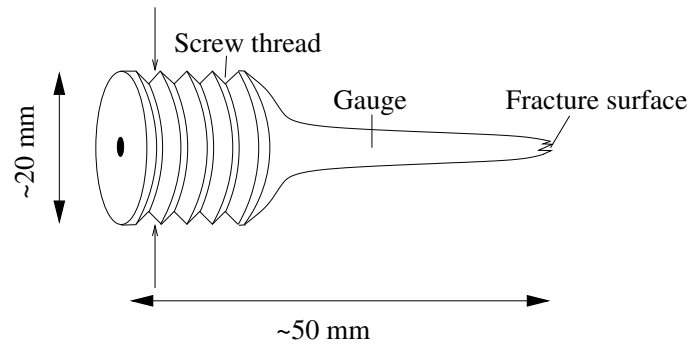

Figure 6.1: Failed creep test specimen. The arrows show the position at which the Barkhausen test specimen was cut.

6.2 Optical microscopy

6.2.1 As-quenched sample

In Figure 6.2, the prior austenite grains and their substructure of packets can clearly be seen. Packets occupy almost the entire grain in some cases, but are much smaller in others. A larger-scale micrograph of the same area allows the packets to be resolved more easily (Figure 6.3).

Temperature / °C	Applied stress / MPa	Time / h
550	278	2347
550	247	5849
550	216	16530
550	185	36191

Table 6.3: Testing conditions of creep specimens provided by Corus (Clarke, personal communication).

6.2.2   Tempering at 500°C

Figure 6.4–Figure 6.7 show specimens tempered at 500°C for a variety of times. Microstructural changes at this temperature are very gradual. The features present in the as-quenched microstructure can still be seen after tempering for 256 h, but their edges have become less distinct.

6.2.3   Tempering at 600°C

Samples tempered at 600°C are shown in Figure 6.8–Figure 6.11. The former martensitic structure is still in evidence, especially at shorter tempering times, but gradual coalescence of the narrow features into larger units can be seen as tempering progresses. The coalescence is more obviously visible in the SEM images presented below.

6.2.4   Tempering at 700°C

Microstructural changes occur much more rapidly on tempering at 700°C, as is evident from Figure 6.12–Figure 6.15, which show the microstructure corresponding to times between 1 and 8 hours. Even after 1 hour, much of the fine structure in the AQ sample has coalesced into larger units, which coarsen with increasing tempering time. Tempering for 8 hours causes most of the original martensitic structure to be lost, and lines of carbides delineate former block boundaries.
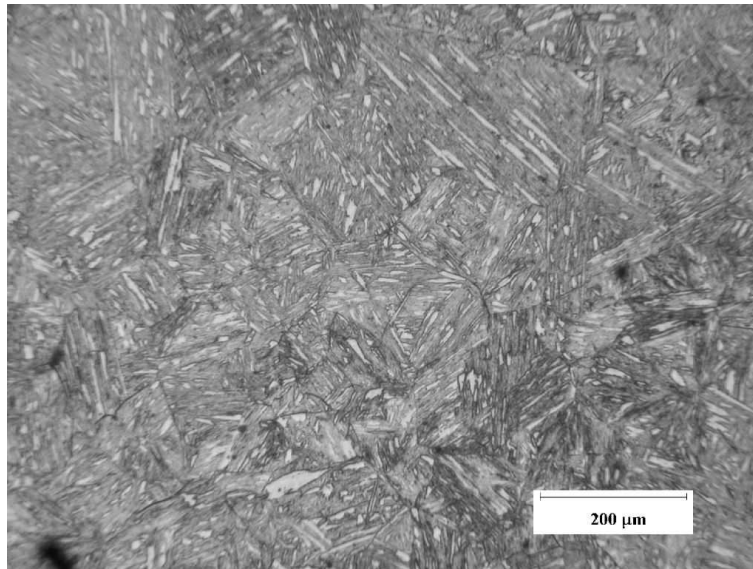
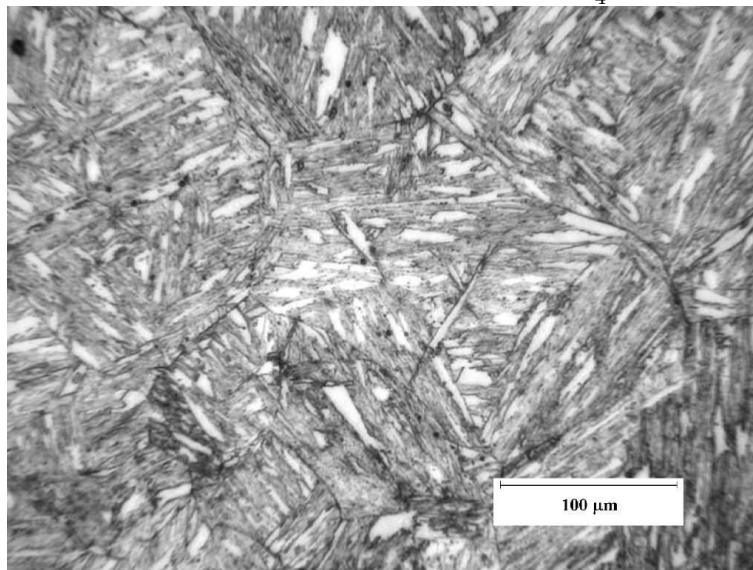Figure 6.2: As-quenched microstructure of $2\frac{1}{4}$Cr1Mo steel.

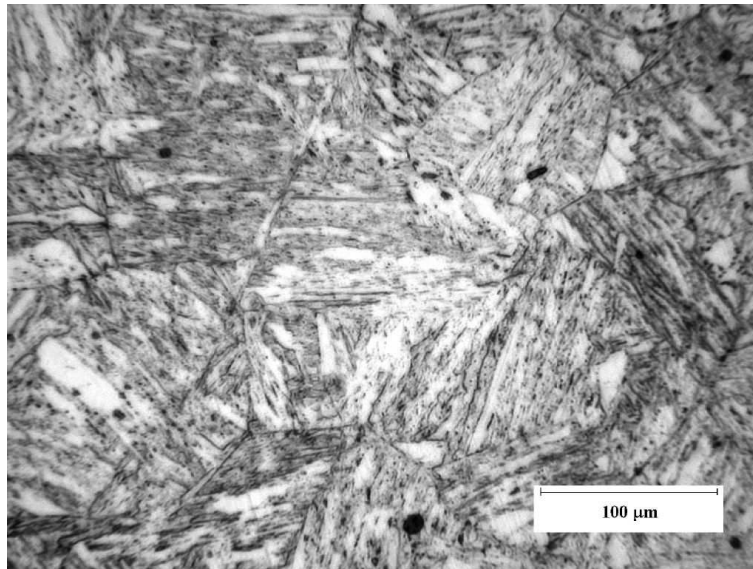Figure 6.3: As-quenched microstructure of $2\frac{1}{4}$Cr1Mo steel.

Figure 6.4: $2\frac{1}{4}$Cr1Mo steel tempered for 1 hour at 500°C.

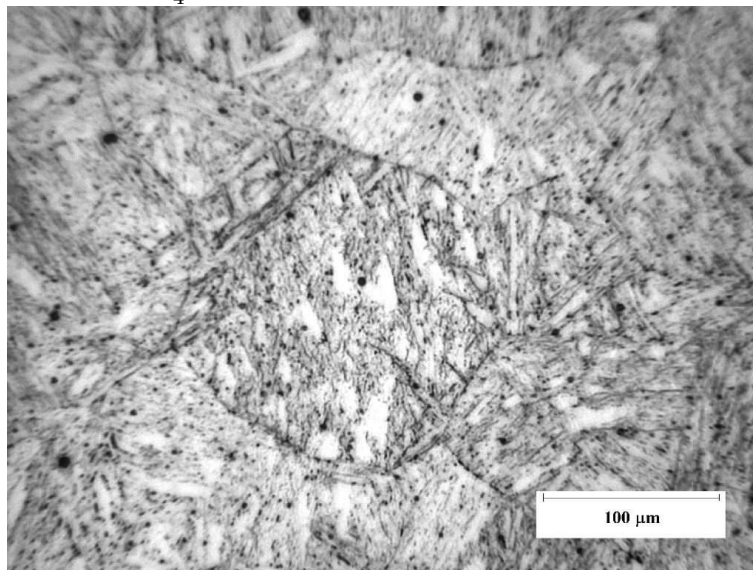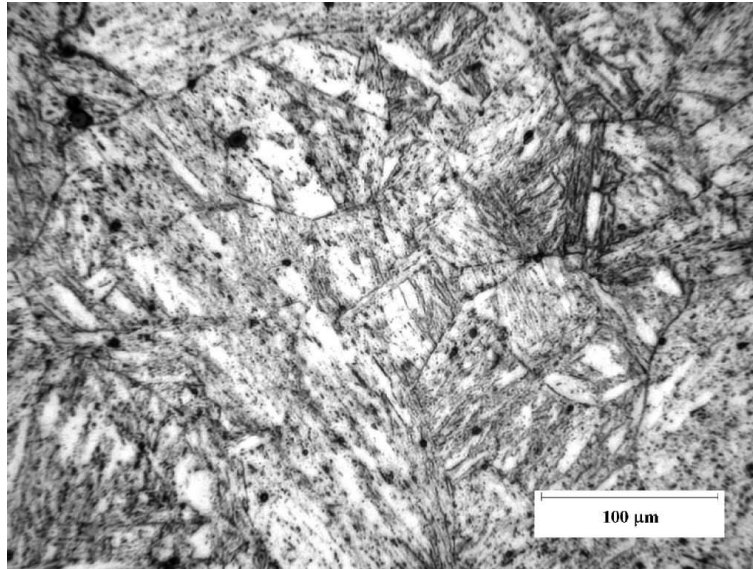Figure 6.5: $2\frac{1}{4}$Cr1Mo steel tempered for 4 hours at 500°C.

Figure 6.6: $2\frac{1}{4}$Cr1Mo steel tempered for 32 hours at 500°C.

Figure 6.7: $2\frac{1}{4}$Cr1Mo steel tempered for 256 hours at 500°C.

Figure 6.8: $2\frac{1}{4}$Cr1Mo steel tempered for 4 hours at 600°C.

Figure 6.9: $2\frac{1}{4}$Cr1Mo steel tempered for 16 hours at 600°C.
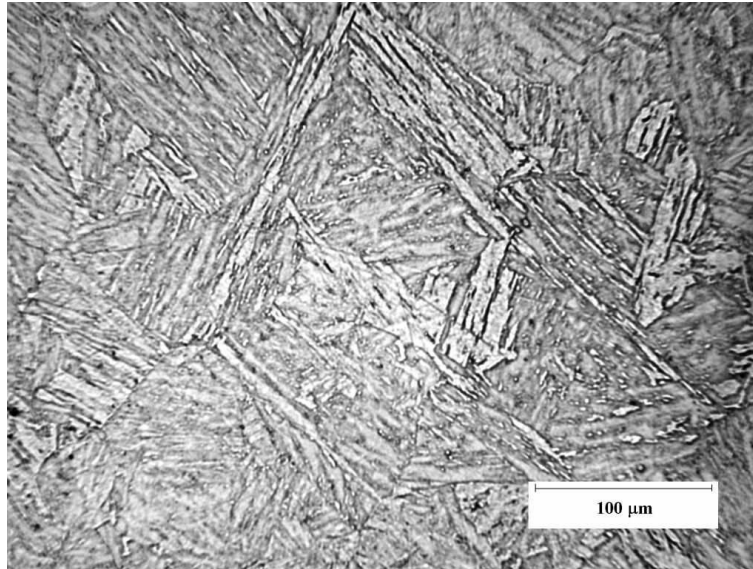
Figure 6.10: $2\frac{1}{4}$Cr1Mo steel tempered for 256 hours at 600°C.
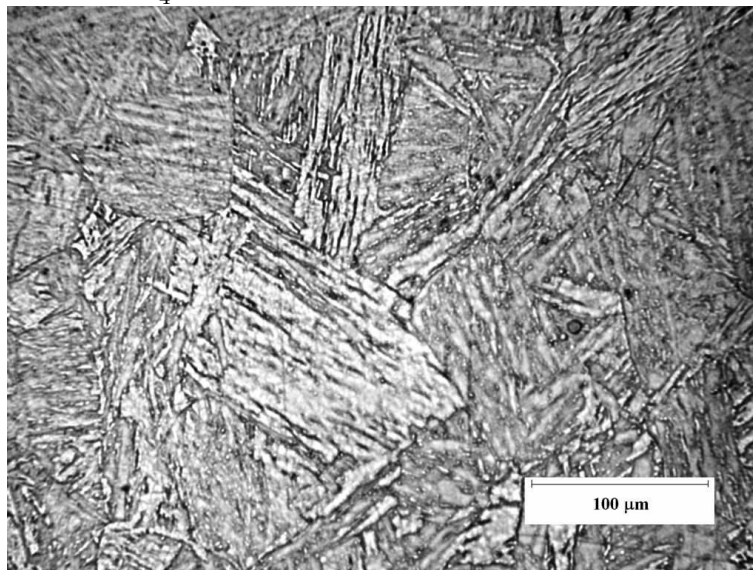
Figure 6.11: $2\frac{1}{4}$Cr1Mo steel tempered for 512 hours at 600°C.
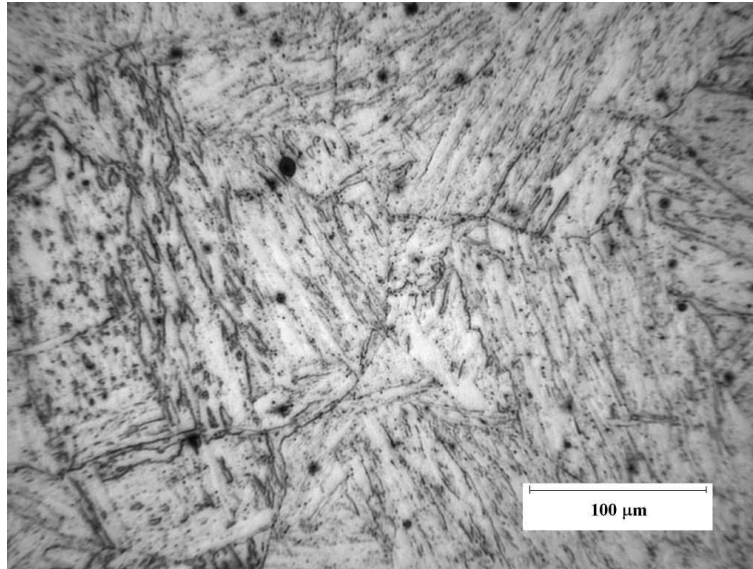
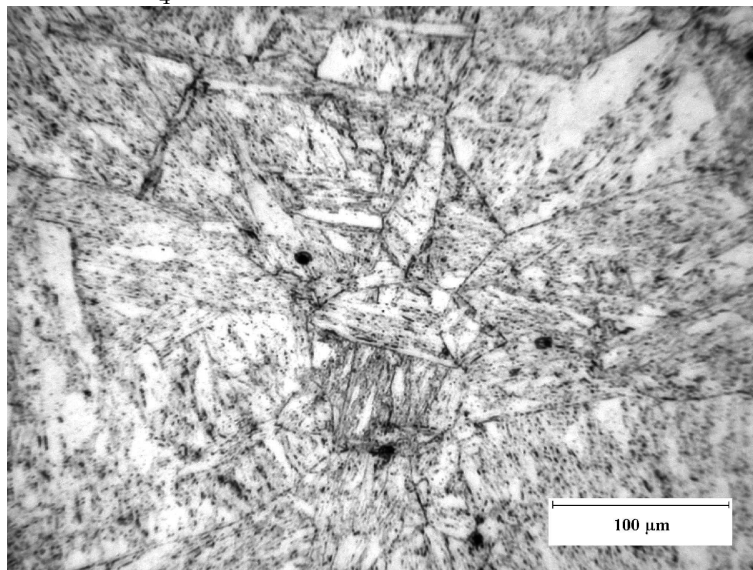Figure 6.12: $2\frac{1}{4}$Cr1Mo steel tempered for 1 hour at 700°C.
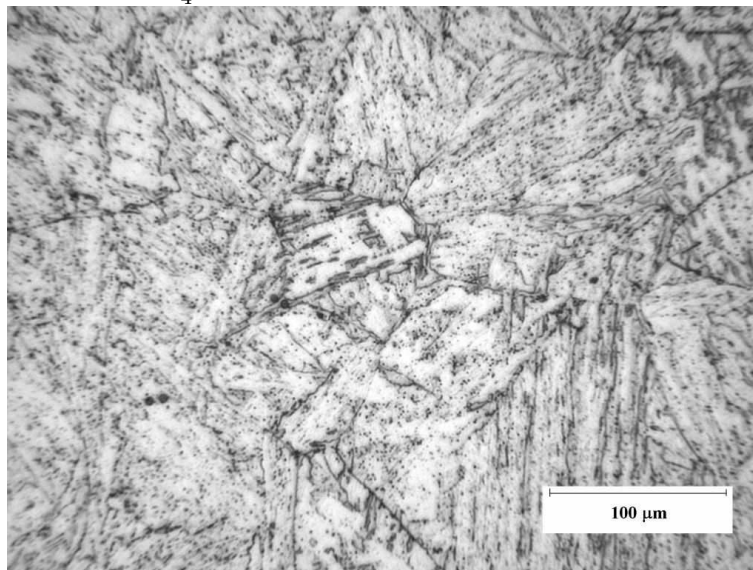
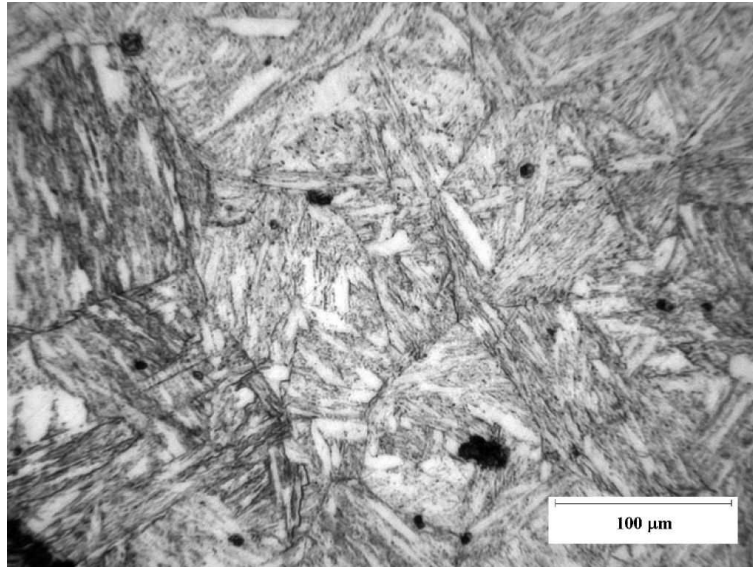Figure 6.13: $2\frac{1}{4}$Cr1Mo steel tempered for 2 hours at 700°C.
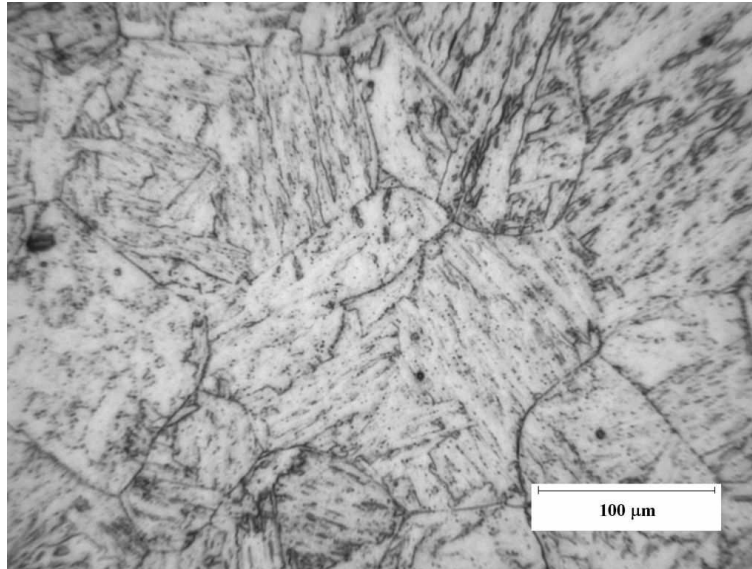
Figure 6.14: $2\frac{1}{4}$Cr1Mo steel tempered for 4 hours at 700°C.
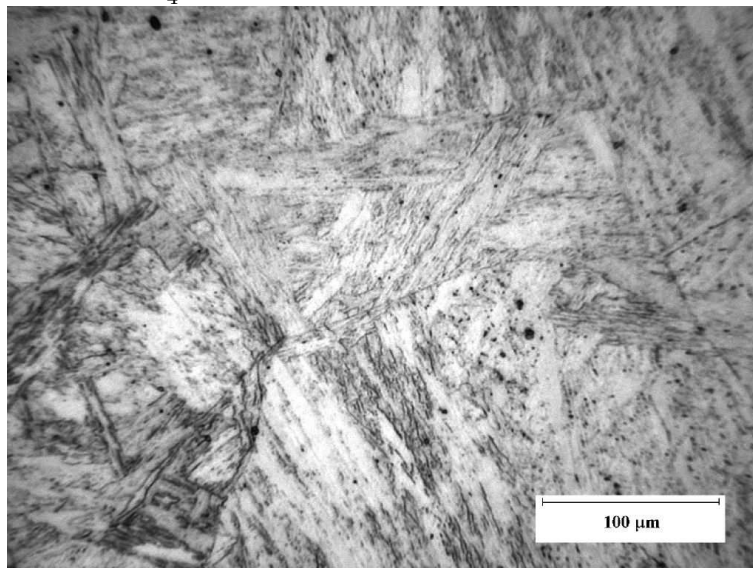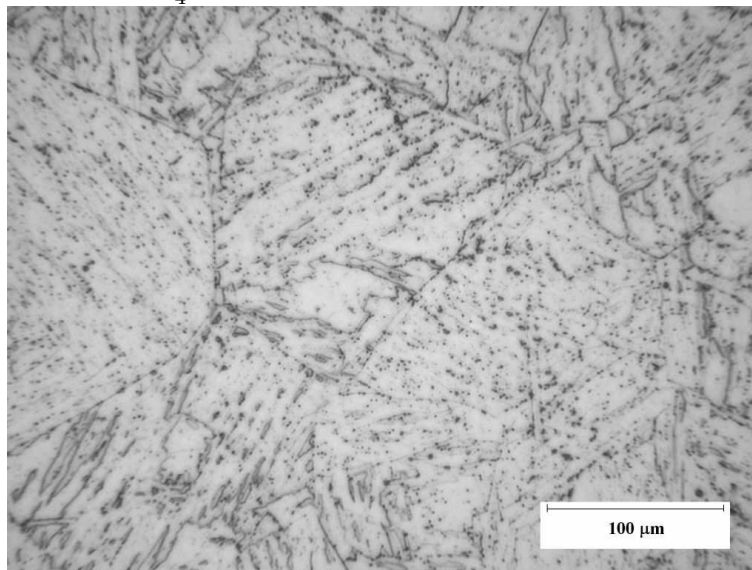

Figure 6.15: $2\frac{1}{4}$Cr1Mo steel tempered for 8 hours at 700°C.
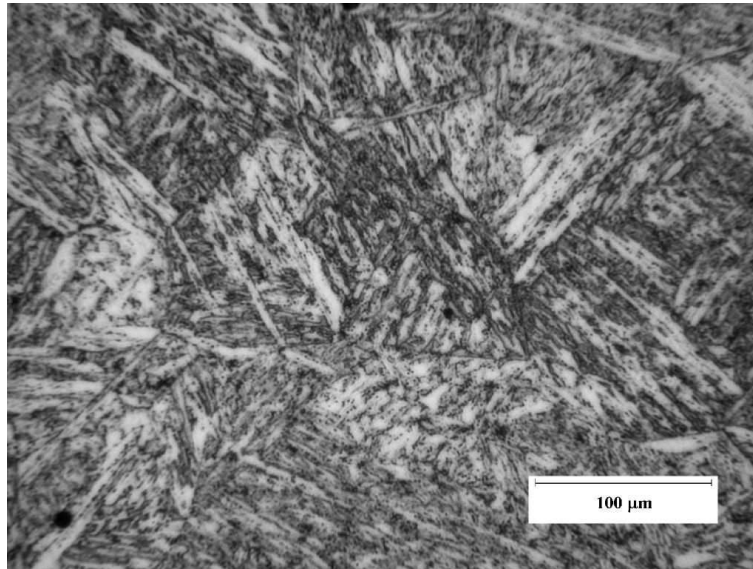
Figure 6.16: 11 wt. % Cr steel heated for 2347 hours at 550°C during creep test.
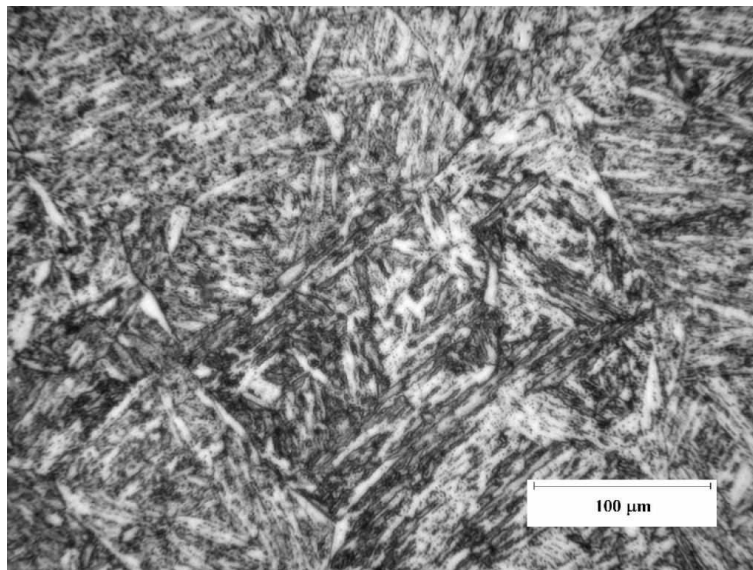
Figure 6.17: 11 wt. % Cr steel heated for 5849 hours at 550°C during creep test.
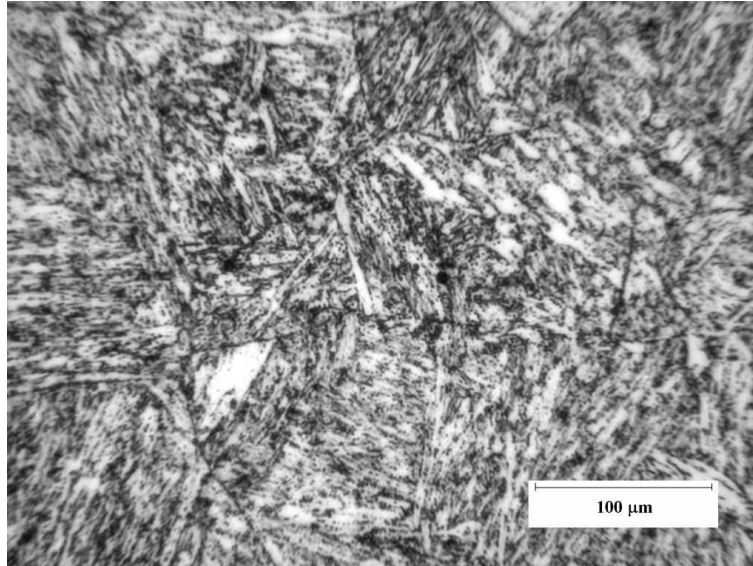
Figure 6.18: 11 wt. % Cr steel heated for 16530 hours at 550°C during creep test.
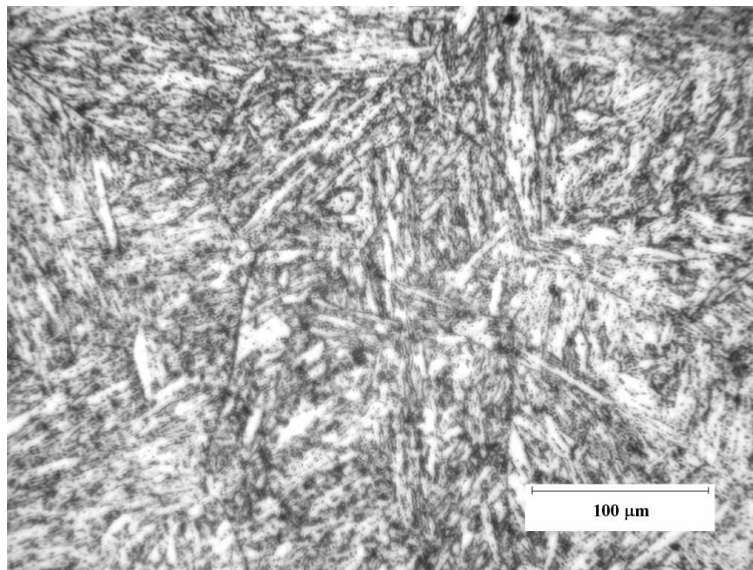
Figure 6.19: 11 wt. % Cr steel heated for 36191 hours at 550°C during creep test.
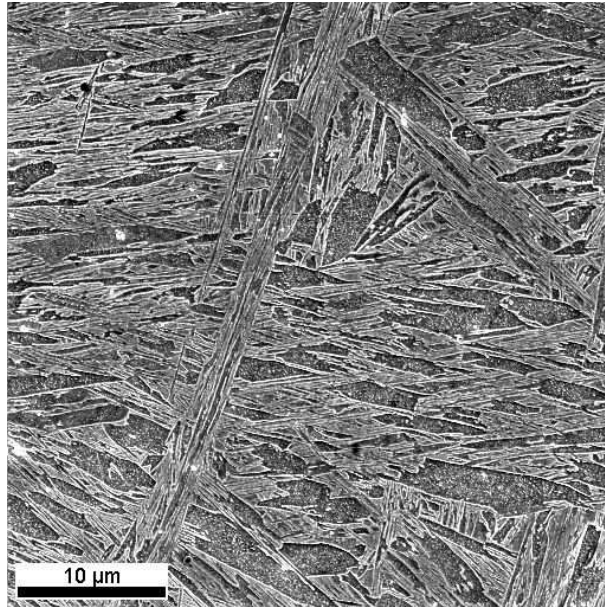
Figure 6.20: SEM micrograph of as-quenched $2\frac{1}{4}$Cr1Mo steel.
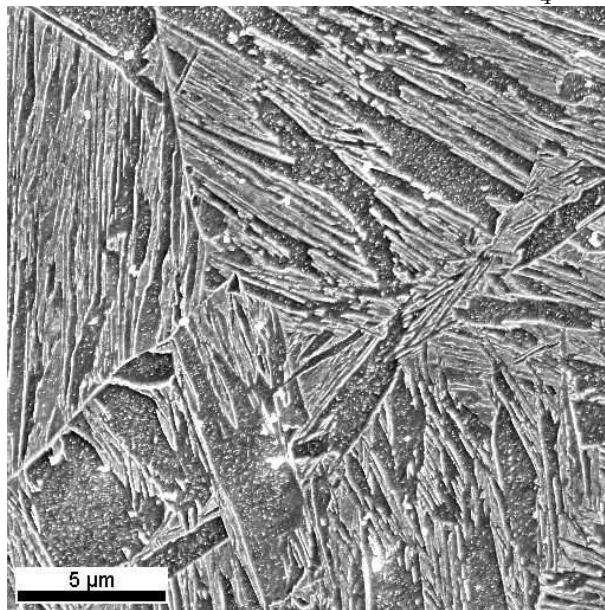
Figure 6.21: SEM micrograph of as-quenched $2\frac{1}{4}$Cr1Mo steel.
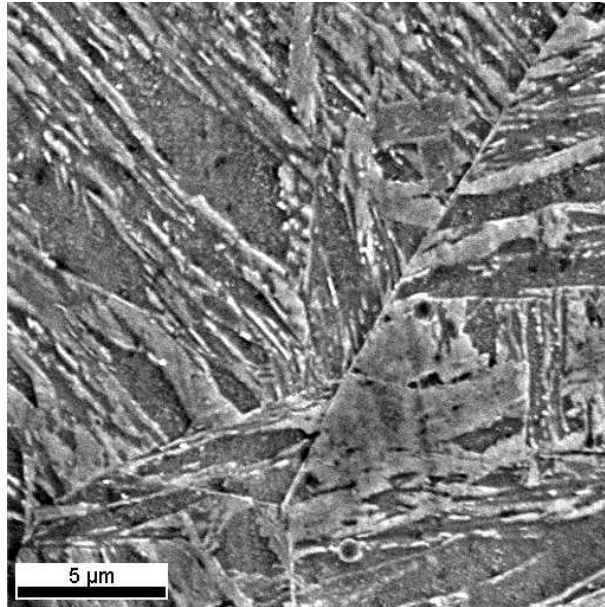
Figure 6.22: SEM micrograph of $2\frac{1}{4}$Cr1Mo steel tempered at 500°C for 1 hour.
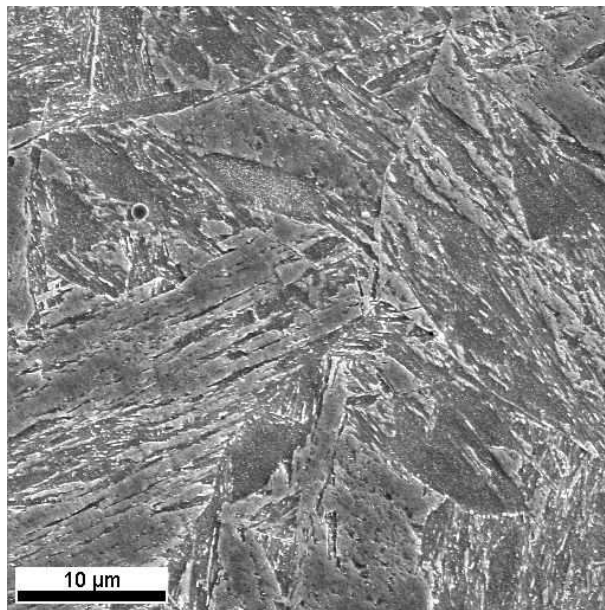
Figure 6.23: SEM micrograph of $2\frac{1}{4}$Cr1Mo steel tempered at 500°C for 256 hours.
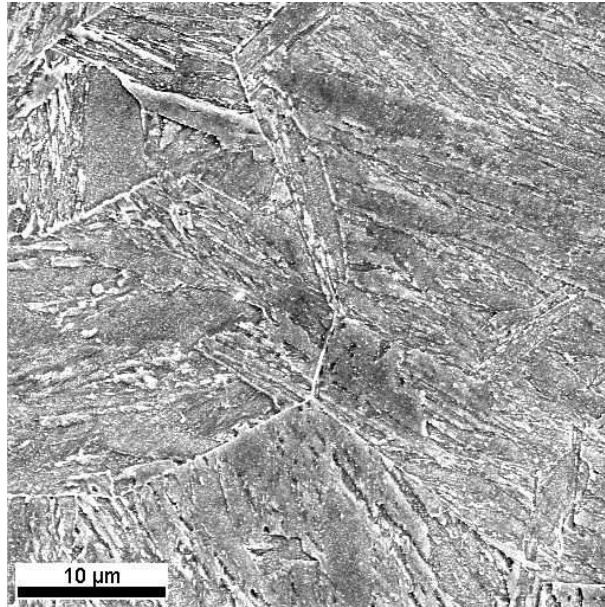
Figure 6.24: SEM micrograph of $2\frac{1}{4}$Cr1Mo steel tempered at 600°C for 16 hours.
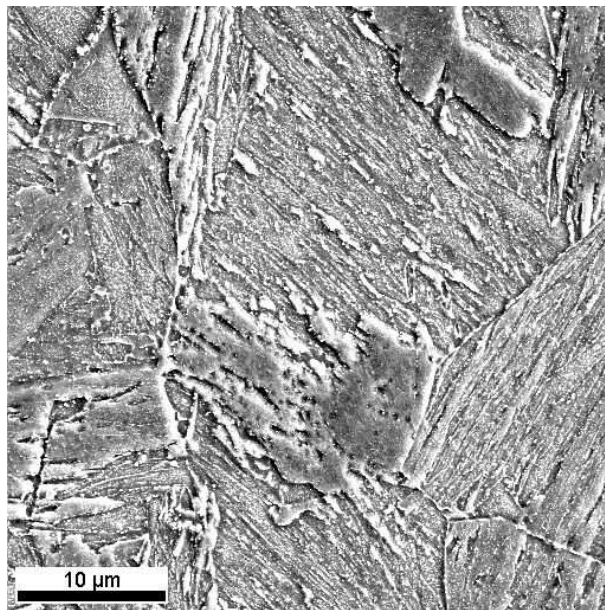
Figure 6.25: SEM micrograph of $2\frac{1}{4}$Cr1Mo steel tempered at 600°C for 256 hours.
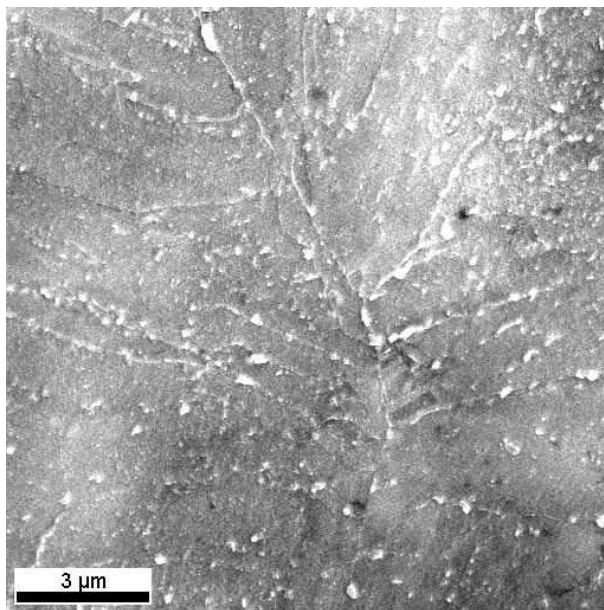
Figure 6.26: SEM micrograph of $2\frac{1}{4}$Cr1Mo steel tempered at 700°C for 1 hour.

6.2.5   Long-term specimens

Figure 6.16–Figure 6.19 are optical micrographs of the 11Cr1Mo wt. % steel specimens. In all of these, the structure is very similar to that of the $2\frac{1}{4}$Cr1Mo steel in its early stages of tempering at 500°C, but finer. There is no obvious microstructural change visible on this scale, even after prolonged tempering (36000 hours). This is as expected since this steel has been deliberately designed to resist microstructural changes in service over much longer periods than this (30 years or more, *i.e.* around 300000 hours).

6.3   Scanning electron microscopy

Figure 6.20 illustrates some of the different lath lengths and orientations within a region of the AQ structure, and Figure 6.21, at a higher magnification, demonstrates how the laths stop at a prior austenite grain boundary.

After even a short tempering treatment of 1 hour at 500°C, some of the laths have coalesced to form wider regions (Figure 6.22). Tempering for a

longer time, 256 hours, at 500°C produces more coalescence (Figure 6.23). The process is accelerated by tempering at 600°C (Figure 6.24, Figure 6.25). After 1 hour at 700°C, only traces of the original structure can be seen (Figure 6.26).

6.4 Feature size measurements

As discussed in previous chapters, the sizes and spacings of microstructural features is believed to affect magnetic domain wall behaviour. In equiaxed, single-phase materials, the grain size is the most important microstructural dimension, but in martensitic steels, there are various levels of structure – laths, blocks, packets and prior austenite grains – any or all of which may affect the magnetic behaviour. Tempering introduces carbides, whose sizes and spacings must be considered, and at high temperatures causes recovery and recrystallisation.

The Heyn linear intercept method described by Vander Voort (1984) was used to determine prior austenite grain sizes. An acetate overlay was placed on an optical micrograph, and the grain boundaries identified and marked. A transparent grid was placed on the overlay, and the intercepts of the horizontal grid lines with grain boundaries were counted. A simple intercept scored 1, a triple junction intercepted by the grid line, $1\frac{1}{2}$, and a tangent hit to a grain boundary, $\frac{1}{2}$. The number of intercepts per unit length N_L was calculated from the total number of grains intercepted N, the total line length L_T and the magnification M as follows:

$$N_L = \frac{N}{L_T/M} \qquad (6.1)$$

The mean lineal intercept (mean intercept length) $\bar{L}_3$ was then obtained from:

$$\bar{L}_3 = \frac{1}{N_L} \qquad (6.2)$$

The intercept measurements were repeated using the vertical grid lines. Prior austenite grain size measurements were obtained from three samples -

AQ, 600°C-8 h and 700°C-8 h - to check that the grain size was the same in each, as expected, and to increase the data set size. Packet size measurements were obtained on the AQ sample using the same Heyn method.

Block size measurements were made using the Heyn method on SEM micrographs of the AQ material. Lath widths were determined by measuring the width of a group of laths parallel to the lath length, then dividing this by the number of laths. The average sizes of the microstructural features are given in Table 6.4.

Feature	Average size / μm
Prior austenite grain	433
Packet (AQ)	97.5
Block (AQ)	1.68
Martensite lath (AQ)	0.25

Table 6.4: Sizes of microstructural features as estimated from micrographs.

6.4.1   Coarsening in 700°C tempered steel

A quantitative measure of microstructural coarsening in the 700°C samples was made using the Heyn method. Prior austenite grain boundaries and former lath, block or packet boundaries were delineated on an acetate overlay and the number of intercepts counted as above. In some cases, it was difficult to determine whether a linear feature was a block boundary or simply a row of carbides, so the method is rather imprecise. Nonetheless, a clear trend towards larger spacings with increasing tempering time is visible in Table 6.5 and Figure 6.27.

Tempering time / hours	1	2	4	8
Spacing (dir. 1) / μm	3.48	3.29	3.70	4.57
Spacing (dir. 2) / μm	4.10	4.36	4.27	5.47
Mean spacing / μm	3.79	3.83	3.99	5.02

Table 6.5: Feature spacings in samples tempered at 700°C: measurements in two perpendicular directions (1 and 2) and mean.
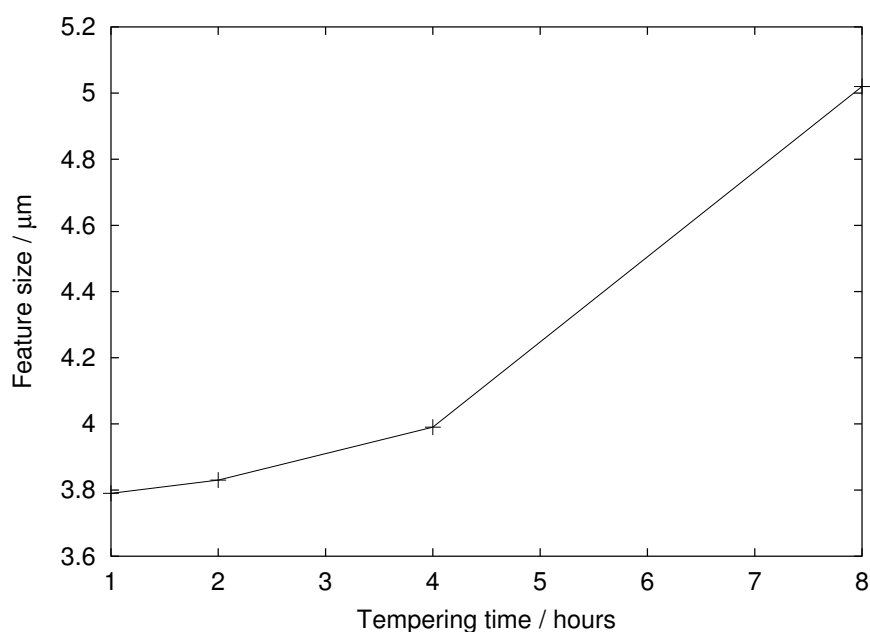
Figure 6.27: Changes in average feature spacing with tempering time at 700°C.

6.4.2 Carbide phases

The carbide phases expected in the tempered samples can be obtained from the carbide stability diagram for $2\frac{1}{4}$Cr1Mo steel (Nutting, 1998; Figure 2.6). The phases present after tempering at 600 and 700°C are shown in Figure 6.28 and 6.29 respectively. The Nutting diagram does not extend down to 500°C, but by extrapolation, M_3C is likely to be the most stable phase until at least 100 hours.

Fujita (2000) characterised the carbides occurring in $2\frac{1}{4}$Cr1Mo steels after tempering at 600°C using TEM. His results are summarised in Table 6.6. These suggest a later onset of M_7C_3 than Figure 6.28 and Figure 6.29.

6.5 Hardness

The hardness of each sample was measured using a Vickers indenter with a mass of 30 kg and an objective of 2/3 ", taking the mean of three indents.
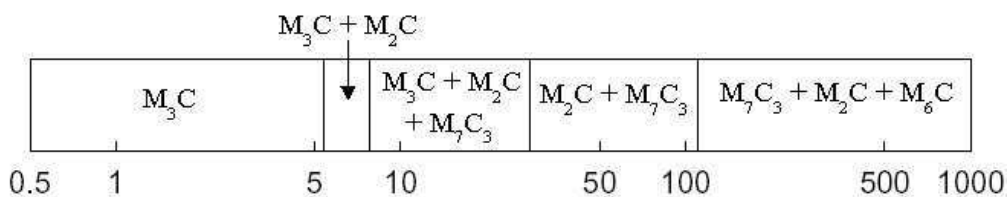
Figure 6.28: Carbide phase stability at 600°C in $2\frac{1}{4}$Cr1Mo steel, after Nutting (1998).
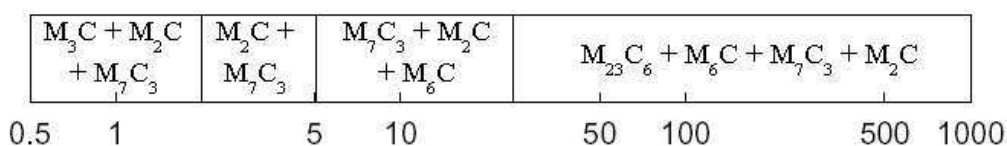
Figure 6.29: Carbide phase stability at 700°C in $2\frac{1}{4}$Cr1Mo steel, after Nutting (1998).

Time / hours	Observations
1	Most precipitates were needle- or plate-like M_3C
10	Most precipitates were needle- or plate-like M_3C
200	M_3C + needle array of M_2C
1000	M_3C + M_2C + blocky M_7C_3

Table 6.6: Carbide phases present in $2\frac{1}{4}$Cr1Mo steel after tempering at 600°C (Data from Fujita, 2000).

Results for the $2\frac{1}{4}$Cr1Mo steel are shown in Figure 6.30. At 500°C, after an initial decrease in the first hour, the change in hardness is very small on further tempering. The hardness is much lower at 600°C, and decreases with increasing tempering time. At 700°C, the rate of hardness decrease is more rapid.

Figure 6.31 shows the hardness of the 11Cr1Mo samples held at 550°C. A clear decrease in hardness with time is visible, but the rate of change is much lower than in the $2\frac{1}{4}$Cr1Mo steel.
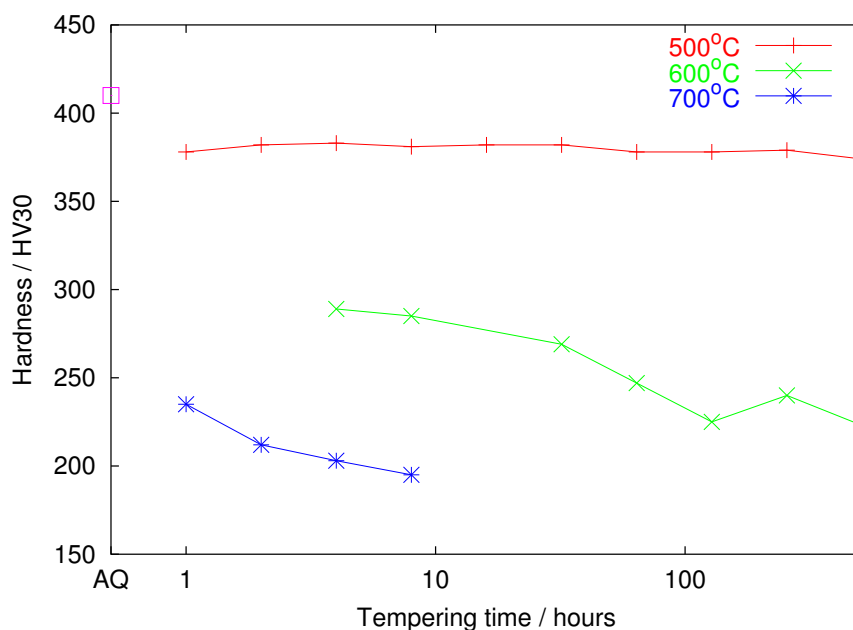
Figure 6.30: Hardness of tempered $2\frac{1}{4}$Cr1Mo steel samples.

6.6   Magnetic hysteresis measurements

The coercive fields of $2\frac{1}{4}$Cr1Mo steel samples tempered at $600°$C for various times were obtained by measuring hysteresis loops using a vibrating sample magnetometer (VSM)[1]. Figure 6.32 shows a rapid decrease in H_C after a short tempering time, followed by a more gradual decrease at longer times. A small peak, probably due to carbide precipitation, is visible at 2 hours.

---

[1]The design and operation of the VSM are described by Foner, 1996.
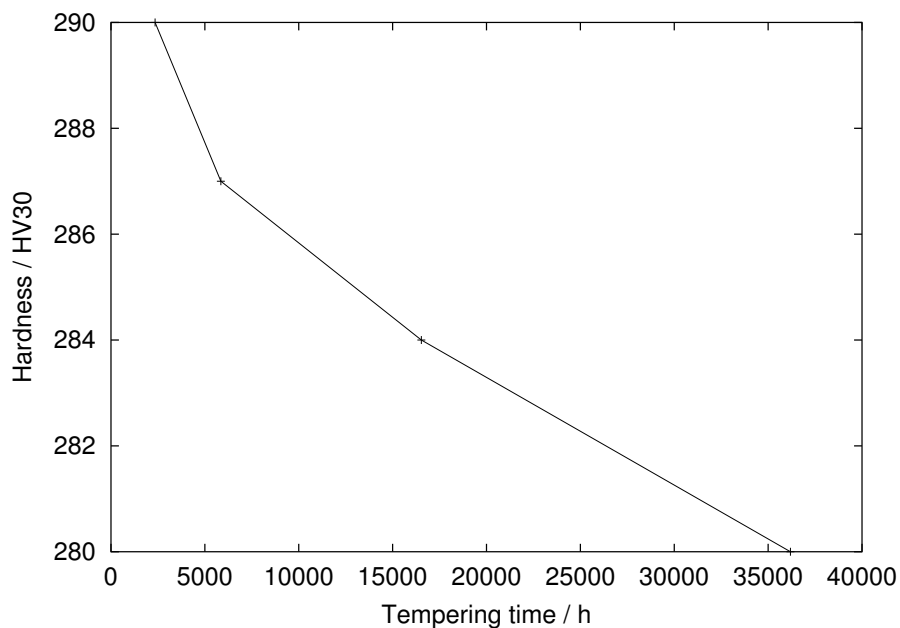
Figure 6.31: Hardness of creep-tested 11Cr1Mo wt. % steel samples.
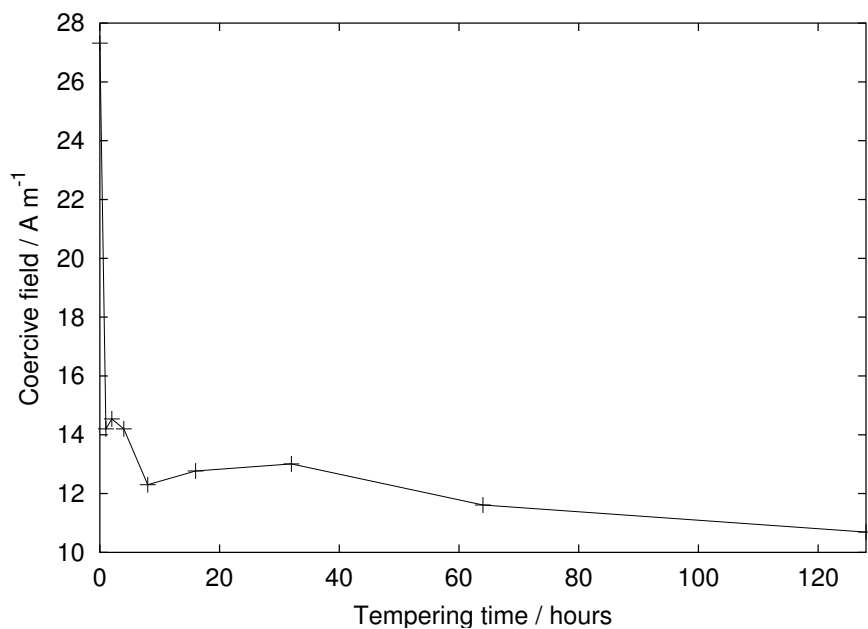
Figure 6.32: Coercive field of $2\frac{1}{4}$Cr1Mo steel tempered at 600°C. Data from M.Sci. dissertation of present author, 1999.

6.7   Conclusion

Changes in microstructure and hardness were very small for $2\frac{1}{4}$Cr1Mo samples tempered at 500°C, although martensite lath coalescence could be seen using SEM. At 600°C, the change in hardness was more pronounced, lath coalescence was observed, but the changes visible in the optical microscope were subtle and gradual. The coercive field decreased rapidly at short tempering times, and more gradually at longer times. Tempering at 700°C caused a rapid reduction in hardness and microstructural coarsening. On tempering at 600°C, needlelike M_2C is expected to form after a few hours of tempering, and spheroidal carbides to appear later. The samples tempered at 700°C should have both M_2C and M_7C_3 in the microstructure, as well as M_3C, at the tempering times used in this study.

In the 11Cr1Mo wt. % samples held at 550°C, there were no visible microstructural changes and a very gradual decrease in hardness with time.

Chapter 7

Orientation Imaging Microscopy and Grain Boundary Analysis in Tempered Power Plant Steel

Over the past decade, the rapid, automated acquisition of large numbers of grain orientation data in the SEM has become possible. The sampling volume for each measurement is sufficiently small that many measurements can be made within a single grain, enabling point-by-point 'maps' of orientation data to be obtained and related directly to microstructure. By comparing data from adjacent points, it is also possible to determine the positions and characteristics of grain boundaries.

Using this technique, grain orientations and grain boundaries in $2\frac{1}{4}$Cr1Mo steels in the as-quenched and tempered states were investigated, giving a more complete microstructural characterisation than would be possible by conventional optical microscopy and SEM. The purpose of the study was to obtain insight into the likely microstructural origins of the changes in the Barkhausen noise signal with tempering.

7.1   Grain orientation

The specification of grain orientations requires the definition of a crystal coordinate system $\mathbf{c}_c$, which is usually chosen with reference to the crystal symmetry, and a sample system $\mathbf{c}_s$. This may be based on rolling, transverse and normal directions if these exist, but is otherwise defined arbitrarily. The crystal orientation is defined by the rotation matrix $\mathbf{G}$ which brings the crystal system into coincidence with the sample system.

$$\mathbf{c}_c = \mathbf{G} \cdot \mathbf{c}_s \tag{7.1}$$

The elements of $\mathbf{G}$ are given by:

$$\mathbf{G} = \begin{pmatrix} \cos\alpha_1 & \cos\beta_1 & cos\gamma_1 \\ \cos\alpha_2 & \cos\beta_2 & cos\gamma_2 \\ \cos\alpha_3 & \cos\beta_3 & cos\gamma_3 \end{pmatrix} \tag{7.2}$$

where α_1, β_1 and γ_1 are the angles between the crystal axis [100] and the specimen axes X, Y and Z respectively and the second and third rows of cosines correspond to the [010] and [001] axes referred to the same sample axes.

Only three independent variables are required to specify a crystal orientation, so the matrix format contains a certain amount of redundant information. A variety of methods have been developed to represent orientation information more succinctly. These include pole figures, inverse pole figures, Euler angles and angle-axis pairs.

7.1.1   Pole figures and inverse pole figures

If a crystal is envisaged at the centre of a sphere, a crystal axis can be described by the point, or pole, at which it intersects the sphere surface. In two dimensions, the stereographic projection of the sphere and the poles, projected with reference to specified sample axes, form a pole figure. An indication of the sample texture can be obtained by plotting the poles of selected crystal axes from a large number of crystals.

If, instead, directions in the sample coordinate system are projected onto the crystal coordinates, the result is an inverse pole figure. Because of crystal symmetry, a single stereographic triangle contains all necessary information. In materials with cubic symmetry, the triangle containing $< 100 >$, $< 110 >$ and $< 111 >$ is used.

7.1.2 Euler angles

The three Euler angles are the angles of rotations which are applied sequentially to bring the sample coordinate system into coincidence with the crystal system. Several alternative conventions for these exist but the Bunge system (Bunge, 1965, 1985) is the most commonly used, and is the system used by the automated orientation analysis software described below.

7.1.3 Angle-axis pairs

Orientations can be described as a single rotation performed about a specified axis to map the crystal coordinates onto the sample coordinates. This notation can be used to describe differences in orientation between adjacent grains (misorientations) as well as the orientations of individual crystals.

The matrix of misorientation $\mathbf{M}$ between grains of orientations $\mathbf{G}_1$ and $\mathbf{G}_2$ is calculated from:

$$\mathbf{M}_{12} = \mathbf{G}_1^{-1}\mathbf{G}_2 \qquad (7.3)$$

where one of the grains is arbitrarily designated as the reference grain, with orientation $\mathbf{G}_1$. The misorientation angle-axis pair, $\theta < UVW >$, where $U^2 + V^2 + W^2 = 1$, and θ is measured in a right-handed sense, is obtained from $\mathbf{M}$ using the equations:

$$\cos\theta = (M_{11} + M_{22} + M_{33} - 1)/2 \qquad (7.4)$$

$$\begin{aligned} U \ &= M_{23} - M_{32} \\ V \ &= M_{31} - M_{13} \\ W \ &= M_{12} - M_{21} \end{aligned} \qquad (7.5)$$

(Santoro and Mighell, 1973).

The angle-axis pair description is commonly used to describe grain misorientations because it can be related to the geometry of the grain boundary separating adjacent grains.

7.2   Grain boundary geometry

A grain boundary is the plane where two crystals of different orientations meet. Figure 7.1 shows an imaginary extension of the lattices of two crystals so that they interpenetrate with a common origin. The misorientation angle-axis pair $\theta < UVW >$ describes the rotation which must be performed to bring Lattice 1 into coincidence with Lattice 2. A possible grain boundary plane is marked on the left-hand diagram, but the position of this is not defined by $\theta < UVW >$. A parameter characterising the grain boundary plane normal is required for a complete macroscopic characterisation of the boundary.

The left-hand diagram is a special case of grain boundary in which $< UVW >$ lies in the grain boundary plane. This is known as a tilt boundary. A general boundary consists of a tilt component and also a twist component (a component of $< UVW >$ perpendicular to the boundary plane); an example of such a boundary is shown in the right-hand diagram.

The imaginary interpenetrating region in Figure 7.1 contains lattice points from both crystal lattices. Certain rotations $\theta < UVW >$ will cause some of the lattice points from Lattice 1 to come into coincidence with Lattice 2 points, giving a superlattice of coincident points. This is known as a coincidence site lattice (CSL) and has already been mentioned briefly in Chapter 3. CSLs are characterised by a parameter Σ, which is the reciprocal of the ratio [number of lattice points in coincidence: total number of lattice points]. A $\Sigma 3$ CSL is thus one in which 1 in 3 lattice points are coincident sites.

7.2.1   The coincidence site lattice model

The CSL is a fictitious concept, since the two lattices do not really interpenetrate, but it has relevance at the grain boundary, where they meet. A CSL
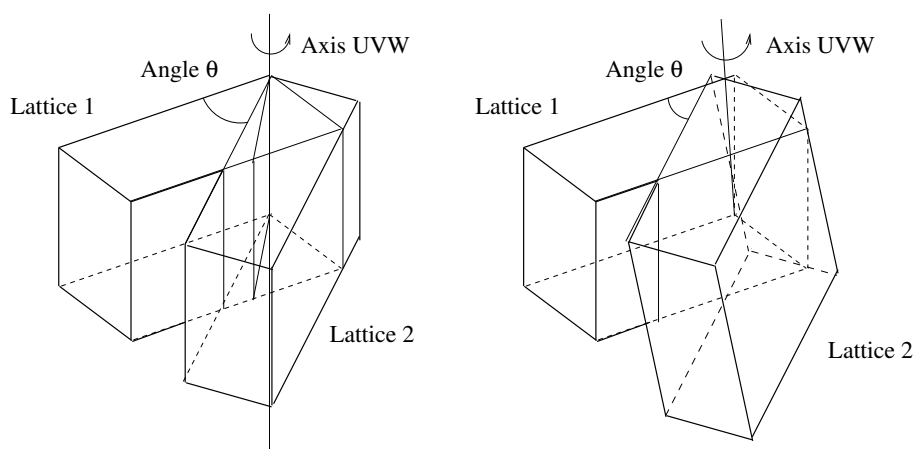
Figure 7.1: The angle-axis pair $\theta< UVW >$ characterises the crystallographic orientation between the two grains but the actual boundary can be anywhere. After Randle and Engler, 2000.

model of grain boundary geometry was proposed by Kronberg and Wilson (1949) and extended by Brandon *et al.* (1964) and Brandon (1966). The number of coincidence sites present on the grain boundary plane depends on the orientation of the plane, as well as the relationship between the two lattices. Planes with a higher proportion of coincidence sites allow better matching and a closer fit than those with few or no such sites, and this special periodicity has been linked with superior materials performance in many applications (*e.g.* Watanabe, 1993, Randle, 1996). Since the existence of a coincidence boundary requires precise angle and axis values, it might be expected that such boundaries would be too rare to be of relevance in general. However, it has been found that boundaries whose angle-axis pairs are close to those for true coincidence can also exhibit special properties. In such cases, the periodicity at the lattice is conserved by the introduction of grain boundary dislocations (Bollmann, 1970). This is similar to the description of low-angle boundaries, of misorientation 10–15° or less, as periodic arrays of dislocations (Read and Shockley, 1950). Low-angle boundaries are included in the CSL model as a special case, $\Sigma 1$, in which all lattice sites coincide in the ideal geometry.

The Brandon criterion, giving the maximum allowable deviation ν_m from

ideal coincidence for a Σ coincidence boundary, is:

$$\nu_m = \nu_0 \Sigma^{-1/2} \qquad (7.6)$$

where ν_0 is a constant of proportionality set to 15°, the maximum allowable deviation for a low-angle ($\Sigma 1$) boundary. Thus, boundaries with smaller Σ accommodate a greater possible deviation. This criterion is almost universally used for the categorisation of grain boundaries (Randle, 1993). The Brandon ratio, characterising the deviation from coincidence, is the actual misorientation normalised by ν_m for that value of Σ. When assessing grain boundary types, the Σ for which the Brandon ratio is smallest is chosen. Boundaries which do not fulfil the criterion for any CSL are designated as random.

The $60° < 111 >$, $\Sigma 3$ boundary type is of particular interest. If the boundary plane is either $\{111\}$ or $\{211\}$ as referred to the crystal lattice, this is a twin boundary, in which all the sites in the plane are coincidence sites. Most other low-Σ CSL boundaries also exhibit twinning on certain planes, but it is the $60° < 111 >$ orientation which is most commonly referred to as a 'twin' orientation in the literature (Randle, 1993).

7.2.2   Estimation of grain boundary energy

Grain boundaries have an intrinsic energy over and above that of the crystal lattice. As reported by Randle (1996), grain boundary energies tend usually to correlate with the free volume at the boundary. The periodicity in CSL arrangements reduces the free volume compared to random boundaries and thus a lower energy is expected. Determination of the misorientation dependence of boundary energies, by calculation or experiment, have mainly been performed on high-symmetry boundaries in pure metals (*e.g.* Tsurekawa *et al.*, 1994; Nakashima and Takeuchi, 2000). General boundaries in alloys are likely to have much higher energy (Randle, 1996). Extrinsic influences on grain boundary energy include precipitates, lattice dislocations, vacancies and impurity atoms, all of which tend to segregate to boundaries because of the increased free volume. It is not, therefore, possible to estimate grain

boundary energies in the $2\frac{1}{4}$Cr1Mo steels in this study based only on misorientation measurements.

7.3 Electron Backscatter Diffraction

The development of SEM-based electron backscatter diffraction (EBSD) techniques dates back to the 1970s (Venables and Harland, 1973; Venables and bin-Jaya, 1977) although backscatter patterns had, in fact, been observed earlier than this (Blackham *et al.*, 1953).

When the SEM is configured to give a focused spot of electrons on one point of the sample rather than a scanning beam, diffraction occurs by the elastic scattering of incident electrons in all directions. A plane wave hitting an isolated atom causes the emission of spherical waves of the same wavelength. If the atom is in a crystal lattice, most of these spherical waves will interfere destructively, but at certain angles they will be in phase. These angles were shown by Bragg (1913) to be related to the interplanar spacing d of the crystal lattice:

$$n\lambda = 2d\sin\theta_B \qquad (7.7)$$

where n is an integer, λ is the wavelength of the radiation and θ_B is the Bragg angle corresponding to diffraction from planes of spacing d.

7.3.1 Formation of Kikuchi patterns

Since the backscattered electrons are scattered in all directions, some will be at the correct Bragg angle θ_B for diffraction from each of the crystal planes in the lattice. Diffraction occurs in all directions, resulting in Kossel cones of diffracted radiation, whose half-apex angle is 90°-θ_B (Figure 7.2). In electron diffraction, for typical values of the electron wavelength, the Bragg angles are around 0.5°, giving cone apex angles of nearly 180°; the cones therefore appear almost flat. Each set of crystal planes produces two cones, which can be considered as emanating from a source between parallel planes, with one cone from the upper and one from the lower side of the source.
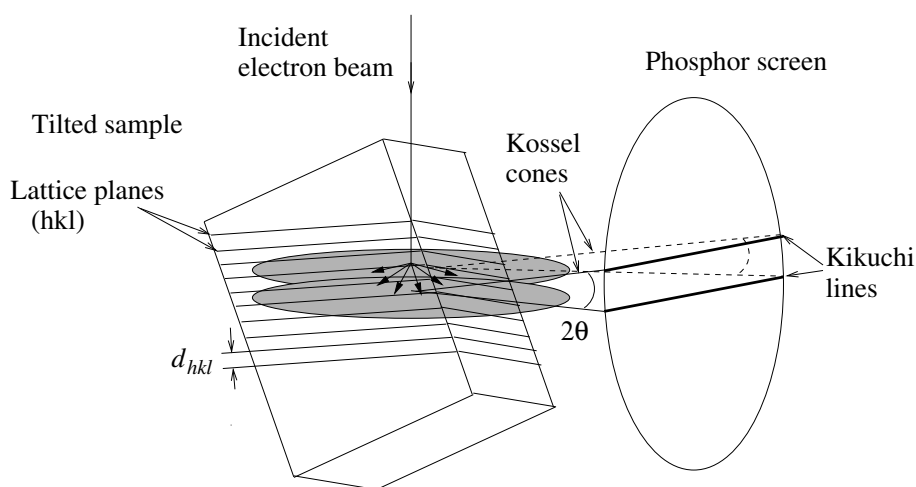
Figure 7.2: Geometry of electron backscatter diffraction; after Randle and Engler, 2000.

When the cones intersect a flat plate such as a phosphor screen, they appear almost as pairs of parallel lines (Kikuchi lines). The Kikuchi pattern is a gnomonic projection of relationships within the crystal (Figure 7.3). If the crystal is envisaged at the centre O of a sphere of radius r, and the phosphor screen is a tangent plane to the sphere at position N, a direction in the crystal is projected as a pole P. Each pair of lines has a characteristic spacing corresponding to the set of planes from which it originates. The points of intersection of Kikuchi bands represent major zone axes in the crystal.

7.3.2   Indexing Kikuchi patterns

Extraction of orientation information from Kikuchi patterns is possible for an experienced user, but over the last decade, an automated system has been developed and demonstrated to be as accurate as manual indexing and many times faster (Adams *et al.*, 1993; Wright, 1993). An algorithm known as the Hough transform is used to recognise the edges of the Kikuchi bands (Wright, 1993). This consists of applying to each pixel the equation:
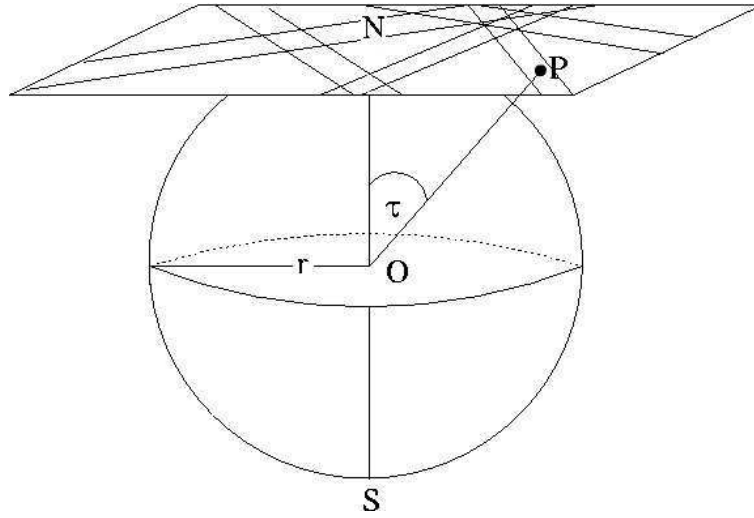
Figure 7.3: The Kikuchi diffraction pattern as a gnomonic projection of angles within the crystal; after Randle and Engler, 2000.

$$\rho_i = x_k \cos\theta_i + y_k \sin\theta_i \tag{7.8}$$

where (x_k, y_k) are the coordinates of a pixel in the original image and (ρ_i, θ_i) are the parameters of a straight line passing through (x_k, y_k). The sinusoidal curves generated by collinear points intersect at a single point, whose values of ρ and θ characterise the line, as described by Krieger Lassen (1996).

For correct indexing, the crystal system, chemical composition, unit cell dimensions and atomic positions of the material must be supplied to the analysis software. A background image is obtained from a large area while the microscope is in scanning mode, stored, and subtracted from the backscatter pattern obtained at every point to ensure that the contrast investigated by the software comes only from the EBSD pattern. Before the system is used, the specimen-to-screen distance and position of the pattern centre are obtained by calibration. An early calibration method is described by Venables and bin-Jaya (1977) and several modern methods by Randle and Engler (2000). When calibrated correctly, an EBSD system can calculate grain misorientations to an accuracy of $\pm 0.5°$ (Dingley and Randle, 1992).

7.3.3 Diffraction geometry in the SEM

Figure 7.4 shows the arrangement of the hardware for automated electron backscatter diffraction. The sample is tilted through an angle of 70° to the horizontal to reduce the path length of backscattered electrons and allow more electrons to escape from the surface and be detected (Venables and Harland, 1973). It lies in the eucentric plane, enabling it to remain in focus when the stage is moved in the surface plane, and is mounted on a piezoelectric stage capable of motions of 0.1 μm. Modern systems use a forward-mounted backscatter detector (the phosphor screen in Figure 7.4) and a camera to record diffraction patterns (Randle and Engler, 2000).
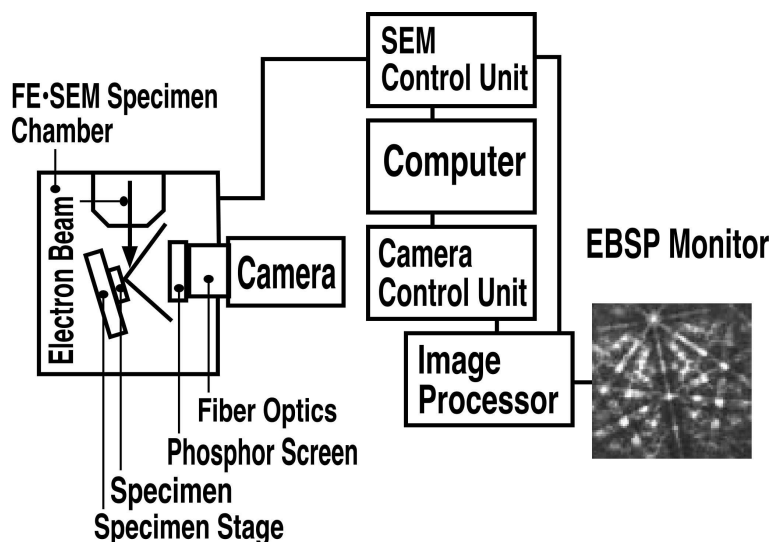
Figure 7.4: Experimental setup for SEM-based EBSD at Tohoku University. Diagram by K. Kawahara; used with permission.

7.4 Automated Orientation Imaging Microscopy

The development of automated Kikuchi pattern indexing led to the new technique of Orientation Imaging Microscopy (OIM). Television-based systems for capturing backscatter patterns and computer systems able both to

control the stage or electron beam position and to index patterns with minimal or no human intervention were developed (Adams *et al.*, 1993; Wright *et al.*, 1993). This allows the rapid acquisition of a large number of orientation data. Current systems are able to solve a Kikuchi pattern in less than one second using a standard PC (Randle and Engler, 2000).

The user typically programs in an array of positions from which orientation data should be acquired by specifying the spatial range and step size of sampling points. A hexagonal or square grid can be chosen but hexagonal tends to be preferred since each hexagon has six nearest neighbours, while in a square grid, four nearest and four next-nearest neighbours must be considered (Randle and Engler, 2000). A single data point is obtained as follows: the stage is moved to a specified point, the camera captures the Kikuchi pattern, and this is analysed and the Euler angles, stage position and image quality (§ 7.4.2) are recorded (Wright, 1993).

7.4.1   Representation of data

Orientation mapping

Automated OIM allows maps of the spatial dependence of orientation data to be plotted and related directly to microstructural features. Colour can be used to represent particular orientations or texture components (Wright, 1993). OIM observations have demonstrated that variations in orientation can occur within a single grain, making the definition of concepts such as grain size less definite than was previously believed (Adams *et al.*, 1993). In addition, boundaries were apparent which could not be seen on a conventional SEM image of the same area.

At grain boundaries, the Kikuchi patterns from neighbouring grains may overlap, producing a complex pattern which cannot be solved correctly by the indexing system (Adams *et al.*, 1993). Various 'clean-up' algorithms are available in the computer software to assign orientation values to such indeterminate points. The criteria used for this operation by the algorithms are described in detail in the software documentation, supplied by Tex-SEM Ltd. The clean-up process does alter the data set and should not be used

carelessly since it may introduce spurious features.

Grain boundary properties

Using the orientation data from neighbouring points, it is possible to determine the positions and misorientation angles of grain boundaries (Wright, 1993). Currently available software can identify coincidence boundaries and produce a colour-coded map according to Σ. Adams *et al.* (1993) noted that some of the boundaries identified appeared to terminate in grain interiors. Since this is topographically impossible, it was attributed to differences in orientation along the boundaries which, in some positions, cause the measured misorientation to fall below the arbitrarily designated minimum misorientation required to identify a grain boundary. OIM analysis is only two-dimensional and does not give information on the grain boundary plane orientation, but serial sectioning techniques have been developed to study this (Wall *et al.*, 2001).

Statistical approaches

The large numbers of data acquired using OIM allow statistical analyses of, for example, the distribution of misorientation angles θ between pairs of sampling points (Wright, 1993). This can be compared with theoretical predictions assuming a random distribution or a particular orientation relationship.

7.4.2   Image Quality

The image quality (IQ) of Kikuchi patterns, as represented by the sharpness of the lines, has been quantified and related to the level of deformation present in specimens (Quested *et al.*, 1988; Wilkinson and Dingley, 1991). The quantification method in current use was proposed by Krieger Lassen *et al.* (1994) and gives IQ values between 0 and 1, where 0 represents the worst image quality (no definition at all) and 1 the best. Since the development of automated OIM, image quality measurements can be obtained at every sampling point and displayed as a map. Minimum-quality points were

found to coincide with grain boundaries (Adams *et al.*, 1993; Wright, 1993) but could also be present in certain areas within grain interiors. This was attributed to high dislocation density. Image qualities were higher in certain grains than in others.

As well as the deformation state, IQ depends on the accelerating voltage, beam current, the state of the vacuum, the filament quality and alignment, and the specimen preparation (Randle and Engler, 2000). It may also depend on orientation but this has not yet been investigated fully. IQ measurements are not, therefore, fully quantitative, but semi-quantitative comparisons can be made within a single scan, enabling heavily deformed regions to be identified.

7.5 OIM observations of martensitic steels

7.5.1 Crystallographic relationships

A martensitic packet identified by optical microscopy or conventional SEM as a region of parallel laths is designated a 'morphological' packet. By contrast, a 'crystallographic' packet is a region of uniform orientation as determined by EBSD. Gourgues *et al.* (2000) studied the relationship between the two packet types in a low-alloy steel. Crystallographic packets were found to be much smaller than morphological packets, and to correspond to the 'blocks' in Figure 2.4. Between neighbouring blocks of the same morphological packet, the misorientation angle-axis pairs were mostly $60° < 111 >$ but occasionally $55° < 110 >$. This suggests that the blocks within a packet have a close-packed plane parallel to the same prior austenite prior austenite $\{111\}$ plane and are mostly twin related. The misorientation angle distribution had a peak for $\theta = 60°$. This was compared with theoretical distributions for Kurdjumov-Sachs and Nishiyama-Wasserman relationships, and it was concluded that Kurdjumov-Sachs corresponded more closely to the real data.

Previous TEM work had shown that each individal martensitic lath could nucleate with one of the six possible crystallographic variants from the same austenite $< 111 >$ (Chilton *et al.*, 1970; Sarikaya *et al.*, 1986). However,

Gourgues *et al.* instead found that martensite formed blocks of many laths with the same orientation.

Low-angle boundaries were found within crystallographic packets (blocks). The internal structure of a packet consists of several slightly misoriented groups of laths. The misorientations are present because of the high dislocation density associated with the shear strain of transformation from austenite to martensite.

In a 9 wt. % Cr steel subjected to a short tempering treatment after quenching, crystallographic packet sizes increased slightly with increasing prior austenite grain size (Barcelo *et al.*, 2002). The pole figures of the $< 200 >$ axis from single prior austenite grains did not correspond directly to either the Kurdjumov-Sachs or the Nishiyama-Wasserman relationship although it showed some similarities to both. In small prior austenite grains ($\sim$15 μm), only a subset of the possible variants predicted by either relationship were observed, but larger grains (> 40 μm) contained all the possible variants.

7.5.2   Creep-deformed martensitic steels

In martensitic 9Cr1Mo, 9Cr3Co and 9Cr3W3Co (wt. %) steels, the microstructure was very inhomogeneous, with some blocks extending to 10 μm and others as small as 1 μm (Nakashima *et al.*, 2000, 2001; Yoshida *et al.*, 2002). Areas of indeterminate orientation were present, but these were eliminated by creep deformation. They were attributed to high dislocation density, which is reduced by dynamic recovery during creep.

The misorientation angle distribution for boundaries with common axis $< 110 >$ was determined. In the 9Cr1Mo steel, peaks were found at low angles and in the regions around 60 and 80° . This agreed reasonably well with the values of 10°, 50.5° and 70.5° predicted from the Kurdjumov-Sachs relationship. Peaks at similar positions were found in the 9Cr3Co and 9Cr3W3Co steels. Creep deformation of the 9Cr1Mo steel decreased the number of grain boundaries with a specific orientation relationship and increased the number of random boundaries.

7.6 Experimental technique

7.6.1 Sample Preparation

An AQ sample and samples tempered at $600°C$ for 4, 16, 64, 128 and 256 hours were selected for observation. They were prepared as described in § 6.1, but instead of the final polishing stage described there, they were polished to 6 μm using diamond paste, and to 0.1 μm using alumina slurry. They were then electropolished using a mixture of 164 cm^3 acetic acid, 18 cm^3 perchloric acid and 18 cm^3 methanol which was cooled in iced water and stirred during polishing. The polishing conditions were 20–30 V for 3–5 minutes, with adjustments made depending on the appearances of the surfaces.

7.6.2 Orientation Imaging Microscopy

A Hitachi S-4200 Field Emission Gun Scanning Electron Microscope (FEG-SEM), belonging to the Materials Design and Interface Engineering Laboratory at Tohoku University, was used for the observations. The OIM system is shown schematically in Figure 7.4.

The accelerating voltage was 30 kV, the beam current 50 pA, and the beam penetration depth several tens of nanometres. A large spot size was used to maximise the backscattered signal. Operation of the OIM system was controlled using purpose-designed software by Tex-SEM Ltd. The step size was set to 0.1 μm, and the magnification to $6000\times$, to allow investigation on the lath scale.

Before acquisition of each data set, EBSD patterns were obtained from points on the sample surface to check the image quality. If this was adequate, a 14 x 15 μm area on the surface was selected and imaged using conventional SEM. After changing to backscatter mode, the scan was begun and left to run automatically. A complete scan took between two and three hours using this system.

Three scans were obtained from each of the steel samples at different positions on the surface. However, since the working distance between the pole piece and surface should be kept at approximately 15 mm for EBSD,

this only gave a limited range of regions for sampling.

7.7   Results

OIM maps and micrographs are presented in Figure 7.7–Figure 7.24. On each page, the top two diagrams are colour-coded maps of the orientation of the sample normal axis with respect to the crystal axes of the lattice. The colour key is given in Figure 7.5. The maps do not give comprehensive information, since there is a degree of freedom in rotation perpendicular to this direction, but it is possible to identify both gradual and abrupt orientation changes by their differences in colour.

The top left-hand diagram contains the raw orientation data, including indeterminate points, and the right-hand diagram is the result of a 'clean-up' algorithm, Grain Dilation. This takes an indeterminate point bordered by points belonging to grains, and assigns an orientation to it based on the orientations of its neighbours. (Full details of its operation are given in the software documentation.) The algorithm is iterative and operates until all points have been assigned to grains. The user is prompted to supply the minimum number of points which must be in a cluster if it is to be considered a grain; in this study, this was set at 4.

Beneath the raw data map is a grey-scale map of image quality. The lighter the colour, the higher the IQ. To the right of this is a grain boundary map calculated from the cleaned orientation data. These were used in preference to the raw data because most of the indeterminate points occurred at grain boundaries, obscuring the true orientation relationships between the grains. Figure 7.6 is the colour key for this map: red represents a low-angle boundary ($2 \leq \theta < 15°$), light green is $\Sigma 3$, black is random, and other colours are used to represent boundaries with different Σ values, as determined by the Brandon criterion. Misorientations of $< 2°$ between adjacent points are not considered to be grain boundaries.

The lowest image is a conventional SEM micrograph of the same area. The electropolishing removes much of the surface relief, so some of these images are of poor quality.
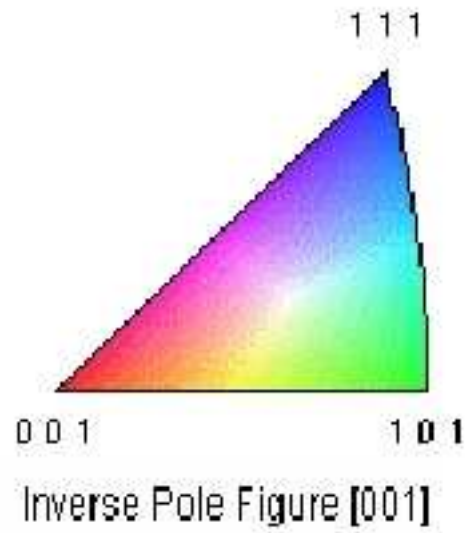
Figure 7.5: Colour-coded pole figure key for orientation maps. Colour corresponds to orientation of [100] specimen axis with respect to crystal axes [001], [111] and [101].
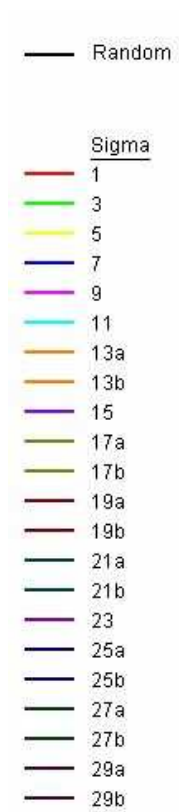
Figure 7.6: Key to grain boundary maps.

3.00 µm = 30 steps   IPF [001]

3.00 µm = 30 steps   IPF [001]

3.00 µm = 30 steps   IQ 65.5...334.4

Boundary levels: 15°

3.00 µm = 30 steps   IQ 65.5...334.4
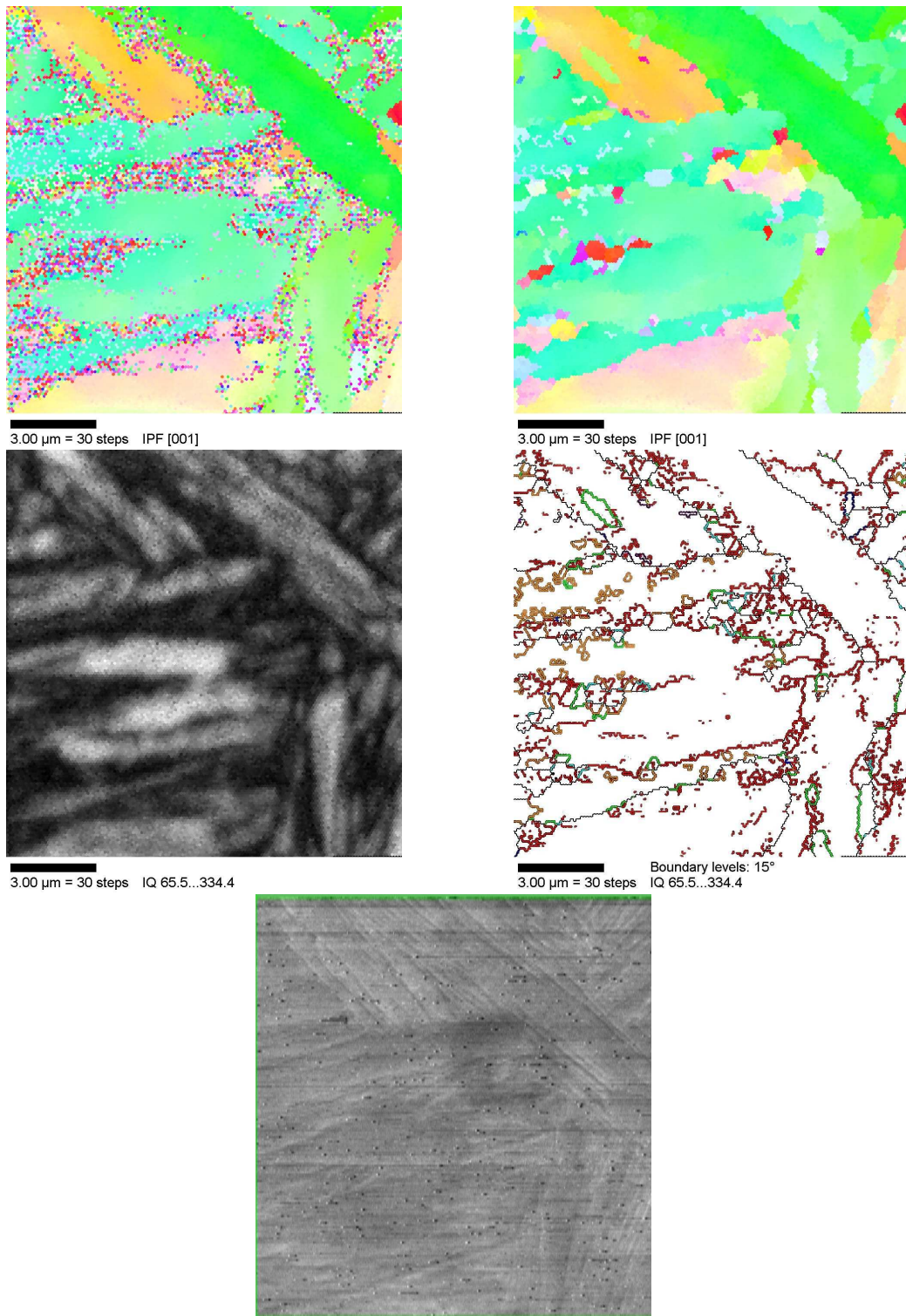
Figure 7.7: $2\frac{1}{4}$Cr1Mo steel, as-quenched
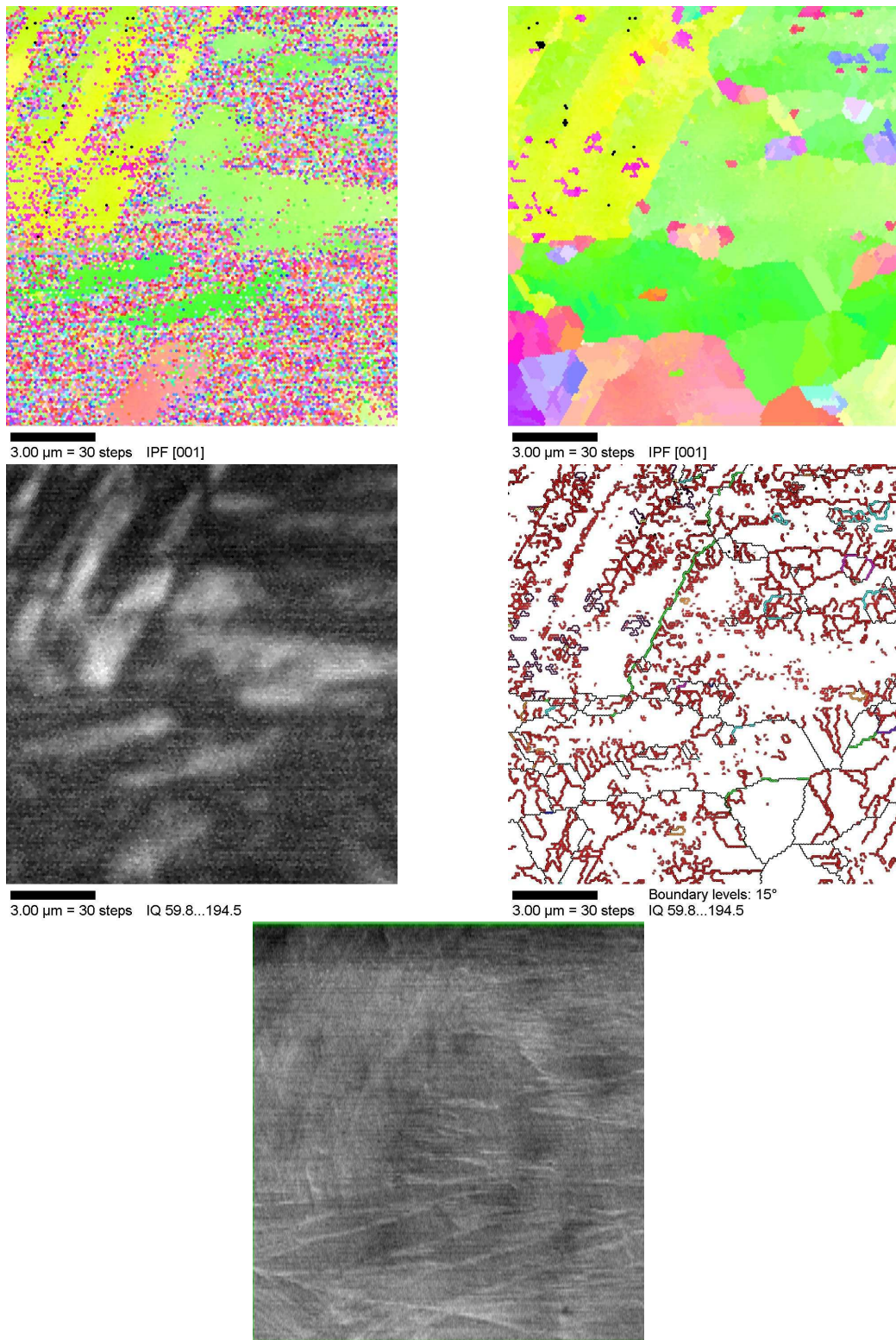
Figure 7.8: $2\frac{1}{4}$Cr1Mo steel, as-quenched

3.00 μm = 30 steps   IPF [001]

3.00 μm = 30 steps   IPF [001]

3.00 μm = 30 steps   IQ 40.1...176.1

Boundary levels: 15°
3.00 μm = 30 steps   IQ 0...176.1
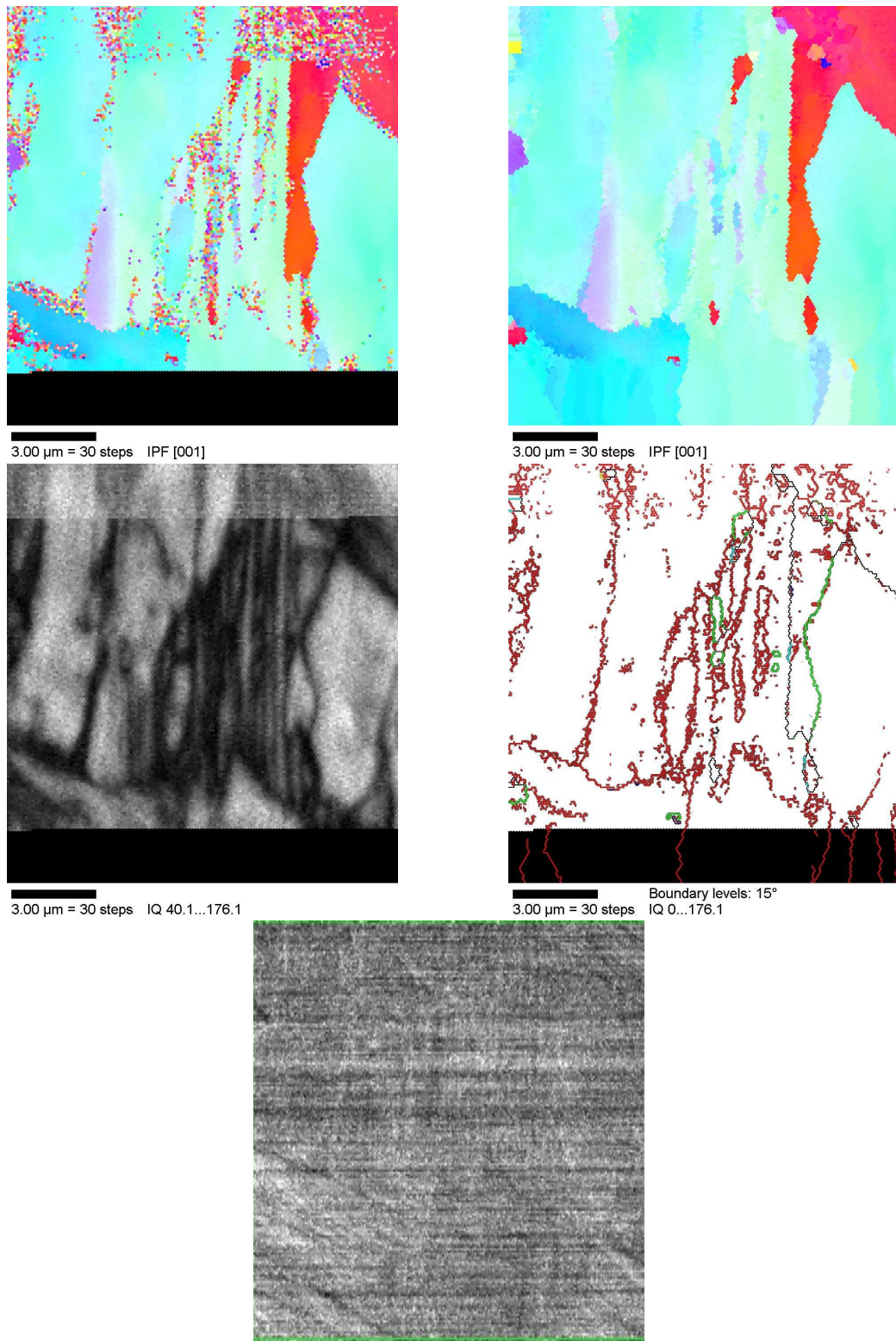
Figure 7.9: $2\frac{1}{4}$Cr1Mo steel, as-quenched

3.00 µm = 30 steps   IPF [001]

3.00 µm = 30 steps   IPF [001]

3.00 µm = 30 steps   IQ 98.7...301.2

Boundary levels: 15°

3.00 µm = 30 steps   IQ 0...301.2

Figure 7.10: $2\frac{1}{4}$Cr1Mo steel, 600 °C, 4 hours tempering

3.00 μm = 30 steps   IPF [001]

3.00 μm = 30 steps   IPF [001]

3.00 μm = 30 steps   IQ 77.7...290.5

Boundary levels: 15°
3.00 μm = 30 steps   IQ 0...290.5

Figure 7.11: $2\frac{1}{4}$Cr1Mo steel, 600 °C, 4 hours tempering

Figure 7.12: $2\frac{1}{4}$Cr1Mo steel, 600 °C, 4 hours tempering

3.00 μm = 30 steps   IPF [001]

3.00 μm = 30 steps   IPF [001]

3.00 μm = 30 steps   IQ 41...161.1

Boundary levels: 15°
3.00 μm = 30 steps   IQ 0...161.1

Figure 7.13: $2\frac{1}{4}$Cr1Mo steel, 600 °C, 16 hours tempering

Figure 7.14: $2\frac{1}{4}$Cr1Mo steel, 600 °C, 16 hours tempering

Figure 7.15: $2\frac{1}{4}$Cr1Mo steel, 600 °C, 16 hours tempering

3.00 µm = 30 steps   IPF [001]

3.00 µm = 30 steps   IPF [001]

3.00 µm = 30 steps   IQ 39...188.1

Boundary levels: 15°

3.00 µm = 30 steps   IQ 39...188.1

Figure 7.16: $2\frac{1}{4}$Cr1Mo steel, 600 °C, 64 hours tempering

3.00 μm = 30 steps   IPF [001]

3.00 μm = 30 steps   IPF [001]

3.00 μm = 30 steps   IQ 51.2...192

Boundary levels: 15°

3.00 μm = 30 steps   IQ 51.2...192
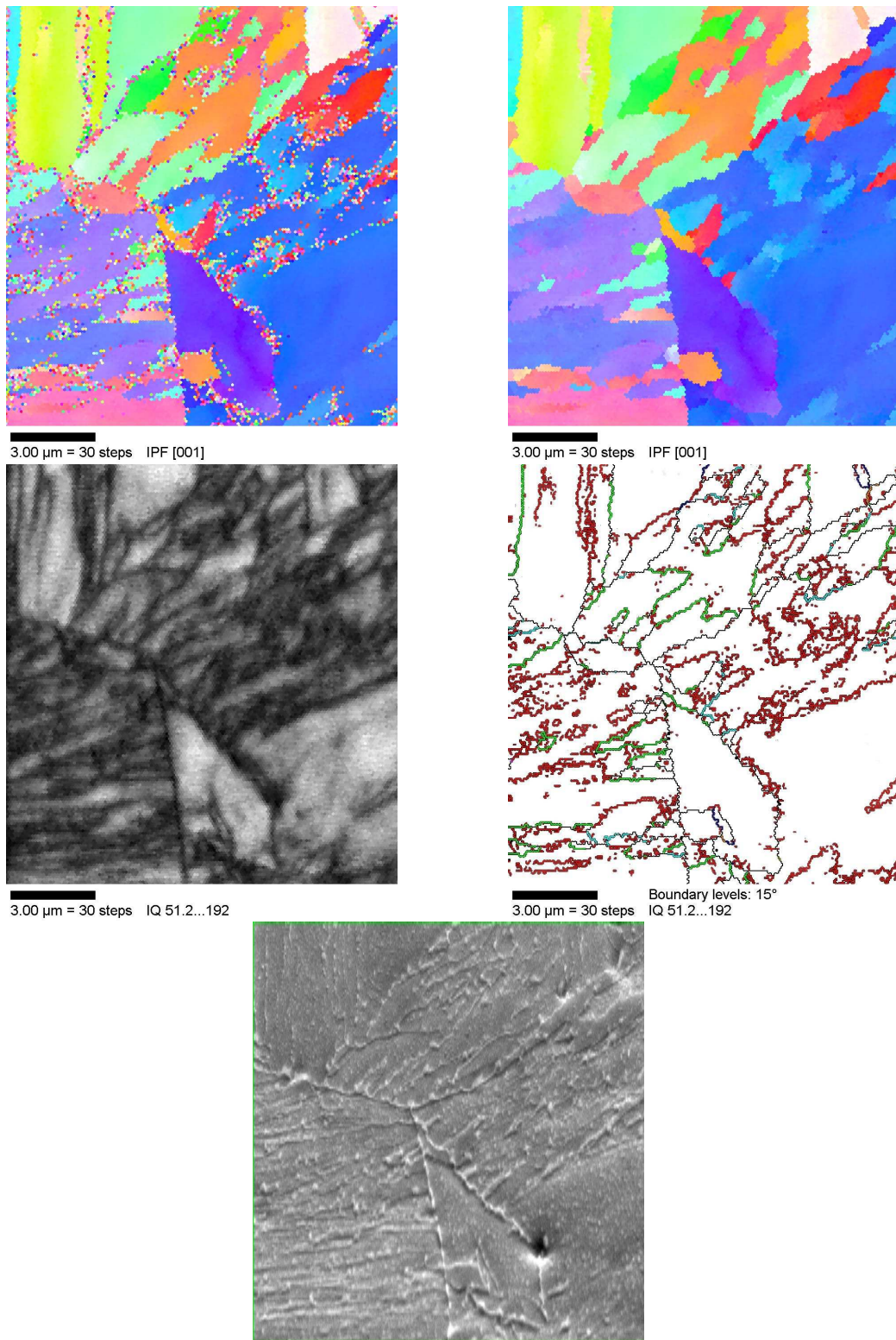
Figure 7.17: $2\frac{1}{4}$Cr1Mo steel, 600 °C, 64 hours tempering
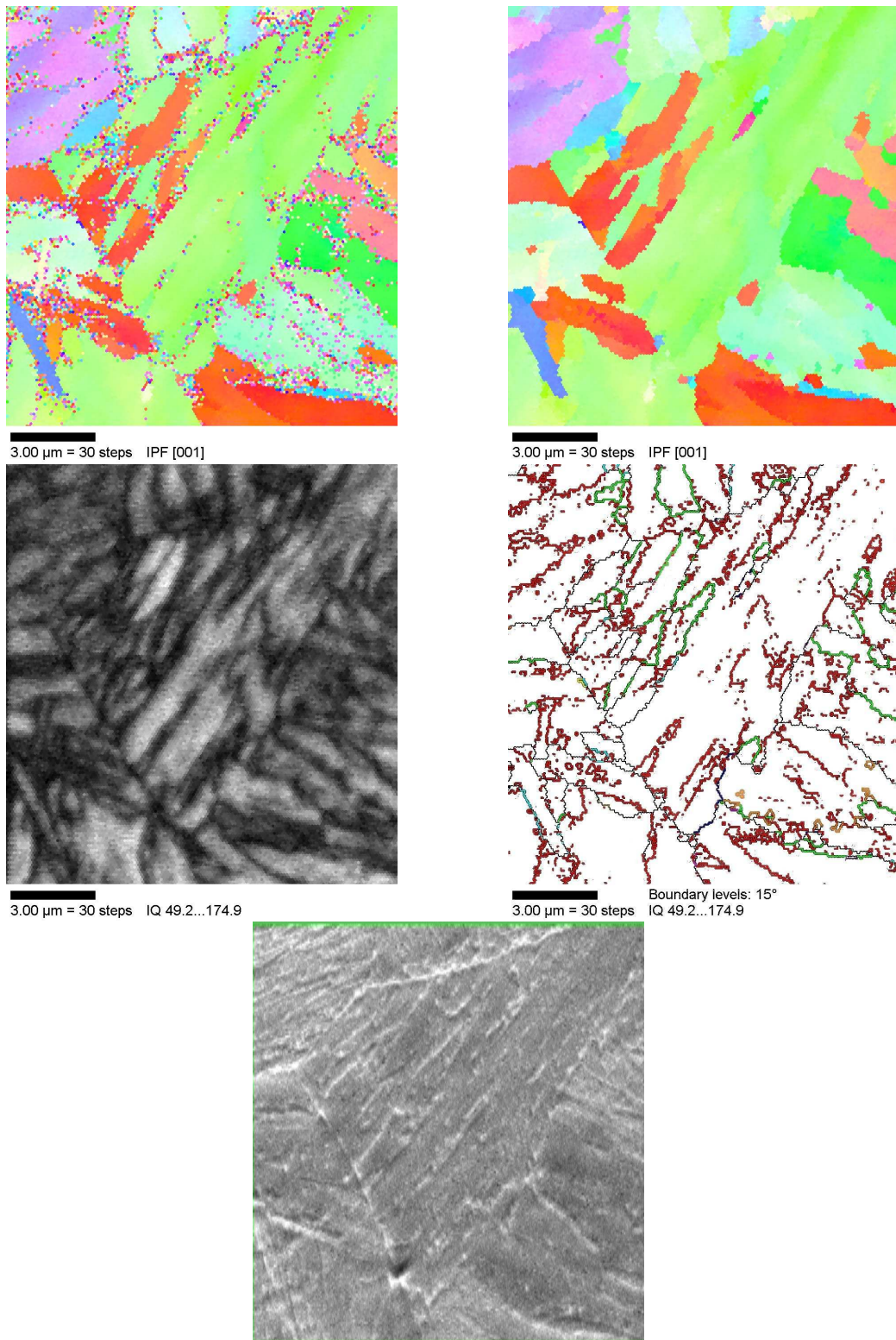
Figure 7.18: $2\frac{1}{4}$Cr1Mo steel, 600 °C, 64 hours tempering

3.00 µm = 30 steps   IPF [001]

3.00 µm = 30 steps   IPF [001]

3.00 µm = 30 steps   IQ 66.7...241.8

Boundary levels: 15°

3.00 µm = 30 steps   IQ 66.7...241.8
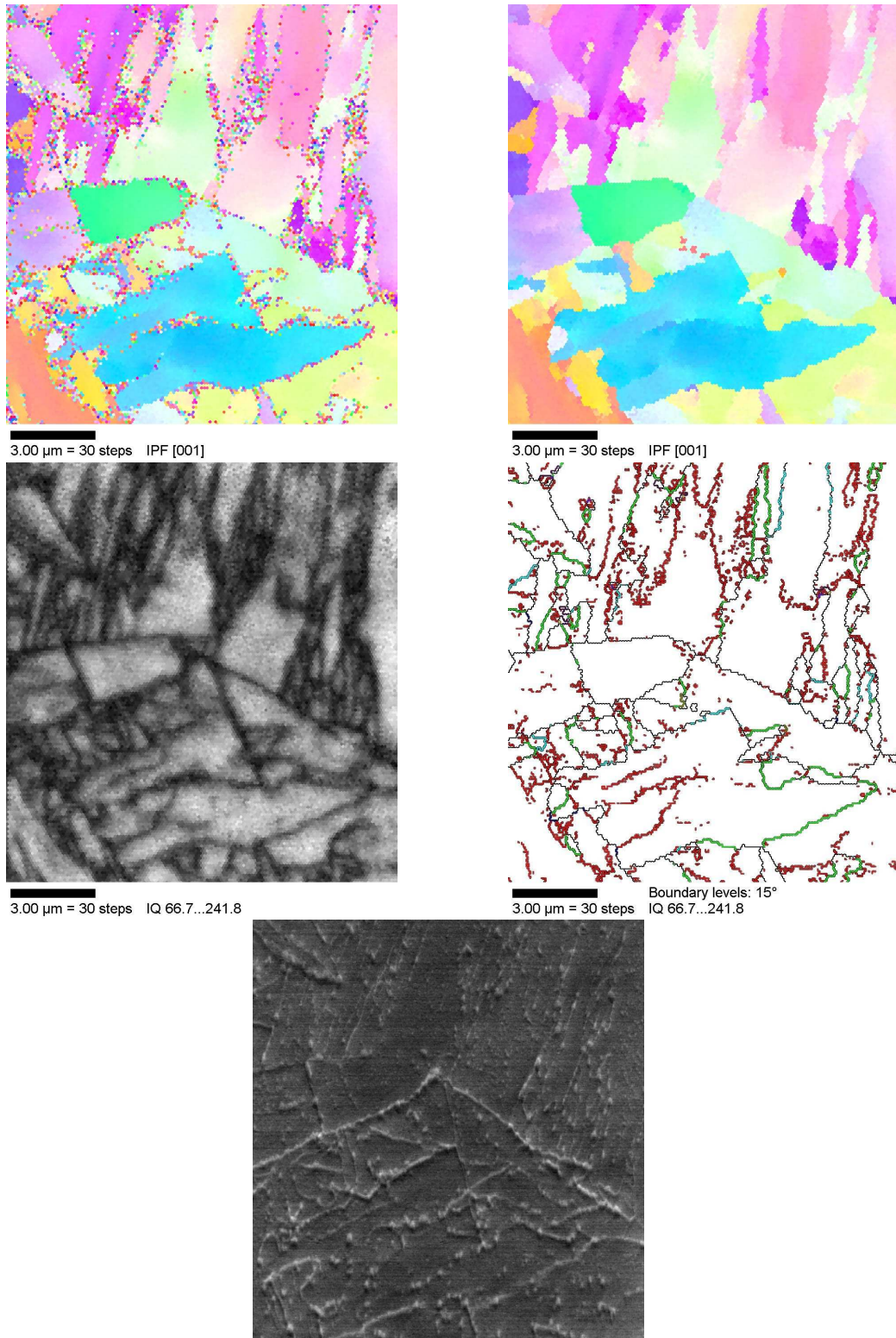
Figure 7.19: $2\frac{1}{4}$Cr1Mo steel, 600 °C, 128 hours tempering
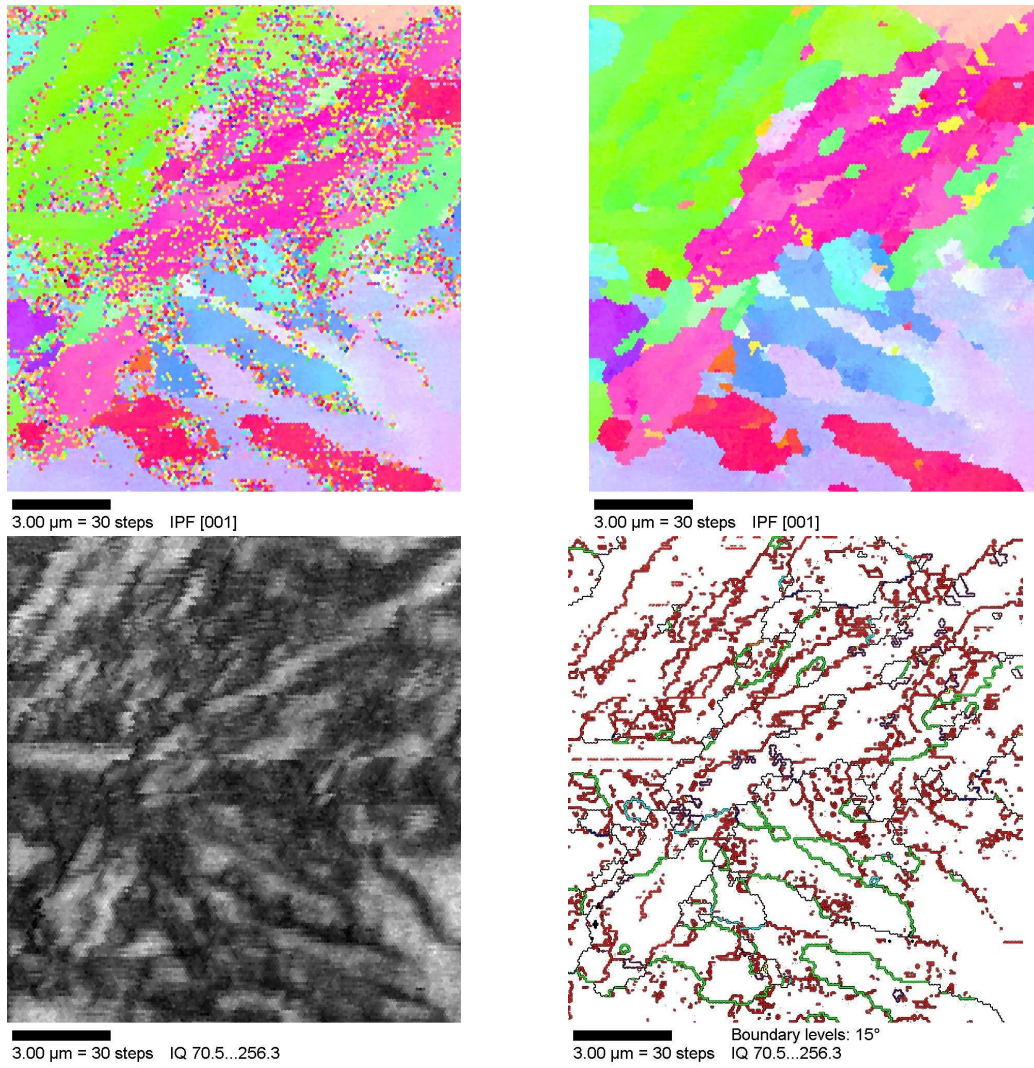
Figure 7.20: $2\frac{1}{4}$Cr1Mo steel, 600 °C, 128 hours tempering
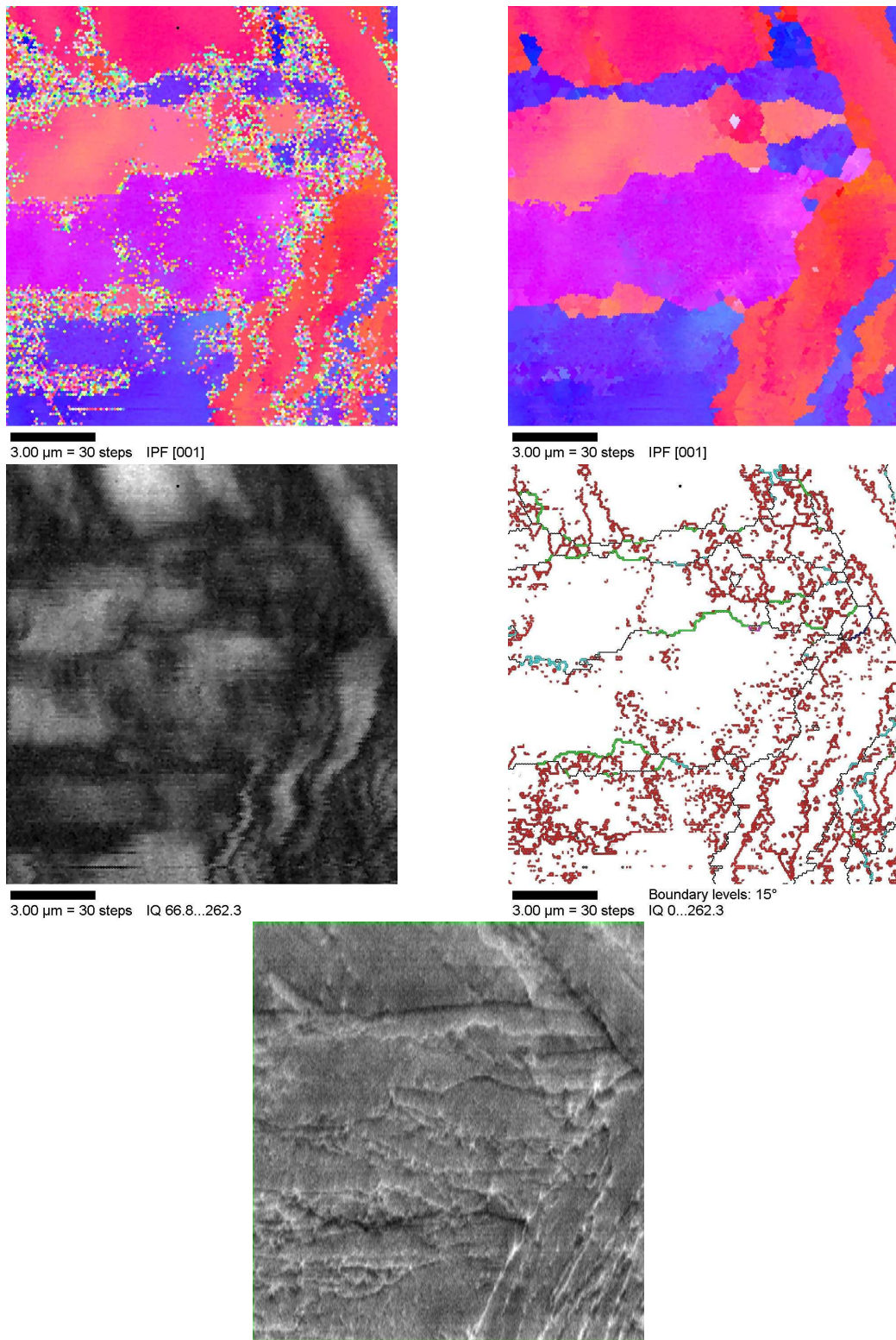
Figure 7.21: $2\frac{1}{4}$Cr1Mo steel, 600 °C, 128 hours tempering

3.00 µm = 30 steps   IPF [001]

3.00 µm = 30 steps   IPF [001]

3.00 µm = 30 steps   IQ 33.8...211.8

Boundary levels: 15°

3.00 µm = 30 steps   IQ 33.8...211.8
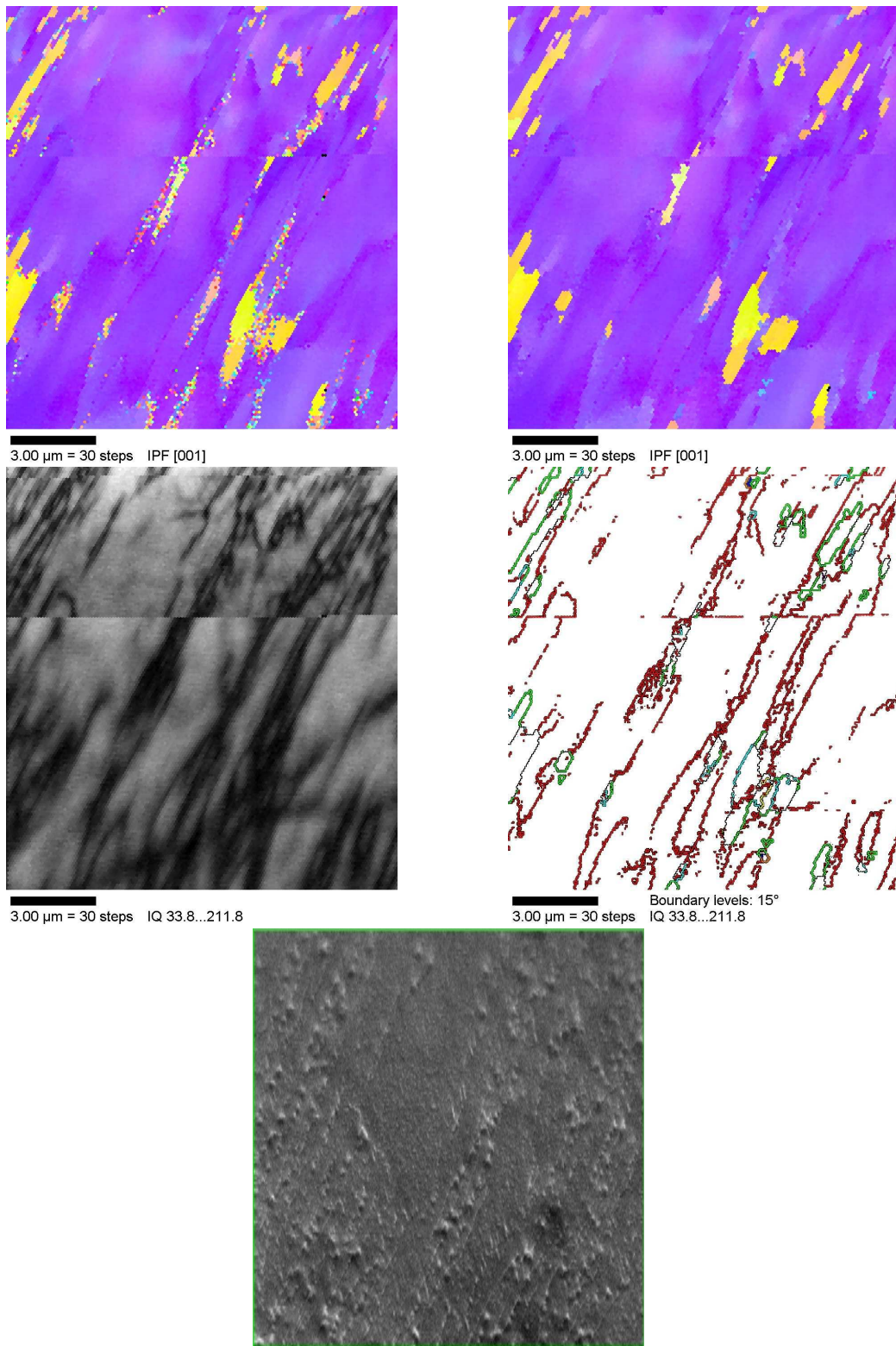
Figure 7.22: $2\frac{1}{4}$Cr1Mo steel, 600 °C, 256 hours tempering
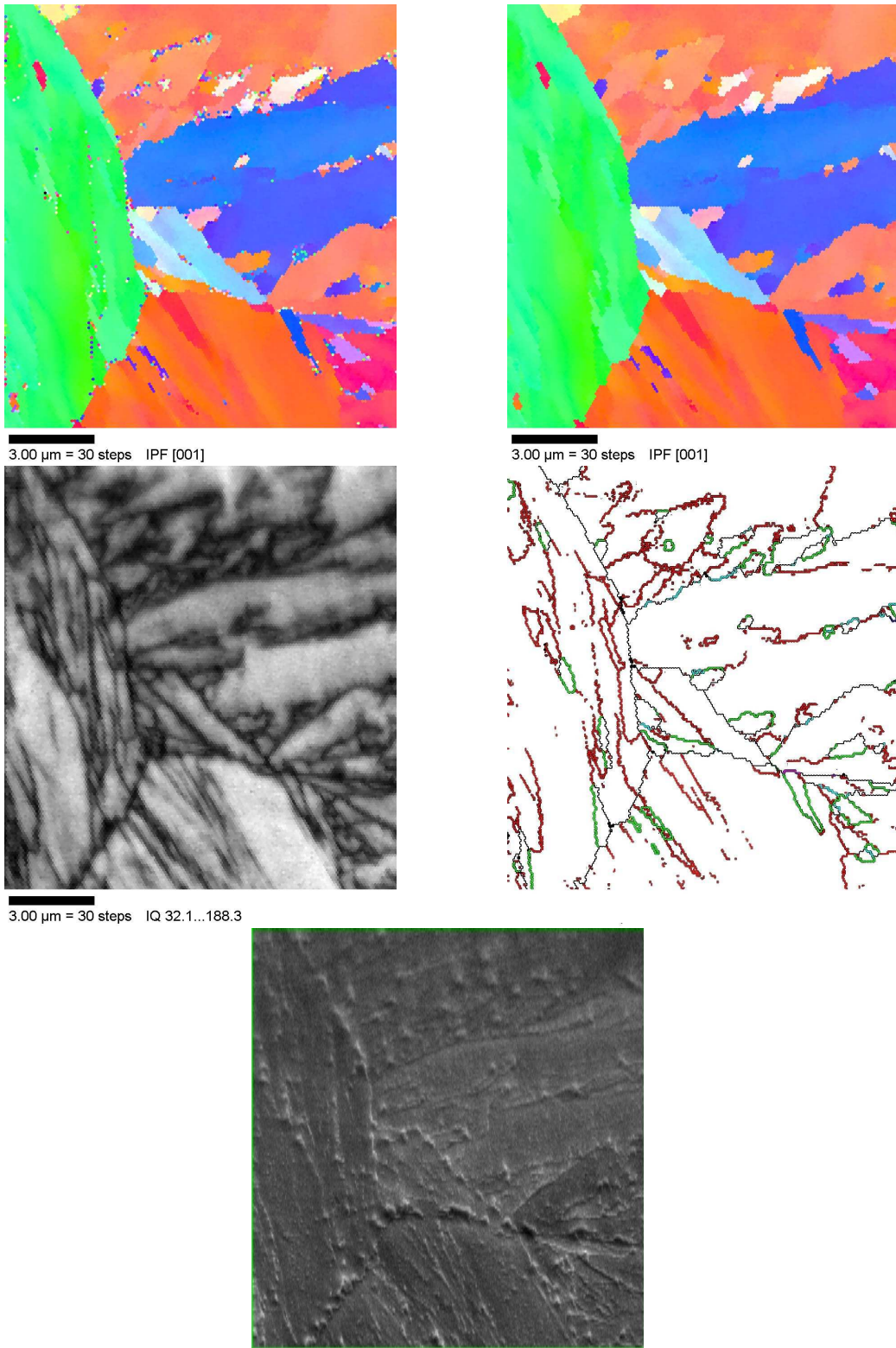
Figure 7.23: $2\frac{1}{4}$Cr1Mo steel, 600 °C, 256 hours tempering

3.00 µm = 30 steps   IPF [001]

3.00 µm = 30 steps   IPF [001]

3.00 µm = 30 steps   IQ 32.8...207.6

Boundary levels: 15°

3.00 µm = 30 steps   IQ 32.8...207.6
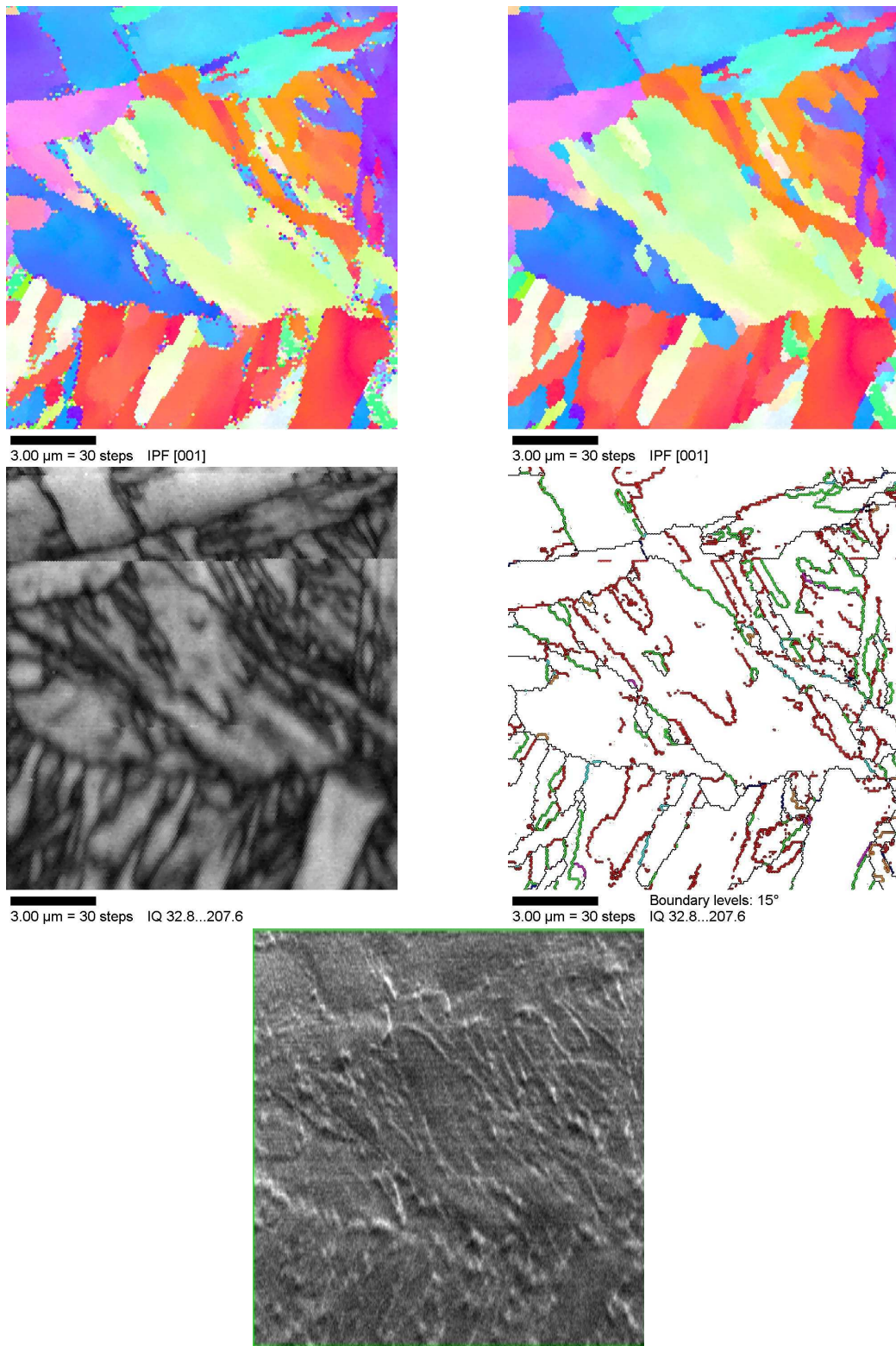
Figure 7.24: $2\frac{1}{4}$Cr1Mo steel, 600 °C, 256 hours tempering
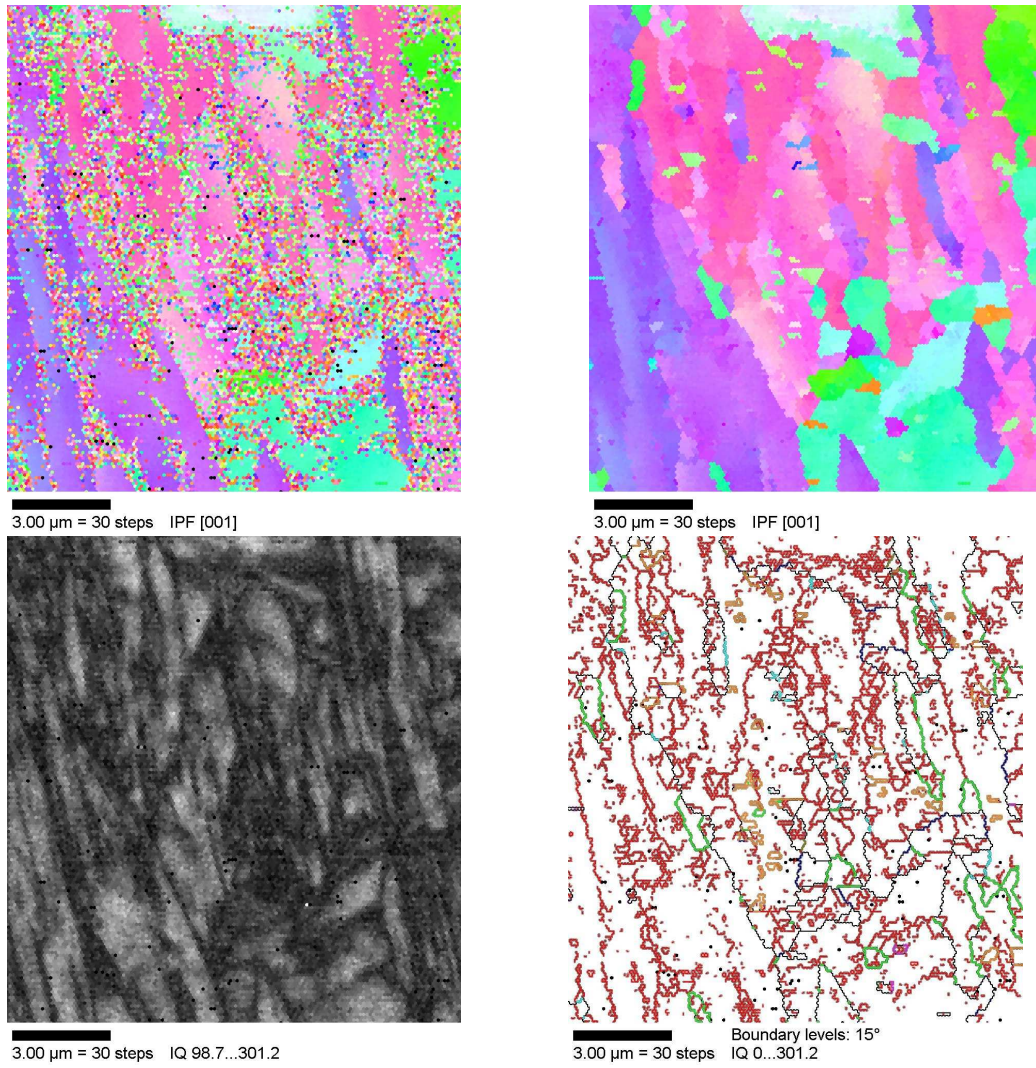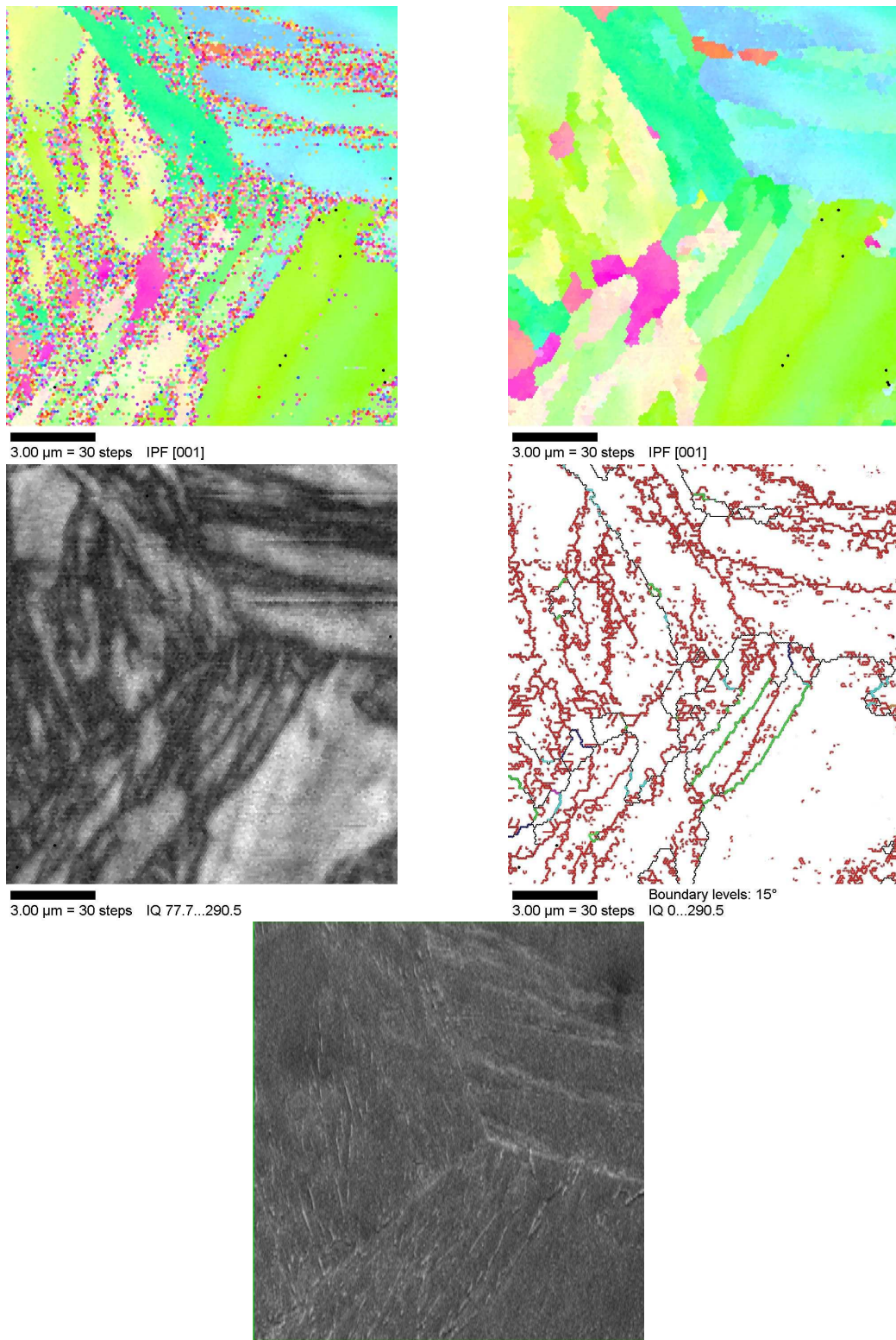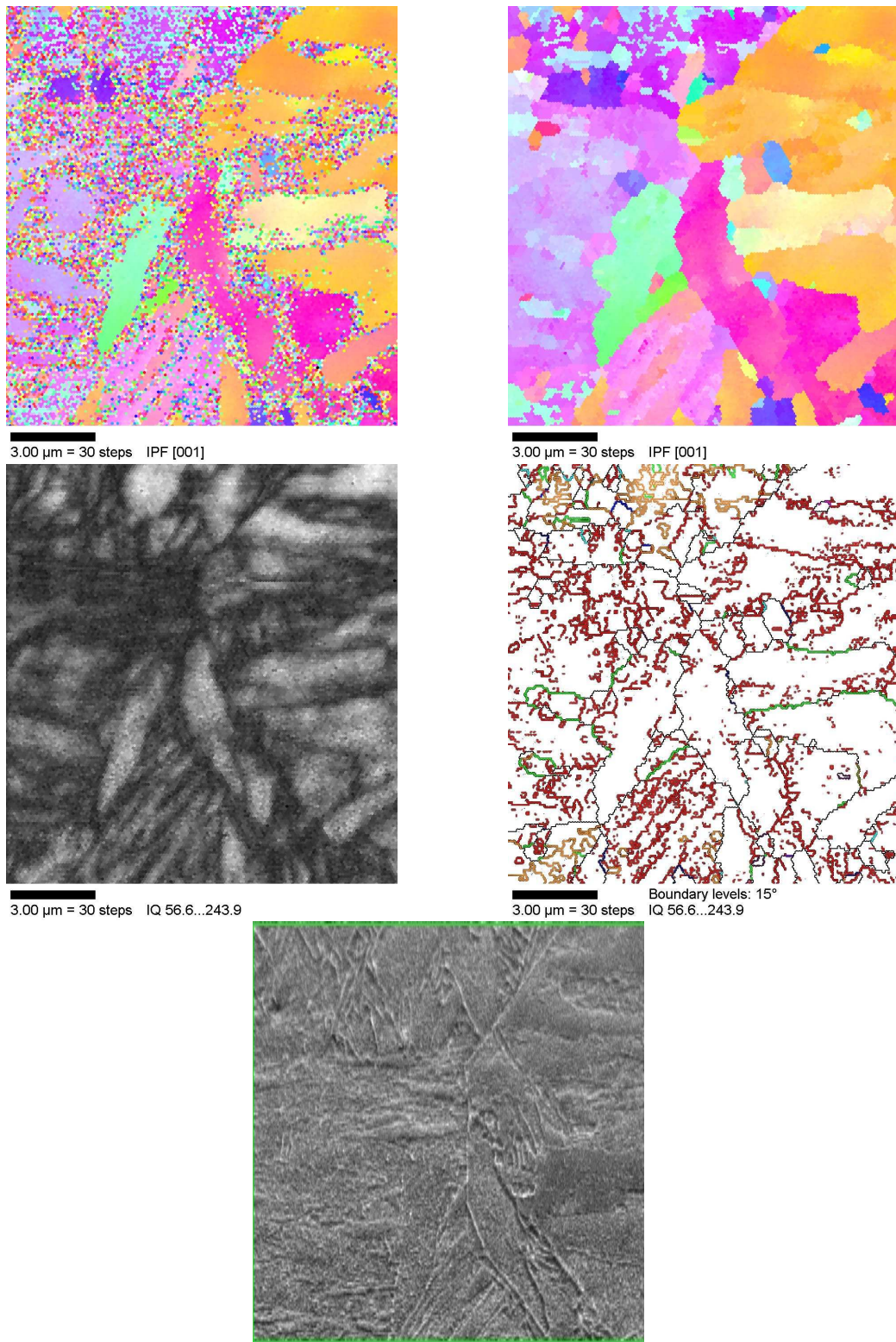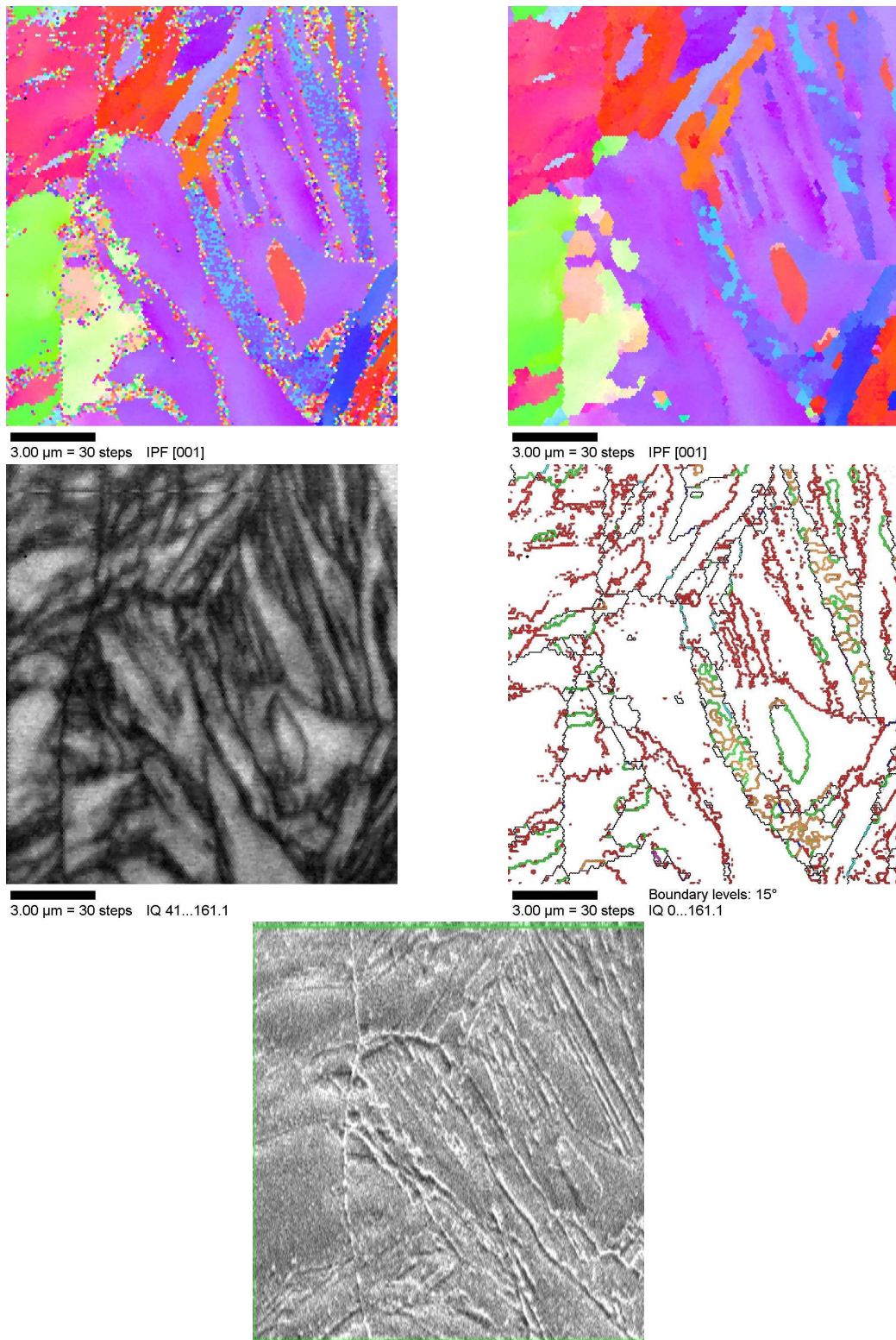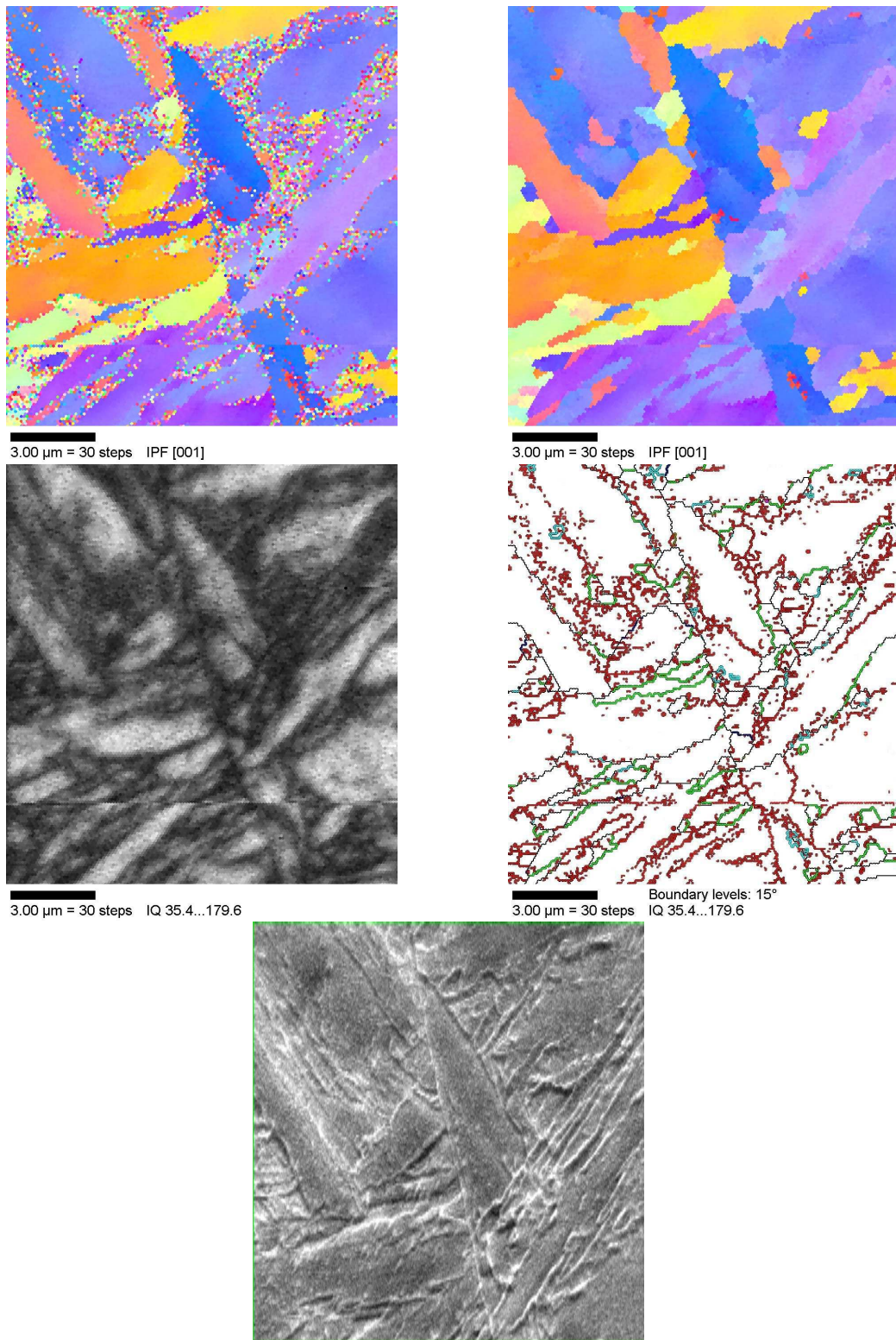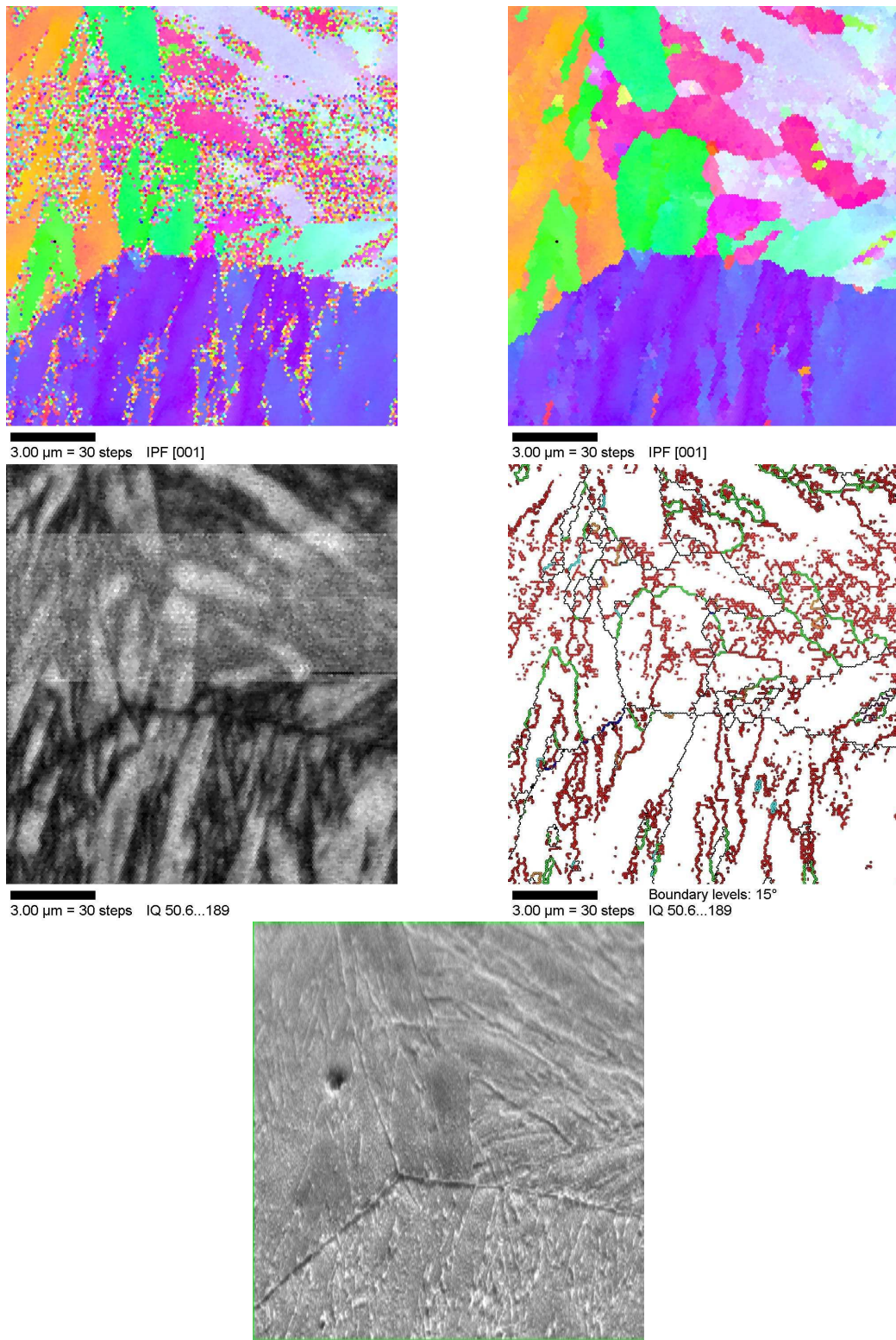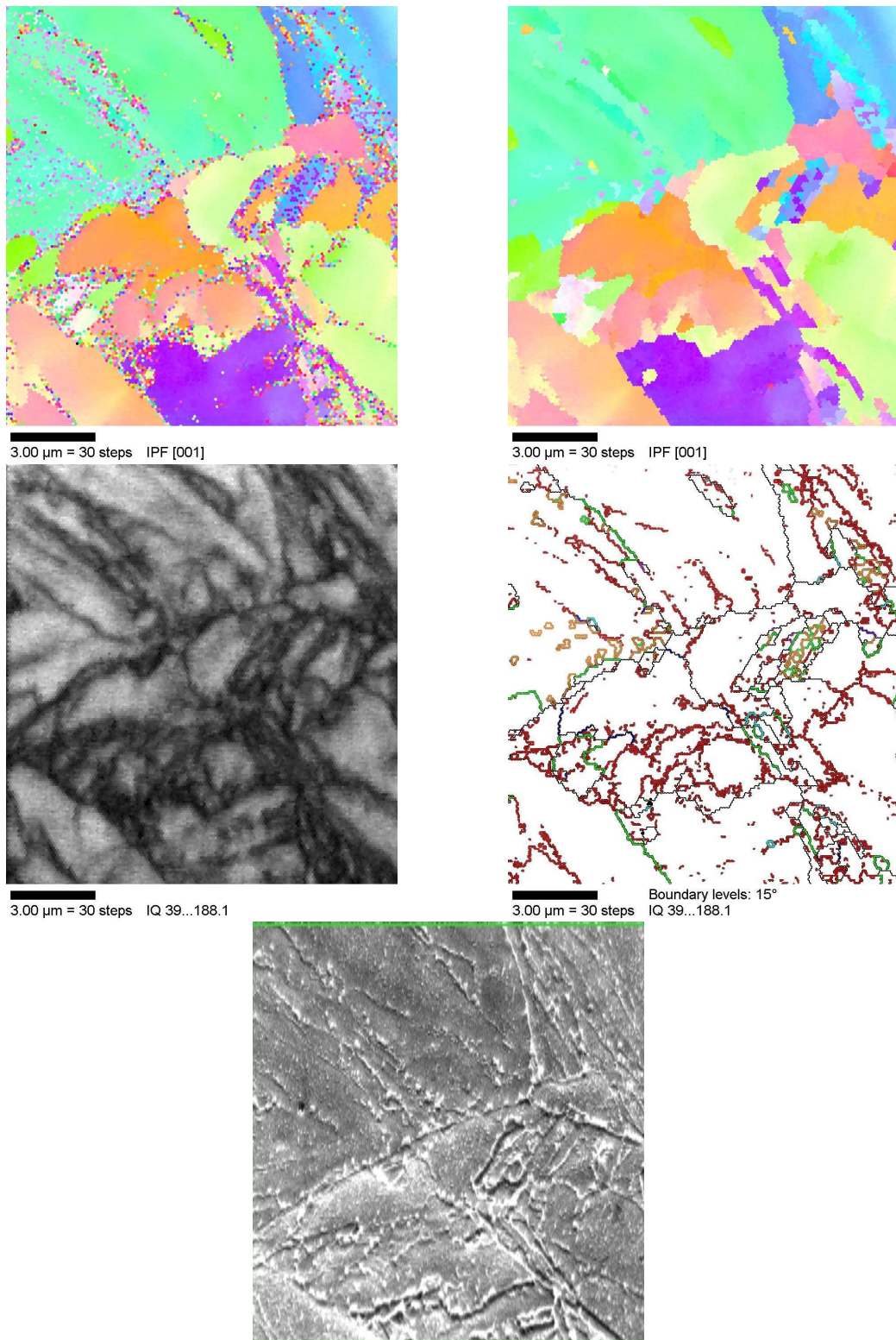
7.7.1   As-quenched data

Figure 7.7

The raw-data orientation map contains large regions of indeterminate points, which coincide with the areas of lowest image quality. On the cleaned map, there are many small regions which have been constructed by the cleaning algorithm from the available data, but it is not clear which, if any, of these correspond to true grain structures. On Figure 7.25, the regions considered by the software as grains are coloured, and the indeterminate areas are white. The cleaning algorithm was intended to deal with only small numbers of indeterminate points and cannot be expected to make correct estimates over such large areas of uncertainty.

   The grain boundary map for this sample may not be reliable because of the large areas of poor IQ. There are many apparent low-angle boundaries which correspond to the small 'grains' in the cleaned image and may be spurious. However, the random boundaries on the map correspond reasonably well in shape and position to features on the SEM image.

Figure 7.8

An even greater proportion of indeterminate points is present in this image than in Figure 7.7, so the cleaned map and grain boundary map are rather untrustworthy. The extent of the indeterminate areas is visible in Figure 7.25; these correspond well to the dark areas on the IQ map. It is difficult to relate any of the OIM maps to the SEM image.

Figure 7.9

Despite being obtained from the same sample as the images in Figure 7.7 and Figure 7.8, this image has little in common with them. The indeterminate point proportion is much lower, and much of the image consists of a single orientation. Long, parallel, vertical features are visible in the central region of the IQ map. Although the SEM image of this region is extremely poor, similar features can just be discerned. Their shape and size suggest that they are individual laths or groups of very few laths, bounded by dis-

3.00 µm = 30 steps   Unique Grain Color

As-quenched; Figure 7.7
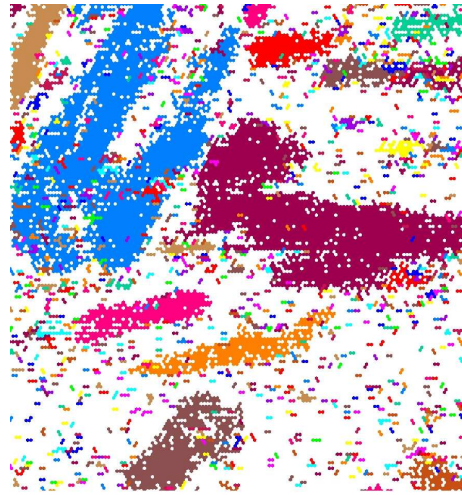
3.00 µm = 30 steps   Unique Grain Color

As-quenched; Figure 7.8

3.00 µm = 30 steps   Unique Grain Color

As-quenched; Figure 7.9

3.00 µm = 30 steps   Unique Grain Color

600°C, 256 hour tempered; Figure 7.23

Figure 7.25: Maps with regions identified as unique grains marked in colour, and indeterminate regions in white.

located regions. Their misorientation angle is very small; since the grain boundary map shows discontinuous low-angle boundaries in this region, it must be around 2°. In other parts of the image, there are gradual orientation variations without any clearly visible lath boundaries. The red region towards the right-hand side is partly bounded by a Σ3 boundary and may be a twin-related variant of the light-blue orientation.

7.7.2   Indeterminate points

The presence of indeterminate points may be due to retained austenite or to martensite tetragonality. The data supplied to the software assumed a body-centred structure, so if other crystal structures were present, their Kikuchi lines would be incorrectly indexed. This would give rise to problems in orientation determination where these phases were prevalent. OIM software can index multiphase microstructures if the correct lattice constants are provided for each, so it is possible to repeat the experiments on these samples to check for other phases. However, another possible origin of the indexing problem is low Kikuchi pattern image quality. This results from high strain and does not depend on the assumed crystal structure. Since regions of low IQ consistently coincide with indeterminate point regions, it is suggested that high strain, rather than incorrect crystal structure data, is the main cause.

7.7.3   600°C, 4 hours tempering

Figure 7.10

Many indeterminate points are still present after four hours of tempering, but they are more evenly distributed. Laths or groups of laths can be identified by their edges on the image quality map and by small changes at their edges on the orientation map. The grain boundary map contains many, probably spurious, discontinuous boundaries but also some more clearly defined low-angle boundaries with equivalents on the other maps.

Figure 7.11

A triple junction of prior austenite grains is visible in the centre of the SEM image. (It appears that the position of the selected region shifted slightly between image and OIM data acquisition so that the junction is not quite central in the OIM maps.) The orientation map contains a combination of wide, homogeneous regions and narrower features with abrupt orientation changes. Some of these may be variants occurring within the same morphological packet. The fraction of indeterminate points is lower than in Figure 7.10, and they are mainly concentrated in boundary regions.

Figure 7.12

This image shares many of the features of Figure 7.11, with a mixture of grain and packet sizes. The mottled blue and purple region appears to be a single grain with two, almost equally favourable, solutions to the Kikuchi pattern.

7.7.4   600°C, 16 hours tempering

Figure 7.13

After 16 hours, a much more distinct grain structure is visible, with obvious correspondence to the SEM micrograph. The indeterminate points are mainly confined to grain boundaries. A clear random prior austenite boundary runs from top to bottom. The purple region contains many subregions slightly misoriented from one another, and red packets, some of which are bounded by Σ3 boundaries.

Figure 7.14

This image has similar features to Figure 7.13, but it appears that the microscope was shaken toward the end of image acquisition since there is a jolt in the micrograph. This can be caused by mechanical vibrations or spontaneous beam jumping (Kawahara, personal communication). The effect is not easily visible in the orientation maps but produces a spurious 'low-angle boundary' in the boundary map.

Figure 7.15

The purple area at the bottom of the image is composed almost entirely of slightly misoriented subregions, whose boundaries correspond to low-IQ features. The bright-coloured band on the IQ map is an artefact of the measuring process. In this type of FEG-SEM, the beam intensity tends to decrease with time, especially just after starting up the microscope. This sometimes requires adjustments of the settings during data acquisition so that the beam intensity is sufficient to obtain backscatter data. This adjustment changes the image quality, giving a bright band (Kawahara, personal communication).

7.7.5   600°C, 64 hours tempering

Figure 7.16 and Figure 7.17

These images have inhomogeneous distributions of image quality and grain or packet sizes. The grain boundary maps correspond well to the SEM and IQ images, particularly in Figure 7.17, which is also notable for a large number of $\Sigma 3$ boundaries. By comparison with the SEM image, it appears that some of these are boundaries between variants within the same morphological packet.

Figure 7.18

The green and orange areas separated by $\Sigma 3$ boundaries in the centre of this image also appear to be variants within a morphological packet. Parallel-sided, slightly misoriented features are present within the green area; these appear to be groups of laths similar to those in the centre of Figure 7.9, but with a reduced dislocation density.

7.7.6   600°C, 128 hours tempering

Figure 7.19

Particularly noticeable in this image are grains or packets with gradual changes of orientation. Over a single grain, the colour can change from green

to white over a distance of 3 μm without any low-angle boundaries. In the IQ map, these grains are of lighter colour and appear relatively strain-free.

Figure 7.20 and Figure 7.21

From the IQ maps of both of these images, it is clear that serious shaking has occurred. Some impression of the orientations and grain structures can be inferred from these maps, but they are not suitable for detailed study.

7.7.7   600°C, 256 hours tempering

Figure 7.22

This interesting region consists of one orientation, in purple, with small yellow 'islands' of a different orientation embedded within it. Many of the islands are bounded by Σ3 (green) or Σ11 (turquoise) boundaries. The image forms part of a single morphological packet, as shown by the parallel lines on the SEM image, but appears different from the 'block' model discussed by Gourgues *et al.* (2000).

A spurious 'low-angle boundary' arising from beam jumping, is present about a third of the way down the image.

Figure 7.23

This raw image contains especially few indeterminate points, and changes very little on cleaning. The IQ map has many light-coloured regions, and the dark regions are narrow and coincide with grain boundaries. The prior austenite grains meeting in the centre contain slightly misoriented regions and small, included regions with Σ3 boundaries in a similar way to the region in Figure 7.22. The orange and blue regions near the top appear, from the SEM image, to be blocks within the same packet.

The small light blue triangle in the centre is bounded on all sides by random boundaries, with no clear relationship to any of the surrounding regions, but its striped structure suggests that it is a prior austenite grain with a former martensite lath substructure, rather than a recrystallisation nucleus.

Figure 7.24

The grains and packets in this image are on a smaller scale than those of Figure 7.22 and Figure 7.23. Clear, parallel-sided former groups of laths are evident, as are Σ3 and Σ11 boundaries.

7.7.8 Summary

The as-quenched data can have very low image quality and a large number of indeterminate points. This is thought to arise from the high levels of strain present after quenching. Tempering improves the IQ and increases the number of points whose Kikuchi patterns can be solved. It is therefore not entirely clear whether tempering changes the orientations significantly or simply helps to reveal the existing microstructure by relaxing the strain.

A typical crystallographic packet in the tempered structure contains many slightly misoriented subunits arising from groups of martensitic laths. Small regions of crystallographically related variants may be embedded in the main variant. These often have Σ3 or Σ11 boundaries. Wide variations in crystallographic packet sizes are possible, from less than a micron to the majority of the micrograph area.

No evidence of recrystallised structure can be seen; instead, even after 256 hours of tempering, the martensitic lath orientation relationships are preserved.

7.8 Statistical analysis

7.8.1 Grain boundary misorientations

The misorientation angles between adjacent points were calculated, and their distribution plotted, for both raw and cleaned data. Figure 7.26, Figure 7.27 and Figure 7.28 demonstrate that there is a wide variation of misorientations in the raw data. The cleaned data for the AQ sample have a variety of peaks, at low angles, 30°, 45° and 50–60° . After intermediate tempering, there is more consistency between data sets, and well-defined peaks are present at low angles, 30° and 50–60° (Figure 7.27). Prolonged tempering suppresses

the 30° peak (Figure 7.28). In the raw data, the indeterminate points contribute to the statistics of misorientations, and it is only by removing them that real relationships can be revealed. However, as discussed above, the cleaning algorithm is not infallible, especially when there are many indeterminate points, so the data from longer tempering times are probably more trustworthy than those from the AQ and 4 hour samples.

These observations agree well with those of Gourgues *et al.*, who also detected a peak at 60°.

7.8.2 Coincidence boundaries

Figure 7.29 shows the variation in the fraction of low-angle, Σ3 and random boundaries, as obtained from the cleaned data, with tempering time. In all of these specimens, the fraction of boundaries of any other type than these three is extremely small. Only one set of data was included for 128 hours because of the image shaking problem affecting the other sets. A decrease in the low-angle boundary fraction and an increase in Σ3 and random boundaries occurs during tempering. This may be a real phenomenon, or simply the result of the disappearance of spurious low-angle boundaries arising from indeterminate points and cleaning.

Low-angle and random boundaries are the predominant types, with a significant minority of Σ3. It can be seen by inspection of grain boundary maps that prior austenite boundaries are always random, and the internal structure of prior austenite grains contains many low-angle boundaries, some Σ3 and some random boundaries.

7.8.3 Statistics of indeterminate points

The number of indeterminate points in each image was quantified by generating an image similar to those in Figure 7.25 and converting it to a black-and-white image as shown in Figure 7.30. An image analysis program, 'ImageTool', was then used to determine the fraction of the image occupied by black points.

Figure 7.31 shows the relationship between the indeterminate point frac-
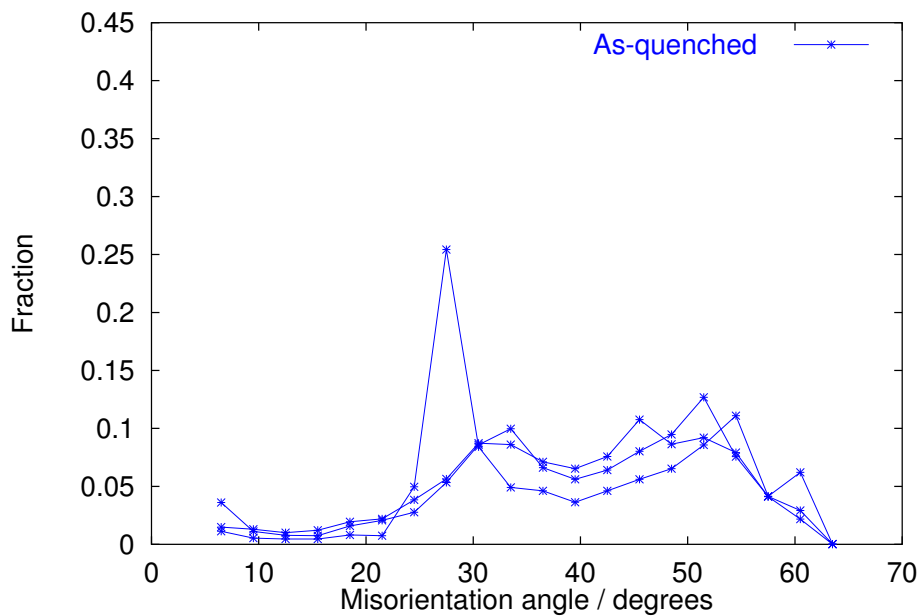
Raw data
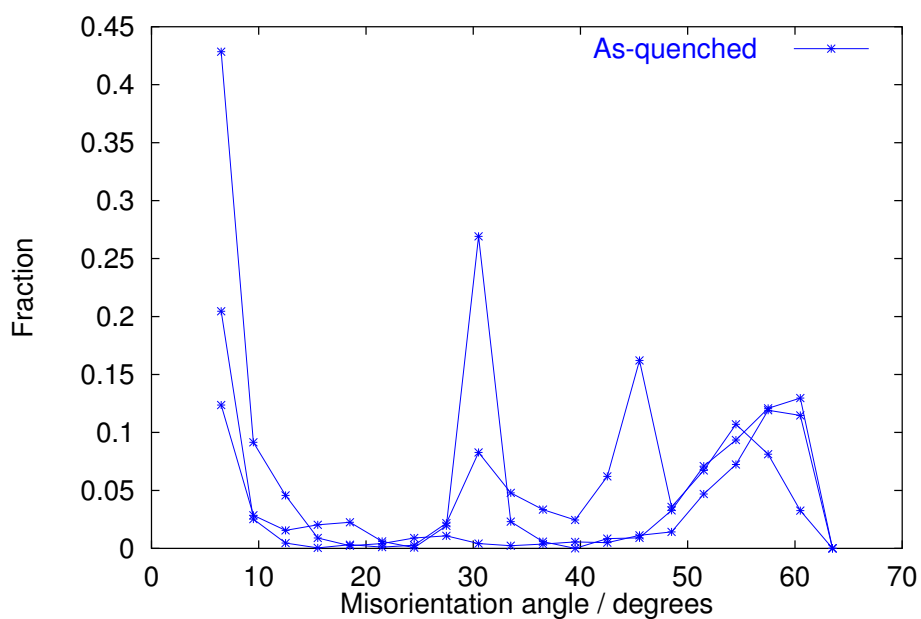
Cleaned data

Figure 7.26: Misorientation angle distributions for AQ data.

Raw data

Cleaned data
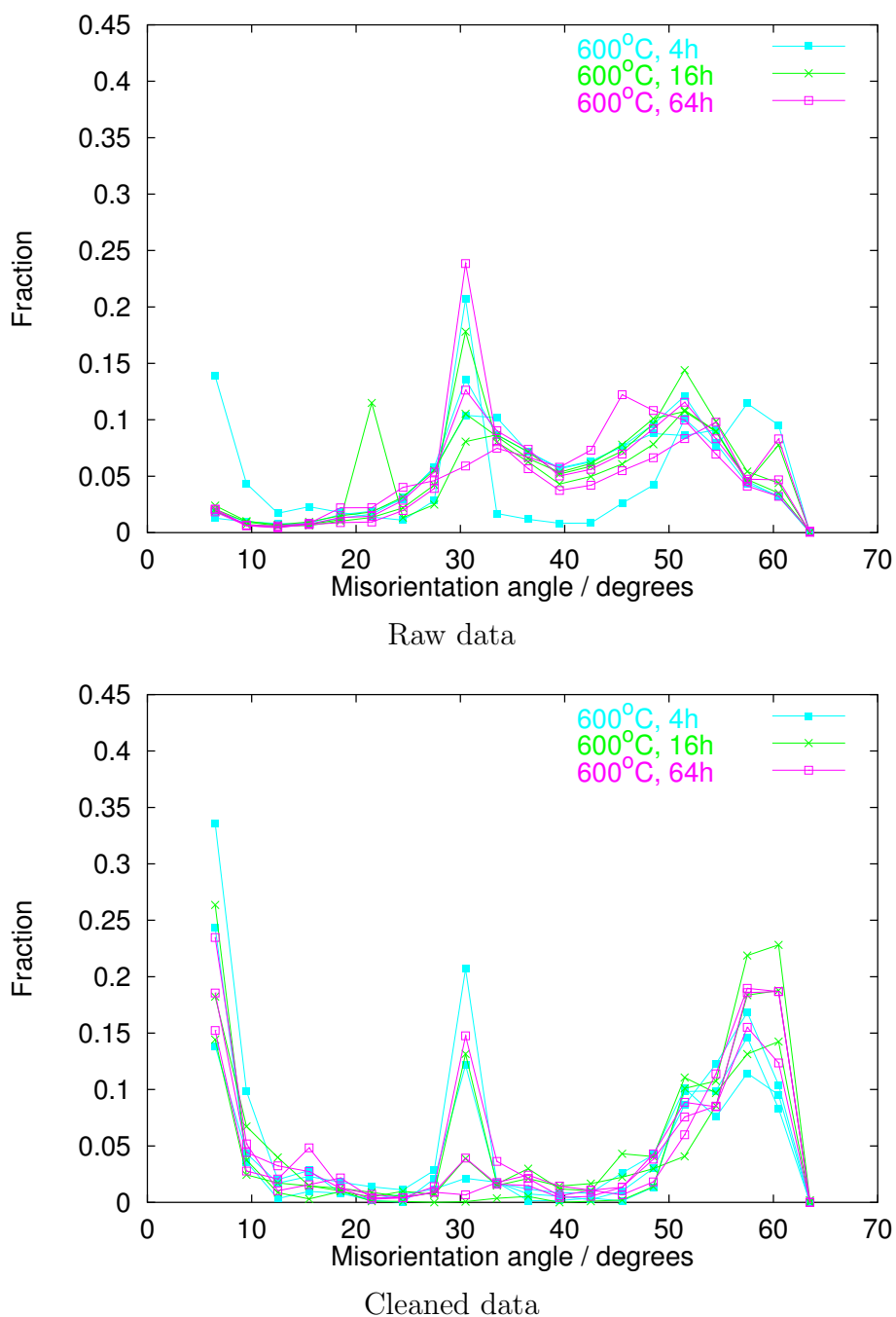
Figure 7.27: Misorientation angle distributions for intermediate tempering times (4–64 hours).
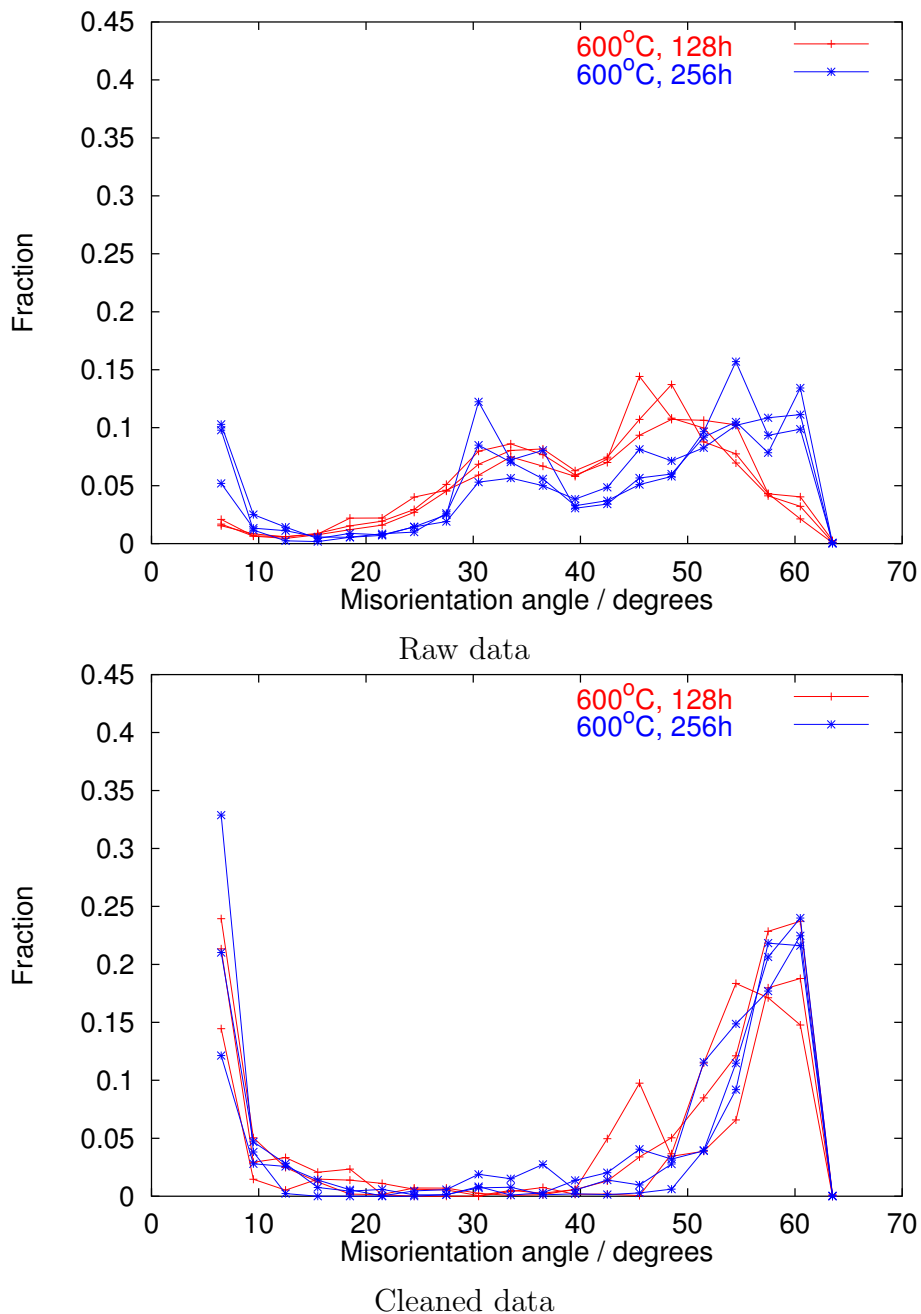
Figure 7.28: Misorientation angle distributions for prolonged tempering (128–256 hours).
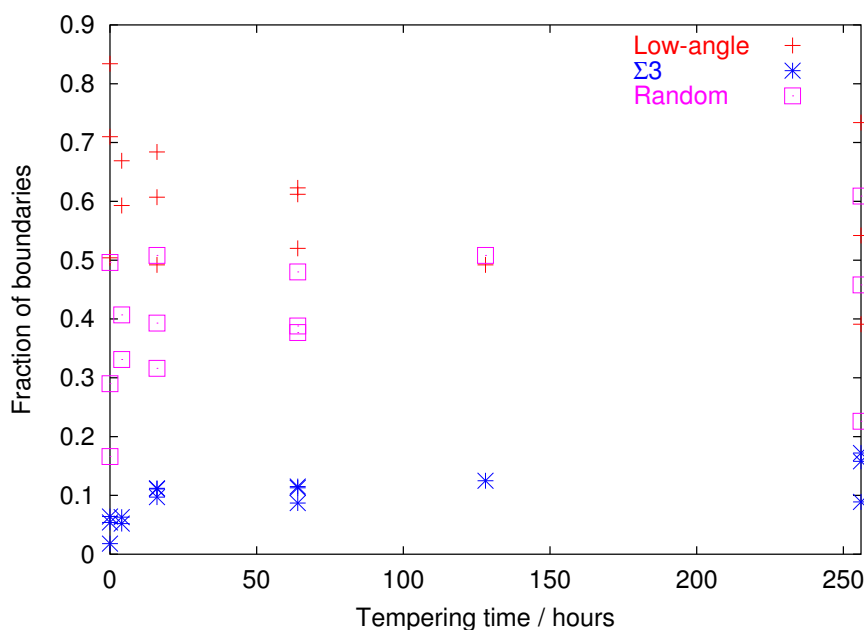
Figure 7.29: Variation in the fraction of low-angle, $\Sigma 3$ and random boundaries.

tion and tempering time. The two 128 hour images subject to shaking were again excluded. Large variations are seen in this fraction in the AQ and 4 hour samples, but at longer tempering times, a steady decrease is seen.

7.8.4　Image quality statistics

'ImageTool' was used to count the pixels of each grey level present in the IQ micrographs. Black is represented by zero, and white by 256. In the AQ samples, wide variations in grey level distributions are seen; dark levels predominate in two of the samples, but in the other, the levels are more evenly spread (Figure 7.32). A higher proportion of lighter greys is seen for intermediate tempering, and after prolonged tempering, there is a noticeable reduction in the proportion of dark levels (Figure 7.33). Grey level data are not fully quantitative, and variations can occur during data acquisition (Figure 7.15), but an indication of the strain reduction can be seen. The grey level data sets from different points on the 256 hour sample are very similar,

As-quenched   600 °C, 64 hours tempering

600 °C, 256 hours tempering
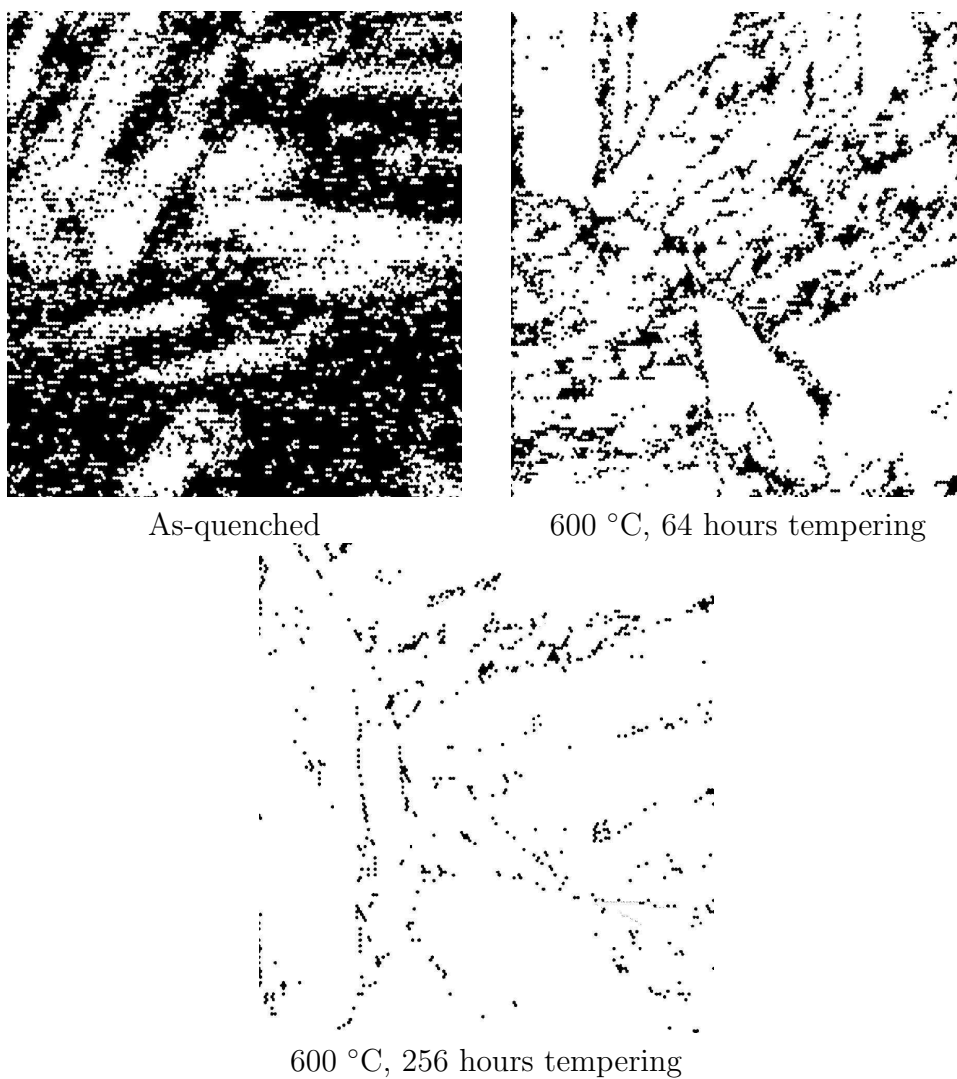
Figure 7.30: Evolution of the number of indeterminate points (in black) with tempering time.
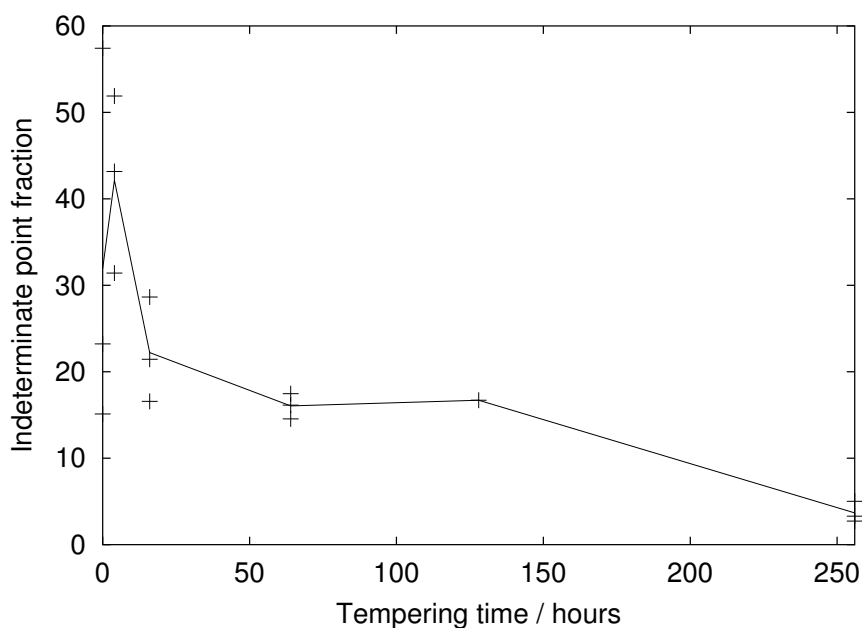
Figure 7.31: Variation in the fraction of indeterminate points.

so it appears that the strain level not only decreases but also becomes more homogeneous after prolonged tempering.

7.9   Orientation relationships

Two of the images, Figure 7.9 and Figure 7.22, come from regions within single prior austenite grains. The data sets for these images were selected for closer analysis. In addition to the individual point-by-point data, the software can calculate average orientation values for each region which it identifies as a grain. These data were used to study orientation relationships. (The alternative method, using adjacent points at grain boundaries to calculate misorientations, is subject to the problem of indeterminate points, as was seen above.)

Grey levels: As-quenched

Grey levels: Intermediate tempering
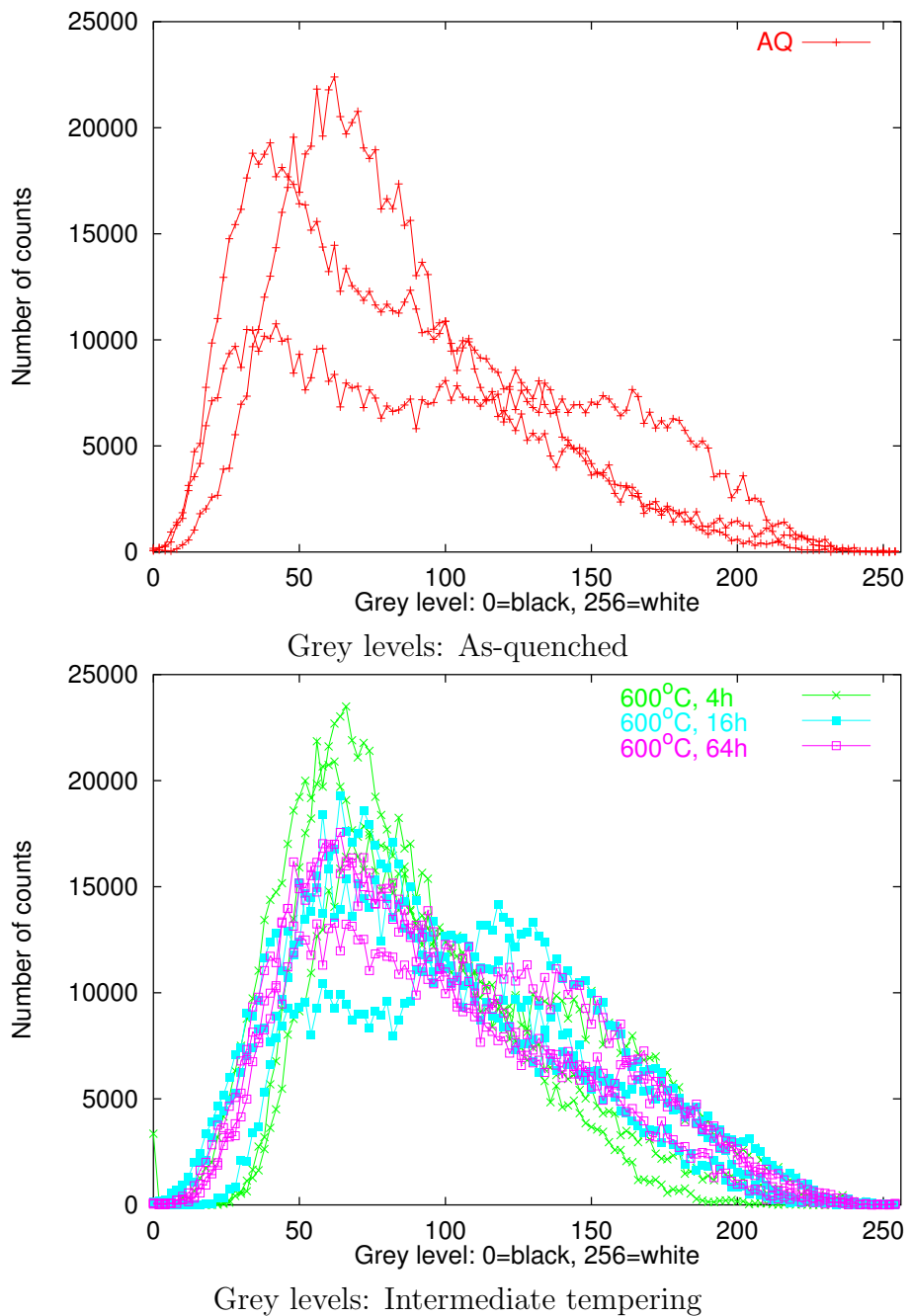
Figure 7.32: Grey levels in AQ and intermediate tempering samples.
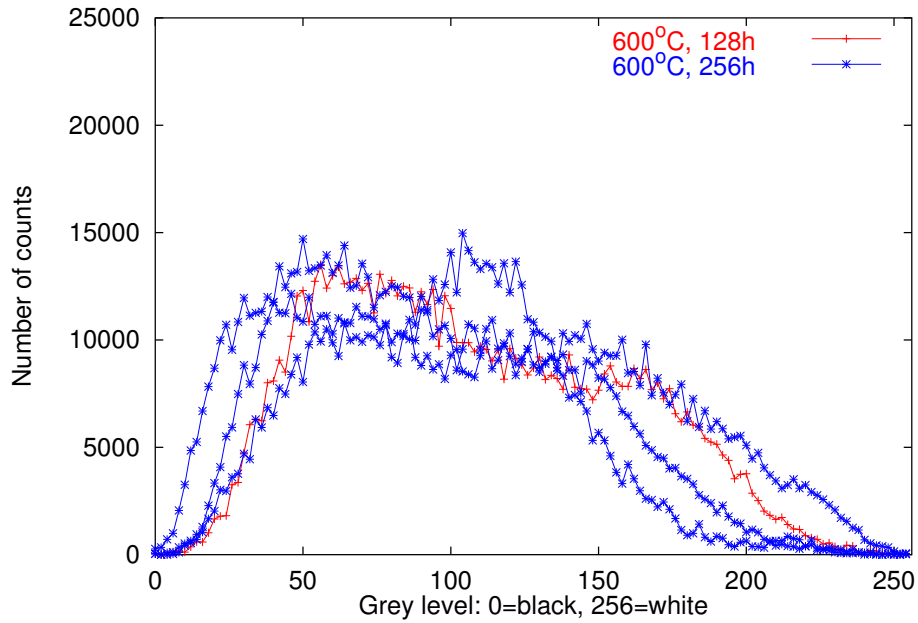
Figure 7.33: Grey levels for prolonged tempering.

7.9.1   256 hour sample

The Euler angles of the grains in the 256 hour sample, Figure 7.22, could easily be separated into six groups of similar values. Only one of the 160 distinct grains identified fell outside any of these groups. Table 7.1 lists the number-average Euler angles and the total area occupied by each of the groups. Orientation I occupies by far the greatest area; this is the large purple area in Figure 7.22. The areas of orientations II and III are also significant, but those of the remaining three groups are very small.

The closest Σ values for the interrelationships between these orientations were calculated using a program written by Dr K. Kawahara, Tohoku University. These are listed in Table 7.2 together with Brandon's ratio to quantify the deviation from exact coincidence. Orientation I has a near-$\Sigma 3$ relationship with four of the other orientations. II and III had an angle-axis pair of 46°<0.03, -0.86, -0.49> rather than 60°<111>. Some relationships close to 46°<0.03, -0.86, -0.49> were also found between other pairs of orientation components. (These are not shown in Table 7.2.)

No.	$\phi1$	Φ	$\phi2$	Area / μm^2
I	334.5	37.3	49.9	187.4
II	230.3	23.3	101.2	7.4
III	100.8	20.6	250.9	4.6
IV	158.5	36.4	218.6	1.0
V	47.2	38.2	301.7	0.3
VI	279.5	38.2	62.5	0.02

Table 7.1: Orientation components found in 256 hour tempered sample.

Pair		Relationship	Brandon's ratio
I	II	$\Sigma3$	0.93
I	III	$\Sigma3$	0.80
II	III	$\Sigma15$	0.97
I	IV	$\Sigma3$	0.70
I	V	$\Sigma3$	0.82
I	VI	Random	2.00 from $\Sigma3$

Table 7.2: Relationships between different orientations in 256 hour tempered sample.

7.9.2   AQ sample

The AQ data in Figure 7.9 contained four main Euler angle sets (Table 7.3). The relationships between these show that I and II are very similar in orientation, as are III and IV (Table 7.4). It is clear from the area fractions that I and II constitute the large turquoise area, and III and IV the red area. The relationships between the two pairs are $\Sigma3$, or close to this. Grains with other Euler angle values were present in this data set, but these had very low image quality values, and were therefore not investigated.

While it is not possible to draw general conclusions from data on such small areas, these results do agree with the observations of Gourgues *et al.* (2000) of the frequent occurrence of near-$\Sigma3$ relationships. A suggestion of the possible arrangements of structural components is given in Figure 7.34.

No.	$\phi1$	Φ	$\phi2$	Area / $\mu\mathrm{m}^2$
I	64.3	39.2	338.8	123.2
II	214.2	48.5	114.4	10.6
III	291.3	5.3	69.8	7.9
IV	335.8	8.7	32.1	5.1

Table 7.3: Orientation components found in AQ sample.

Pair		Relationship	Brandon's ratio
I	II	$\Sigma1$	0.56
I	III	$\Sigma3$	0.75
I	IV	Random, near $\Sigma3$	1.21 from $\Sigma3$
II	III	$\Sigma3$	0.72
II	IV	$\Sigma3$	0.90
III	IV	$\Sigma1$	0.60

Table 7.4: Relationships between different orientations in as-quenched sample.

7.10   Relationship to magnetic properties

In the $2\frac{1}{4}$Cr1Mo samples of Moorthy *et al.* (1997b, 1998, 2000), recrystallisation began to occur after prolonged tempering at 650°C. In this study, however, there was no recrystallisation. The clear lath structure in the AQ sample disappeared during tempering, but orientation relationships between microstructural components appeared to remain constant. The most obvious change was the reduction in strain evident from the increase in image quality.

The effect of such a structure on magnetic properties depends on whether domain walls interact more strongly with strain, or with the magnetostatic energy arising from misorientations at grain boundaries.

If strain is more important, domain walls in the AQ sample will undergo a large number of pinning and unpinning events, with a short mean free path. Within a single variant, if the domain walls are oriented parallel to the lath lengths, the mean free path will be of the order of the lath width. After tempering, the interlath strain energy decreases and the laths coalesce into a continuum with slight orientation variations. This would allow easier
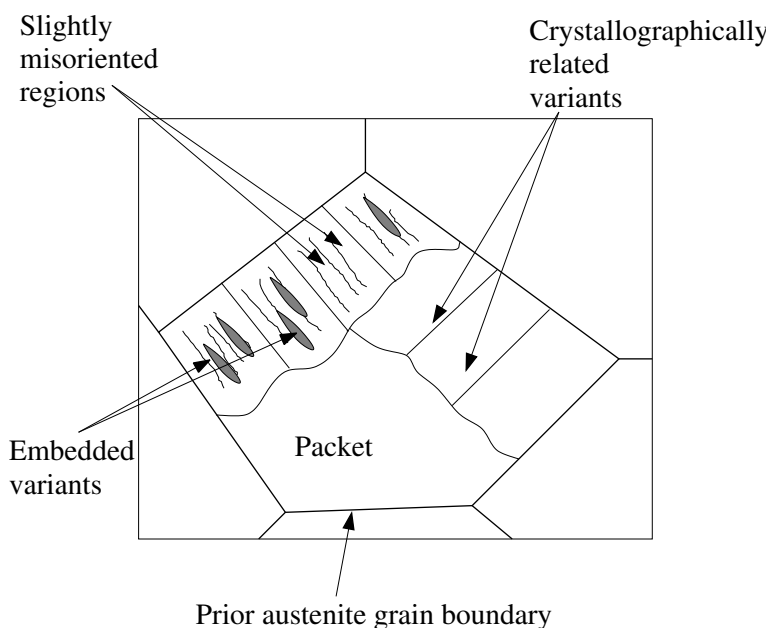
Figure 7.34: Possible levels of structure in 2.25Cr1Mo wt. % martensite, as deduced from OIM observation.

passage for domain walls; the main obstacles to their motion would be block, packet and prior austenite grain boundaries. However, tempering also causes the precipitation of carbides, which pin domain walls. In these samples, the strain reduction appears to be gradual rather than sudden, so the changes in BN peak shape and position may be rather smaller than those observed by Moorthy *et al.*

If, instead, misorientations are more important in domain wall pinning, there would be very little difference between the behaviour of domain walls in the AQ and tempered samples apart, perhaps, from the effect of carbides.

7.11   Conclusions

OIM observations of as-quenched and tempered $2\frac{1}{4}$Cr1Mo have been made. The most pronounced effects of tempering were a reduction in the lattice strain, and an increase in the number of points from which a diffraction pattern can be indexed with confidence by the software. This was attributed

to a decrease in strain due to a reduction in dislocation density at grain and lath boundaries.

Prior austenite grain boundaries were always random, and within the prior austenite grains a combination of low-angle, $\Sigma 3$ and random boundaries occurred. Individual crystallographic packets contained many slightly misoriented groups of laths. Variants related by $\Sigma 3$ were found; in some cases one variant was found in small regions embedded in large areas of another variant.

An estimation of the likely effect of these tempered mirostructures on BN has been made, and will be tested in Chapter 8.

Chapter 8

Barkhausen Noise Experiments on Power Plant Steels

8.1 Experimental Method

8.1.1 Sample Preparation

The samples for BN testing were prepared as described in § 6.1. A 2% nital etch was used for the $2\frac{1}{4}$Cr1Mo steel samples, and a Kalling's No. 2 etch for the 11Cr1Mo samples.

8.1.2 Instrumentation

The BN measurements were taken at the University of Newcastle Design Unit under the supervision of Dr V. Moorthy, using a commercially available 'μSCAN 500' testing machine manufactured by Stresstech Oy - AST (Figure 8.1). Such instruments are used routinely in industry for a variety of nondestructive testing applications, such as detecting residual stresses at surfaces (Stresstech, WWW site). Figure 8.2 is a schematic diagram of the measurement system. The BN unit generates a sinusoidally varying current which, after amplification and filtration, is supplied to a coil wound around a yoke made of a ceramic ferrite material. The yoke is placed directly onto the sample, taking care to ensure good contact between the sensor and the surface. A pickup coil, wound around a core of the same ceramic ferrite, acquires the BN voltage signal, which is amplified and filtered. The unit is

connected to a standard PC with purpose-written software installed. This is used to control the magnetising current and analyse the output.
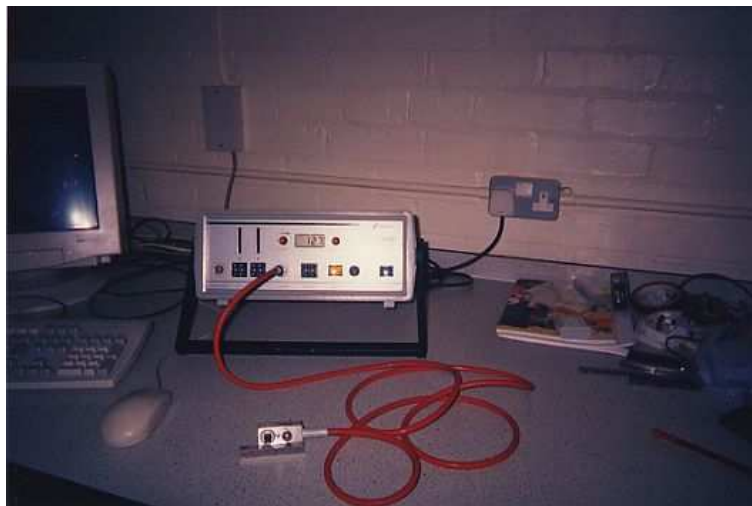
Figure 8.1: BN testing unit at the University of Newcastle.

The yoke and pickup apparatus constitute a commercially available sensor produced by the manufacturers of the BN unit (Figure 8.3). However, the core and the vertical pieces of the yoke can be removed and replaced.

8.1.3 Operating Conditions

Two modes of operation have been designed by the manufacturers of the instrument: 'microscan' and 'rollscan'. The former enables the application of excitation frequencies up to 125 Hz, and uses a hardware filter which allows output frequencies between 0.3 and 2.5 MHz. The latter permits excitation frequencies up to 30 Hz and output frequencies between 3 and 15 kHz. In this series of experiments, the 'rollscan' mode was used, with an excitation frequency of 4 Hz, since this was found by Moorthy *et al.* (2001) to give the optimal combination of signal amplitude and peak fine structure resolution on this instrument.

The applied magnetising current used was ±0.7 A. (The instrument does not automatically translate this into an applied field.) A suitable signal

amplification, which gave a visible signal for the full range of samples investigated, was 30 dB. Signals obtained at different amplifications cannot be compared with complete certainty (Blaow, personal communication), so it was necessary to use the same value throughout.

Signal Analysis

Figure 8.4 is a screenshot showing the sinusoidal excitation current in blue, and the resulting noise signal in black. Data were acquired over four current cycles. In Figure 8.5, the rectified average of the forward (increasing-field) and reverse (decreasing-field) directions can be seen. Smoothed curves have also been plotted. The degree of smoothing can be controlled by the operator but in these experiments, the default settings were used.

The two smoothed signals are plotted on the same axes in Figure 8.6. The forward and reverse signals should be mirror images of one another. If there is asymmetry, this indicates that the sample was magnetised in one direction prior to testing. If this is the case, it is passed across a demagnetiser, which produces a rapidly oscillating field, several times and then the BN measurement is conducted again. If necessary, this process is repeated until a symmetrical signal is obtained (Moorthy, personal communication).

The software can be used to 'filter' the signal by displaying only the noise occurring within a particular frequency range. This facility was used for the analysis in § 8.3.
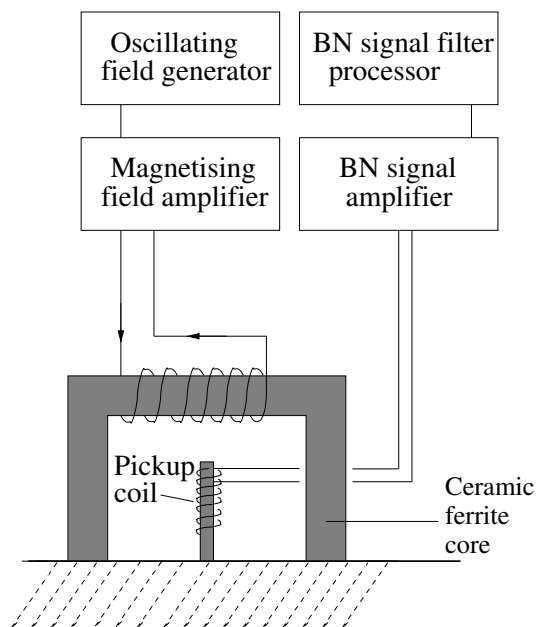
Figure 8.2: Schematic diagram of BN measurement equipment (after Blaow, 2001).
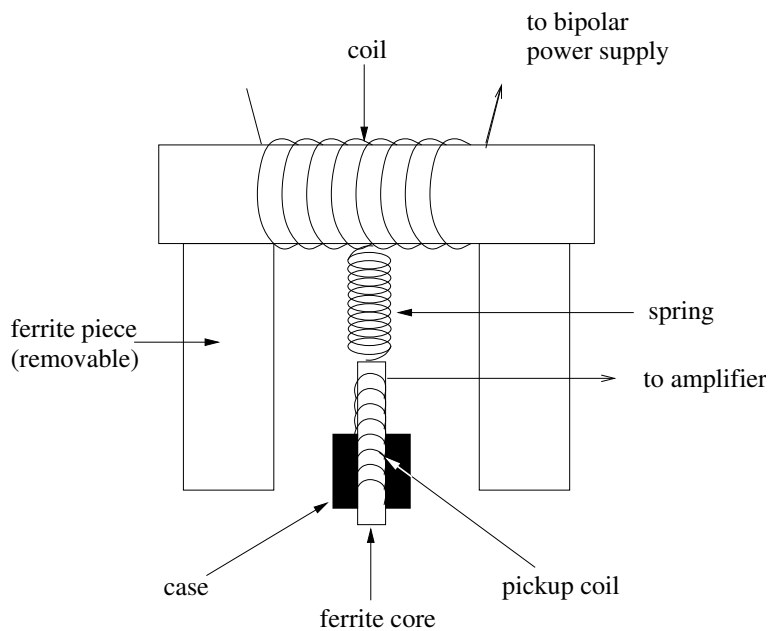
Figure 8.3: Schematic diagram of BN sensor.
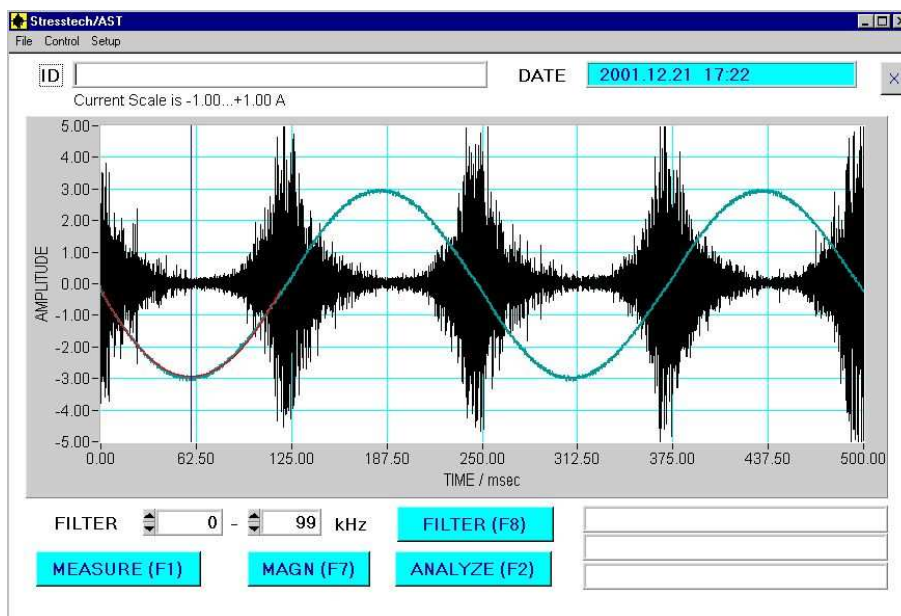
Figure 8.4: Screenshot from the software used at the University of Newcastle, showing the raw noise and magnetising current. This diagram and Figures 8.5 and 8.6 supplied by M. Blaow.
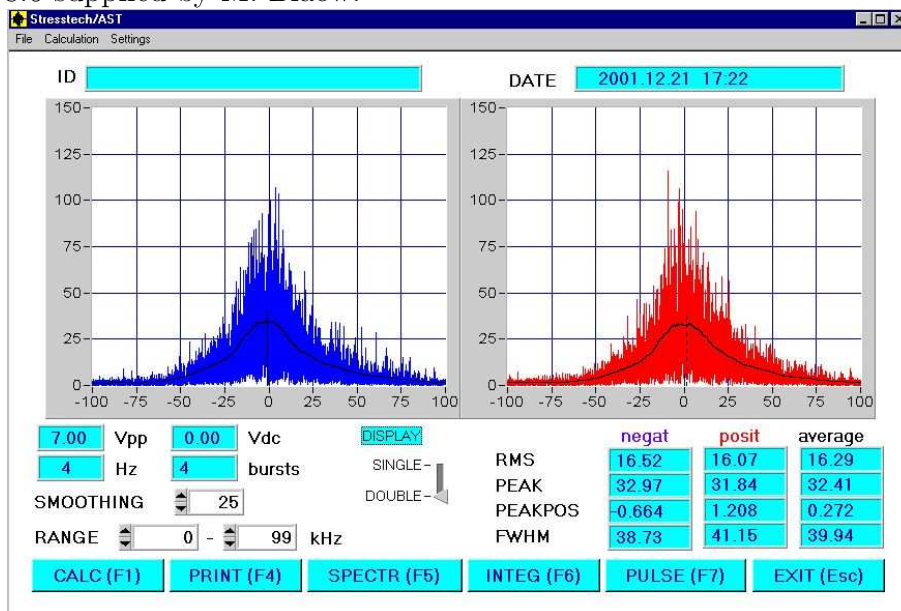
Figure 8.5: Screenshot showing the forward and reverse rectified BN.
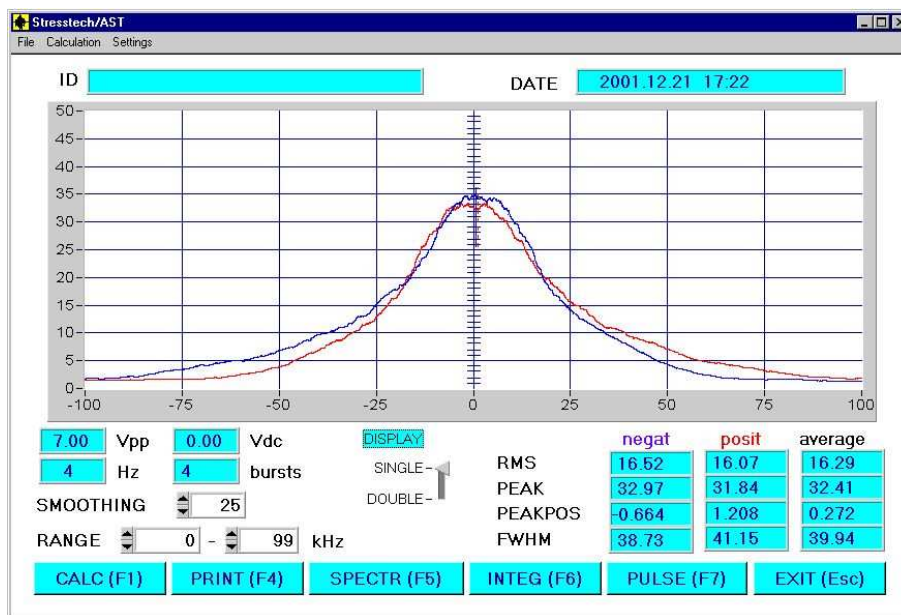
Figure 8.6: Screenshot showing the forward and reverse signals on the same axes.

8.2   Results

The rectified and smoothed BN signals were plotted against magnetising current for each of the samples tested. In each case, only the forward direction has been shown, since the reverse signal is almost identical. The scale on the horizontal axis is the applied magnetising current, and the vertical scale, quantifying the noise voltage, is given as a percentage of 5 V. These scales tend to be regarded as rather arbitrary, and not to be compared with the output from testing equipment with different geometries (Moorthy, personal communication).

500°C tempering

Figure 8.7 and Figure 8.8 show the BN signals for samples tempered at 500°C. On both graphs, the as-quenched (AQ) peak is shown for comparison.

For all the tempered specimens, the peaks are higher than for AQ. There appears to be a trend towards higher, narrower peaks with higher tempering time, but there is some scatter in this. The dramatic peak height increase between AQ specimens and those tempered even for a short time agrees well with the behaviour observed by Moorthy *et al.* in their tempering experiments. The onset of Barkhausen activity occurs at a lower current in the tempered sample than in the as-quenched sample in all cases.

Samples tempered for longer times (Figure 8.8) show much less variation in BN peak shape and position than those tempered for shorter times (Figure 8.7). In all the 500°C samples, an approximately symmetrical peak centred at a current of around 0.1 A is followed by a change in slope near 0.2 A, giving a gradual decrease of noise at high current.

600°C tempering

Figure 8.9 and Figure 8.10 show the noise signals from samples tempered at 600°C, with the AQ signal for reference. The maximum peak height observed in this series is larger than in the 500°C series.

The peak heights do not show much variation, apart from the peak at 256 hours, which is significantly higher than the others. The shape of the

32 hour peak seems anomalous.

The onset of noise occurs at a lower current in this set of samples than in the 500°C samples. The 600°C peaks are rather broader than the 500°C peaks, and enclose a larger area. However, the curve shapes may still be interpreted as an initial peak followed by a slope change to a less steep slope.

700°C tempering

Peaks from samples tempered at 700°C (Figure 8.11) are significantly broader than those from lower tempering temperatures; more activity occurs both at currents below zero and at high currents. There is no obvious trend between peak height and tempering time, or between peak position and tempering time.

Long-term 11Cr1Mo wt. % samples

The peak occurs at a noticeably higher current for the 11Cr1Mo samples (Figure 8.12) than for the tempered $2\frac{1}{4}$Cr1Mo steels, as illustrated by comparison with the $2\frac{1}{4}$Cr1Mo AQ peak. The peak heights are mostly smaller than those for tempered $2\frac{1}{4}$Cr1Mo steel, but there is no obvious systematic variation of height with tempering time.

8.2.1   Peak height, width and position

For each data set, the maximum height, the full width half maximum (FWHM), and the position on the applied current axis of the maximum height, were determined and plotted against tempering time (Figure 8.13, Figure 8.15 and Figure 8.17).

The Larson-Miller parameter P can be used to relate tempering time and temperature conditions on the same scale:

$$P = T(C + \log t) \tag{8.1}$$

where T is the absolute temperature (in K), t is the time in hours, and C is a constant with a value around 20.

The BN peak height, FWHM and position were plotted against P, which was calculated with $C = 16.7$ (Figure 8.14, Figure 8.16 and Figure 8.18).

There is no clear relationship between peak height and tempering time (Figure 8.13) but the $2\frac{1}{4}$Cr1Mo steel values increase approximately linearly with P, while the 11Cr1Mo values fall into a different regime (Figure 8.14). Similarly, there is a more obvious relationship of FWHM with P than with time, although some outliers are present (Figure 8.16).

The most obvious trend in these data is the decrease in peak position with P (Figure 8.18), which is followed by all the $2\frac{1}{4}$Cr1Mo steel values. The 11Cr1Mo steel values are again in a different regime.
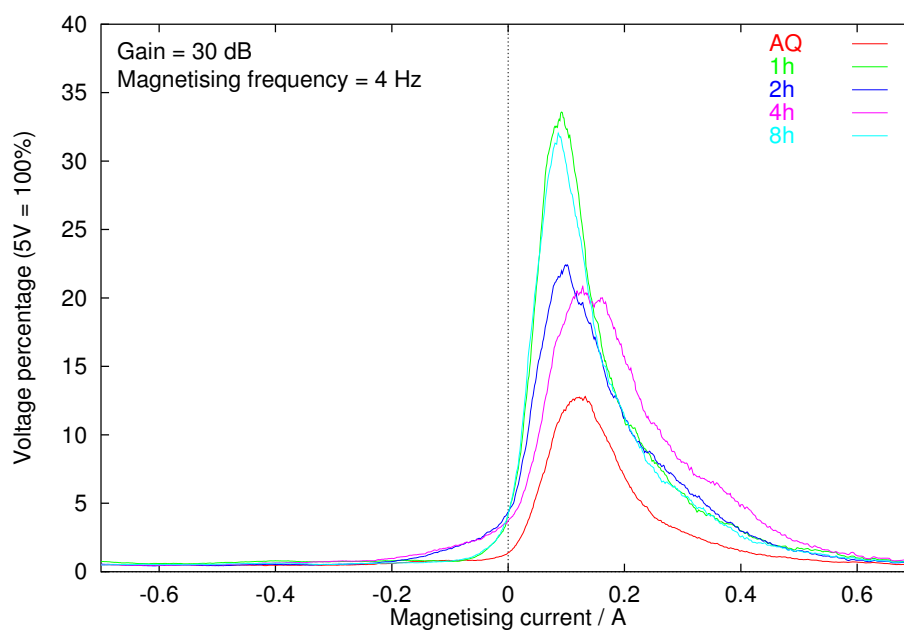
Figure 8.7: BN voltage versus magnetising current for samples tempered at 500°C (1–8 h).
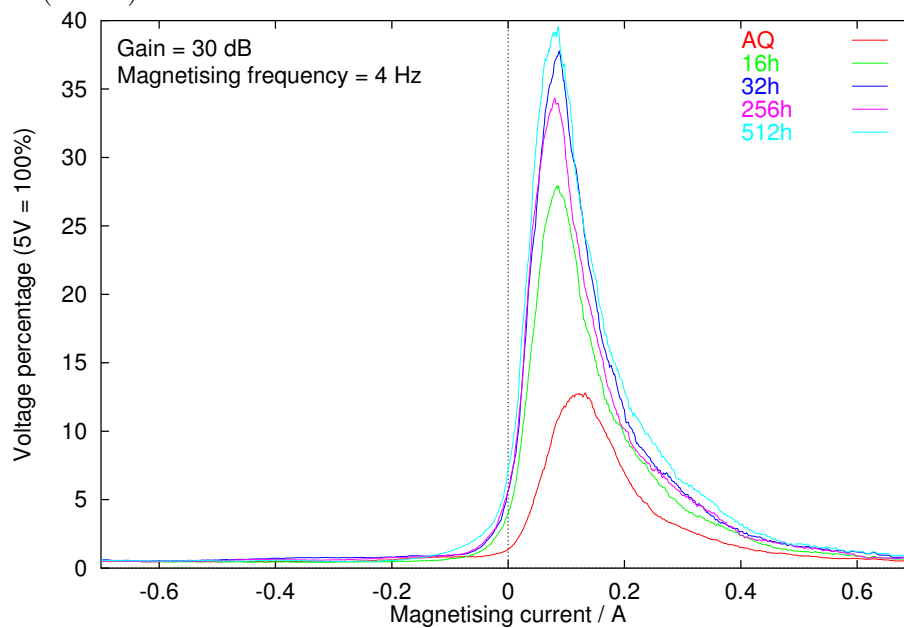
Figure 8.8: BN voltage versus magnetising current for samples tempered at 500°C (16–512 h).
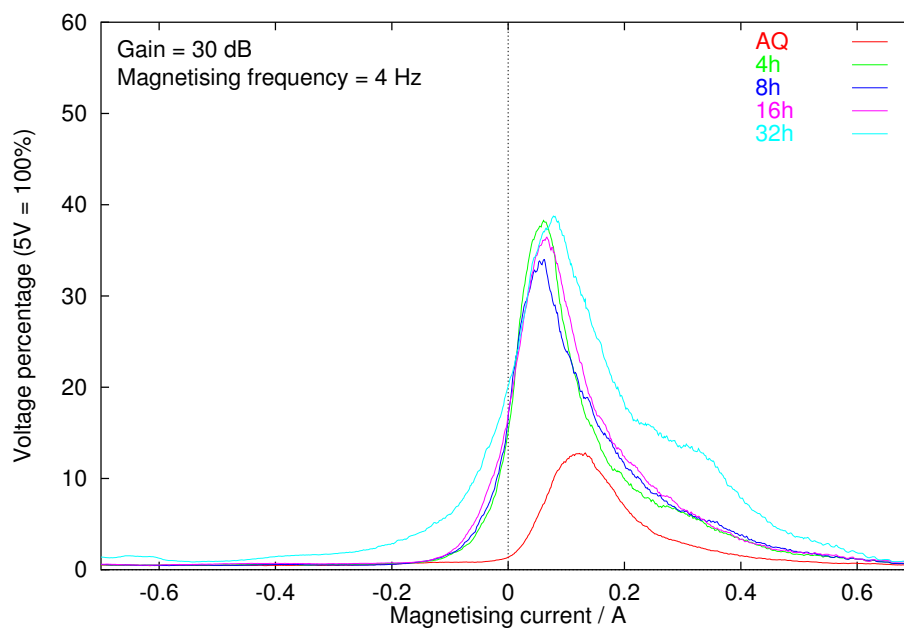
Figure 8.9: BN voltage versus magnetising current for samples tempered at 600°C (1–32 h).
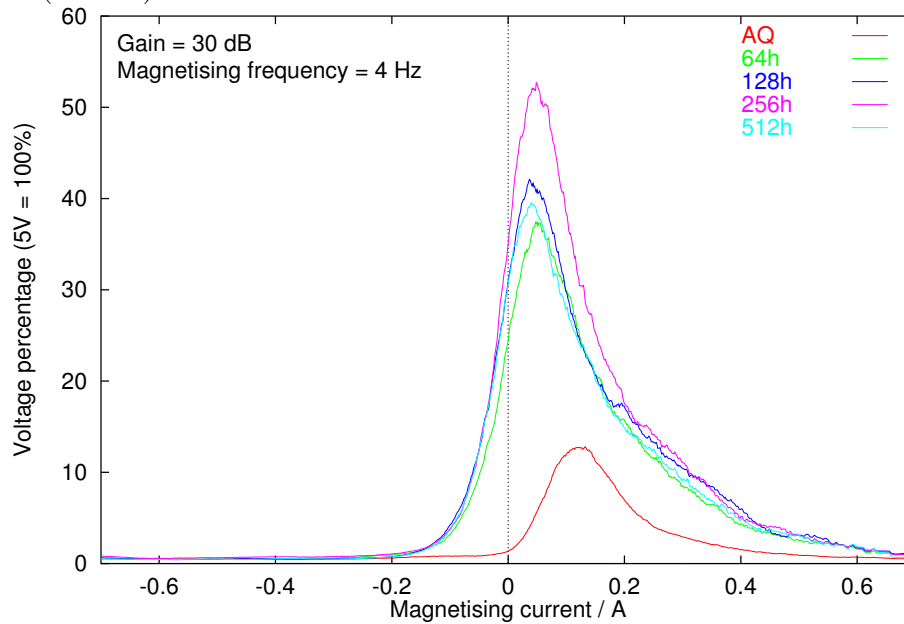
Figure 8.10: BN voltage versus magnetising current for samples tempered at 600°C (64–512 h).
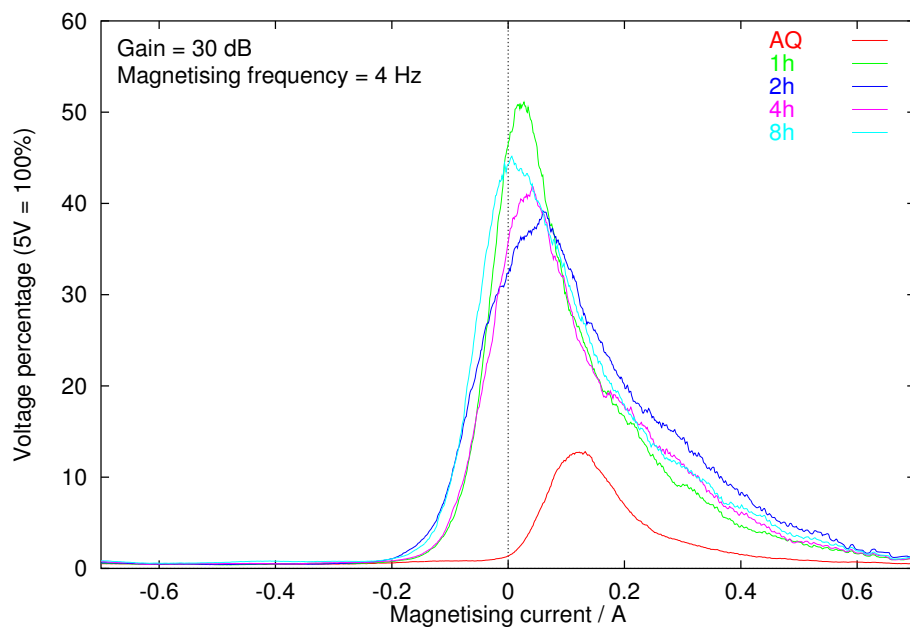
Figure 8.11: BN voltage versus magnetising current for samples tempered at 700°C.
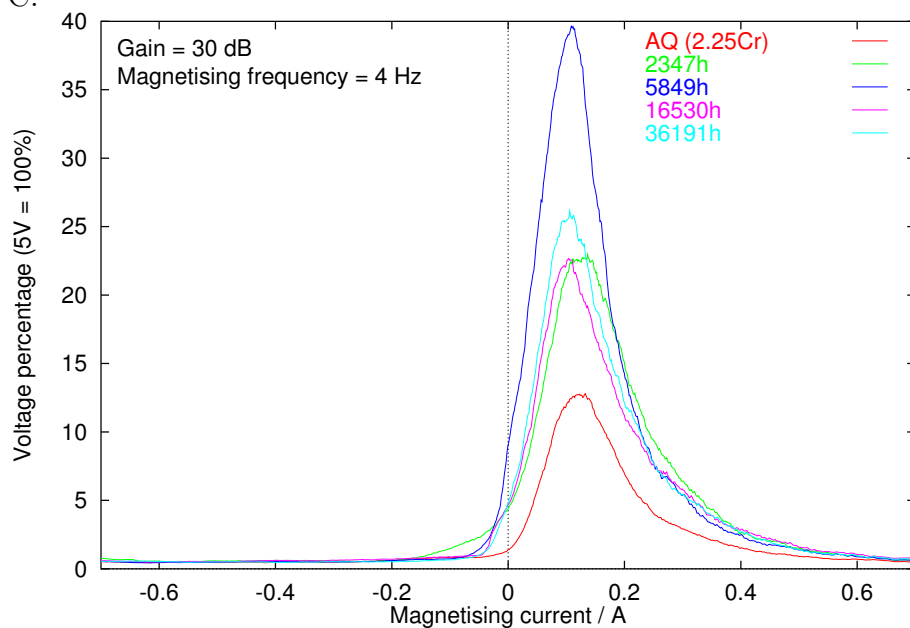
Figure 8.12: BN voltage versus magnetising current for 11Cr1Mo wt. % specimens.
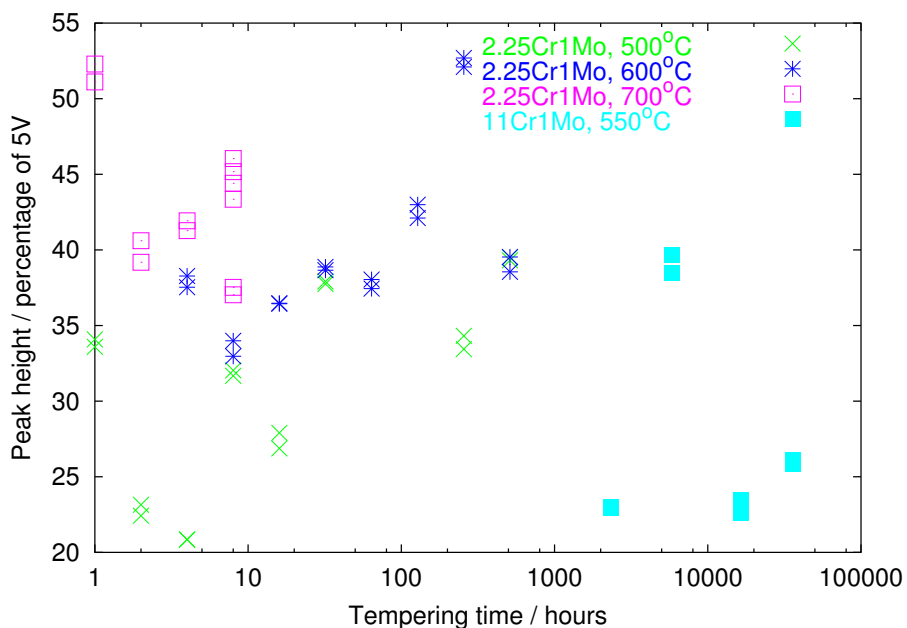
Figure 8.13: BN peak height versus tempering time.
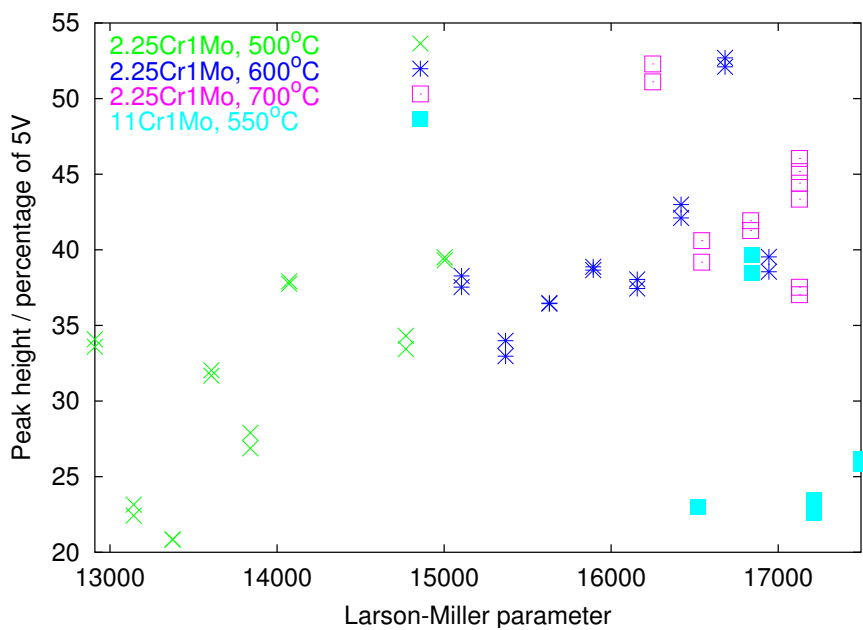
Figure 8.14: BN peak height versus Larson-Miller parameter.
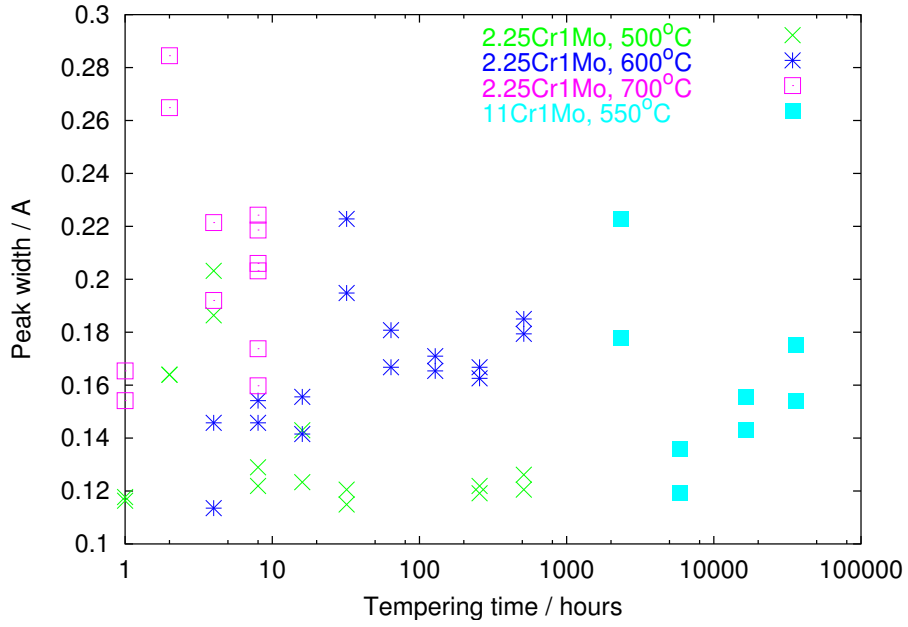
Figure 8.15: BN peak width (FWHM) versus tempering time.
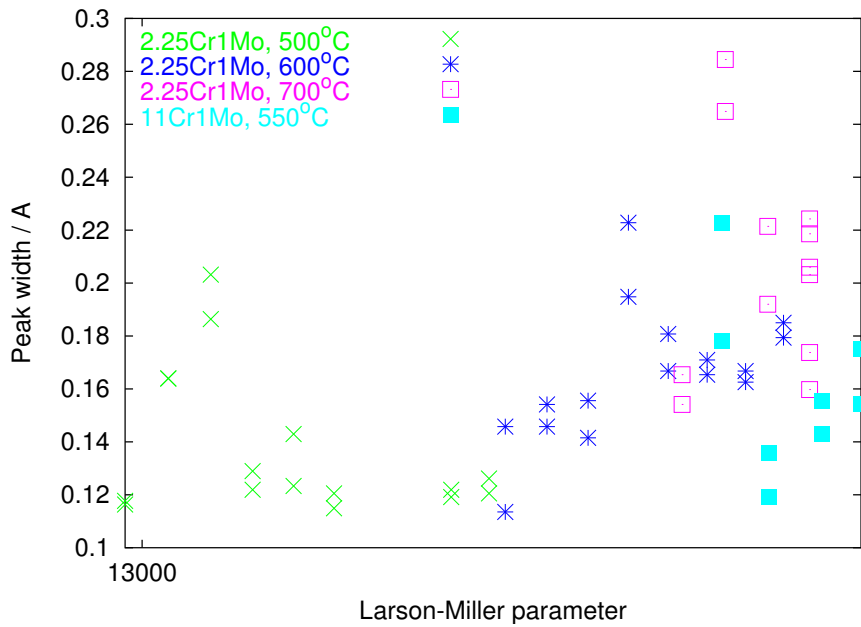
Figure 8.16: BN peak FWHM versus Larson-Miller parameter.
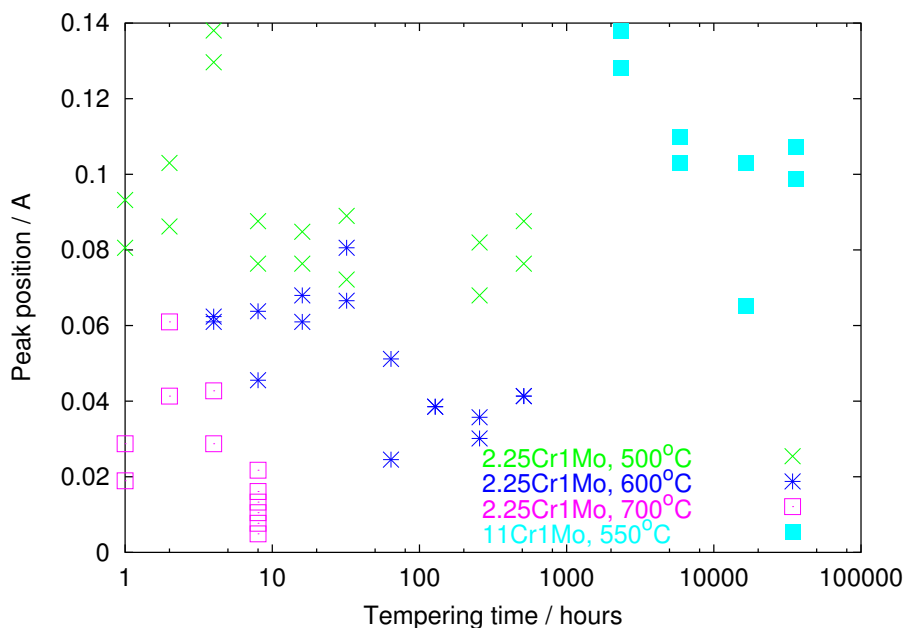
Figure 8.17: BN peak position versus tempering time.
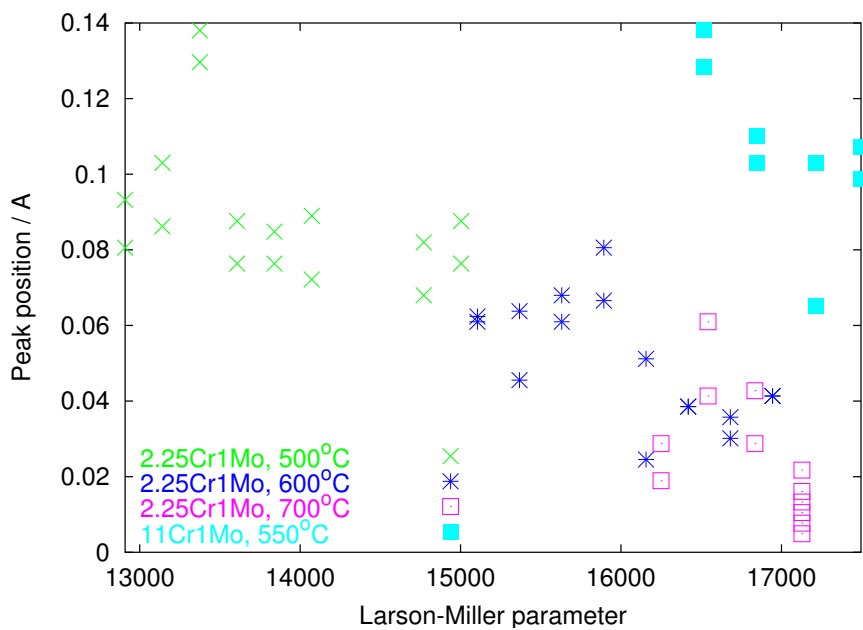
Figure 8.18: BN peak position versus Larson-Miller parameter.

8.2.2   Comparison with results of Moorthy *et al.*

Figure 8.19 shows a selection of the results obtained here together with some results on a $2\frac{1}{4}$Cr1Mo steel obtained by Moorthy *et al.* (1998, 2000) using apparatus of type (a) in Figure 4.2; the University of Newcastle apparatus is of type (b). The tempering temperatures are not the same in the two cases because the present work was intended to be complementary to those of Moorthy *et al.* rather than repeats of the same experiments. Also, Moorthy *et al.* did not quench their samples. The actual amplitudes of the noise signals measured depend on such factors as experimental geometry and signal amplification, so it is not possible to compare the values directly, and they are plotted on different vertical axes. However, the range of values on the horizontal axis should be the same since the current varies within the same range.

In the results of Moorthy *et al.*, the noise peaks occur at higher currents. The two sets of results are consistent in that the peak becomes higher, and moves to a lower current, after tempering. The change in height on tempering is more pronounced in the results of Moorthy *et al.* than in this study. The AQ peak from this study and the normalised peak of Moorthy *et al.* are similar in shape, but the tempered sample peak shapes in the present study are much less symmetrical than the Moorthy *et al.* peaks. The peak height changes seen by Moorthy *et al.* are much more dramatic than those in Figure 8.9, Figure 8.10 and Figure 8.11. Some of these differences can be accounted for by the greater severity of tempering in the Moorthy *et al.* experiment[1]. However, the comparative positions of the AQ and normalised peaks suggest that there is also some influence from the apparatus configuration.

The double-peak behaviour observed by Moorthy *et al.* at long tempering times is completely absent in all the measurements made in this study. This may be because 600°C is too low a temperature to produce this behaviour even at long tempering times, while the tempering at 700°C was carried out

---

[1]The highest Larson-Miller parameter value in the Moorthy *et al.* study was just under 18000, whereas the highest value in the present study was 17000.
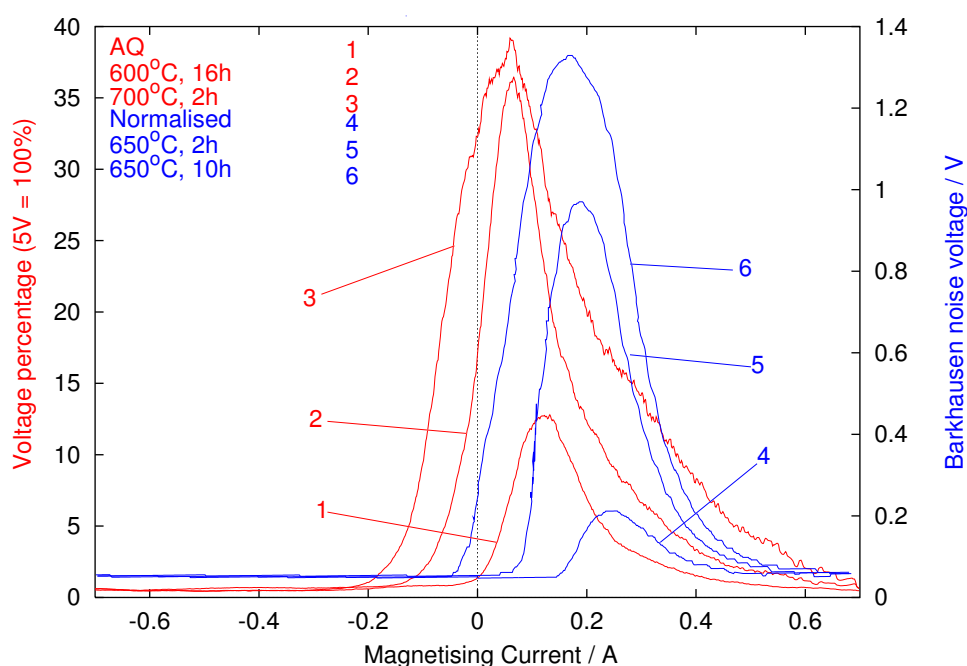
Figure 8.19: A comparison between results obtained in this study (red) and results obtained by Moorthy *et al.* (1998, 2000) (blue).

for too short a time for double peaks to be seen. An alternative explanation is that double-peak behaviour should be present in some of the samples, but it is suppressed because the noise contributing to the second peak is at a frequency which is filtered out. Previous work at the University of Newcastle using this apparatus suggests that the second explanation is possible (Blaow, personal communication).

8.2.3   Experiments on tempered plain-carbon steel

Double-peak behaviour in tempered plain-carbon steels has been observed in a number of investigations (Buttle *et al.*, 1987c; Kameda and Ranjan, 1987a; Moorthy *et al.*, 1998). The capacity of this apparatus to detect a second peak can therefore be tested using samples of a steel which is known to produce double peaks when tested with other apparatus.

Three samples of a water-quenched 0.1 wt. % C steel were tested. One

of these had been tempered for 0.5 hours, and another for 100 hours. Two measurements were taken on each sample. In Figure 8.20, a clear difference in peak position can be seen between the AQ and the tempered samples. There is no second peak visible in any of the signals, but the tempered samples show a slope change, which is absent in the AQ signal, after the initial peak. This may be equivalent to the slope changes seen in the tempered $2\frac{1}{4}$Cr1Mo steels: the only manifestation of high-current activity visible with this apparatus.

It is interesting to note the large difference in peak height from the two measurements on the AQ sample. This may be due to large-scale inhomogeneities in the AQ microstructure such as those observed using OIM (Chapter 7), or it may be indicative of a lack of repeatability with this apparatus.
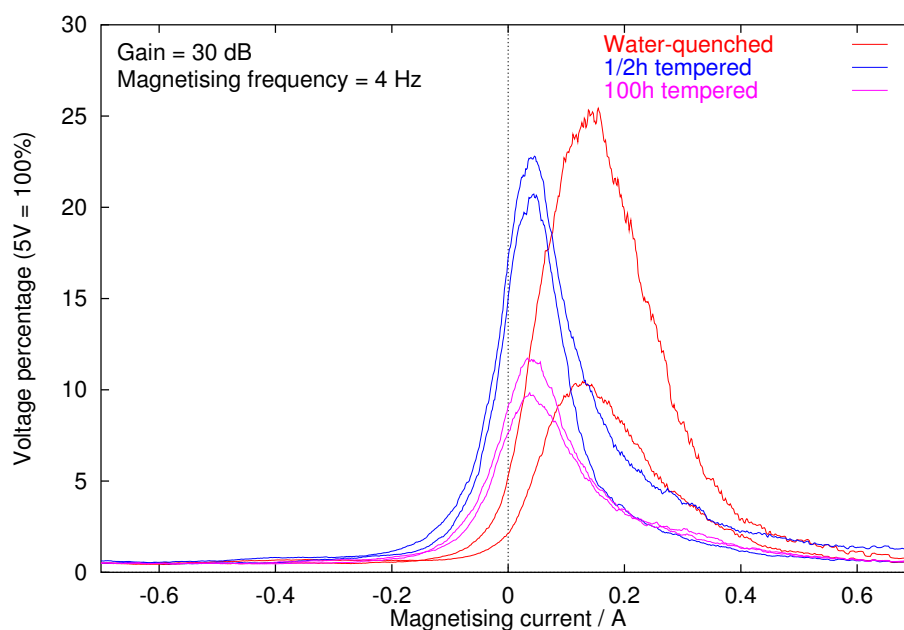
Figure 8.20: Plain-carbon steel tempering

The evidence from this experiment supports the suggestion that the apparatus would suppress any double peaks which should be present. However, this does not in itself confirm that a given sample should display a second peak as opposed to a change in slope. In order to investigate this question, the noise frequency of different samples and the shape of the noise signal

within particular frequency ranges was investigated.

8.3   Frequency analysis

The filtering hardware used by the Barkhausen measurement system in the 'rollscan' mode suppresses frequencies above 15 kHz and below 3 kHz, using a trapezium-shaped filter (Figure 8.21). However, it is believed that some interesting microstructural information is contained in the part of the signal below 3 kHz (Moorthy, personal communication).

Frequency content of the noise signal

Figure 8.22 shows the signals for the AQ sample and the shortest and longest tempering times at 500 and 700°C. The 'amplitude' on the vertical axis is the sum of the amplitudes of all the noise pulses occurring at a particular frequency.

For all the samples, the signal reaches its greatest amplitude near the centre of the unfiltered region (3–15 kHz). There is almost no noise at frequencies below 1 kHz, then a sharp peak at around 2 kHz. This occurs in all BN measurements and is believed to be an artefact of the measuring process (Moorthy, personal communication). The noise amplitude increases steeply between 2 and 3 kHz but decreases much more slowly beyond 15 kHz. The AQ signal has the smallest amplitude throughout the frequency range. For 500°C tempering, the amplitude is higher but there is no noticeable difference between the longer and shorter tempering times. The 700° samples have a higher amplitude, and a small amplitude increase is visible between the 1 hour and 8 hour data. Yamaura *et al.* (2001), in a similar analysis on pure iron, observed large peaks at 3 and 60 kHz but no such structure is visible here, possibly because of the narrowness of the filtering window.

It appears that frequencies below 3 kHz are more severely attenuated than those above 15 kHz with this filter. The discrepancies between the data obtained with this apparatus and those in the literature are therefore probably attributable mainly to the absence of the lower-frequency part of the signal.
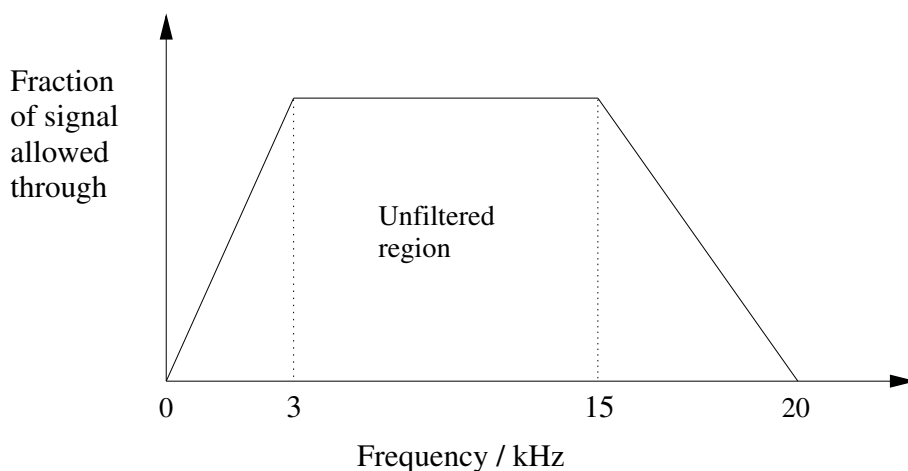
Figure 8.21: Frequency filter in 'rollscan' mode (Blaow, personal communication).

Signal analysis in narrow frequency ranges

Moorthy *et al.* (2001) noted the lack of the expected second peak in quenched and tempered 0.1 wt. % C steel using this apparatus, and analysed the signal within narrow frequency ranges to study the low-frequency noise. A clear second peak was visible in the tempered steel in the range 4–5 kHz, while only a single peak was seen in the AQ sample at all frequencies.

The signals from the 600°C $2\frac{1}{4}$Cr1Mo steel samples were analysed in a similar way to test whether a second peak was visible at low frequencies. The first analysis considered noise with frequencies between 0 and 3 kHz. The signal amplitude was low, owing to filtering, so the highest available amplification, 99 dB, was applied. Figure 8.23 shows some evidence of a second peak centred around a current between 0.3 and 0.4 A; this is particularly prominent in the 256 h signal. However, some evidence of activity at 0.4 A is also visible in the AQ sample, which should have only a single peak. The large peak, although at a similar position to the peaks in Figure 8.9 and Figure 8.10, is narrower and more symmetrical.

Setting the upper frequency limit to 5 kHz (Figure 8.24) gives peaks which more closely resemble those in Figure 8.9 and Figure 8.10. However, there
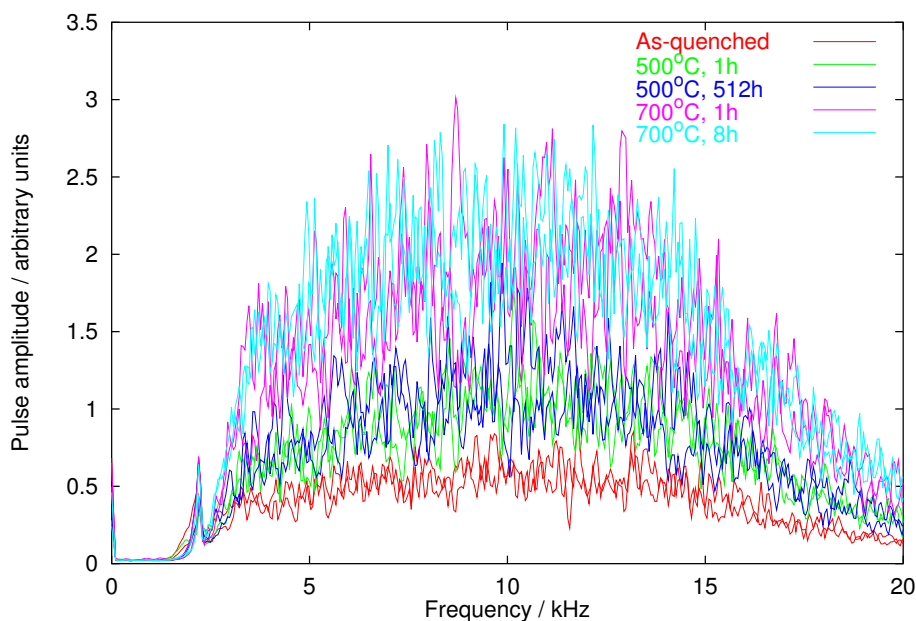
Figure 8.22: Frequency content of various noise datasets

is still evidence of activity in the high-current region. A clear slope change is visible in some peaks, notably those corresponding to shorter tempering times.

Analyses of frequencies within narrower ranges for individual samples are shown in Figure 8.25 (4 hours, 600°C) and Figure 8.26 (8 hours, 600°C). In both, a large, broad, high-current peak is visible for frequencies below 1 kHz. However, its smooth shape, compared to the typical roughness of the other curves, suggests that it may be an artefact of the measuring and filtering system rather than a true noise measurement. Double peaks or pronounced slope changes are visible in the 2–3 and 3–4 kHz ranges for both samples.

In Figure 8.27 (256 hours, 600°C) and Figure 8.28 (512 hours, 600°C), comparison between the signal content in the 0–3 kHz and the 0–5 kHz ranges can be seen. From the shape change between the two ranges, it is evident that there is significant activity in the range 0.2–0.4 A between 3 and 5 kHz.

These results strongly suggest that the low-frequency ranges do contain useful information, especially from events occurring at high applied currents.
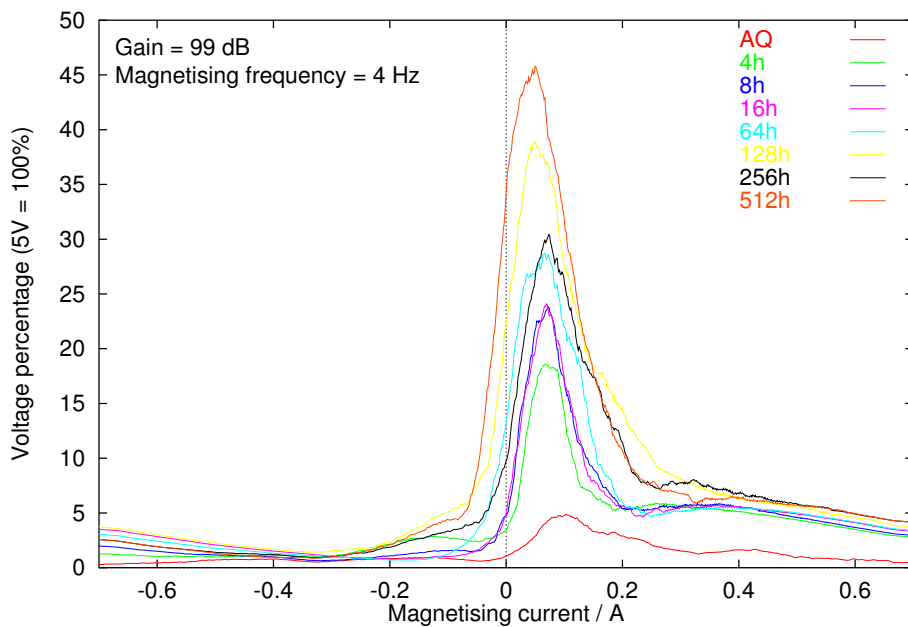
Figure 8.23: 0–3 kHz component of Barkhausen signal for 600°C tempered steels.
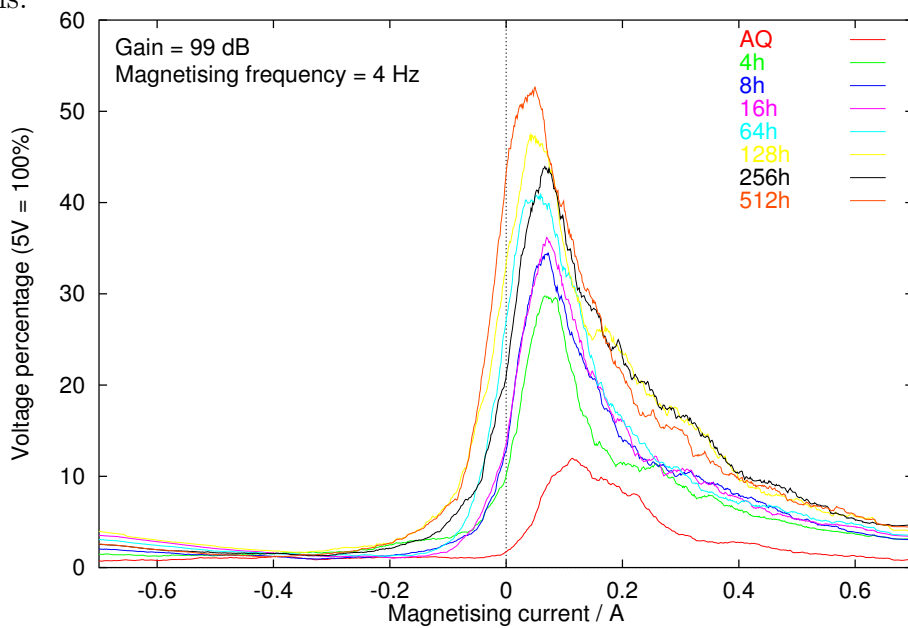
Figure 8.24: 0–5 kHz component of Barkhausen signal for 600°C tempered steels.
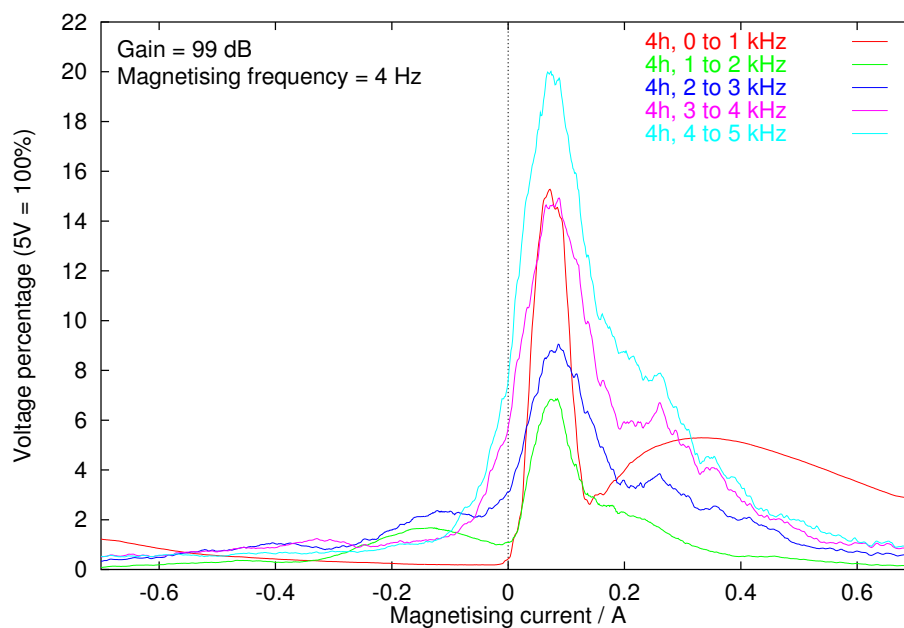
Figure 8.25: 600°C, 4 hour tempering: signals obtained from different frequency ranges.
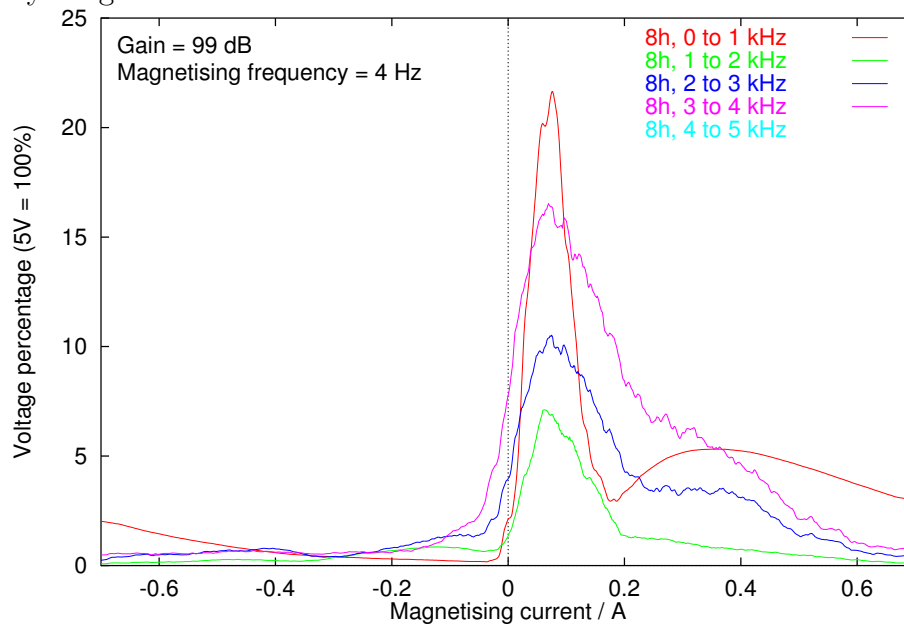
Figure 8.26: 600°C, 8 hour tempering: signals obtained from different frequency ranges.
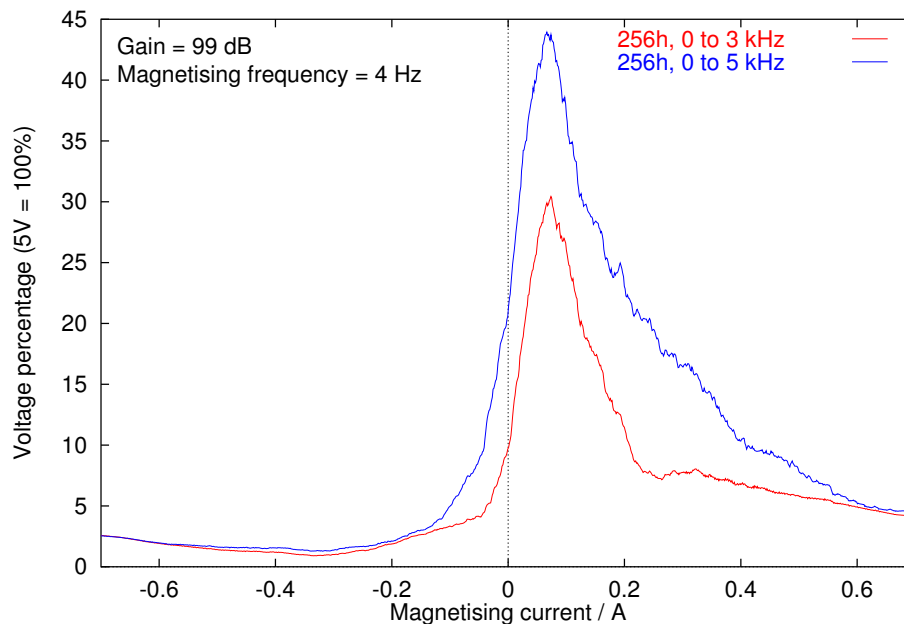
Figure 8.27: 600°C, 256 hour tempering: comparison of 0–3 kHz and 0–5 kHz ranges.
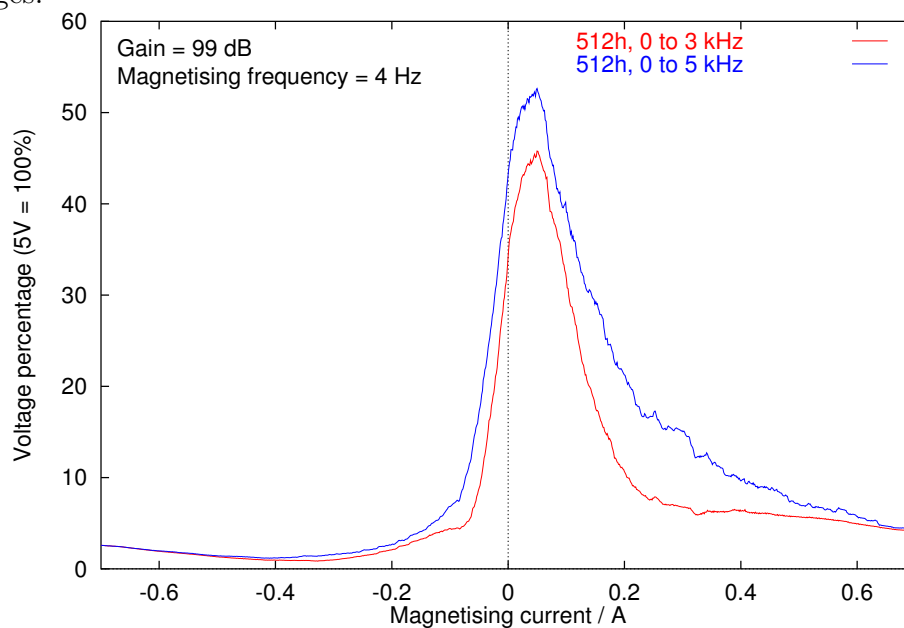
Figure 8.28: 600°C, 512 hour tempering: comparison of 0–3 kHz and 0–5 kHz ranges.

8.3.1 Checks on validity of results

Repeatability

Repeat measurements were taken on selected samples to determine the intrinsic experimental variability of the measurement system. Figure 8.29 shows both the forward and the reverse parts of three measurements from the same sample (8 hours, 700°C). The peak position and shape are consistent between measurements, but the peak height appears more variable. The overall range of peak heights observed in tempered $2\frac{1}{4}$Cr1Mo steels is 20–55 units on the vertical scale, but it appears from Figure 8.29 that variations can occur over almost a third of this total range.
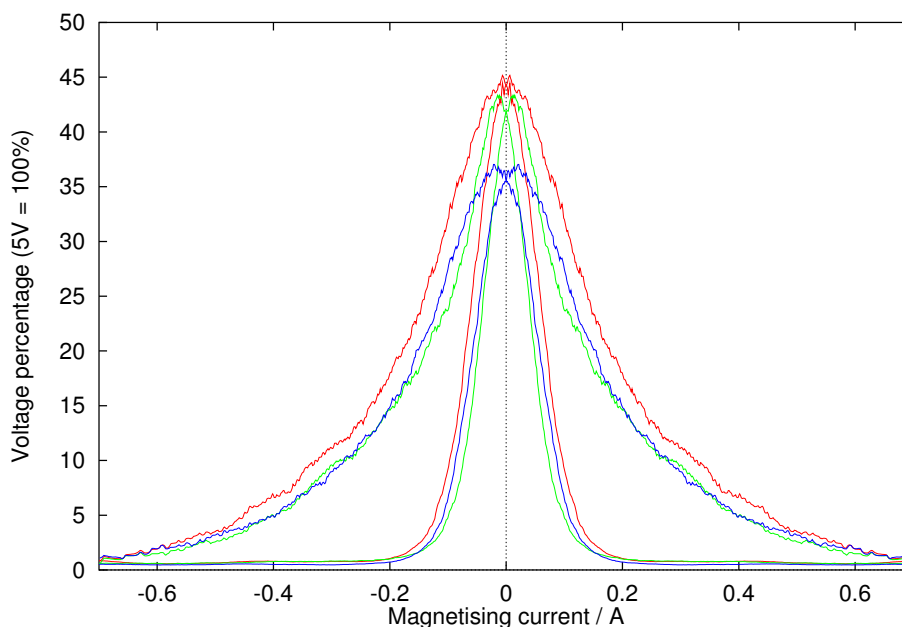
Figure 8.29: Repeatability study on sample tempered at 700°C for 8 hours.

Ferrite probe geometry

The original ferrite pole pieces for this apparatus were rectangular in section, but subsequently the effect of using round-ended pieces was investigated (Blaow, personal communication). These gave better repeatability, which was attributed to the smaller contact area. However, more recently,

a new set of rectangular-section pieces, with improved grinding, have been found to give good results; these last were used for the experiments described in this chapter. It now appears that the more critical part of the apparatus is the pickup coil core, which should be ground to a smooth shape to give good signal quality (Blaow, personal communication). Since this requires manual grinding, which is a difficult procedure, the scope for improvements is limited.

Figure 8.30 is a comparison of the signals obtained from the same sample (512 hours, 500°C) using three sets of pole pieces. The data from the new pieces were acquired using a higher amplification and are therefore plotted on a different scale on the right-hand vertical axis. The new pieces give a smoother curve, and better agreement between forward and reverse signal shapes. It is noticeable that, for the round-ended pieces, the peak position is different and the peak is broader than in the other cases.

Although it is difficult to tell what constitutes a 'better' or 'more accurate' signal without an external point of reference, it is reasonable to expect that greater smoothness and symmetry between forward and reverse directions is indicative of a more even acquisition of noise pulses. Whether or not this is the case, it is clear that the observed signal is sensitive to the shape and grinding quality of the pieces. Another issue which may contribute to the differences seen in Figure 8.30, however, is that the technique of taking Barkhausen measurements requires some skill and practice. The data from the new probe were obtained later than those from the other two probes, so this could be part of the reason for the improved smoothness.

Overall magnetising geometry

It would be useful to investigate whether the difference in geometry between the contact-type sensor used here, and the yoke-type apparatus used in much of the previous work in this field, gives any systematic differences in results. However, such a comparison is not possible unless the filtering applied in the two systems is the same. New measurement apparatus of both geometries is currently being constructed at the University of Newcastle in order to investigate this question.
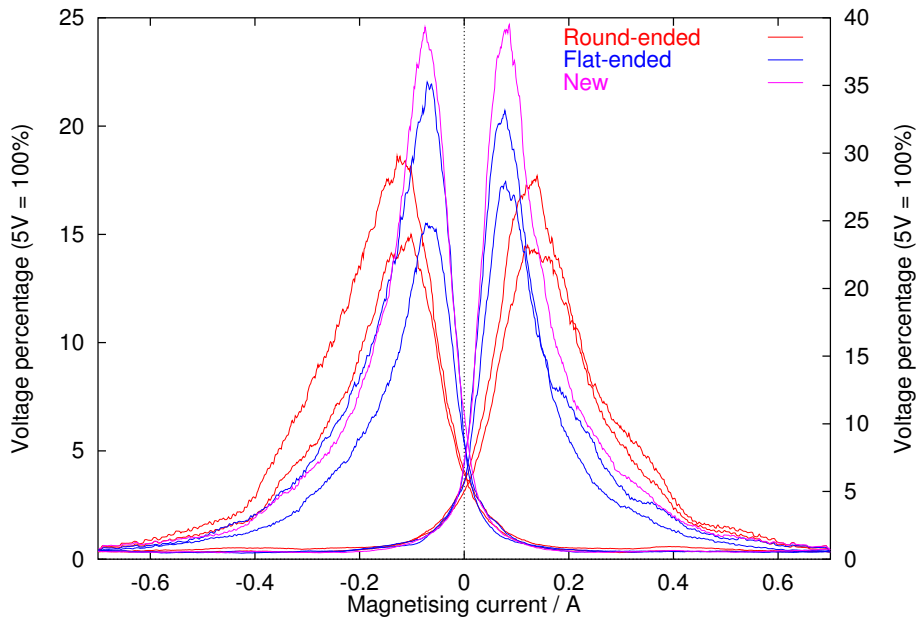
Figure 8.30: Effect of different pole-piece shapes on the 500°C, 512 hours signal.

8.4 Discussion

8.4.1 Tempered $2\frac{1}{4}$Cr1Mo steels

If the BN activity at higher currents corresponds to the second peak seen by Moorthy *et al.* (1997b) and attributed by them to unpinning of domain walls by carbides, then it appears that this activity is predominantly low-frequency noise. The other peak, occurring at a lower current and associated with unpinning from grain boundaries, is prominent at all frequencies. If the frequency is approximately the reciprocal of the 'time of flight' of the domain wall between pinning sites (Saquet *et al.*, 1999), then more closely spaced sites will produce noise of higher frequencies. When the applied current is small, the domain walls will be pinned by both weak and strong pinning sites, and the time interval between pinning events will be small. Increasing the current allows domain walls to bypass weaker pinning sites and move longer distances between events. If it is assumed that the domain wall velocity is approximately constant, then this would give noise of lower frequencies.

(Equation 5.15, however, gives the domain wall velocity as proportional to the difference between the applied field and H_C, so that walls would move faster at higher currents. Since this would tend to increase the frequency of events occurring at high currents, it appears that the jump size effect is dominant over the wall velocity effect in the system under investigation.)

Since it is believed that there is important information missing in these data sets as a result of filtering, it is not possible to interpret the signal shapes for the tempered steels with a great deal of confidence. However, the broadening of the peaks at higher temperatures and longer tempering times are indicative of a wider distribution of pinning site strengths, and the shift of the noise onset to a lower applied current after longer tempering corresponds to the appearance of weaker pinning sites.

8.4.2   11Cr1Mo steels

Steels designed for creep resistance contain, after tempering, a high concentration of fine alloy carbide particles to confer long-term microstructural stability. The high currents at which the peaks occur in this steel, and their similarity in shape to the AQ peak (Figure 8.12), suggest that little or no microstructural coarsening has taken place. This is borne out by an examination of the optical micrographs (Figure 6.16–6.19), which closely resemble the $2\frac{1}{4}$Cr1Mo steel in the very early stages of its tempering at 500 or 600°C.

Coarsening, with its associated loss of creep resistance, may be detectable in this steel by a shift of the noise onset to a lower current.

8.5   Conclusions

BN measurements were carried out on $2\frac{1}{4}$Cr1Mo and 11Cr1Mo steels tempered in a wide variety of conditions. In the $2\frac{1}{4}$Cr1Mo samples, some of the characteristics observed in previous work by Moorthy *et al.* could be seen; between the as-quenched and the tempered states the peak height increased, and its position moved to a lower current. Evidence of a second peak at higher current was present, but much suppressed by the hardware filtering, because it is composed primarily of noise with frequencies below the filtering

range of the system. Because of the difficulties in observing this second peak, detailed analysis of its relationship to tempering conditions and carbide sizes could not be carried out.

In the $2\frac{1}{4}$Cr1Mo samples, the maximum BN voltage occurs at a lower applied current with increasing Larson-Miller parameter. The 11Cr1Mo wt. % steel samples displayed peaks at a high current even after long-term heat treatment. It is believed that this is due to the coarsening resistance conferred by fine alloy carbides.

Measured BN data are very sensitive to experimental conditions such as frequency filtering and the shape and surface roughness of the yoke contact points and pickup coil core. This sensitivity may go some way towards explaining the discrepancies between results in the literature. Taking this into account, it would be advisable to develop a standard instrument and technique if BN measurements are to be used for safety-critical NDT applications.

Chapter 9 discusses the fitting of the model developed in Chapter 5 to these data sets.

Chapter 9

Model Fitting to Power-Plant Steel Data

9.1 Data and fitting procedure

The output from the BN measurement software is a text file containing only the forward and reverse RMS noise data. From the BN unit control software, it was known that the applied current amplitude was ±0.7 A. A program was written to extract the two sets of data and assign current values to them, assuming that BN data points were acquired at equally spaced intervals of current. It was further assumed, as in Chapter 5, that the current was proportional to the applied field experienced by the domain walls. Models 1 and 2 were fitted using the programs described in the Appendix.

9.2 Results

Figure 9.1–Figure 9.6 show examples of fitting using Model 1 and Model 2. Both models give a close fit, although Model 2 is rather better at correctly fitting the leading edge. Table 9.1 gives the errors calculated by the programs for all the data sets examined. The mean error of all the data sets, shown in the final row of the table, is smallest for Model 2 and largest for empirical fitting. The difference between the goodness of fit of Model 1 and Model 2 is less pronounced than for the data fitted in Chapter 5. The double peaks in those data increase the difficulty of fitting using a model which is physically
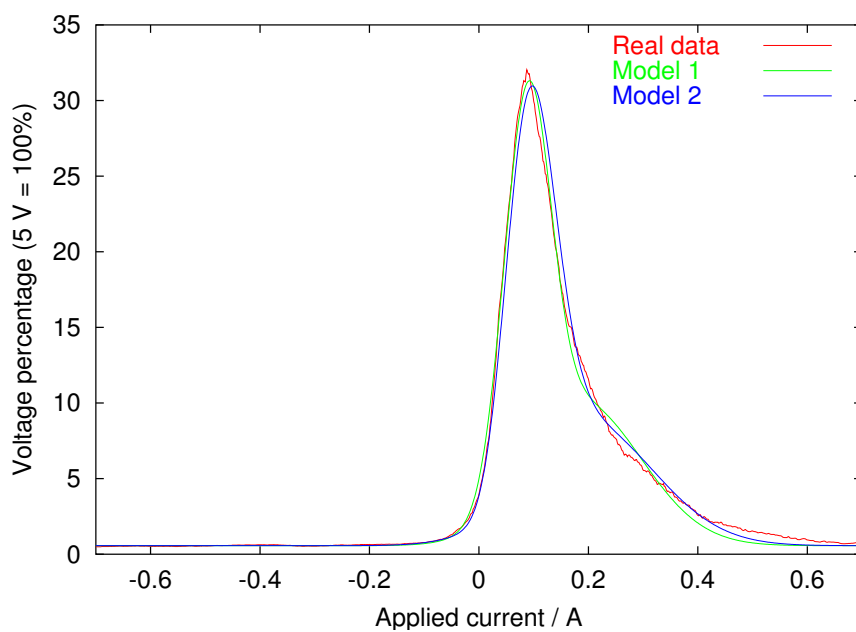
Figure 9.1: $2\frac{1}{4}$Cr1Mo steel, 500°C, 8 h

inaccurate, whereas a single peak with a slope change can be approximated more easily even by empirical fitting.
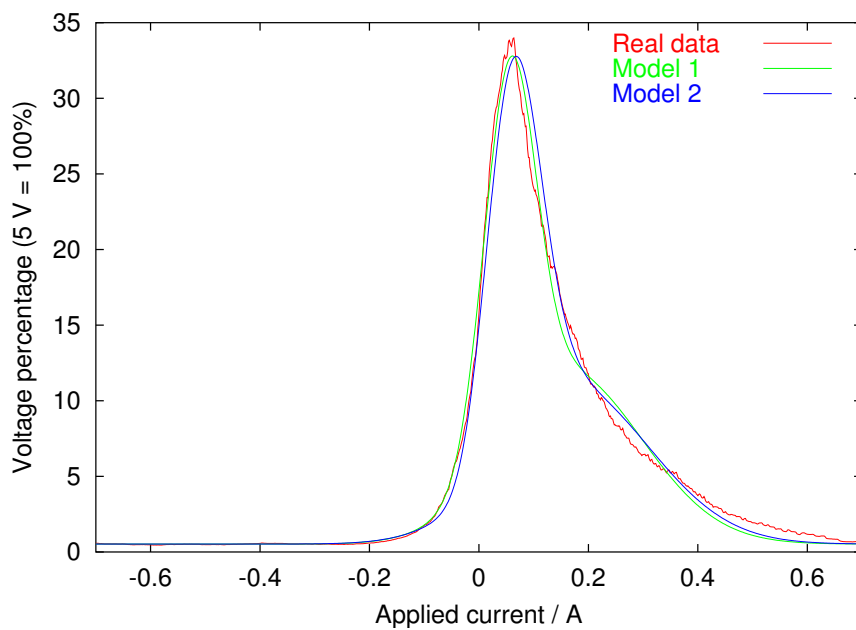
Figure 9.2: $2\frac{1}{4}$Cr1Mo steel, 600°C, 8 h
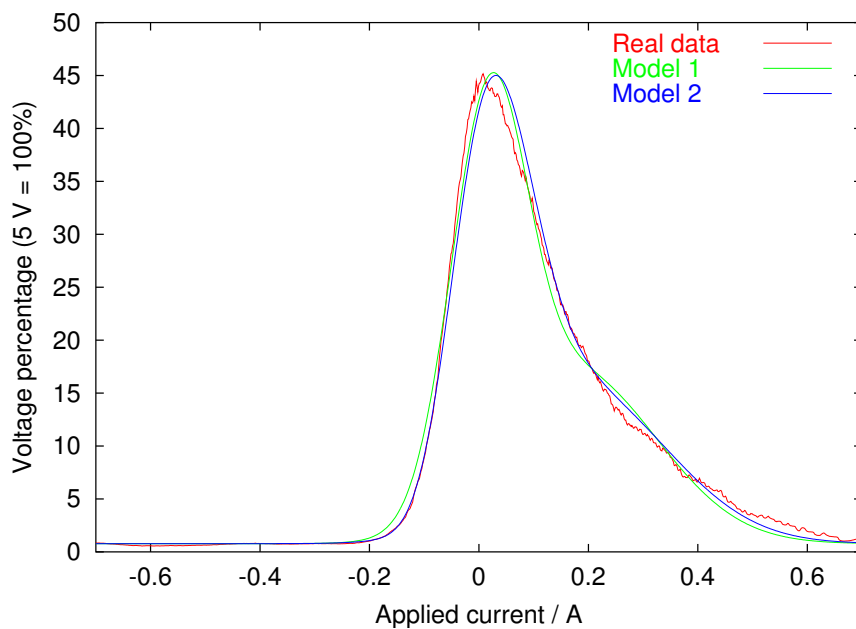
Figure 9.3: $2\frac{1}{4}$Cr1Mo steel, 700°C, 8 h
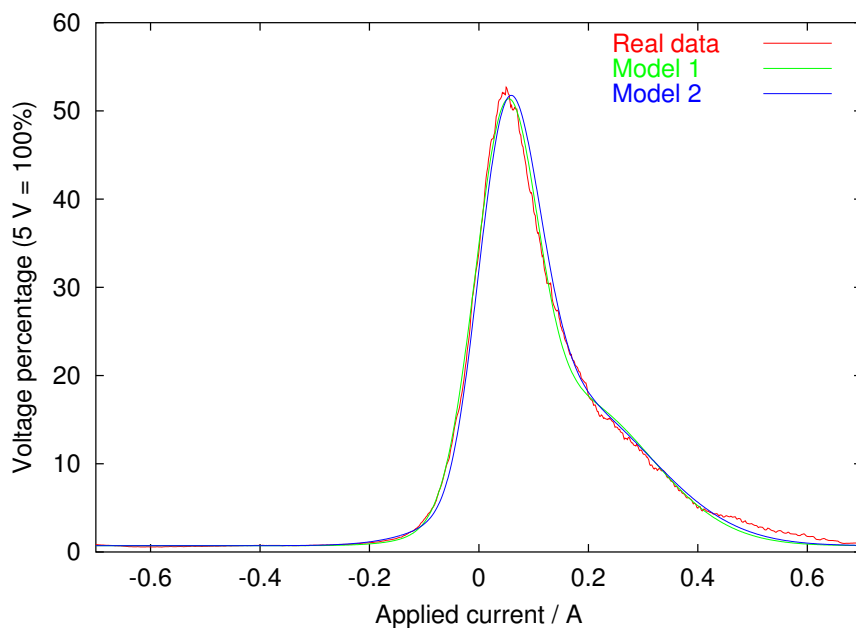
Figure 9.4: $2\frac{1}{4}$Cr1Mo steel, $600°$C, 256 h
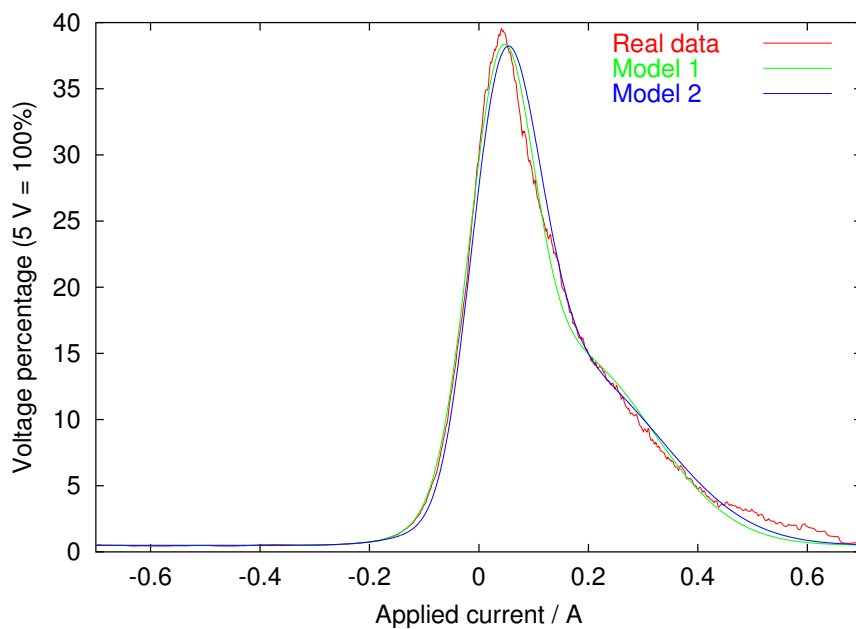
Figure 9.5: $2\frac{1}{4}$Cr1Mo steel, $600°$C, 512 h
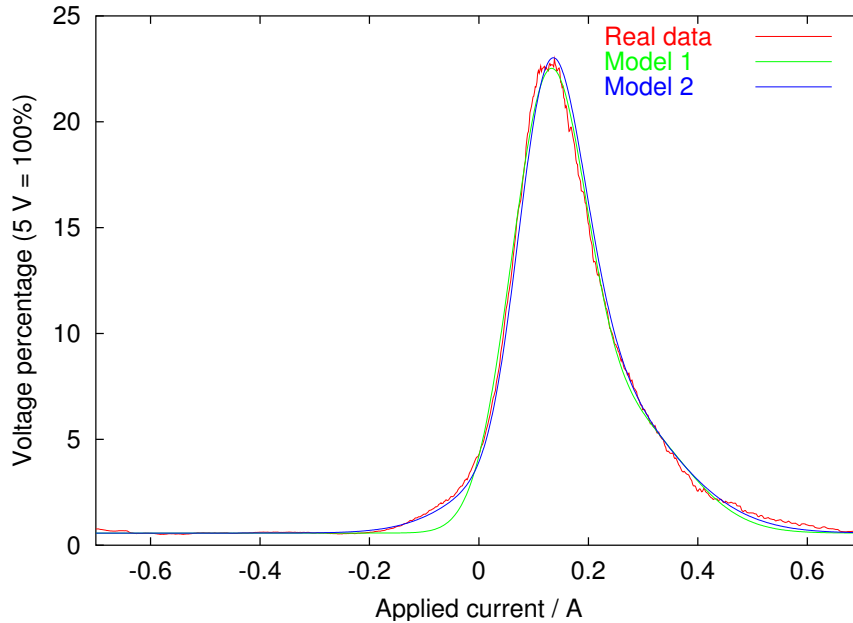
Figure 9.6: 11Cr1Mo wt. % steel, 550°C, 2347 h

9.3 Fitting parameters

9.3.1 Comparison of Model 1 and Model 2

The Model 2 parameters $e^{<x>} + S_b$ and $< S >_2$ are plotted against tempering time in Figure 9.7 and Figure 9.8. These characterise the average pinning strengths of the log-normal and normal distributions respectively. The $e^{<x>} + S_b$ values are divided into clear bands based on tempering temperature. Within the 500°C and 600°C bands, the values decrease with increasing time. The relationship between $< S >_2$, temperature and time is not so clear-cut, but the trends seem similar.

For comparison, the Model 1 fitting parameters $< S >_1$ and $< S >_2$ were also plotted against tempering time, giving very similar results. As discussed above, because of the lack of a distinct second peak, it is likely that Model 1 could be used in place of Model 2 to fit these data without a great loss of accuracy.

Temperature	Time	Error (%)		
/°C	/ hours	Peak-fitting	Model 1	Model 2
$2\frac{1}{4}$Cr1Mo steel				
As-quenched		4.09	4.44	4.23
500	1	6.03	5.69	4.67
500	2	8.40	5.19	4.20
500	4	7.32	4.97	4.01
500	8	6.57	6.11	5.19
500	16	6.41	6.12	5.40
500	32	6.60	6.22	4.41
500	256	7.48	7.33	6.03
500	512	7.23	6.92	5.94
600	4	6.05	5.89	6.71
600	8	7.87	7.51	6.71
600	16	4.74	4.23	4.37
600	32	8.76	8.53	9.90
600	64	5.30	5.21	4.36
600	128	4.56	4.27	3.73
600	256	5.05	4.60	3.56
600	512	6.10	5.75	5.09
700	1	6.97	6.14	5.42
700	2	4.82	3.75	3.03
700	4	4.30	3.80	3.50
700	8	7.34	7.13	5.10
11Cr1Mo steel				
550	2347	3.61	5.41	2.46
550	5849	4.44	4.12	4.64
550	16530	5.69	5.78	5.35
550	36191	5.23	5.40	4.58
Plain-carbon steel				
As-quenched		10.68	4.46	3.18
?	0.5	2.95	3.16	3.76
?	100	4.16	4.22	4.15
Mean				
		6.03	**5.44**	**4.77**

Table 9.1: Fitting errors of empirical peak-fitting, Model 1 and Model 2
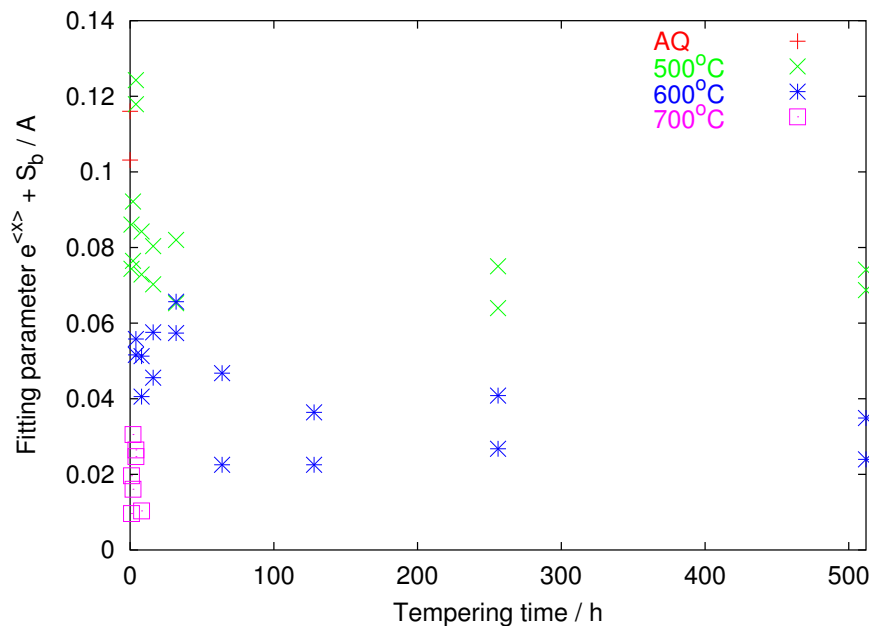
Figure 9.7: $e^{<x>} + S_b$ versus tempering time for Model 2, $2\frac{1}{4}$Cr1Mo steel.
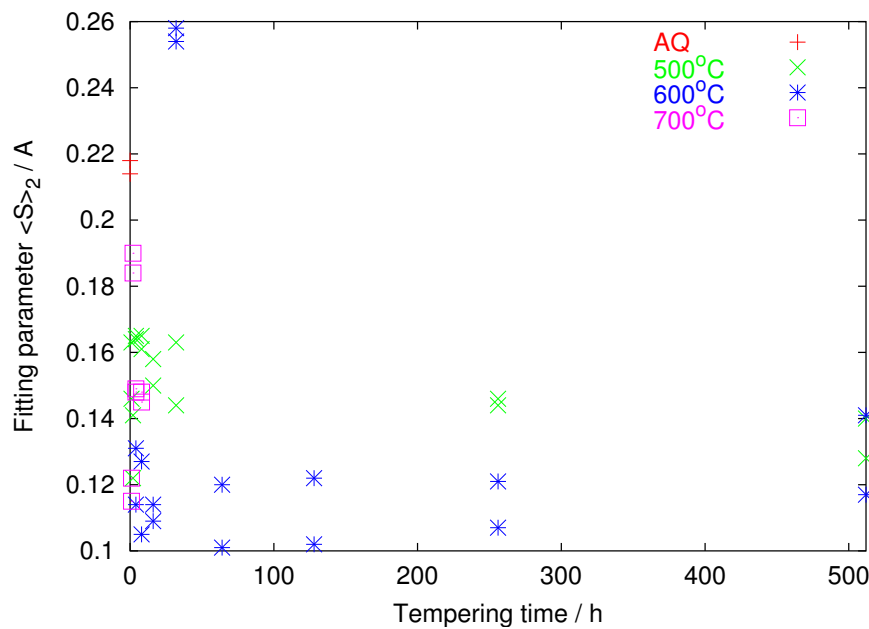
Figure 9.8: $< S >_2$ versus tempering time for Model 2, $2\frac{1}{4}$Cr1Mo steel.
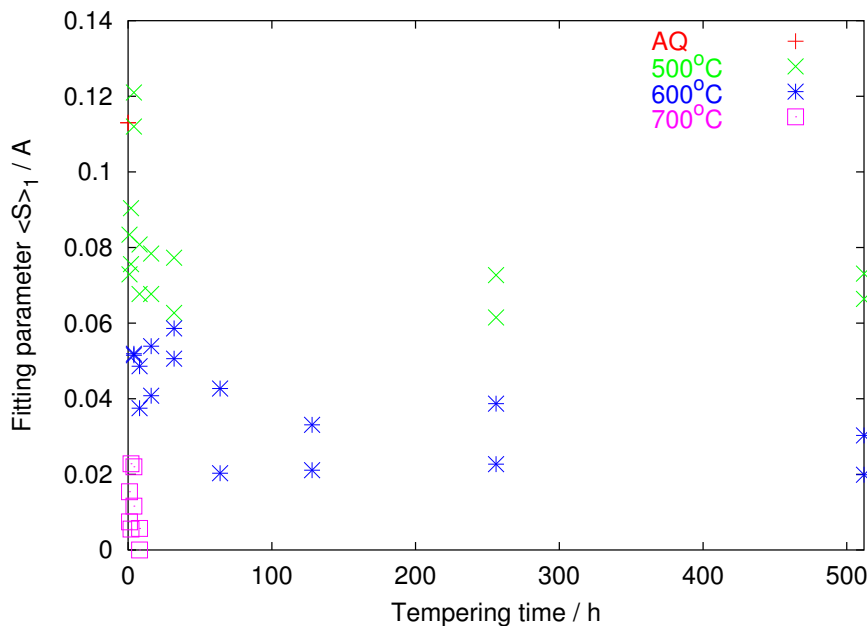
Figure 9.9: $< S >_1$ versus tempering time for Model 1, $2\frac{1}{4}$Cr1Mo steel.
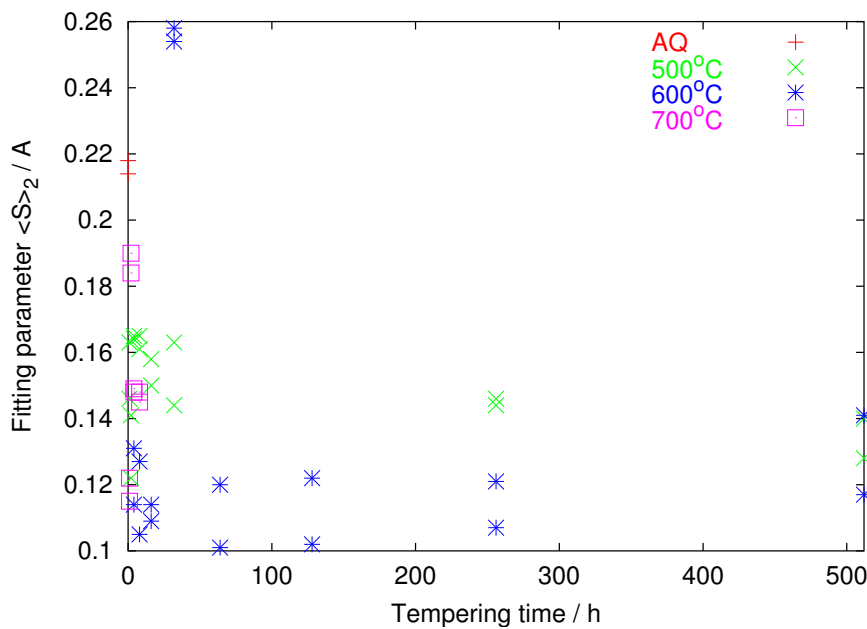
Figure 9.10: $< S >_2$ versus tempering time for Model 1, $2\frac{1}{4}$Cr1Mo steel.

9.3.2 Model 2 parameter variations with Larson-Miller parameter

The combination $e^{<x>} + S_b$ is plotted against the Larson-Miller parameter P in Figure 9.11. This is very similar in appearance to Figure 8.18, with a monotonic decrease in $e^{<x>} + S_b$ with P for all the $2\frac{1}{4}$Cr1Mo samples. The 11Cr1Mo samples have higher $e^{<x>} + S_b$ values than the $2\frac{1}{4}$Cr1Mo. $< S >_2$ decreases with P at short times, then increases again at longer times (Figure 9.12).

A_1 and A_2 both increase monotonically with increasing P in the $2\frac{1}{4}$Cr1Mo steel samples. The 11Cr1Mo values fall below these curves. A_2 has around half the value of A_1.

The distribution widths Δx and ΔS_2, shown in Figure 9.15 and Figure 9.16 respectively, tend to higher values at higher P, but there is more scatter than for A_1, A_2 and $e^{<x>} + S_b$.
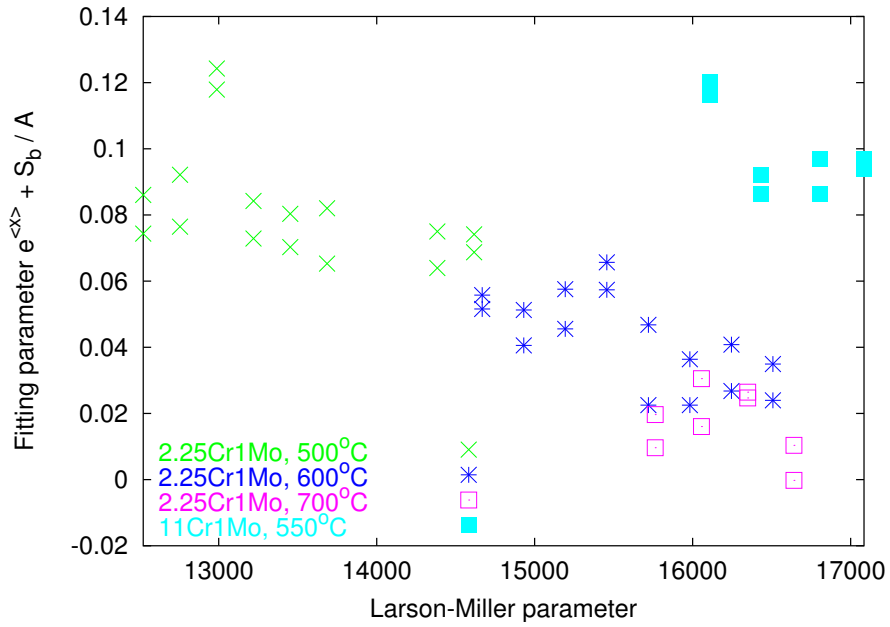
Figure 9.11: $e^{<x>} + S_b$ versus Larson-Miller parameter.
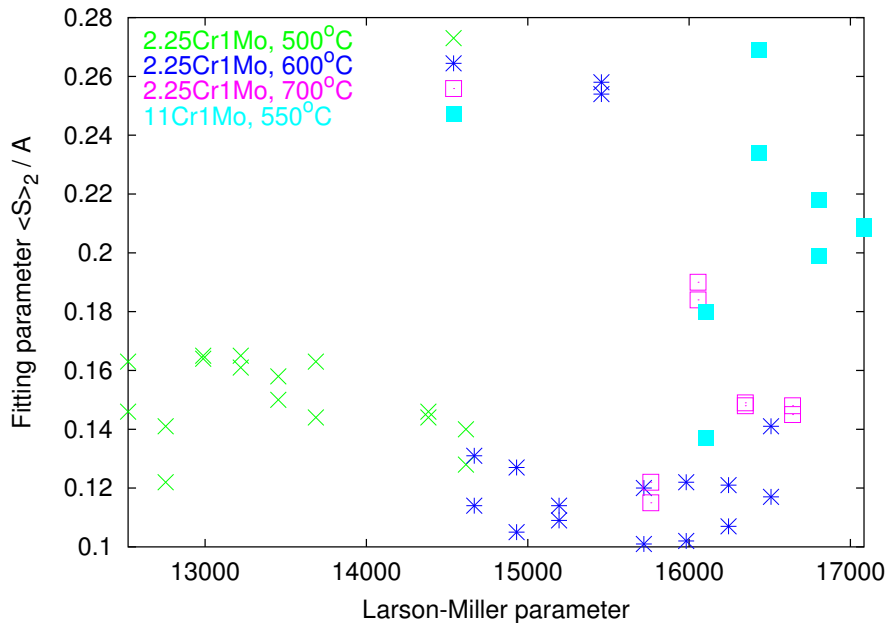
Figure 9.12: $< S >_2$ versus Larson-Miller parameter.
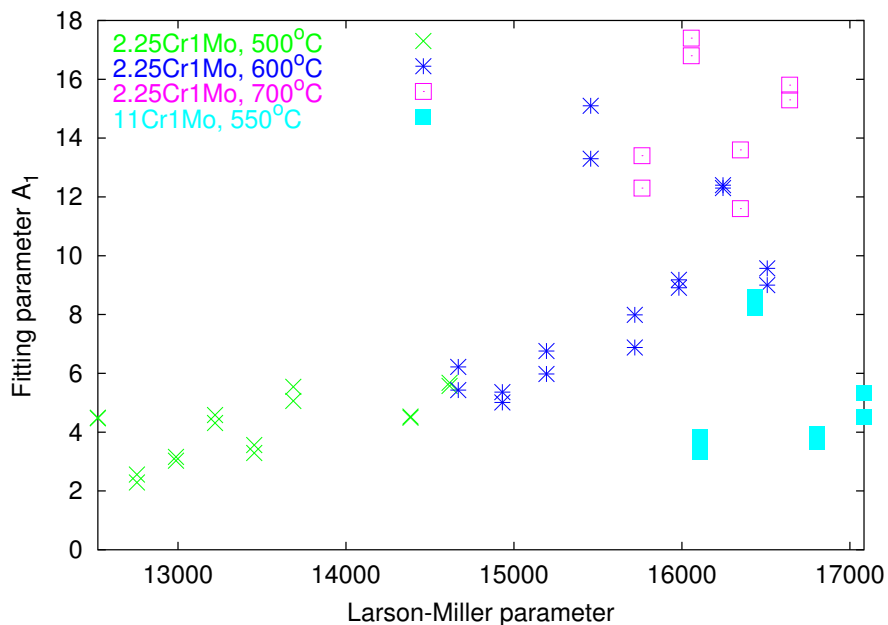
Figure 9.13: A_1 versus Larson-Miller parameter.
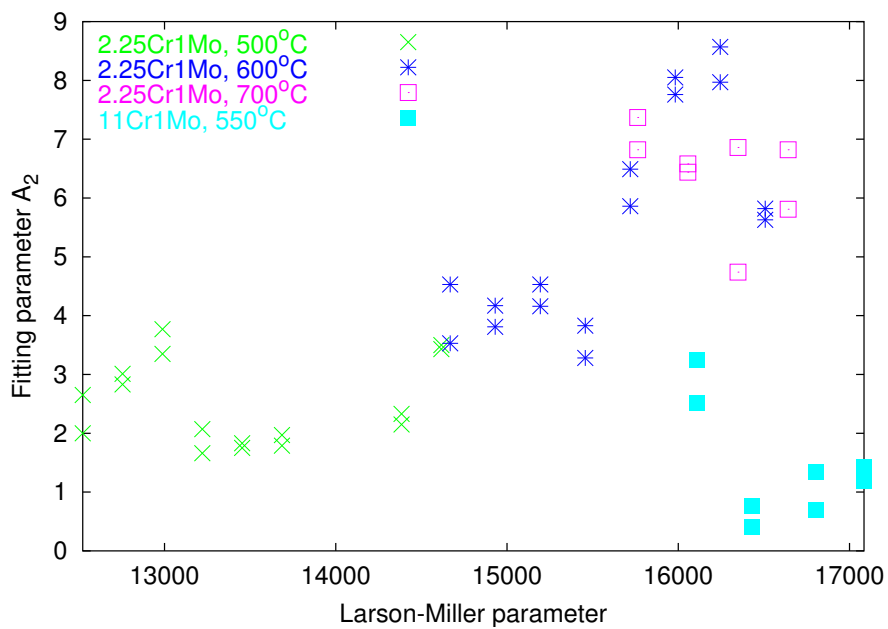
Figure 9.14: A_2 versus Larson-Miller parameter.
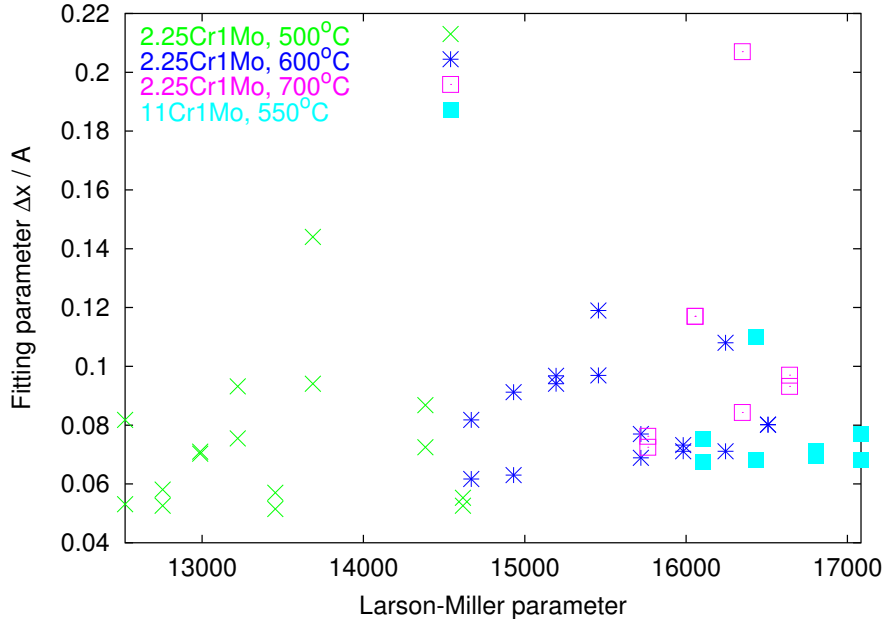
Figure 9.15: Δx versus Larson-Miller parameter.
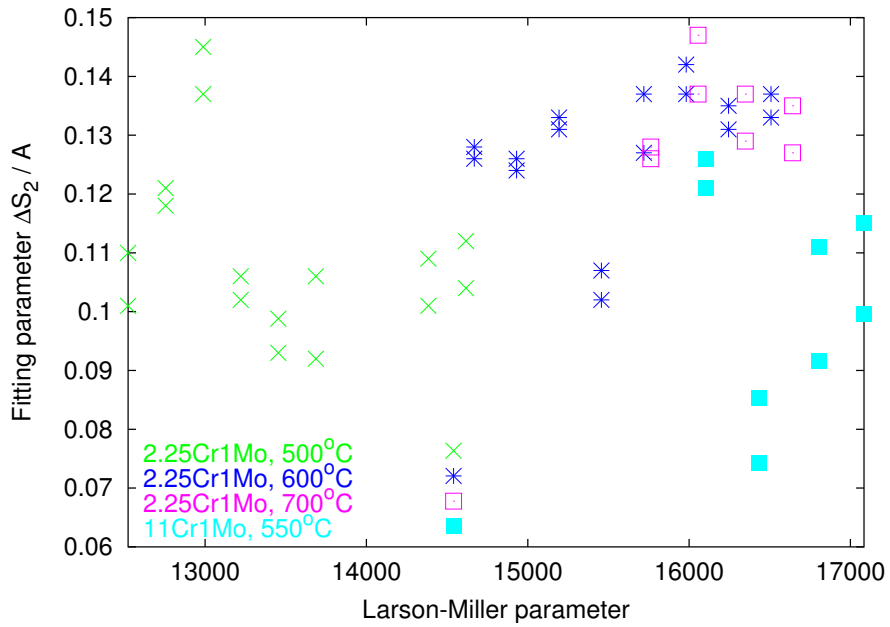
Figure 9.16: ΔS_2 versus Larson-Miller parameter.

9.4   Discussion

9.4.1   Relationship of fitting parameters to microstructure

It was seen in Chapter 6 that $2\frac{1}{4}$Cr1Mo steel samples tempered at 700°C underwent rapid microstructural coarsening and softening, but at 500 and 600°C, changes were much more gradual. Despite these differences, if the Larson-Miller parameter is used to combine temperature and time conditions, it can be seen that the BN model parameters from this steel fall into the same regime of behaviour. In particular, there is a very clear relationship between $e^{<x>} + S_b$ and the Larson-Miller parameter; this accurately replicates the relationship between peak position and P seen in Chapter 8. This large peak is believed to correspond to the lower-field peak observed by Moorthy *et al.* and attributed to interactions between domain walls and grain boundaries. If this is so, the results of Chapter 7 suggest that the gradual reduction of strain at grain boundaries during tempering reduces the strength of their interactions with domain walls. The lack of any clear changes in grain boundary character distribution during tempering at 600°C leads to the conclusion that the main changes are in magnetoelastic rather than magnetostatic energy, and are associated with changes in the dislocation density at grain boundaries. In as-quenched steel, adjacent martensitic laths within the same packet are separated by a highly strained boundary, but the misorientation between the laths is very small. Tempering reduces the dislocation density, and this decreases the strength and density of obstacles to domain wall motion.

No recrystallisation has been observed in any of the samples in this study. If the temperature and time were increased sufficiently to allow this, a different regime of BN behaviour, in which magnetostatic energy changes are important, may result.

The initial decrease of $<S>_2$ with tempering time may be related to the dissolution of M_3C and its replacement with fine, needlelike M_2X carbides, giving a reduction in pinning strength. The subsequent appearance and rapid growth of spheroidal M_7C_3 carbides and other coarse phases at longer times

increases $< S >_2$ again. It would be useful to repeat these experiments using BN apparatus which is capable of detecting double-peak behaviour to investigate the high-field region more fully.

The A parameters characterising the number of pinning sites show an unexpected monotonic increase with tempering time. It would be expected that the number of pinning sites from grain boundaries would fall as coarsening occurs, and the number of carbides may vary in a complex way during the precipitation sequence. The observed behaviour of A suggests that the model is not currently physically accurate in this respect. The width ΔS_2 does follow the expected behaviour of a carbide size distribution, increasing with tempering time as the carbide sizes become more varied, but Δx is more difficult to interpret.

The 11Cr1Mo steel BN parameters do not follow the same relationships as those of the $2\frac{1}{4}$Cr1Mo steel, although there is a suggestion in Figure 9.11 that its $e^{<x>} + S_b$ values may lie on a parallel line to the $2\frac{1}{4}$Cr1Mo steel values. However, more data, with a larger range of tempering conditions, would be needed to test this.

9.5 Conclusion

Model 2 fits these experimental data well, but almost as good a fit can be obtained using Model 1, possibly because the lack of a distinct second peak makes fitting easier. Clear relationships between the microstructural characteristics and the Model 2 parameters have been observed. From a comparison between microscopy, orientation measurements and modelling results, it has been concluded that the principal influence on magnetic behaviour in these samples is the reduction of the high levels of strain initially present in the quenched microstructure. However, it would be advisable to repeat the experiments using more suitable apparatus to check these conclusions.

Chapter 10

Barkhausen Noise in PM2000 Oxide Dispersion Strengthened Alloy

10.1   Oxide dispersion strengthened alloys

PM2000 is an oxide dispersion strengthened (ODS) alloy of composition 20 Cr, 0.5 Ti, 0.5 Y_2O_3, 5.5 Al, balance Fe (wt. %), manufactured by mechanically alloying the metallic components with fine particles of Y_2O_3 (Krautwasser *et al.*, 1994). It has been proposed as a suitable material for biomass-based power plant with an operating temperature of around 1100°C and a pressure of 15–30 bar (Capdevila *et al.*, 2001). A material for this application must have good oxidation resistance, which in PM2000 is provided by the aluminium, and good creep performance. At such a high temperature, this is only achieved using a very coarse grain size in combination with an oxide dispersion.

Powders of the components are severely deformed by ball milling to produce a mixture with a uniform distribution of oxide particles. This is consolidated by hot isostatic pressing, then extruded into tubular form. The microstructure of the material at this stage consists of very fine equiaxed grains (Sporer *et al.*, 1993). These are less than 1 μm wide and heavily strained because of the cold deformation.

Recrystallisation, to give a coarse microstructure for creep resistance, re-

quires a temperature approximately 0.9 of the absolute melting temperature T_M, as compared to around $0.6T_M$ in non-ODS iron alloys. The resulting microstructure consists of columnar grains with their long axes parallel to the extrusion direction (Elliot *et al.*, 1990; Timmins *et al.*, 1990).

A heat treatment of 90 minutes at 1380°C is sufficient to produce a fully recrystallised microstructure (Capdevila Montes, personal communication).

A TEM micrograph of oxide particles in the microstructure is shown in Figure 10.1, and Figure 10.2 gives data on the particle size distributions. It can be seen that the modal particle size is between 20 and 40 nm.
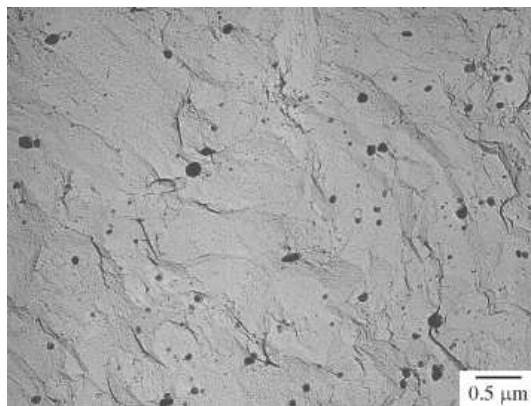
Figure 10.1: Oxide particles in PM2000 microstructure. Micrograph by C. Capdevila Montes; used with permission.

10.2 Relevance of PM2000 to magnetic property studies

It is believed that magnetic properties are influenced both by grain boundaries and by second-phase particles. In PM2000, the oxide particle distribution is not changed to any great extent by recrystallisation, so the effects of grain boundaries on BN can be isolated in this material.

In addition, by comparison with an oxide-free sample with otherwise the same composition, the effect of the particles can be studied. The oxide particles are small compared to the typical domain wall width of 80–100 μm
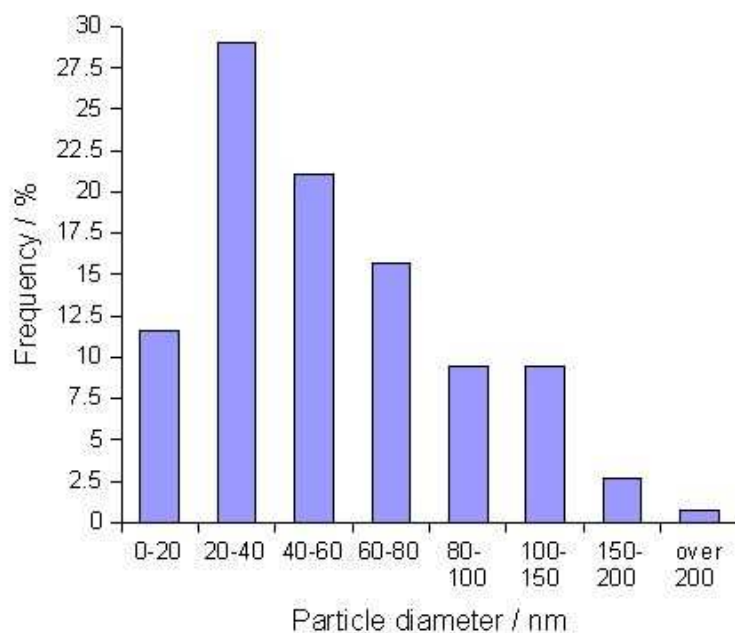
Figure 10.2: Oxide particle size distribution (Capdevila Montes, personal communication).

in ferrous materials, so it was not certain before these experiments were carried out whether there would be a detectable particle effect. However, carbides of ~ 0.2 μm strongly influenced hysteresis and BN in plain carbon steel (Lopez *et al.*, 1985; Gatelier-Rothéa *et al.*, 1992). Some oxide particles of this size exist in the PM2000.

10.3   Experimental Method

10.3.1   Sample preparation

PM2000 is supplied in tubular form, with internal and external diameters of 49 mm and 53.5 mm respectively, by Plansee GmbH. Sections were cut from the tube and heated in a furnace at 1380°C for a range of times between 10 and 90 minutes, then air-cooled. As-received samples were also retained.

Flat surfaces were prepared for BN testing and microscopy by cutting the samples parallel to the tube axis as shown in Figure 10.3, using an 'Accutom'
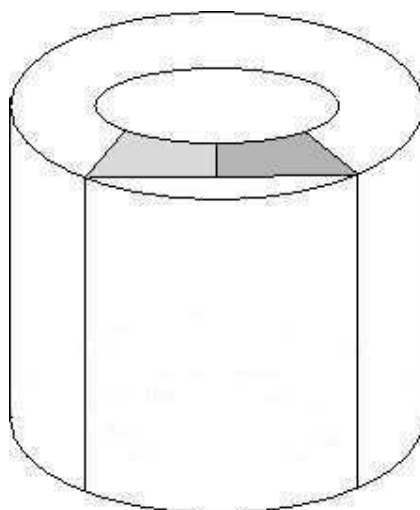
Figure 10.3: Origin of the tube-section samples, marked in grey.

rotary cutter. This geometry allows regions from the inner to the outer surface to be studied; this is important since experiments by Capdevila *et al.* (2001) demonstrated that recrystallisation began at the outer surface and moved as a front towards the inner region.

The surfaces were ground, polished to 1 μm using diamond paste and then etched with Kalling's No. 2 reagent (2 g $CuCl_2$, 40 ml HCl, and 40-80 ml ethanol). A further sample was melted to float away the oxide particles, then prepared in the same way as the others.

10.3.2   BN measurement

BN measurements were made using the same apparatus and conditions as described in Chapter 8, the only difference being the use of a different, and possibly inferior, set of ferrite pieces in the probe since these experiments were carried out earlier than those described in Chapter 8. A magnetising frequency of 4 Hz was used, except in a group of experiments to determine the effect of frequency. It was necessary to adjust the signal amplification because of the wide range of signal amplitudes from this group of samples. As mentioned in Chapter 8, however, signals obtained using different amplifications may not be directly comparable.

10.4 Microstructures

10.4.1 Naked-eye observations

The changes in microstructure on recrystallisation in PM2000 are visible even to the naked eye. Figure 10.4 shows drawings of the microstructures, with the horizontal direction parallel to the tube length. The edge of the sample closest to the outer surface is at the top in all cases. It can be seen that recrystallisation begins near the outer surface and proceeds towards the inner surface.

No features are visible on the unrecrystallised sample, which has a dull surface after etching, but after 10 minutes at 1380°C, a clearly visible boundary between recrystallised and unrecrystallised regions appears towards the outer edge of the sample. The recrystallised area, with a more reflective appearance, expands, and after 40 minutes at 1380°C it has occupied the entire visible area. Grain boundaries are few in number, and lie parallel to the extrusion direction. The grain width is variable but of the order of 10 mm.

10.4.2 Optical micrographs

Figure 10.5 shows an unrecrystallised region (top) and a recrystallised region (bottom) in the same sample. The unrecrystallised region has striations parallel to the tube axis but no discernible individual grains. This microstructure occurs uniformly across the unrecrystallised sample. Recrystallised regions are largely featureless and have a more reflective appearance to the naked eye. All observations of partially recrystallised PM2000 showed a similar combination of fully recrystallised and completely unrecrystallised regions, with no intermediate grain growth stages visible.

10.4.3 TEM observation

Figure 10.6 shows the microstructure of unrecrystallised PM2000 on a smaller scale. Individual grains can be resolved, but their extremely small size is evident.

<div align="center">Unrecrystallised   10 minutes, 1380°C</div>

<div align="center">20 minutes, 1380°C   30 minutes, 1380°C</div>

<div align="center">40 minutes, 1380°C   70 minutes, 1380°C</div>
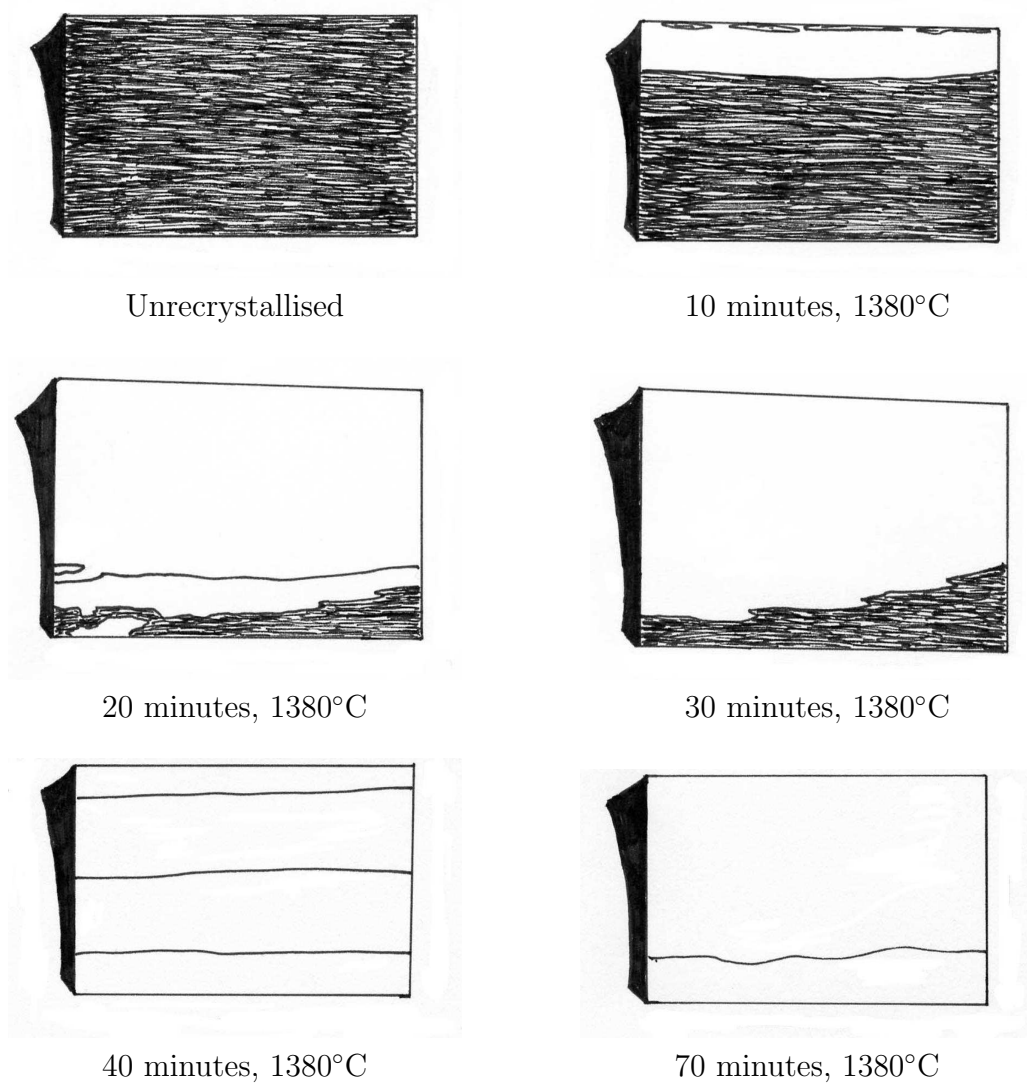
Figure 10.4: Sketches of microstructures of ODS material after different heat treatments. The tube axis is horizontal and the upper edge closer to the outer tube edge.
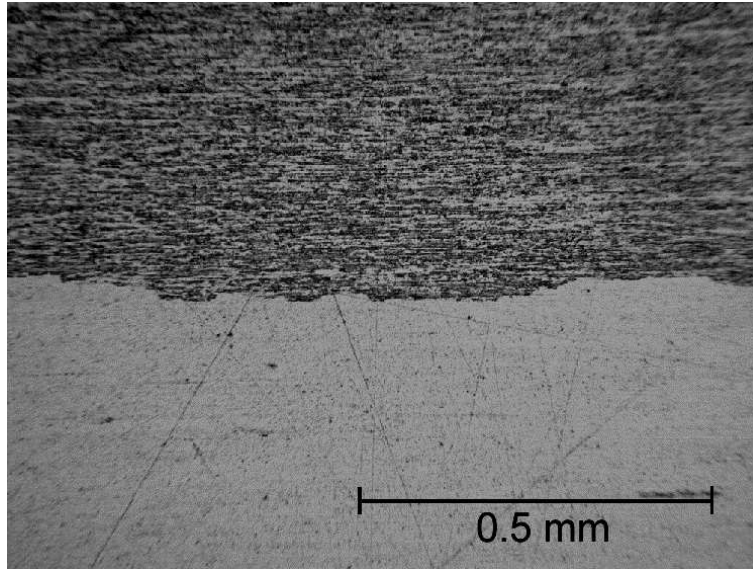
Figure 10.5: Optical micrograph showing recrystallised and unrecrystallised regions.
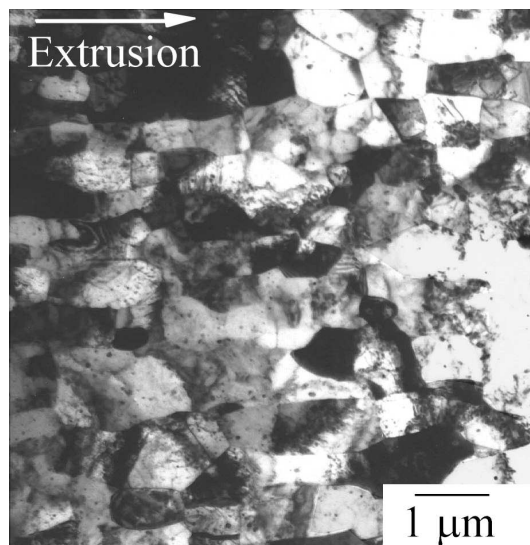
Figure 10.6: Unrecrystallised material observed using TEM. Micrograph by C. Capdevila Montes; used with permission.

10.4.4   Melted (oxide-free) sample

The melted sample shows a more conventional solidification microstructure with a variety of grain shapes and sizes and smooth, rounded grain boundaries (Figure 10.7). Naked-eye observations show that the grains are elongated perpendicular to the sample long axis, with the finest grains near the outside edges where solidification began.
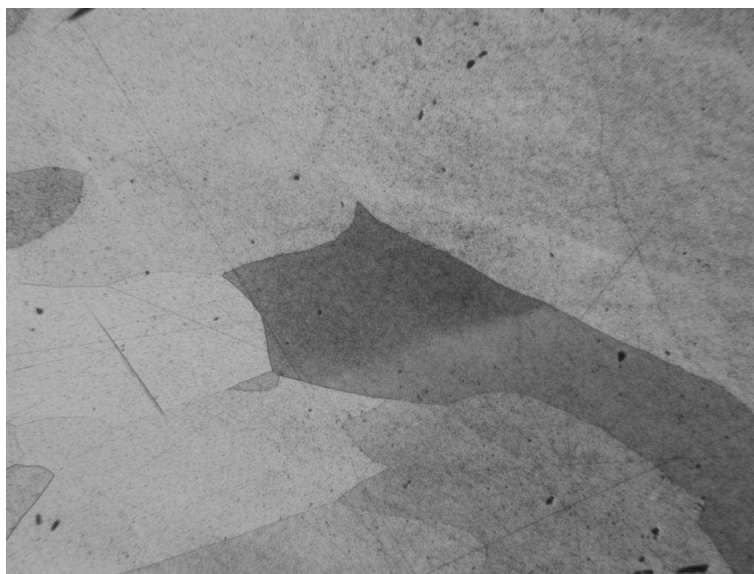
Figure 10.7: Melted, oxide-free sample.

10.5   Hardness measurements

The hardness of the samples was measured using a Vickers indenter with a mass of 30 kg and a 2/3" objective. Ten indents were made on each sample, five close to each edge parallel to the tube long axis. Care was taken to place the indent with its axes parallel and perpendicular to the tube axis so that the hardness in these directions could be measured. For each edge, the overall mean hardness and the means in the parallel (longitudinal) and perpendicular (transverse) directions were calculated (Table 10.1).

Figure 10.8 shows the difference between the mean hardnesses of the inner

Time at	Outer edge			Inner edge		
1380°C/ min	L	T	Overall	L	T	Overall
0	324	332	328	325	321	323
10	292	299	296	292	292	292
20	250	270	260	283	284	284
30	255	275	265	261	276	269
40	248	264	256	264	272	268
50	253	270	262	254	272	263
60	261	271	266	263	278	270
70	250	273	262	150	150	150
80	250	265	258	254	266	260
90	251	271	261	251	269	260

Table 10.1: Hardness (HV30) of recrystallised PM2000 samples. L=longitudinal, T=transverse.

and outer edges of the sample. Softening begins even before a large recrystallised area has formed. The outer edge hardness decreases more rapidly as the recrystallisation front moves from the outer side inwards. When both sides have recrystallised, the difference between hardness is less prominent but the outer edge is usually softer. The exception to this is the 70 minute sample, whose inner edge is anomalously soft (Table 10.1). This sample tapered more towards the inner edge than the others, perhaps giving an insufficient depth of material at the edge for correct hardness determination.

The hardness, as determined from the width of the indent, is similar when measured in transverse and longitudinal directions at short heat treatment times, but is consistently larger in the transverse direction at longer times (Figure 10.9, Figure 10.10). This can be attributed to the alignment of the strengthening oxide particles along the extrusion direction. Before recrystallisation, the fine grains and high dislocation density dominate the behaviour, but as coarsening occurs, strengthening by oxides becomes significant.

The melted sample has a mean hardness value of 211 HV30, which is softer than that of any of the oxide-containing samples, apart from the anomalous measurement discussed above.
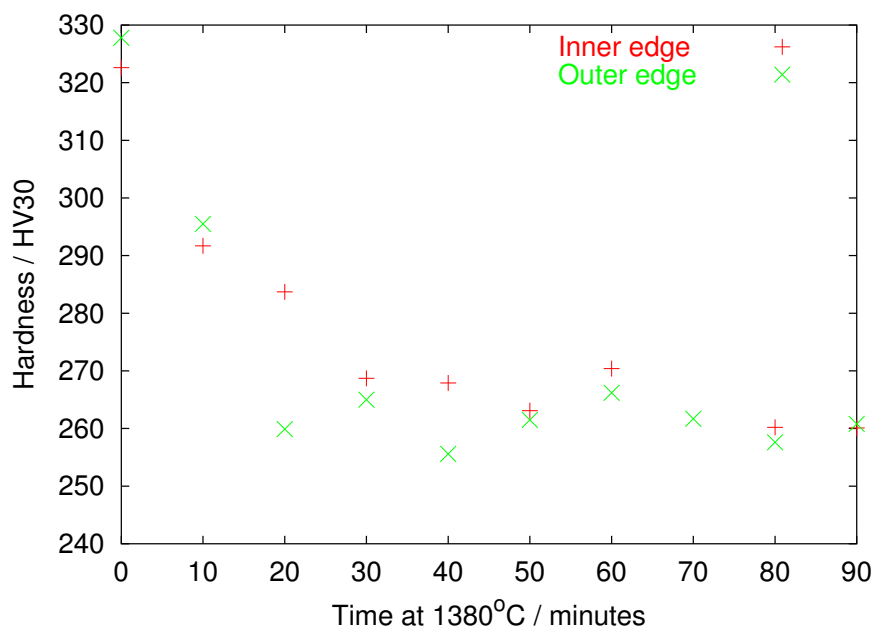
Figure 10.8: Hardness changes on heating PM2000 at 1380°C.
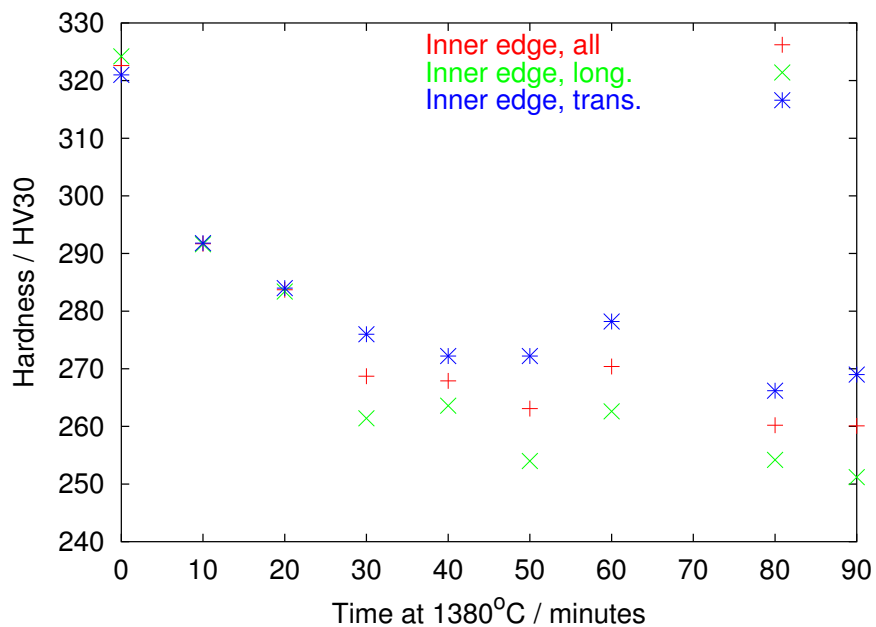
Figure 10.9: Hardness in longitudinal and transverse directions for inner edge.
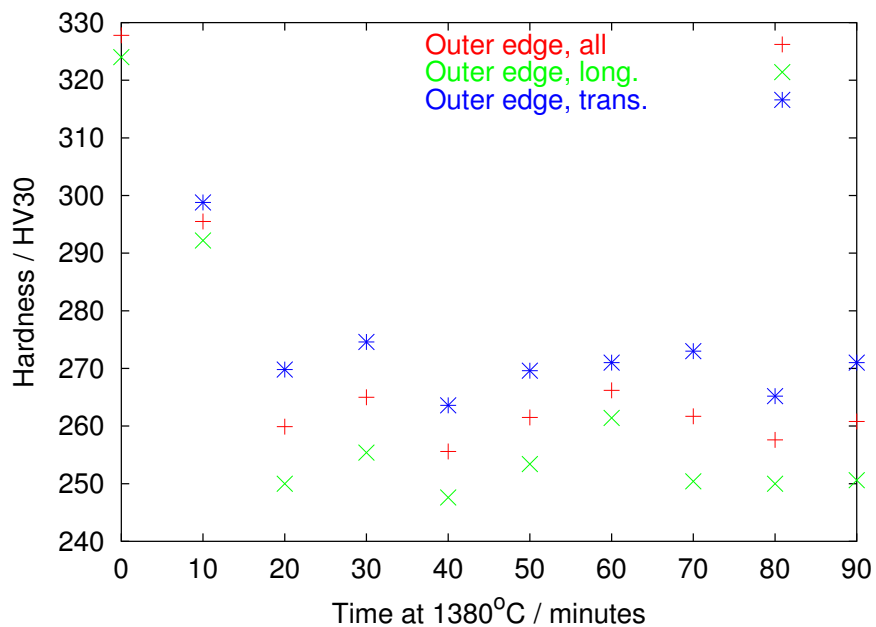
Figure 10.10: Hardness in longitudinal and transverse directions for outer edge.

10.6 Comparison between unrecrystallised, melted and recrystallised PM2000

Initially, the magnetic properties of the unrecrystallised, melted and fully recrystallised (90 minute) sample were compared.

10.6.1 Hysteresis

Hysteresis loops were measured using a VSM on cylindrical samples of length 10 mm and diameter 3 mm. The maximum available magnetising field, 8×10^5 A m^{-1}, was applied to ensure complete saturation. Figure 10.11 shows the central regions of these loops, including the coercive field and remanent magnetisation. Unrecrystallised samples have greater H_C and M_R than either recrystallised or melted samples.

The hysteresis loops in Figure 10.11 are distorted towards the edges of the plot. This effect is believed to be caused by the VSM itself, since it has been observed in other data sets acquired using the apparatus. The loop also appears to be offset on the axes, since the positive and negative H_C and M_R do not have the same magnitudes. In addition, H_C and M_R were found to depend strongly on the rate of change of applied field;[1] this should not occur at the rates used in a VSM, so it was suggested that the experiments be repeated using alternative apparatus (Moorthy, personal communication).

Figure 10.12 shows hysteresis loops measured using a more basic laboratory hysteresis unit, which allows a larger sample size than the VSM. The hysteresis is measured as a voltage per unit length of sample. The samples all had the same diameter so this is equivalent to a voltage per unit volume. The difference between the unrecrystallised and the other two samples is clear, and the recrystallised sample is more hysteretic than the melted sample. This suggests that the oxide particles do affect the ease of passage of domain walls.

---

[1]These observations were described in the CPGS dissertation of the present author, 2000.

10.6.2 Barkhausen noise

BN data were obtained with the magnetising field in longitudinal (L) and transverse (T) directions on the unrecrystallised and recrystallised samples, and in two arbitrary perpendicular directions on the melted sample. Figure 10.13 shows the RMS noise envelope for these samples from magnetisation at 4 Hz. In the melted and recrystallised samples, the peaks are close to $H = 0$. The unrecrystallised material has a large peak at around 0.3 A in the longitudinal direction, and much smaller peak at around 0.1 A in the transverse direction. The peak positions indicate that domain wall pinning is stronger in the unrecrystallised sample than the others, as would be expected given the high level of strain in the microstructure.

If the magnetising frequency is decreased from 4 to 2 Hz, the comparative heights of the BN peaks are changed (Figure 10.14). The unrecrystallised longitudinal peak shrinks, but the melted and recrystallised sample peaks remain in approximately the same proportion.

The change in frequency causes large differences in the frequency spectra from the unrecrystallised and recrystallised samples, but little difference for the melted material (Figure 10.15, Figure 10.16). As discussed in Chapter 8, the filter allows through frequencies between 3 and 15 kHz, and a part of the signal immediately below and above this. The melted sample noise level is approximately constant across this window, but both the recrystallised and unrecrystallised samples have a higher level of activity towards the higher-frequency end. Noise frequency is considered to be related to domain wall obstacle spacing (Saquet *et al.*, 1999); this would imply here that the spacing is very similar in recrystallised and unrecrystallised material. This, in turn, leads to the conclusion that oxide particles do act as pinning sites, since the difference in grain boundary spacing between these two samples is several orders of magnitude. However, as discussed in Chapter 8, the filtering window is narrow, and it is believed to exclude frequencies of interest, so it may be that this observation does not give a complete characterisation of the BN behaviour of this material.

10.6.3   Conclusion

This comparison demonstrates that both grain boundaries and oxide particles play a role in the magnetic behaviour of PM2000. Oxide particles affect the hysteresis properties. The inter-particle spacing, rather than the grain size, appears to be the factor controlling the noise frequency. The pinning strength is much greater when the sample is unrecrystallised, owing to the presence of high-energy grain boundaries, dislocations or both. In addition, in this sample, there is a large difference in signal amplitude when magnetising perpendicular and parallel to the tube axis. This may be due to the elongation of the grains along the extrusion direction, which gives a larger spacing between obstacles and a larger possible domain wall jump size in this direction.

10.7   BN across a grain boundary

The coarse grain structure of the recrystallised material allows a comparison of noise signals from the grain interior and across a boundary. Figure 10.17 shows the positions at which measurements were taken, and Figure 10.18 the resulting signals. The peak height is lower when the noise is measured across the grain boundary than along it or in the bulk.

10.8   Recrystallisation sequences

The BN behaviour of intermediate stages between unrecrystallised and fully recrystallised material were studied. In these experiments, a different set of ferrite pieces was used from in the experiment described above, giving some differences in the results. Measurements were made at several positions on each sample to test the influence of grain boundaries and recrystallised and unrecrystallised regions on the BN signal.

10.8.1 Unrecrystallised sample

This sample required an amplification of 70 dB to obtain a visible signal; this is in contrast to the previous set of experiments in which peaks could be seen at a much lower amplification. The reason for this may be the differences in ferrite pole piece geometry.

In Figure 10.19, two types of behaviour are observed: a smaller peak closer to zero current, and a larger peak in the higher-current range. All the transverse measurements show the former type of behaviour, but in the longitudinal direction, examples of both types can be seen. It appears that BN behaviour depends very much on position in this sample.

10.8.2 Effect of heat treatment

Figure 10.20 shows a comparison between noise signals in the unrecrystallised region and on the boundary between recrystallised and unrecrystallised material in the transverse direction. The gain used in this measurement is still 70 dB but the boundary region gives larger, more uniform, lower-field signals than the unrecrystallised area. In the longitudinal direction, too, there is a clear difference between these regions but in this case, the signals are much larger, requiring only a gain of 40 dB (Figure 10.21).

After 20 minutes of heat treatment, the gain could again be reduced, to 5 dB. The difference between longitudinal and transverse behaviour decreased (Figure 10.22). Despite the presence of a small unrecrystallised region, the positions of the peaks were much more uniform than in the samples described previously.

The longest heating time for which an unrecrystallised region was present was 30 minutes. When the signal was measured in the longitudinal direction, there was a clear difference in peak position from the recrystallised and unrecrystallised regions and the boundary (Figure 10.23).

In the samples heated for longer times than this, measurements were made within grains and across grain boundaries to test whether the presence of a boundary always affected the signal in the same way as found previously (§ 10.7). However, no consistent relationship could be found between peak

amplitudes or positions and the presence of grain boundaries in the longi-
tudinal direction. Peaks measured along grain boundaries in the transverse
direction tended to be slightly larger than those measured elsewhere. This
is illustrated in Figure 10.24 for a 70 minute heat treatment, but was not
observed in all the samples.

In general, the repeatability between measurements can be very poor,
with large differences in peak height and position arising from neighbouring
regions on the same grain. It may be that variations in oxide particle content
are responsible, but this is unlikely since the volume sampled by the BN
probe is very large relative to the particle volume and spacing. Much more
likely is that the variations arose from the measurement technique. As noted
in Chapter 8, using the equipment requires a certain amount of skill and
experience, and the results are affected by the quality of grinding of the
ferrite pieces. The measurements discussed here were made earlier than those
discussed in Chapter 8, using an older, less well ground set of ferrite pieces,
so this may have caused the lack of repeatability.
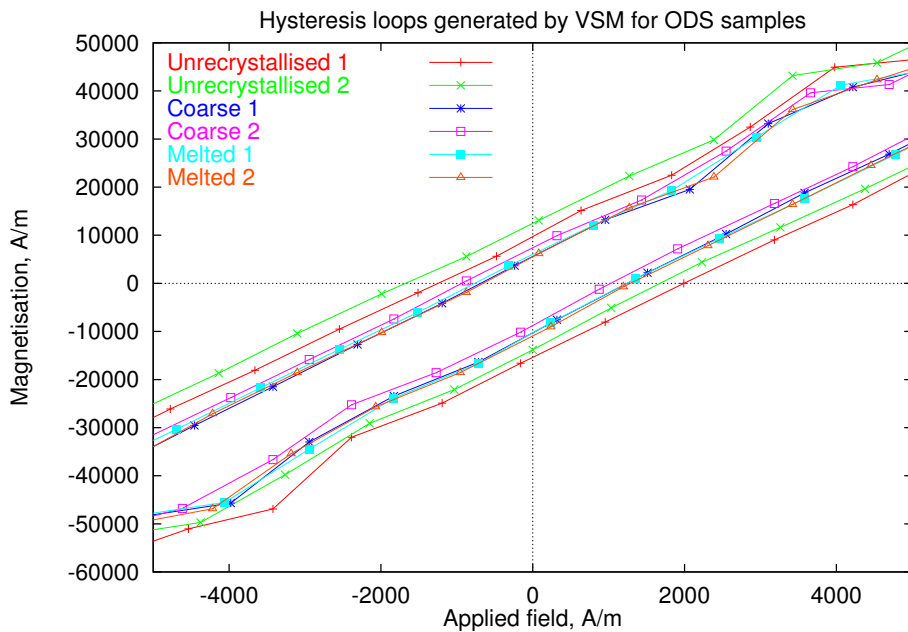
Figure 10.11: Magnetic hysteresis loops as measured by VSM.
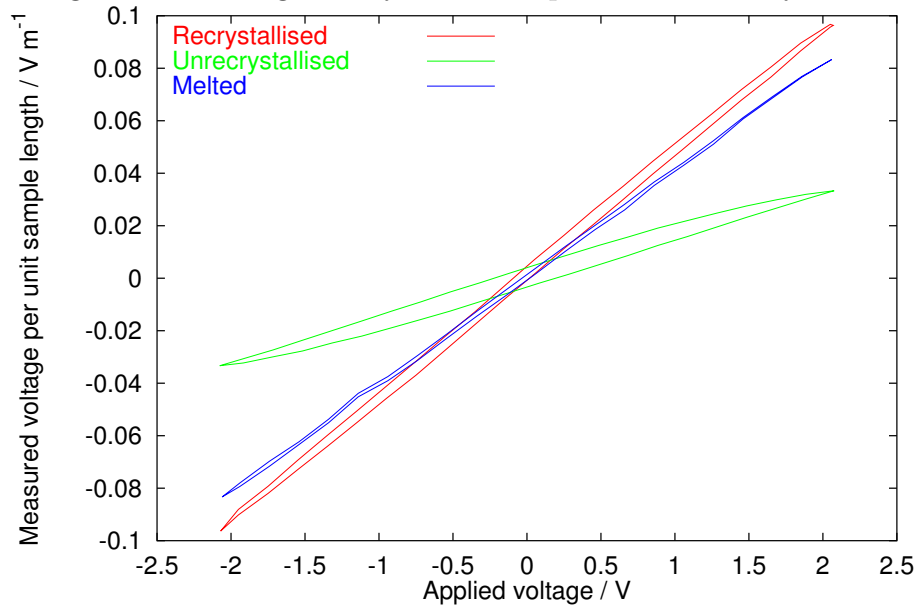
Figure 10.12: Magnetic hysteresis loops as measured by hysteresis unit.
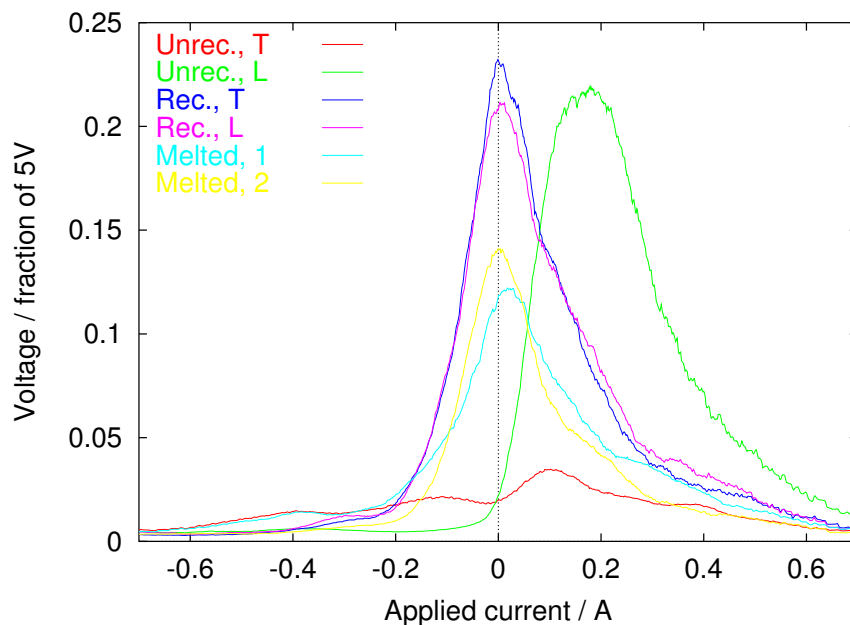
Figure 10.13: BN signals from unrecrystallised, recrystallised and melted PM2000 magnetised at 4 Hz.
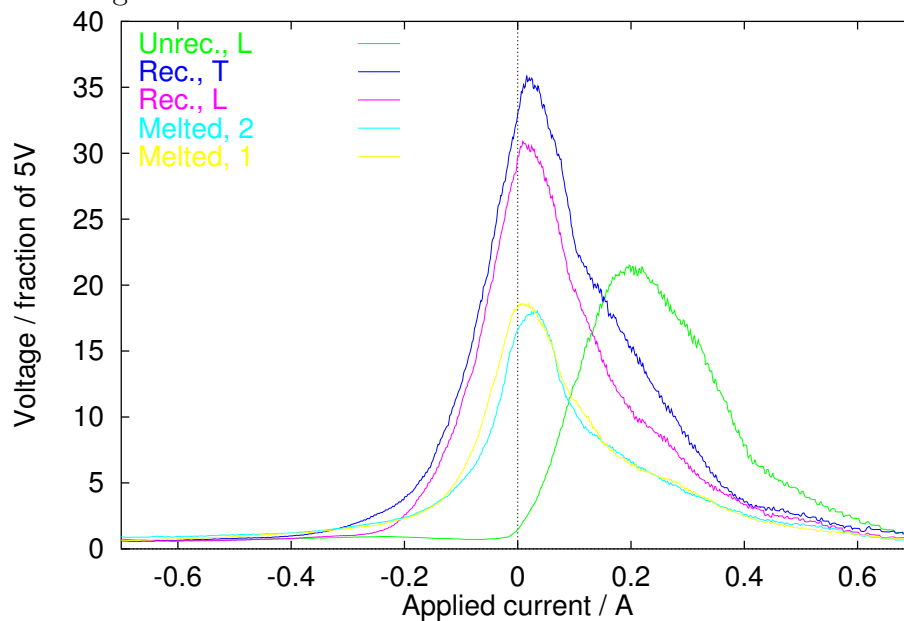
Figure 10.14: BN signals from unrecrystallised, recrystallised and melted PM2000 magnetised at 2 Hz.
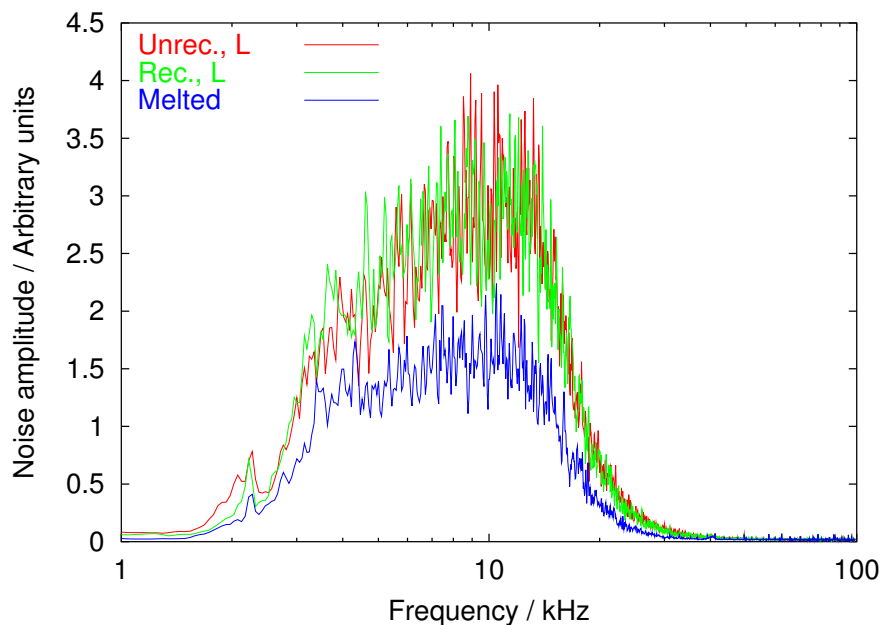
Figure 10.15: Frequency spectra from unrecrystallised, recrystallised and melted PM2000 magnetised at 4 Hz.
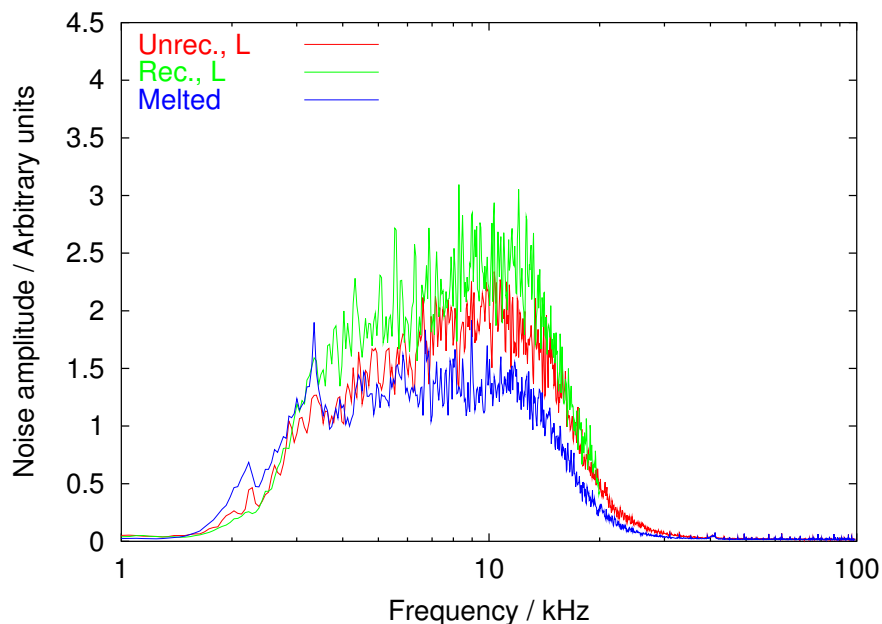
Figure 10.16: Frequency spectra from unrecrystallised, recrystallised and melted PM2000 magnetised at 2 Hz.
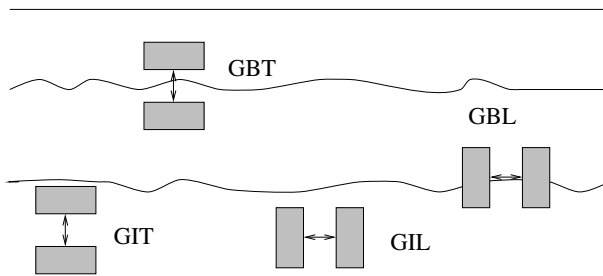
Figure 10.17: Positions in which Barkhausen signal was measured. GB, GI are grain boundary and grain interior; L and T are longitudinal and transverse.
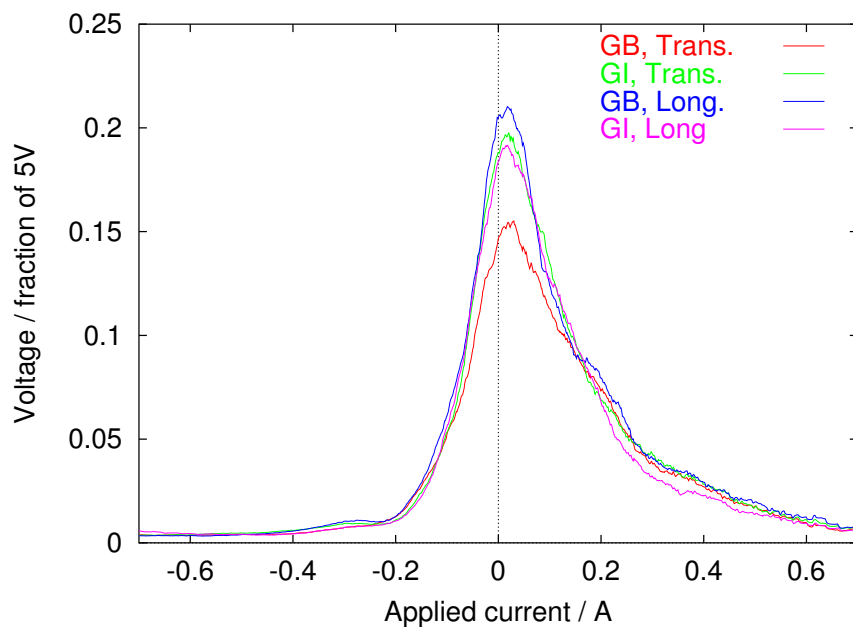
Figure 10.18: Effect on Barkhausen signal of magnetising across a grain boundary (GB) or grain interior (GI) in recrystallised PM2000.
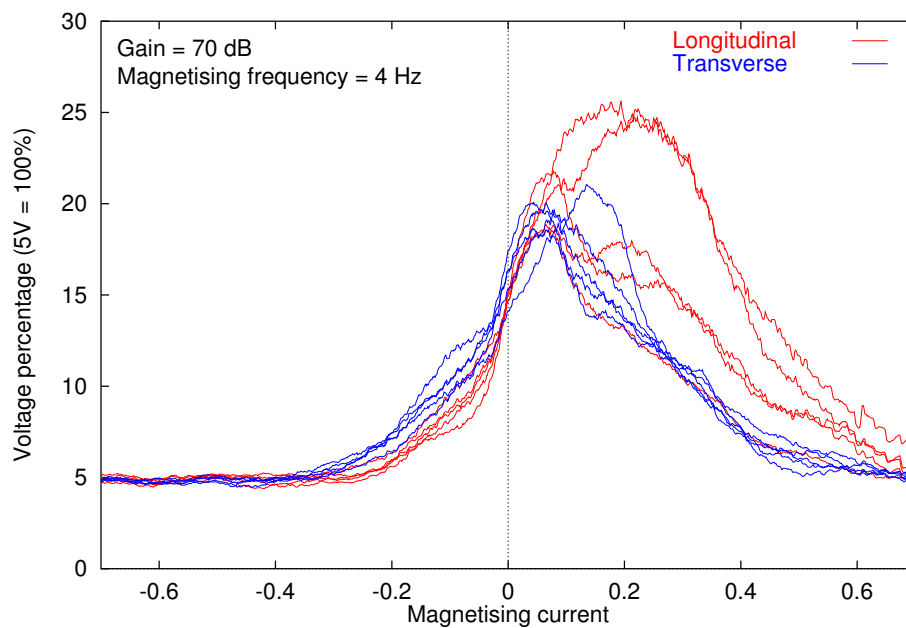
Figure 10.19: BN signal from unrecrystallised sample.
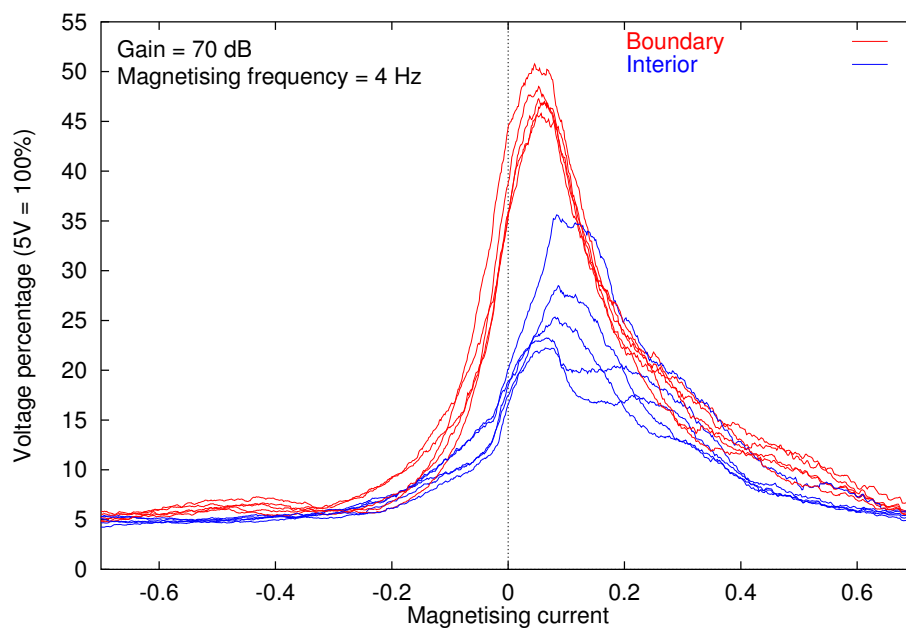
Figure 10.20: BN signals from samples heated at 1380°C for 10 minutes, measured perpendicular to tube length.
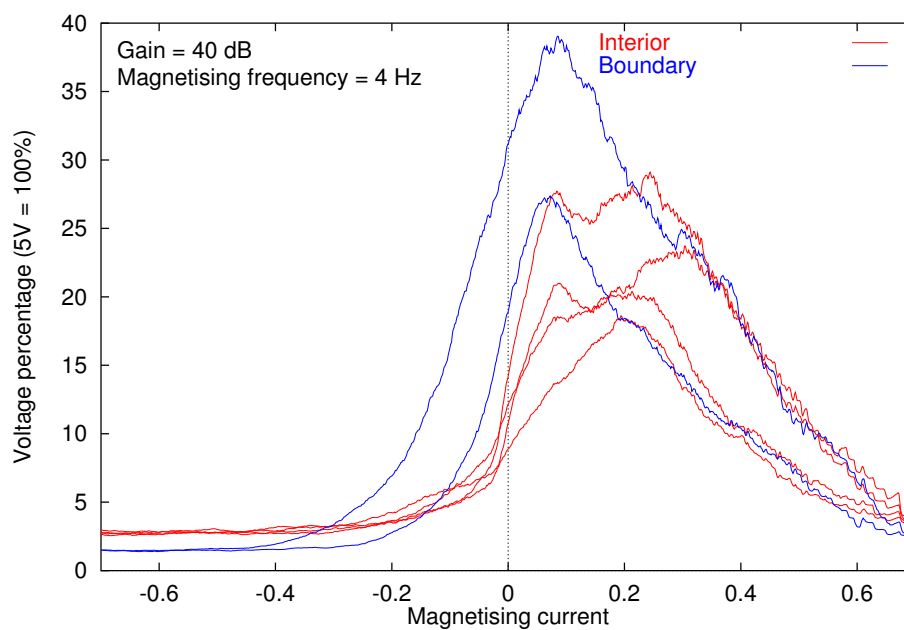
Figure 10.21: BN signals from samples heated at 1380°C for 10 minutes, measured parallel to tube length.
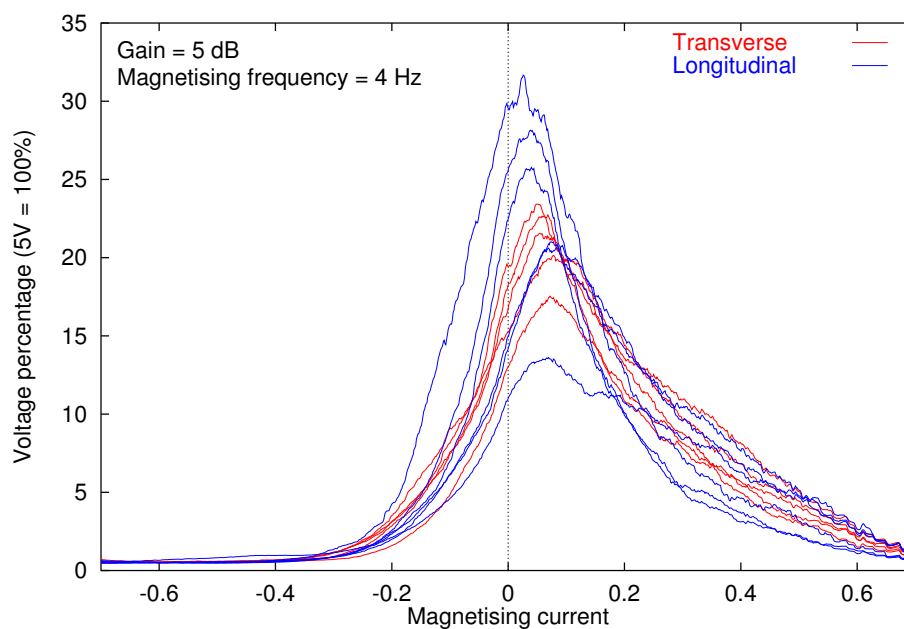
Figure 10.22: BN signals from samples heated at 1380°C for 20 minutes.
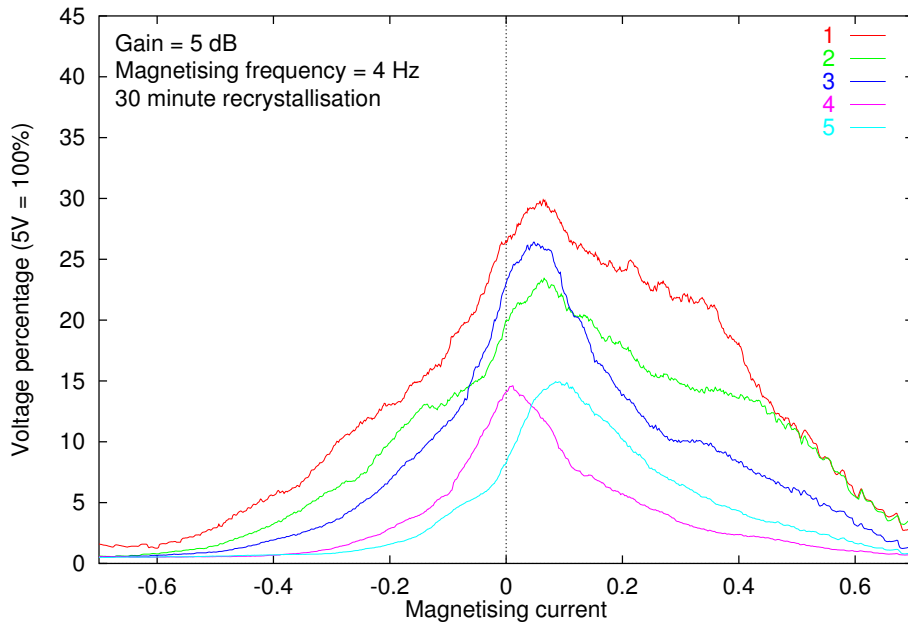
Figure 10.23: BN signals from samples heated at 1380°C for 30 minutes, measured in longitudinal direction. Line 4 was measured on the recrystallised/unrecrystallised boundary, line 5 in the unrecrystallised region, and the others in the recrystallised region.
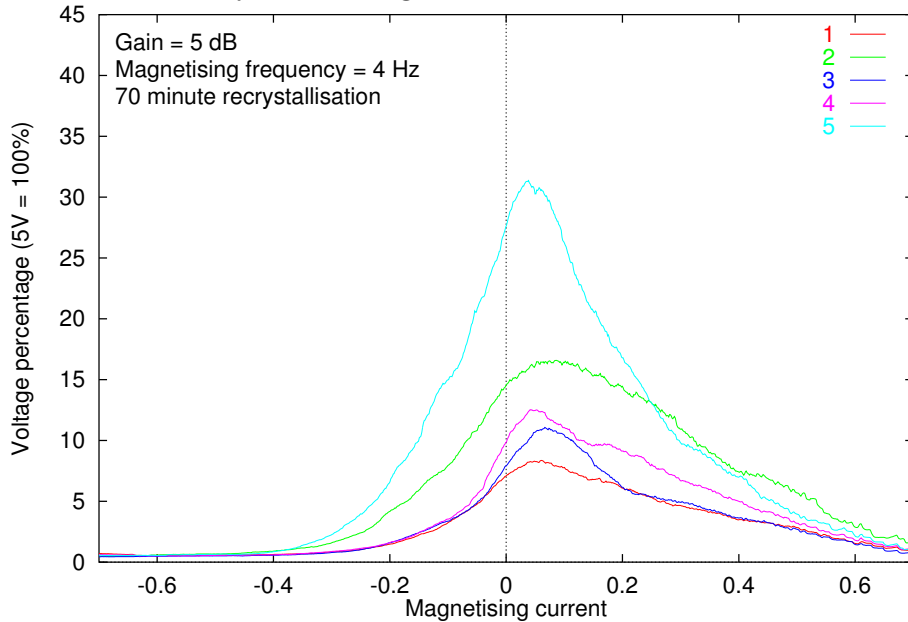
Figure 10.24: BN signals from samples heated at 1380°C for 70 minutes, measured in longitudinal direction. Lines 2 and 4 are signals measured along grain boundaries, and the others come from within the grains.

10.9   Tests on unprepared samples

Pieces of the recrystallised material in their original tube-section shape were also tested to determine whether it was possible to obtain a meaningful signal without sample preparation, since this would be useful for nondestructive testing. Because of the tube and probe geometry, it was only possible to take BN measurements in the longitudinal direction.

The outer surface was smooth, so measurements could be obtained easily, but the inner surface was irregular and posed greater difficulty in measurement. However, two or three measurements could be taken on the inner and outer surfaces of a series of samples: unrecrystallised and 20, 30 and 80 minutes.

A pronounced difference in BN signal amplitude between inner and outer surfaces was observed in the unrecrystallised, 20 and 30 minute samples. The amplification required to obtain a signal was 10 or 20 dB on the outer surface, but 70 dB on the inner surface (Figure 10.25). By contrast, the 80 minute sample requires only 10 dB amplification on both surfaces. The inner edge is more heavily deformed during extrusion, is the last part of the sample to be reached by the recrystallisation front, and is therefore highly stressed until recrystallisation is complete.

These changes are very obvious and could be used as a simple test for full recrystallisation in this material, should one be required. Examination of the actual noise signals shows that the characteristic high-field peak of the unrecrystallised material only occurs on the outer surface, and on the inside, this peak is close to an applied current of zero (Figure 10.26, Figure 10.27). The reason for this is not clear.
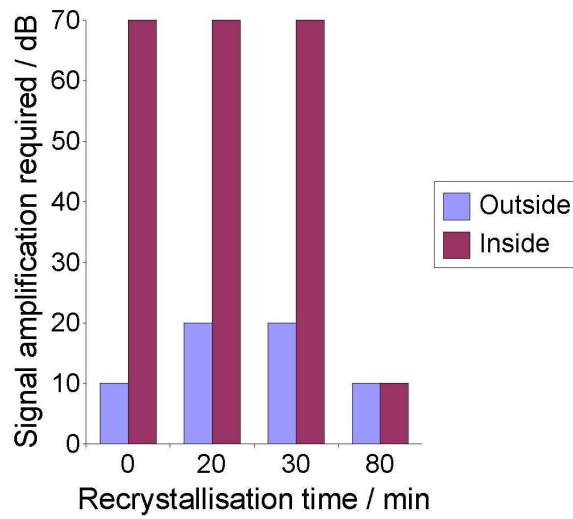
Figure 10.25: The amplifications needed for a visible signal from unprepared samples of PM2000.
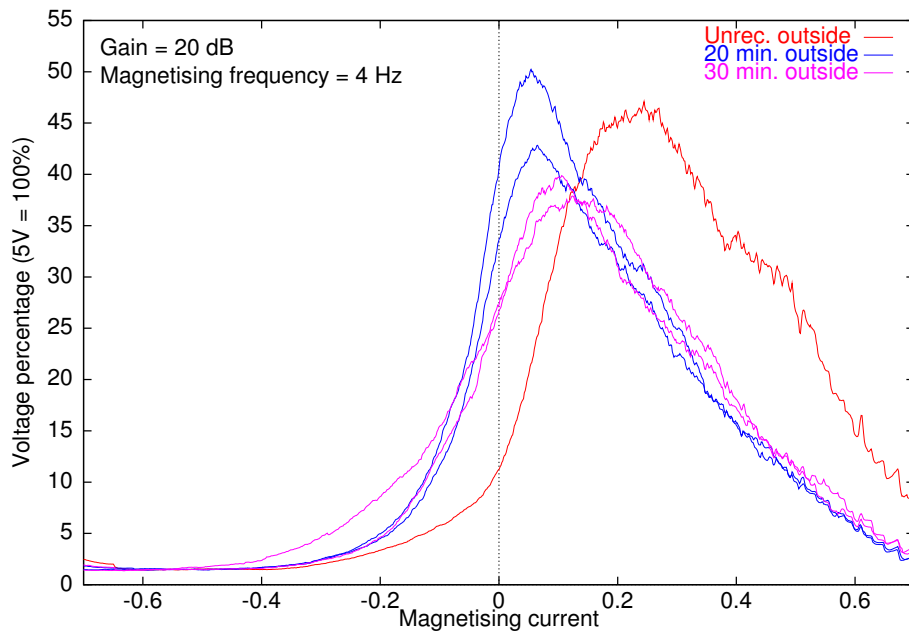
Figure 10.26: Barkhausen signal for outer surfaces of curved samples.
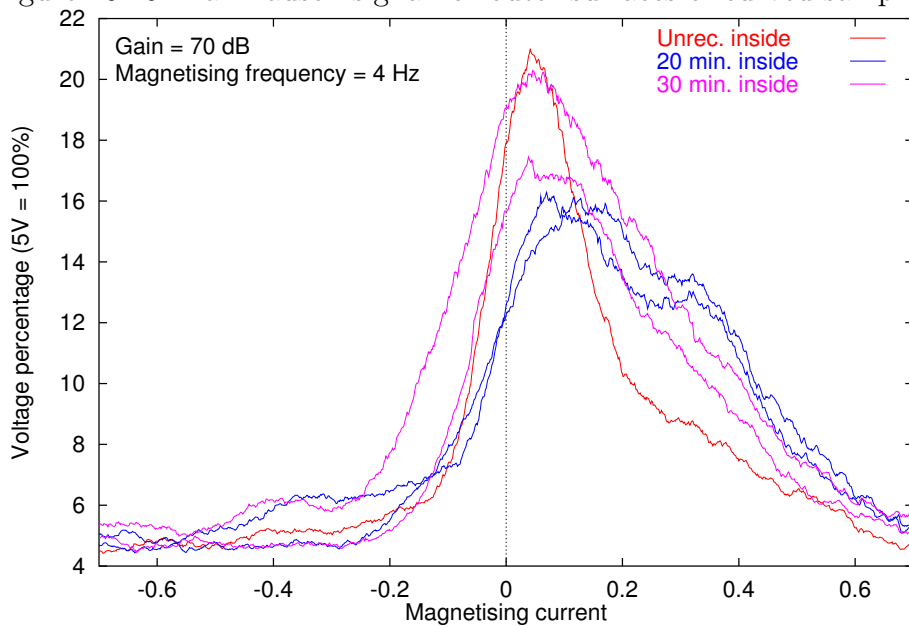
Figure 10.27: Barkhausen signal for inner surfaces of curved samples.

10.10 Conclusions

The transformation from a fine- to a coarse-grained microstructure gives a clear change in BN behaviour, even on unprepared, curved tube sections. The oxide particles in the microstructure also have an effect on magnetic properties, although this is more obviously visible in hysteresis than in BN measurements. Recrystallised and unrecrystallised regions within the same sample could also easily be discerned on the basis of their BN behaviour. A large difference between longitudinal and transverse noise signals was observed in unrecrystallised material, but this decreased on recrystallisation. The changes in BN are not directly related to the hardness, because the oxide particles influence the hardness strongly, but the BN only weakly.

The effect of grain boundaries in recrystallised PM2000 has not been clarified. Initial studies gave a clear difference between noise amplitude when measured across a grain boundary and within the bulk, but attempts to reproduce this result on other samples did not succeed. Overall, the repeatability seemed rather poor.

As mentioned in Chapter 8, the frequency filtering range used in these measurements is narrow and there is the possibility of important information going unrecorded. If possible, these experiments should be repeated using apparatus with a larger frequency range to check the conclusions.

Chapter 11

Summary, Conclusions and Suggestions for Further Work

11.1   Summary and conclusions

The existing literature on the dependence of magnetic properties on microstructure has been reviewed. The consensus from this is that particles, dislocations and grain boundaries all affect the domain wall behaviour. The effect of particles depends on their size and is most pronounced when they are evenly spaced. Dislocations interact with domain walls and appear to suppress domain nucleation and annihilation, making a deformed sample more difficult to saturate than an annealed sample of the same material. Grain boundaries appear to exert a weaker pinning effect than carbides or dislocations, but they can nonetheless limit domain wall jump sizes.

In as-quenched or normalised and air-cooled ferritic steel, the RMS Barkhausen noise signal is a small peak at a high applied field. On tempering, this increases in height and moves to a lower field. Prolonged tempering causes splitting into two peaks. This was attributed to separate distributions of pinning strengths from grain boundaries and carbides. On tempering, the pinning strength of grain boundaries decreases, and that of carbides increases.

Using this interpretation, a model has been developed based on two statistical distributions of pinning site strengths. The first attempt at modelling treated these both as normal distributions, and the second (Model 2) used a log-normal distribution for the weaker sites. Both models fitted published

data well, but linear relationships were observed between Model 2 fitting parameters and the dimensions of microstructural features.

Samples of austenitised, quenched and tempered $2\frac{1}{4}$Cr1Mo power plant steel were prepared. Changes in microstructure and hardness were slow at lower tempering temperatures, but accelerated at higher temperature. 11Cr1Mo steel samples, which had been heated for several thousands of hours, showed a very gradual change in hardness and no discernible microstructural coarsening. Orientation imaging microscopy observations on $2\frac{1}{4}$Cr1Mo samples tempered at 600°C revealed that the main change occurring was a strain reduction, which appeared as an increase in image quality. Even after tempering for over 250 hours, the relationships from the martensitic structure were preserved. Blocks, consisting of slightly misoriented groups of laths, often had $\Sigma 3$ relationships with their neighbours within a packet. It is expected that, as the dislocation density reduces during tempering, it will become progressively easier for a domain wall to move through the structure.

The BN peaks obtained from these samples were different in shape from those observed previously on tempered $2\frac{1}{4}$Cr1Mo steel. Peak-splitting had been expected after prolonged tempering in the $2\frac{1}{4}$Cr1Mo samples, but it was not observed; neither could it be seen in tempered plain-carbon steel samples which were known to give a double peak using other apparatus. It was suspected that the filtering in the apparatus used in this study excluded important low-frequency information. Analysing only low-frequency noise gave evidence of a second peak at high current values.

The BN peak moves toward lower currents with larger Larson-Miller parameter P in the $2\frac{1}{4}$Cr1Mo samples. In the 11Cr1Mo steel, the peak remains at a position close to that of the as-quenched $2\frac{1}{4}$Cr1Mo samples, even after prolonged tempering. This agrees well with the lack of microstructural change and the very small hardness change in this sample.

Model 2 was fitted to the new experimental data, and in all cases, a good fit was obtained. The model parameter characterising the pinning strength of the weaker pinning points decreased with P, following the same curve shape as the peak positions, in the $2\frac{1}{4}$Cr1Mo steel. This weaker distribution is

believed to arise from pinning by grain boundaries. Taking into account the optical and OIM measurements, it can be concluded that the pinning strength of this distribution is related to the degree of strain in the microstructure, and in particular the dislocation density at lath and grain boundaries. As this is decreased by tempering, domain wall motion becomes easier. The pinning strength of the distribution attributed to carbides had a minimum at an intermediate value of P. This may be associated with the dissolution of Fe_3C and the precipitation of fine particles of more stable carbides, since it occurs at an appropriate value of P as determined from the carbide stability diagram.

The modelling parameter values also suggested that the number of grain- or lath-boundary pinning sites increased with greater severity of tempering. In reality, the opposite is likely, since lath boundaries become less well defined on tempering. The initial assumptions made when developing the model were very simple, so it may be necessary to modify some of these to obtain a physically meaningful model of the number of sites.

The fitting parameters for the 11Cr1Mo steel lay in a different regime from those of the $2\frac{1}{4}$Cr1Mo steel, and their variations with P could not be determined because all the points had very similar P values. More data, from a wide range of tempering conditions, are needed to study this.

In the ODS alloy, it was possible to isolate the effects of grain boundaries and particles, and to demonstrate that both influence magnetic properties. However, possibly because of the small size of the particles in this material, grain boundaries dominated the Barkhausen noise behaviour. The Barkhausen peak moves from a higher to a lower applied current on re-crystallisation from a fine-grained, heavily strained microstructure to coarse columnar grains. This is comparable to the change in peak position occurring on tempering of $2\frac{1}{4}$Cr1Mo steel, and lends support to the interpretation that the $2\frac{1}{4}$Cr1Mo steel BN behaviour is mainly due to effects at grain boundaries.

In summary, the large Barkhausen noise peak observed in these steels is believed, on the basis of experiment and modelling, to originate from domain wall interactions with grain and lath boundaries. During tempering, the dislocation density at these boundaries decreases, and this reduces their pinning

strength. The peak therefore shifts to a lower field. The peak position, and the modelling parameter based on this, decrease smoothly with increasing severity of tempering, as characterised by the Larson-Miller parameter.

11.2 Future work

11.2.1 Experimental work

Since there is a clear relationship between BN peak position and P in the $2\frac{1}{4}$Cr1Mo steel, it would be interesting to investigate whether similar relationships exist in other steel compositions, including an extension of the existing work on 11Cr1Mo. Comparisons with samples which are in an unsatisfactory microstructural condition, both overcoarsened and creep-deformed, should be obtained so that criteria for a safe condition can be determined.

Two new sets of BN measuring apparatus, of types (a) and (b) in Figure 4.2, are being built at the University of Newcastle. The filtering ranges of these will be set to allow analysis of low-frequency noise. Repeating the experiments in this study using the new apparatus should enable high-field, low-frequency peaks to be detected where these exist. Careful characterisation of the effects of changing experimental conditions should be carried out to enable repeatability between results. Once this has been achieved, a wide variety of samples can be tested to verify existing interpretations of the role of microstructure in Barkhausen noise, and to gain new insights.

Time limitations prevented a detailed investigation of the carbides in the $2\frac{1}{4}$Cr1Mo steel in this study. Carbon replica measurements can be used to measure particle shapes and sizes, and the identity of the species determined using electron diffraction in the TEM. These can be compared with BN signals obtained from a full frequency range. As Moorthy *et al.* (1998) suggested, it may be possible to relate changes in the BN behaviour to the dissolution of the fine needles of M_2X which are beneficial to creep properties, and the precipitation of spheroidal carbides in their place. This would be extremely useful for estimation of the creep resistance of the microstructure.

Finally, magnetic domain imaging, using the techniques described in § 3.4,

could be used to give a more complete understanding of the interaction processes between domain walls and microstructural features in these steels.

11.2.2 Modelling

The Model 2 average pinning site strength values have clear relationships with microstructural or tempering parameters, but the other parameters, characterising the number of sites and the distribution widths, are less obviously related to microstructure. This may well be due to the assumptions used in the model, so it would be useful to test modifications to these, to attempt to produce a more physically reasonable model. For example, it may be necessary to introduce a demagnetising field, a variable number of domain walls, or a more complex arrangement of pinning sites.

Modification of the model fitting program is also necessary to eliminate unphysical solutions. This could take the form of constraints on allowable fitting parameter values. A further suggested alteration to the fitting procedure is discussed in the Appendix.

Bibliography

Abe, F., Fourth International Conference on Recrystallisation and Related Phenomena, The Japan Institute of Metals, 1999, 289–294

Abe, F., Proceedings of Ultra-Steel 2000, National Research Institute for Metals, Tsukuba, Japan, 2000, 119–129

Adams, B. L., Wright, S. I. & Kunze, K., *Metallurgical Transactions A*, **24A** (1993), 819–831

Alessandro, B., Beatrice, C., Bertotti, G. and Montorsi, A., *Journal of Applied Physics*, **68(6)** (1990), 2901–2907

Alessandro, B., Beatrice, C., Bertotti, G. & Montorsi, A., *Journal of Applied Physics*, **68(6)** (1990), 2908–2915

Andrews, K. W. & Hughes, H., *J. Iron Steel Inst.*, **193** (1959), 304–311

Andrews, K. W., Dyson, D. J. & Keown, S. R., 'Interpretation of electron diffraction patterns', Hilger and Watts, London (1967)

Anglada-Rivera, J., Padovese, L. R. & Capó-Sanchez, J., *Journal of Magnetism and Magnetic Materials*, **231** (2001), 299–306

Ara, K., 'Evaluation of ferrous material properties using Barkhausen noise', ISIJ Special Symposium 'Development of nondestructive evaluation methods using magnetic properties', March 2002

Bibliography

Ashby, M. F. & Jones, D. R. H., 'Engineering Materials 1: An Introduction to their Properties and Applications', Pergamon (1989)

Astié, B., Degauque, J., Porteseil, J. L. & Vergne, R., *IEEE Transactions on Magnetics*, **MAG-17(6)** (1981), 2929–2931

Astié, B., Degauque, J., Porteseil, J. L. & Vergne, R., *Journal of Magnetism and Magnetic Materials*, **28** (1982), 149–153

Baker, R. G. & Nutting, J., *Journal of the Iron and Steel Institute*, **192** (1959), 257–286

Balluffi, R. W., Cohen, M. & Averbach, B. L., *Trans Am. Soc. Met.*, **43** (1951), 497–526

Banbury, J. R. & Nixon, W. C., *J. Sci. Inst.*, **44** (1969), 889–892

Barcelo, F., Brachet, J. C. & de Carlan, Y., 'Influence of Prior Austenitic Grain Size on the Microstructure of 9% Cr Martensitic Steel Characterised by EBSD', unpublished work

Barkhausen, H., *Phys. Z.*, **20** (1919), 401–403

Beale, A. D., Jakubovics J. P., Hetherington, M. G., Scruby, C. B., Lewis, B. A. & Davies, K. J., *Journal of Magnetism and Magnetic Materials*, **104–107** (1992), 365–367

Beech, S. M., Selway, J. W. & Batte, A. D., in 2nd Int. Conf. 'Creep and fracture of engineering materials and structures', Swansea, Pineridge Press, 1984, 925–936

Berger, C., Beech, S. M., Mayer, K. H., Staubli, M. & Thornton, D. V., International Joint Power Generation Conference, USA (1993)

Bibliography

Bhadeshia, H. K. D. H., Strang, A. & Gooch, D. J., *International Materials Reviews*, **43(2)** (1998), 45–69

Bhadeshia, H. K. D. H., Proceedings of Ultra-Steel 2000, National Research Institute for Metals, Tsukuba, Japan, 2000, 205–214

Bitter, F., *Physical Review*, **38** (1931), 1903–1905

Bjärbo, A., 'Microstructural Changes in 12 wt. % Cr Steel During Creep', Royal Institute of Technology, Stockholm, Sweden

Blackham, M. N., Alam, M. & Pashley, D. W., *Proceedings of the Royal Society of London*, **A221** (1953), 224–242

Blamire, M., personal communication, 2000

Blaow, M., 'Magnetic Barkhausen Noise and Non-destructive Testing' Postgraduate Conference paper (unpublished work), University of Newcastle, 2001

Blaow, M., personal communication, 2002

Blitz, J., 'Electrical and Magnetic Methods of Nondestructive Testing', Adam Hilger (1991)

Bloch, F., *Phys. Z.*, **3** (1943), 44–76

Bloor, D. & Martin, D. H., *Proc. Phys. Soc.* **B73** (1959) 694

Boersch, H. & Raith, H., *Naturwissenschaften,* **46** (1959) 574

Bollmann, W., 'Crystal Defects and Crystalline Interfaces', Springer, Berlin (1970)

Bragg, W. L., *Proc. Camb. Phil. Soc.* **17**, (1913), 43

Bibliography

Brandon, D. G., Ralph, B., Ranganathan, S. & Wald, M. S. *Acta Metallurgica* **12**, (1964), 813

Brandon, D. G. *Acta Metallurgica* **14** (1966), 1479

Brooks, H., *Physical Review*, **58** (1940), 909–918

Brown, W. F., Jr., 'Micromagnetics', Wiley (1963)

Bunge, H.-J., *Z. Metallk.* **56** (1965), 872

Bunge, H.-J., in 'Preferred Orientation in Deformed Metals and Rocks: an Introduction to Modern Texture Analysis' (Ed. H.-R. Wenk), Academic Press, UK (1985), p. 73

Bussière, J. F., Lord, M. & Nott, M., Non-Destructive Testing, Pergamon Press, p. 1863

Buttle, D. J., Scruby, C. B., Jakubovics, J. P. & Briggs, G. A. D., *Philosophical Magazine A*, **55(6)** (1987), 717–734

Buttle, D. J., Jakubovics, J. P. Briggs, G. A. D. & Scruby, C. B., *Philosophical Magazine A*, **55(6)** (1987), 735–756

Buttle, D. J., Scruby, C. B., Briggs, G. A. D. & Jakubovics, J., *Proceedings of the Royal Society of London A*, **414** (1987), 469–497

Capdevila, C., Chen, Y. L., Lassen, N. C. K., Jones, A. R. & Bhadeshia, H. K. D. H., *Materials Science and Technology*, **17** (2001), 693–699

Capdevila Montes, C., personal communication, 2001

Carey, R., *Proc. Phys. Soc.* **B76** (1960) 567

Carpenter, K. H., *IEEE Transactions on Magnetics*, **27(6)** (1991), 4404–4406

Bibliography

Cerjak, H., Hofer, P. & Schaffernak, *Key Eng. Mater.*, **171-174** (2000), 453

Chen, D-X., Brug, J. A. & Goldfarb, R. B., *IEEE Transactions on Magnetics*, **27(4)** (1991), 3601–3619

Chilton, J. M., Barton, C. J. & Speich, G. R., *J. Iron Steel Inst.* **208** 1970 184–193

Clapham, L., Jagadish, C. & Atherton, D. L., *Acta Metallurgica et Materialia*, **39(7)** (1991), 1555–1562

Clarke, P., personal communication, 2002

Clatterbuck, D. M., Garcia, V. J., Johnson, M. J. & and Jiles, D. C., *Journal of Applied Physics*, **87(5)** (2000), 4771–4773

Cole, D., 'Design of Creep-Resistant Steels', Ph.D. Thesis, University of Cambridge (2000)

Craik, D. J. & Tebble, R. S., 'Selected Topics in Solid State Physics Volume IV: Ferromagnetism and Ferromagnetic Domains', North-Holland (1965)

Cullity, B. D., *Journal of Metals*, **23** (1971), 35–41

Cullity, B. D., 'Introduction to Magnetic Materials', Addison-Wesley (1972)

Curie, M., *Bull. de la Soc. d'Encouragement* 3 (1898)

Darbyshire, J. M. & Barford, J., Central Electricity Research Laboratory Report (1966)

Davis, N., *Journal of Physics D: Applied Physics*, **4** (1971), 1034–1039

Degauque, J. & Astié, B., *Physica Status Solidi (a)*, **74** (1982), 201–210

Bibliography

Degauque, J., Astié, B., Porteseil, J. L. & Vergne, R., *Journal of Magnetism and Magnetic Materials* **28** (1982) 149

Del Moral Hernandez, E., Muranaka, C. S. & Cardoso, J. R., *Physica B*, **275** (2000), 212–215

Devine, M. K. *JOM* (Oct. 1992), 24–30

Dhar, A. & Atherton, D. L., *IEEE Transactions on Magnetics*, **28(6)** (1992), 3363–3366

Dijkstra, L. J. & Wert, C. *Journal of Applied Physics* **79** (1950) 979

Dingley, D. J. & Randle, V., *Journal of Materials Science*, **27** (1992), 4545–4566

Döring, W., *Zeitschrift für Physik* **108** (1938) 137

Dupré, L., Van Keer, R. & Melkebeek, J. A. A., *Journal of Applied Physics*, **85(8)** (1999), 4376–4378

Dupré, L., Sablik, M. J., Van Keer, R. & Melkebeek, J., *Journal of Physics D: Applied Physics*, **35** (2002), 2086–2090

Dykstra, L. J., 'Nonmagnetic Precipitate in a Ferromagnetic Matrix', in 'Magnetism and Metallurgy', ed. A. E. Berkowitz & E. Kneller, Academic Press, New York, 1969

Edmonds, D. V. & Honeycombe, R. W. K., *Journal of the Iron and Steel Institute*, **211** (1973), 209–216

Elliot, C. & Hack, G. A. J., in 'Structural Applications of Mechanical Alloying' (Eds. J. Froes & G. Barbadillo), ASM, Myrtle Beach, USA, 1990, p 15–21

Bibliography

English, A. T., *Acta Metallurgica*, **15** (1967), 1573–1580

Evans, R. W. & Wilshire, B., 'Creep of Metals and Alloys', Institute of Materials (1985)

Evans, R. W. & Wilshire, B., 'Introduction to Creep', Institute of Materials (1993)

Evershed, S., *Journ. IEE*, **63** (1925), 725–821

Ewing, J. A., 'Magnetic Induction in Iron and other Metals', London (1900) 95

Fathers, D. J., Jakubovics, J. P. & Joy, D. C., *Philosophical Magazine A*, **27** (1973), 765–768

Foner, S., *J. Appl. Phys.*, **79(8)** (1996), 4740–4745

Fowler, C. A., Jr., & Fryer, E. M., *Physical Review*, **86** (1952) 426

Fowler, C. A., Jr., & Fryer, E. M., *Physical Review*, **104** (1956), 552–553

Frost, H. J. & Ashby, M. F., 'Deformation-mechanism maps: the plasticity and creep of metals and ceramics', Pergamon Press (1982)

Fujita, N., 'Modelling Carbide Precipitation in Alloy Steels', Ph.D. Thesis, Universtiy of Cambridge (2000)

Gatelier-Rothéa, C., Fleischmann, P., Chicois, J. & Vincent, A., *Nondestr. Test. Eval.*, **8–9** (1992), 591–602

Gatelier-Rothéa, C., Chicois, J., Fougeres, R. & Fleischmann, P., *Acta Materialia*, **46(14)** (1998), 4873–4882

Bibliography

Gingell, A. D. B., Bhadeshia, H. K. D. H., Jones, D. G. & Mawella, K. J. A., *Journal of Materials Science*, **32** (1997), 4815–4820

Globus, A. & Guyot, M., *Physica Status Solidi (b)* **52** (1972), 427

Gourgues, A.-F., Flower, H. M. & Lindley, T. C., *Materials Science and Technology*, **16** (2000), 26–40

Goodenough, J. B., *Physical Review*, **93(4)** (1954), 917–932

Hald, J., in EPRI/National Power Conference 'New steels for advanced plant up to 620°C', The Society of Chemical Industry, Ed. E. Metcalfe, 152–173

Hale, M. E., Fuller, H. W. & Rubinstein, H., *Journal of Applied Physics*, **30(5)** (1959), 789–791

Halmshaw, R., 'Non-destructive testing (2nd Ed.)', Edward Arnold (1991)

Heisenberg, W., *Z. Physik*, **49** (1928), 619–636

Hetherington, M. G., Jakubovics, J. P., Szpunar, J. A. & Tanner, B. K., *Philosophical Magazine B*, **56(5)** (1987), 561–577

Hildebrand, H., *ISIJ International*, **37(1)** (1997), 65–73

Hilzinger, H. R. & Kronmüller, H., *Journal of Magnetism and Magnetic Materials*, **2** (1976), 11–17

Hilzinger, H. R. & Kronmüller, H., *Physica B*, **86-88B** (1977), 1365–1366

Hill, R., Geng, R. S., Cowking, A. & Mackersie, J. W., *NDT&E*, **24(4)** (1991), 179–186

Honda, K. & Kaya, S. *Sci. Rep. Tohoku Imperial University* Series 1, **15** (1926) 721

Bibliography

Honeycombe, R. W. K. & Bhadeshia, H. K. D. H., 'Steels: Microstructure and Properties (2nd Ed.)', Edward Arnold (1995)

Hubert, A. & Schäfer, R., 'Magnetic Domains: The Analysis of Magnetic Microstructures', Springer (2000)

Igarashi, M. & Sawaragi, Y., 'Development of 0.1C-11Cr-3W-3Co-V-Nb-Nd-N Ferritic Steel for USC Boilers, ICOPE '97, Tokyo, Vol. 2., 107–112

Irvine, K. J., Crowe, D. J. & Pickering, F. B. , *Journal of the Iron and Steel Institute* **386** 405

Ishii, R., Tsuda, Y., Yamada, M. & Miyazaki, M. in Advanced Heat Resistant Steel for Power Generation, (Eds. R. Viswanathan & J. Nutting), San Sebastian, Spain, 1998, 277-287

Iwanaga, K., Tsuchiyama, T. & Takaki, S., *Tetsu-to-Hagané* **84**, (1998), 896

Jagadish, C., Clapham, L. & Atherton, D. L., *Journal of Physics D: Applied Physics*, **23** (1990), 443–448

Jakubovics, J. P., 'Magnetism and Magnetic Materials', Institute of Materials (1994)

Janovec, J., Vyrostkova, A. & Svoboda, M., *Metallurgical Transactions A*, **25A** (1994), 267–275

Jiles, D. C. & Atherton, D. L., *IEEE Transactions on Magnetics*, **MAG-19** (1983), 2183–2185

Jiles, D. C. & Atherton, D. L., *Journal of Applied Physics*, **55** (1984), 2115–2120

Jiles, D. C. & Atherton, D. L., *Journal of Magnetism and Magnetic Materials*, **61** (1986), 48–60

Bibliography

Jiles, D. C., *Journal of Physics D: Applied Physics*, **21** (1988), 1186–1195

Jiles, D. C., *Journal of Physics D: Applied Physics*, **21** (1988), 1196–1204

Jiles, D. C., Thoelke, J. B. & Devine, M. K., *IEEE Transactions on Magnetics*, **28(1)** (1992), 27–35

Jiles, D. C., Sipahi, L. B. & Williams, G, *Journal of Applied Physics*, **73(10)** (1993), 5830–5832

Jiles, D. C., 'Introduction to Magnetism and Magnetic Materials (2nd Ed.)', Chapman & Hall (1998)

Kameda, J. & Ranjan, R., *Acta Metallurgica*, **35(7)** (1987), 1515–1526

Kameda, J. & Ranjan, R., *Acta Metallurgica*, **35(7)** (1987), 1527–1531

Kawahara, K., Yagyu, Y., Tsurekawa, S. & Watanabe, T., *Materials Research Society Symposium Proceedings*, **568** (2000), 169–174

Kawahara, K., Ando, Y., Nogiwa, K., Yagyu, Y., Tsurekawa, S. & Watanabe, T., *Annales de chimie Science des materiaux, suppl.*, **27** (2002), S269–S278

Kawahara, K., personal communication, 2002

Kersten, M., *Phys. Z.*, **3** (1943), 44–76

Kersten, M., 'Ferromagnetische Hysterese und Koerzitivkraft', S. Hirsel (1943)

Kim, H. C., Hwang, D. G. & Kim, C. G., *Nondestr. Test. Eval.*, **8–9** (1992), 575–590

Kittel, C. A., *Physical Review,* **76** (1949) 1827

Bibliography

Kittel, C. & Galt, J. K., *Solid State Physics*, **3** (1956), 437–565

Kneller, E., 'Ferromagnetismus', Springer-Verlag (1962)

Krautwasser, P., Czyrsja-Filemonowic, A., Widera, M. & Carsughi, F. *Materials Science and Engineering,* **A177** (1994) 199–208

Krieger Lassen, N. C., Juul Jensen, D. & Conradsen, K., *Mat. Sci. Forum* **157–162**, (1994), 149

Krieger Lassen, N. C., *Materials Science and Technology*, **12** (1996), 837–843

Krill C. E., III & Chen, L.-Q., *Acta Materialia*, **50** (2002), 3057–3073

Kronberg, M. L. & Wilson, F. H., *Metallurgical Transactions,* **185** (1949), 501

Kubon, Z., Foldyna, V. & Vodárek, V., in Proceedings of the fourth international Charles Parsons turbine conference, Eds. A. Strang, W. M. Banks, R. D. Conroy & M. J. Goulette, 309–321

Kuo., K., *Journal of the Iron and Steel Institute*, **173** (1953), 363–375

Kurdjumov, G. & Sachs, G., *Z. Phys.***64** (1930), 325–343

Kurdzylowski & Zielinski, *Metal Science*, **18** (1984), 223–224

Kushima, H., Kimura, K. & Abe, F., *Tetsu-to-Hagané* **85**, (1999), 841

Kuznetsov, I. A., Somova, V. M. & Bashkirov, Yu. P., *Soviet Journal of NDT*, **8** (1982), 506–511

Kwun, H. & Burkhardt, G. L., *J. Appl. Phys.*, **61(4)** (1987), 1576–1579

Landau, L. D. & Lifshitz, E, *Phys. J. Sowjetunion*, **8** (1935), 153–169

Bibliography

Langevin, M., *Annales de Chimie et de Physique*, **5** (1905), 70–127

Lee, S. J., Zhu, B., Lo, C. C. H., Clatterbuck, D. M. & Jiles, D. C., *IEEE Transactions on Magnetics*, **37(4)** (2001), 2340–2342

Lin, I-N., Mishra, R. K. & Thomas, G., *IEEE Transactions on Magnetics*, **MAG-20** (1984), 134–139

Lo, C. C. H., Jakubovics, J. P. & Scruby, C. B., *Journal of Applied Physics*, **81(8)** (1997), 4069–4071

Lo, C. C. H., Jakubovics, J. P. & Scruby, C. B., *IEEE Transactions on Magnetics*, **33(5)** (1997), 4035–4037

Lo C. C. H. & Scruby, C. B., *Journal of Applied Physics*, **85(5)** (1999), 5193–5195

Lo, C. C. H., Lee, S. J., Kerdus, L. C. & Jiles, D. C., *Journal of Applied Physics*, **91(10)** (2002), 7651–7653

Lopez, J. M., Degauque, J., Astié, B., Garigue, J. & Redoules, J. P., 'Corrélation entre différents états de la précipitation de la cémentite et les propriétés magnétiques et magnétomécaniques d'alliages fer pur - carbone', *Mémoires et Études Scientifiques Revue de Métallurgie* (1985)

Lord, A. E., 'Acoustic Emission', in 'Physical Acoustics', Vol. XI (ed. W. P. Mason & R. N. Thurston), Academic Press, 1975

Mager, A., *Z. Angew. Physik* **14(4)** (1962) 230

Maki, T., Tsuzaki, K. & Tamura, I., *Trans. Iron Steel Inst. Jpn*, **20** (1980), 207–214

Bibliography

Mann, S. D., McCulloch, D. G. & Muddle, B. C., *Metallurgical and Materials Transactions A*, **26A** (1995), 509–520

Marder, J. M. & Marder, A. R., *Trans. ASM*, **62** (1969), 1

Martin, J. W., 'Micromechanisms in Particle-Hardened Alloys', Cambridge University Press (1980)

Maruyama, K., Sawada, K., & Koike, J., *ISIJ International*, **41(6)** (2001), 641–653

Masuyama, F., *ISIJ International*, **41(6)** (2001), 612–625

McMichael, R. D., Swartzendruber, L. J. & Bennett, L. H., *Journal of Applied Physics*, **73(10)** (1993), 5848–5850

Mihram, G. A., 'Simulation - Statistical Foundations and Methodology', Academic Press, London (1972)

Mikheev, M. N., Morozova, V. M., Morozov, A. P., Neizvestnov, B. M., Surin, G. V. & Zakharova, G. N., *Soviet Journal of NDT*, **14** (1978), 9–16

Mikheev, M. N., *Soviet Journal of NDT*, **19** (1983), 1–8

Mitra, A., Govindaraju, M. R. & Jiles, D. C., *IEEE Transactions on Magnetics*, **31(6)** (1995), 4053–4055

Moorthy, V., Vaidyanathan, S., Laha, K., Jayakumar, T., Bhanu Sankara Rao, K. & Raj, B., *Materials Science and Engineering*, **A231** (1997), 98–104

Moorthy, V., Vaidyanathan, S., Jayakumar, T. & Raj, B., *Journal of Magnetism and Magnetic Materials*, **171** (1997), 179–189

Bibliography

Moorthy, V., Vaidyanathan, S., Jayakumar, T. & Raj, B., *Philosophical Magazine A*, **77(6)** (1998), 1499–1514

Moorthy, V., Vaidyanathan, S., Raj, B., Jayakumar, T. & Kashyap, B. P., *Metallurgical and Materials Transactions A*, **31A** (2000), 1053–1065

Moorthy, V., Shaw, B. A. & Evans, J. T., 'Effect of Magnetizing and Analysing Frequency on Magnetic Barkhausen Noise', unpublished work, 2001

Moorthy, V., personal communication, 2002

Morris, P. F., personal communication, 2001

Nagashima, T., *Berichte Arbeitsgemeinschaft Ferromagnetisimus* **148** (1959)

Nakai, N., Furuya, Y. & Obata, M., *Materials Transactions, JIM*, **30** (1989), 197–199

Nakashima, H., Proceedings of Ultra-Steel 2000, National Research Institute for Metals, Tsukuba, Japan, 2000, 215–224

Nakashima, H. & Takeuchi, *Tetsu-to-Hagané*, **88(5)** (2000), 73–78

Nakashima, H., Terada, D., Yoshida, F., Hayakawa, H. & Abe, H., *ISIJ International*, **41,** Supplement (2001), S97–S100

Néel, L., *Cahiers de Physique*, **25** (1944), 21–44

Ng, D. H. L., Lo, C. C. H. & Jakubovics, J. P., *Journal of Applied Physics*, **75(10)** (1994), 7009–7011

Ng, D. H. L., Yu, C. C., Qin, C.-D., Lo, C. C. H. & Jakubovics, J. P., *Journal of Applied Physics*, **79(2)** (1996), 6057–6059

Bibliography

Ng, D. H. L., Cheng, K., Cho, K. S., Ren, Z. Y., Ma, X. Y. & Chan, S. L. I.,
 IEEE Transactions on Magnetics, **37(4)** (2001), 2734–2736

Nickel, H., Ennis, P. J. & Wachter, O., p. 237–243, Am. Soc. Met./JSME,
 Pressure Vessels and Piping Conference

Nishiyama, Z., *Sci. Rep. Res. Inst. Tohoku University*, **23** (1934), 637

Nogiwa, K., B. Eng. Thesis, Tohoku University (2000)

Nutting, J. Advanced Heat Resistant Steel for Power Generation, eds
 R. Viswanathan and J. Nutting, Institute of Materials, London, 1999,
 12–30

Okazaki, K. & Conrad, H. , *Trans. JIM* **13** , (1972) 198

Pande, C. S. , *Acta Metallurgica* **35** (1987) 2671

Parakka, A. P., Jiles, D. C., Gupta, H. & Zang, M., *Journal of Applied
 Physics*, **81(8)** (1997), 5085–5086

Pardavi-Horvath, M., 'Magnetic noise, Barkhausen effect' in 'Wiley Encyclo-
 pedia of Electrical and Electronics Engineering', Wiley (1999)

Pasquale, M., Bertotti, G., Jiles, D. C. & Bi, Y., *Journal of Applied Physics*,
 85(6) (1999), 4373–4375

Pfeffer, K. H., *Physica Status Solidi* **19** (1967) 735; **20** (1967) 395; **21** (1967)
 837; **21** (1967) 857

Pickering, F. B., in 'Microstructural development and stability in high
 chromium ferritic power plant steels' (Eds. A. Strang & D. J. Gooch),
 London, The Institute of Materials, 1997, 1–29

Pitsch, W. & Schrader, A., *Arch. Eisenhüttenw.* **29**, (1958), 715

Bibliography

Porteseil, J. L. & Vergne, R., *Journal de Physique*, **40** (1979), 871–881

Preisach, F., *Zeit. Phys.* **94**, (1935), 277

Quested, P. N, Henderson, P. J. & McLean, M., *Acta Metallurgica*, **36(10)** (1988), 2743–2752

Ramesh, A., Jiles, D. C. & Roderick, J. M., *IEEE Transactions on Magnetics*, **32(5)** (1996), 4234–4236

Ramesh, A., Jiles, D. C. & Bi, Y., *Journal of Applied Physics*, **81(8)** (1997), 5585–5587

Randle, V., 'The Measurement of Grain Boundary Geometry', IOP Publishing (1993)

Randle, V., 'The Role of the Coincidence Site Lattice in Grain Boundary Engineering', The Institute of Materials (1996)

Randle, V. & Engler, O., 'Introduction to Texture Analysis: Macrotexture, Microtexture and Orientation Mapping', Gordon & Breach (2000)

Ranjan, R., Jiles, D. C. & Rastogi, P. K., *IEEE Transactions on Magnetics*, **MAG-22(5)** (1986), 511–513

Ranjan, R., Jiles, D. C. & Rastogi, P. K., *IEEE Transactions on Magnetics*, **MAG-23(3)** (1987), 1869–1876

Ranjan, R., Jiles, D. C., Buck, O. & Thompson, R. B., *Journal of Applied Physics*, **61(8)** (1987), 3199–3201

Ranjan, R., Buck, O. & Thompson, R. B., *Journal of Applied Physics*, **61(8)** (1987), 3196–3198

Bibliography

Raynor, D., Whiteman, J. A. & Honeycombe, R. W. K., *Journal of the Iron and Steel Institute*, **1966** (349), 354–

Read, W. T. & Shockley, W., *Physical Review* **78** (1950), 275

Reed-Hill, R. & Abbaschian, R., 'Physical Metallurgy Principles', PWS Kent, Boston (1992)

Rhines, F. N. & Patterson, B. R. *Metallurgical Transactions A* **13A** 1982 985

Robson, J. D., 'Modelling of Precipitation in Power Plant Steels', Ph.D. Thesis, University of Cambridge (1996)

Sablik, M. J. & Jiles, D. C., *IEEE Transactions on Magnetics*, **29** (1993), 2113–2123

Sablik, M. J. & Augustyniak, B., 'Magnetic methods of nondestructive evaluation' in 'Wiley Encyclopedia of Electrical and Electronics Engineering', Wiley (1999)

Sablik, M. J., *Journal of Applied Physics*, **89** (2001), 5610–5613

Sakamoto, H., Okada, M. & Homma, M., *IEEE Transactions on Magnetics*, **MAG-23(5)** (1987), 2236–2238

Sakuma, T., Yong Wey, M. & Nishizawa, T., *Trans Japan. Inst. Met.*, **22** (1981), 733–742

Santoro, A. & Mighell, A. D. *Acta Cryst.* **A29**, (1973), 171

Saquet, O., Chicois, J. & Vincent, A., *Materials Science and Engineering*, **A269** (1999), 73–82

Sarikaya, M., Tokushige, H. & Thomas, G., *Proc. Conf. ICOMAT, Tokyo* (1986) , The Japan Institute of Metals , 613–618

Bibliography

Scherpereel, D. E., Kazmerski, L. L. & Allen, C. W., *Metallurgical Transactions*, **1** (1970), 517–524

Seeger, A., Kronmüller, H., Rieger, H. & Träuble, H, *Journal of Applied Physics*, **35(3)** (1969), 740–748

Senior, B. A., *Materials Science and Engineering*, **119A** (1989), L5–L9

Shi, Y. M., Jiles, D. C. & Ramesh, A., *Journal of Magnetism and Magnetic Materials*, **187** (1998), 75–78

Shibata, M. & Sasaki, H, *Hihakai-kensa (Nondestructive testing)*, **36(10)** (1987), 772–777

Shilling, J. W. & Houze, G. L., Jr., *IEEE Transactions on Magnetics*, **MAG-10(2)** (1974), 195–223

Shilling, J. W. & Soffa, W. A., *Acta Metallurgica*, **26** (1978), 413–427

Sipahi, L. B., Jiles, D. C. & Chandler, D., *Journal of Applied Physics*, **73(10)** (1993), 5623–5625

Sipahi, L. B., *Journal of Applied Physics*, **75(10)** (1994), 6978–6980

Sporer, D. & Lempenauer, K., in 13th International Plansee Seminar (Eds. H. Bildstein & R. Eck), Metallwerk Plansee, Reutte, Austria, 1993, 796–801

Strang, A. & Vodárek, V., *Materials Science and Technology*, **12** (1996), 552–556

Strang, A, Vodárek, V. & Bhadeshia, H. K. D. H., in 'Modelling of Microstructural Evolution in Creep Resistant Materials' (Eds A. Strang and M. McLean), The Institute of Materials, London, 1999, 129–150

Bibliography

Stresstech Oy, http://www.stresstech.fi/

Swartzendruber, L. J., in 'Concise Encyclopedia of Magnetic and Superconducting Materials', ed. J. E. Evetts, Pergamon, 1992

Tanner, B. K., personal communication, 2000

Tanner, B. K., Szpunar., J. A., Willcock, S. N. M., Morgan, L. L. & Mundell, P. A., *Journal of Materials Science*, **23** (1988), 4534–4540

Tex-SEM Ltd., OIM system documentation

Thomson, R. C., 'Carbide Composition Changes in Power Plant Steels as a Method of Remanent Creep Life Prediction', Ph.D. Thesis, University of Cambridge (1992)

Traüble, H., Moderne Probleme der Metallphysik, Ed. A. Seeger, Vol. 2, Springer-Verlag, Berlin (1966)

Träuble, H., 'Crystal Defects in Ferromagnetic Single Crystals', in 'Magnetism and Metallurgy', ed. A. E. Berkowitz & E. Kneller, Academic Press, New York, 1969

Tiitto, S. I., *IEEE Transactions on Magnetics*, **MAG-14(5)** (1978), 527–529

Tillman, C. J. & Edmonds, D. V., Metals Technology, p. 456–461

Timmins, T. & Artz, E., in 'Structural Applications of Mechanical Alloying' (Eds. J. Froes & G. Barbadillo), ASM, Myrtle Beach, USA, 1990, 67–75

Tobin, A. G. & Paul, D. I., *Journal of Applied Physics*, **40(9)** (1969), 3611–3614

Tsurekawa, S., Tanaka, T. & Yoshinaga, H., *Materials Science and Engineering*, **A176** (1994), 341–348

Bibliography

Uesaka, M., Sukegawa, T., Miya, K., Takahashi, S., Echigoya, J., Yamada, K., Kasai, N., Morishita, K., Ara, K., Ebine, N. & Isobe, Y., in 'Relationship between Magnetic and Structural Properties', The Iron and Steel Institute of Japan, 59–66, 2001

Vander Voort, G. F., 'Metallography: Principles and Practice', McGraw-Hill (1984)

Venables, J. A. & Harland, C. J., *Philosophical Magazine*, **27** (1973), 1193–1200

Venables, J. A. & bin-Jaya, R., *Philosophical Magazine*, **35(5)** (1977), 1317–1332

Vodárek, V. & Strang, A., International Conference on Microstructural Stability of Creep Resistant Alloys for High Temperature Plant Applications, Sheffield, UK, 1997

Wall, M. A., Schwartz, A. J. & Nguyen, L., *Ultramicroscopy*, **88** (2001), 73–88

Warburg, E., *Ann. Physik* **13** (1881) 141

Wassermann, G., *Arch. Eisenhüttenwes.*, **6** (1933), 347–321

Watanabe, T., *Metallurgical Transactions A*, **14A** (1983), 531–545

Watanabe, T., *Materials Science and Engineering*, **A166** (1993), 11–28

Watanabe, T., Tsurekawa, S., Matsuzaki, T. & Furuya, Y., in Proceedings of International Symposium on Relationship between Magnetic and Structural Properties: Basis and Applications, Hanamaki, Japan, 2000, 39–46

Weiss, P., *Comptes Rendus de l'Académie des Sciences*, **143** (1906), 1136–1169

Bibliography

Weiss, P., *Journal de Physique*, **6** (1907), 661–690

Weiss, P. & Foex, G., 'Le Magnétisme', Armand Colin (1926)

Wilkinson, A. J. & Dingley, D.J., *Acta Metallurgica et Materialia*, **39** (3047), 3055–

Williams, H. J., *Physical Review*, **70** (1947), 646–647

Williams, H. J., Shockley, W. & Kittel, C., *Physical Review* **80** (1950), 1090

Williams, H. J., Foster, F. G. & Wood, E. A., *Physical Review*, **82** (1951), 119–120

Willcock, S. N. M. & Tanner, B. K., *IEEE Transactions on Magnetics*, **Mag-19(5)** (1983), 2145–2147

Willcock, S. N. M. & Tanner, B. K., *IEEE Transactions on Magnetics*, **Mag-19(5)** (1983), 2265–2270

Woodhead, J. H. & Quarrel, A. G., *Journal of the Iron and Steel Institute*, **203** (1965), 605–620

Wright, S. I., *Journal of Computer-Assisted Microscopy*, **5(3)** (1993), 207–221

Yamada, K., Igarashi, M., Muneki, S. & Abe, F., *ISIJ International*, **42(7)** (2002), 779–784

Yamaura, S., Furuya, Y. & Watanabe, T., *Acta Materialia*, **49** (2001), 3019–3027

Yardley, V. A., 'Changes in Magnetic Hysteresis on Tempering of Steels', M.Sci. Dissertation, University of Cambridge (1999)

Bibliography

Yardley, V. A., 'Magnetic Detection of Microstructural Change in Power Plant Steels', CPGS Dissertation, University of Cambridge (2000)

Yi, J-K., Lee, B-W. & Kim, H. C., *Journal of Magnetism and Magnetic Materials*, **130** (1994), 81–91

Yong Wey, M., Sakuma, T. & Nishizawa, T., *Transactions of the Japan Institute of Metals*, **22(10)** (1981), 733–742

Yoshida, F., Terada, D., Nakashima, H. & Abe, H., 'EBSP Observations of Creep Deformed Microstructure of Martensitic Steel', in 'Practical Electron Microscopy and its Application to Materials', Maruzen, 2002

Yoshikawa, K., Iseda, A., Yano, M., Masuyama, F., Daikoku, T. & Haneda, H.: 1st International Conference on Improved Coal-Fired Power Plants, Palo Alto, CA (1986)

Yoshino, M., Tanabe, H., Sakamoto, T., Suzuki, N. & Yaji, Y., *Mat. Sci. Forum.*, **210–213** (1996), 45–54

Zatsepin, N. N., Astashenko, P. P., Potapova, N. A., Kaverin, V. D. & Smirnova, T. M., *Soviet Journal of NDT*, **19** (1983), 158–159

Appendix: Modelling Program

The following pages give the code used for fitting Model 2 to a set of BN data. The principal steps used to determine the fitting parameters are listed below, with the program unit names given in parentheses.

1. The real data are read as (s, y) pairs, where s is the applied field or current, and y the RMS noise voltage (MAIN).

2. The background noise level is found by dividing the y axis into 'bins' and counting the number of s points falling into each bin. The mean background noise is obtained from those points falling in the most highly populated bin and the three bins above and three bins below it on the y axis (NOISE).

3. The onset of the BN peak (S_b) is identified by finding the position at which the background noise is exceeded by a critical amount (BASEL).

4. The s-axis is divided into bins and the mean y value within each bin calculated. Comparison of these values enables determination of whether the data set contains a single peak, double peak or shoulder, and the approximate position of the centres of these. This method is only successful if the number of bins is appropriate; it was found by trial and error that 20 was a suitable number. Following successful identification, the exact s values of the peaks can be found (MAXY2).

5. The peak s value thus identified are used as starting values for the centres of the distributions $e^{<x>} + S_b$ and $< S >_2$. If only a single peak is found by MAXY2, the starting $< S >_2$ is obtained by incrementing $e^{<x>} + S_b$ by a small amount (STARTS).

Appendix

6. Each peak is fitted separately to obtain A and ΔS_2 or Δx values, using only the data from around that peak, and fitting a single-distribution model, which is log-normal for the lower-field peak and normal for the higher-field peak (ADLOG, ADLIN).

7. The starting values obtained by these procedures are sent into the double-peak model for fitting of all seven parameters S_b, $< x >$, $< S >_2$, Δx, ΔS_2, A_1 and A_2 to obtain the best combination of these parameters (TWOPEAK).

The fitting in (6) and (7) is an iterative process. The starting values of the fitting parameters are used to calculate a Barkhausen voltage value for each s value. The error in fitting compared to the real y data is calculated using Equation 5.60. One of the fitting parameters is adjusted at a time. If its original value is Q_i, $(Q_i + 1)/100$ and $(Q_i - 1)/100$ are calculated and the new fitting errors obtained. If one of these gives a smaller error than did Q_i, it is adopted as Q_{i+1}. The process is repeated until a Q value is found whose error is smaller than that for either $(Q + 1)/100$ or $(Q - 1)/100$, *i.e.* a minimum error is found. The next parameter is then adjusted in the same way. When all the parameters have been fitted, the whole cycle is repeated. It was found by experience that it was necessary to force the program to iterate the cycle at least ten times to avoid spurious solutions appearing after one or two iterations.

In the case of Model 1, the procedure was very similar. The calculation for the lower-field peak used a normal rather than a log-normal expression, and the parameter S_b did not appear in the program since it is not necessary to specify such a value for a normal distribution. The 'arbitrary peak-fitting' in Chapter 5 used the same fitting method as Model 1, with the only difference being in the details of the model calculation.

Tests have shown that the same values of the fitting parameters could be obtained using arbitrary starting parameters varying over several orders of magnitude. It therefore appears that steps (4) and (5) are not strictly necessary, although they may reduce computation time. They do not appear to be useful in preventing unphysical solutions from being calculated, since

Appendix

this has occurred occasionally using this program. Now that a large number of real data have been fitted, producing consistent values of the fitting parameters, a more informed choice of starting parameters can be made. This may be as good as, or better than, the use of steps (4) and (5) from the point of view of speed and accuracy.

```fortran
C PROGRAM TO FIT A TWO-PEAK MODEL IN WHICH ONE DISTRIBUTION OF PINNING
C SITE STRENGTHS IS LOG-NORMAL AND THE OTHER IS NORMAL.
C INPUT IS A DATA FILE WHOSE LOCATION IS SPECIFIED IN A TEMPLATE FILE.
C OUTPUTS ARE:    1. A FILE CONTAINING REAL AND FITTED DATA,
C                 2. A LOGFILE WITH DETAILS OF PROGRESS AND ERRORS
C                 3. A GNUPLOT SCRIPT FILE TO AUTOMATICALLY PLOT (1.)

      IMPLICIT NONE
      INTEGER I, M
      REAL S(1000), Y(1000)
      REAL S1, S2
      REAL A1, D1
      REAL A2, D2
      REAL AVSUM
      INTEGER NLINES, IMAX, LIM1, LIM2, IMIN
      REAL SYMAX, YMAX, SYMAX1
      REAL NB
      REAL BL
      INTEGER IBL
      CHARACTER LOC*21
      CHARACTER F*14
      CHARACTER D*14
      CHARACTER SU*14
      INTEGER L1, L2, L3

      LOC = 'C:/Data/Barkhausen02/'

C CREATE A FILE TO DUMP TEMPORARY DATA

      OPEN(3, FILE =LOC//'temp')
      CALL OPEN(F, D, SU, L1, L2, L3)

C READ IN REAL DATA POINTS

      NLINES = 0
      DO 1 I = 1, 1000
         READ(2, *, IOSTAT = M) S(I), Y(I)
         IF (M .LT. 0) THEN
            GOTO 6
         ELSE IF (M .GT. 0) THEN
            WRITE (6,*) 'ERROR IN OPENING FILE'
            WRITE (8,*) 'ERROR IN OPENING FILE'
            GOTO 6
         ENDIF
         NLINES = NLINES + 1
    1 CONTINUE
    6 REWIND(2)

C FIND THE VALUE OF THE NOISE BASELINE

      CALL MAXY(S, Y, 0, NLINES, SYMAX, YMAX, IMAX)
      CALL NOISE(S, Y, NLINES, YMAX, NB)
      CALL BASEL(S, Y, NLINES, BL, IBL, NB)

C OBTAIN STARTING VALUES OF S1 AND S2

      S1 = 1.0
      S2 = 0.0
      CALL STARTS(S, Y, NLINES, SYMAX1, S2, IMIN)
      S1 = LOG(SYMAX1 - BL)

C OBTAIN STARTING VALUES OF A1 AND D1

      IF (IMIN .EQ. 0) THEN
         LIM1 = IBL
         LIM2 = NLINES
         A1 = 0.1
         D1 = 0.1
```

```fortran
      CALL ADLOG(S, Y, A1, D1, S1, BL, AVSUM, LIM1, LIM2, NLINES, NB)

C GIVE SECOND PEAK A SLIGHTLY DIFFERENT STARTING VALUE

      S2 = SYMAX1 + (SYMAX1/100)
      A2 = A1 + (A1/100)
      D2 = D1 + (D1/100)
      ELSE

C FIRST MAXIMUM: FIT PEAK

      LIM1 = IBL
      LIM2 = IMIN
      A1 = 0.01
      D1 = 0.1
      CALL ADLOG (S,Y,A1,D1,S1,BL,AVSUM,LIM1,LIM2,NLINES,NB)

C SECOND MAXIMUM: FIT PEAK

      LIM1 = IMIN
      LIM2 = NLINES
      A2 = 0.01
      D2 = 0.1
      CALL ADLIN(S, Y, A2, D2, S2, AVSUM, LIM1, LIM2, NLINES, NB)
      ENDIF

C WRITE DOWN STARTING VALUES

      WRITE (6,*) 'STARTING VALUES'
      WRITE (6,*) 'BL = ', BL
      WRITE (6,*) 'S1 = ', S1
      WRITE (6,*) 'S2 = ', S2
      WRITE (6,*) 'A1 = ', A1
      WRITE (6,*) 'A2 = ', A2
      WRITE (6,*) 'D1 = ', D1
      WRITE (6,*) 'D2 = ', D2
      WRITE (8,*) 'STARTING VALUES'
      WRITE (8,*) 'BL = ', BL
      WRITE (8,*) 'S1 = ', S1
      WRITE (8,*) 'S2 = ', S2
      WRITE (8,*) 'A1 = ', A1
      WRITE (8,*) 'A2 = ', A2
      WRITE (8,*) 'D1 = ', D1
      WRITE (8,*) 'D2 = ', D2

C FIT THE TWO-PEAK MODEL USING ITERATION METHOD

      CALL TWOPEAK(S, Y, A1, A2, D1, D2, S1, S2, BL, AVSUM, NLINES, NB)
      CALL GNU(F, D, SU, L1, L2, L3, A1, A2, D1, D2, S1, S2, BL)
      END

      SUBROUTINE BASEL(S, Y, NLINES, BL, IBL, NB)

C FIND THE BASELINE OF THE FIRST (LOG) PEAK BY USING A BIGGER-THAN-NOISE
C CRITERION OF 1.25

      IMPLICIT NONE
      REAL S(1000), Y(1000)
      REAL NB, BL
      INTEGER I, NLINES, IBL

      DO 1 I = 1, NLINES
         IF (Y(I) .GT. (NB+0.01)) THEN
            BL = S(I)
            IBL = I
            WRITE(6,*) 'BASELINE FOUND AT ', BL
            WRITE(8,*) 'BASELINE FOUND AT ', BL
            GOTO 2
```

```fortran
         ENDIF
1     CONTINUE
2     RETURN
      END

      SUBROUTINE OPEN(F, D, S, L1, L2, L3)

      IMPLICIT NONE
      CHARACTER LOC*21
      CHARACTER F*14
      CHARACTER D*14
      CHARACTER S*14
      INTEGER L1, L2, L3

      LOC = 'C:/Data/Barkhausen02/'

C READ THE LOCATION OF THE DATA FILE FROM A TEMPLATE

      OPEN(4, FILE =LOC//'Programs/template', STATUS = 'OLD')
      READ(4,*)
      READ(4,*)
      READ(4,9) D
      CALL SHORTEN (D,L1)
      READ(4,9) S
      CALL SHORTEN (S,L2)
      READ(4,9) F
      CALL SHORTEN (F, L3)
      REWIND(4)
      CLOSE(4)
9     FORMAT(A14)

C MAKE FILE TO OUTPUT REAL DATA AND MODEL FIT
      OPEN(1, FILE = LOC//D(1:L1)//'/'//S(1:L2)//'/'//F(1:L3)//
     &'_logfit')
C OPEN REAL DATA FILE
      OPEN(2, FILE = LOC//D(1:L1)//'/'//S(1:L2)//'/'//F(1:L3),
     & STATUS = 'OLD')
C MAKE LOGFILE TO OUTPUT PROGRESS, FITTING PARAMETERS AND ERRORS
      OPEN(8, FILE = LOC//D(1:L1)//'/'//S(1:L2)//'/'//F(1:L3)//
     &'_log.log')
C MAKE GNUPLOT SCRIPT TO PLOT GRAPH WITH FITTING PARAMETERS
      OPEN(7, FILE=LOC//'/Plotfile/logfit'//F(1:L3)//'.gnu')
      WRITE (6,*) 'ANALYSING DATA FROM FILE'//LOC//D(1:L1)//'/'
     &//S(1:L2)//'/'//F(1:L3)//' USING LOG-LINEAR MODEL'
      WRITE (8,*) 'ANALYSING DATA FROM FILE'//LOC//D(1:L1)//'/'
     &//S(1:L2)//'/'//F(1:L3)//' USING LOG-LINEAR MODEL'
      END

      SUBROUTINE SHORTEN(NAME, LEN)

C TO FIND LENGTH OF CHARACTER STRING AND REMOVE BLANK SPACES IN
C FILENAMES

      IMPLICIT NONE
      CHARACTER NAME*14
      CHARACTER*1 A(14)
      CHARACTER*1 BLANK
      PARAMETER(BLANK = ' ')
      INTEGER N, LEN

      DO 1 N = 1, 14
         A(N)  = NAME(N:N+1)
         IF (A(N) .EQ. BLANK) THEN
            GOTO 1
         ELSE
            LEN = N
         ENDIF
1     CONTINUE
```

```fortran
      RETURN
      END

      SUBROUTINE GNU(F, D, S, L1, L2, L3, A1, A2, D1, D2, S1, S2, BL)

C TO WRITE A GNUPLOT SCRIPT TO DISPLAY REAL DATA, MODEL AND FITTING
C PARAMTERS ON SCREEN AND IN MONO AND COLOUR .EPS FILES

      CHARACTER LOC*21
      CHARACTER F*14
      CHARACTER D*14
      CHARACTER S*14
      INTEGER L1, L2, L3
      REAL A1, A2, D1, D2, S1, S2, BL

      LOC = 'C:/Data/Barkhausen02/'

      WRITE(7,*) '# Instructions to Gnuplot - to plot model and'
     &//' real data'
      WRITE(7,*) 'set autoscale'
      WRITE(7,*) 'set nologscale'
      WRITE(7,*) 'set nogrid'
      WRITE(7,*) 'set nolabel'
      WRITE(7,*) 'set key top right Left'
      WRITE(7,*) 'set title "Log-linear two-point model fit for'
     &//LOC//D(1:L1)//'/'//S(1:L2)//'/'//F(1:L3)//'"'
      WRITE(7,*) 'set xlabel "Magnetising current/A "'
      WRITE(7,*) 'set ylabel "RMS Barkhausen voltage/V"'
      WRITE(7,*) 'set label 1 "Model parameters" at graph 0.02, 0.95'
      WRITE(7,*) 'set label 2 "A_1 = ', A1,'" at graph 0.02, 0.90'
      WRITE(7,*) 'set label 3 "A_2 = ', A2,'" at graph 0.02, 0.85'
      WRITE(7,*) 'set label 4 "{/Symbol=14 D}S_1 = ', D1,'" at'
     &//' graph 0.02, 0.80'
      WRITE(7,*) 'set label 5 "{/Symbol=14 D}S_2 = ', D2,'" at'
     &//' graph 0.02, 0.75'
      WRITE(7,*) 'set label 6 "<S>_1 = ', S1,'" at graph 0.02, 0.70'
      WRITE(7,*) 'set label 7 "<S>_2 = ', S2,'" at graph 0.02, 0.65'
      WRITE(7,*) 'set label 8 "b = ', BL,'" at graph 0.02, 0.60'
      WRITE(7,*) 'set xrange [-0.7:0.7]'
      WRITE(7,*) 'set terminal x11'
      WRITE(7,*) 'plot "'//LOC//D(1:L1)//'/'//S(1:L2)//'/'
     &//F(1:L3)//'_logfit" using 1:2 title "Real data" with lines 1'
      WRITE(7,*) 'replot "'//LOC//D(1:L1)//'/'//S(1:L2)//'/'
     &//F(1:L3)//'_logfit" using 1:3 title "Model" with lines 3'
      WRITE(7,*) 'set output  "'//LOC//D(1:L1)//'/'//S(1:L2)//'/'
     &//F(1:L3)//'_log_mono.ps"'
      WRITE(7,*) 'set terminal postscript eps enhanced mono dashed'
     &//'"Helvetica" 20'
      WRITE(7,*) 'replot'
      WRITE(7,*) 'set output  "'//LOC//D(1:L1)//'/'//S(1:L2)//'/'
     &//F(1:L3)//'_log_colour.ps"'
      WRITE(7,*) 'set terminal postscript eps enhanced color solid'
     &//'"Helvetica" 20'
      WRITE(7,*) 'replot'
      WRITE(7,*) 'set terminal x11'
      WRITE(7,*) 'replot'
      WRITE(7,*)
      WRITE(7,*)
      RETURN
      END

      SUBROUTINE MAXY(S, Y, LIM1, LIM2, SYMAX, YMAX, IMAX)

C FINDS THE LARGEST VALUE OF Y IN THE DATA SET

      IMPLICIT NONE
      INTEGER I, LIM1, LIM2, IMAX
      REAL Y(1000), S(1000), SYMAX, YMAX
```

```fortran
      YMAX = 0.0
      SYMAX = 0.0
      IMAX = 0

      DO 1 I = LIM1, LIM2
         IF (Y(I) .GT. YMAX) THEN
            YMAX = Y(I)
            SYMAX = S(I)
            IMAX = I
         ENDIF
 1    CONTINUE
      RETURN
      END

      SUBROUTINE MINY(S, Y, LIM1, LIM2, SYMIN, YMIN, IMIN)

C FINDS THE SMALLEST VALUE OF Y IN THE DATA SET

      IMPLICIT NONE
      INTEGER I, LIM1, LIM2, IMIN
      REAL Y(1000), S(1000), SYMIN, YMIN

      YMIN = Y(LIM1)
      SYMIN = 0.0
      IMIN = 0

      DO 1 I = LIM1, LIM2
         IF (Y(I) .LT. YMIN) THEN
            YMIN = Y(I)
            SYMIN = S(I)
            IMIN = I
         ENDIF
 1    CONTINUE
      RETURN
      END

      SUBROUTINE BIN(S, Y, YMAX, NLINES, COUNT, BINA)

C DIVIDES DATA INTO 'BINS' ACCORDING TO SIZE

      IMPLICIT NONE
      INTEGER I, J, NLINES, COUNT(1000)
      REAL Y(1000), S(1000), YMAX, BINA, BINU, BINL

      BINA = YMAX/REAL(NLINES)
      BINL = 0.0
      BINU = 0.0

      DO 1 I = 1, NLINES
         BINL = BINU
         BINU = REAL(I)*BINA
         COUNT(I) = 0
         DO 2 J = 1, NLINES
            IF ((Y(J) .GE. BINL) .AND. (Y(J) .LT. BINU)) THEN
               COUNT(I) = COUNT(I) + 1
            ENDIF
 2       CONTINUE
 1    CONTINUE
      END

      SUBROUTINE NOISE(S, Y, NLINES, YMAX, NB)

C FINDS THE VALUE OF THE NOISE BASELINE AND LIMITS AROUND IT.

      IMPLICIT NONE
      REAL S(1000), Y(1000), YMAX, BINA
      INTEGER I, NLINES, COUNT(1000), MAXC, IMAXC
```

```fortran
      REAL NB
      REAL BBINUP, BBINDO, NOISUM
      INTEGER INC, J

      NB = 0.0
      MAXC = 0
      IMAXC = 0

C DIVIDE DATA INTO BINS
      CALL BIN(S, Y, YMAX, NLINES, COUNT, BINA)
C FIND BIN WITH LARGEST NUMBER OF DATA POINTS IN IT
C THIS IS THE 'NOISE BASELINE' BIN
      DO 1 I = 1, NLINES
         IF (COUNT(I) .GT. MAXC) THEN
            MAXC = COUNT(I)
            IMAXC = I
         ENDIF
   1     CONTINUE

C FIND AVERAGE OF ALL POINTS THAT ARE IN THIS BIN OR OTHERS AROUND IT
C CHANGE VALUE '3' TO ANOTHER INTEGER TO CHANGE SENSITIVITY.

      BBINUP = REAL(IMAXC + 3)*BINA
      BBINDO = REAL(IMAXC - 3)*BINA

      INC = 0

      DO 2 J = 1, NLINES
         IF ((Y(J) .GE. BBINDO) .AND. (Y(J) .LT. BBINUP)) THEN
            NOISUM = NOISUM + Y(J)
            INC = INC + 1
         ENDIF
   2  CONTINUE

      NB = NOISUM/REAL(INC)
      WRITE (6,*) 'NOISE = ', NB
      WRITE (8,*) 'NOISE = ', NB
      RETURN
      END

      SUBROUTINE MAXY2(S, Y, NLINES, SYMAX1, SYMAX2, YMAX1, YMAX2, IMIN)

C TO FIND THE POSITIONS OF THE PEAK(S) AND MINIMUM IF IT EXISTS

      IMPLICIT NONE
      REAL S(1000), Y(1000)
      REAL AVES(20), AVEY(20), SSUM, YSUM
      REAL AVEM1, AVEM2, AVEM3
      REAL SYMAX1, SYMAX2, SYMIN
      REAL YMAX1, YMAX2, YMIN
      INTEGER NLINES, COUNT, I, J, POINTS
      INTEGER JM1, JM2, JM3, TEMP
      INTEGER IMAX1, IMAX2, IMIN
      INTEGER LIM1, LIM2

C DIVIDE THE POINTS INTO TWENTY GROUPS AND FIND THE AVERAGE.

      POINTS = NLINES/20

      DO 1 J = 1, 20
         COUNT = 0
         YSUM = 0.0
         SSUM = 0.0
         DO 2 I = (J-1)*POINTS, J*POINTS
            YSUM = YSUM + Y(I)
            SSUM = SSUM + S(I)
            COUNT = COUNT+1
   2     CONTINUE
```

```fortran
            AVEY(J) = YSUM/REAL(COUNT)
            AVES(J) = SSUM/REAL(COUNT)
            WRITE(3,*) J, AVES(J), AVEY(J)
    1    CONTINUE

         AVEM1 = 0.0
         AVEM2 = 0.0
         AVEM3 = 0.0
         JM1 = 0
         JM2 = 0
         JM3 = 0

C FIND THE TWO LARGEST VALUES OF THE AVERAGE

         DO 3 J = 1, 20
            IF (AVEY(J) .GT. AVEM1) THEN
               AVEM2 = AVEM1
               JM2 = JM1
               AVEM1 = AVEY(J)
               JM1 = J
            ELSE IF ((AVEY(J) .GT. AVEM2) .AND. (AVEY(J) .LE. AVEM1)) THEN
               AVEM2 = AVEY(J)
               JM2 = J
            ENDIF
    3    CONTINUE
         WRITE (6,*) 'LARGEST TWO VALUES ARE AT ', JM1, JM2
         WRITE (8,*) 'LARGEST TWO VALUES ARE AT ', JM1, JM2


C ARE THE TWO MAXIMA NEXT TO EACH OTHER?

         IF (ABS(JM1 - JM2) .NE. 1) THEN

C IF NOT, THEN WE CAN EASILY FIND THE PEAKS AND THE MINIMUM BETWEEN THEM
C MAKE JM1 THE SMALLER OF THE TWO J-VALUES

            IF (JM1 .GT. JM2) THEN
               TEMP = JM1
               JM1 = JM2
               JM2 = TEMP
            ENDIF

C FIND THE MAXIMUM NEAR J1 PRECISELY

            LIM1 = (JM1-1)*POINTS
            LIM2 = (JM1+1)*POINTS

            CALL MAXY(S, Y, LIM1, LIM2, SYMAX1, YMAX1, IMAX1)

C FIND THE MINIMUM NEAR J2 PRECISELY

            LIM1 = (JM2-1)*POINTS
            LIM2 = (JM2+1)*POINTS
            CALL MAXY(S, Y, LIM1, LIM2, SYMAX2, YMAX2, IMAX2)

C FIND THE MINIMUM SITUATED BETWEEN THESE TWO MAXIMA

            LIM1 = IMAX1
            LIM2 = IMAX2
            CALL MINY(S, Y, LIM1, LIM2, SYMIN, YMIN, IMIN)
            WRITE(6,*) 'MAXIMUM 1 AT ', SYMAX1, ' HEIGHT ', YMAX1
            WRITE(6,*) 'MINIMUM AT ', SYMIN, ' HEIGHT ', YMIN
            WRITE(6,*) 'MAXIMUM 2 AT ', SYMAX2, ' HEIGHT ', YMAX2
            WRITE(8,*) 'MAXIMUM 1 AT ', SYMAX1, ' HEIGHT ', YMAX1
            WRITE(8,*) 'MINIMUM AT ', SYMIN, ' HEIGHT ', YMIN
            WRITE(8,*) 'MAXIMUM 2 AT ', SYMAX2, ' HEIGHT ', YMAX2
         ELSE
```

```fortran
C IF THE TWO MAX AVERAGE VALUES ARE NEXT TO ONE ANOTHER
C TRY AND FIND ANOTHER PEAK IN THE AVERAGE VALUES

         DO 4 J = 2, 19

C IS J THE POSITION OF A PEAK?

            IF ((AVEY(J) .GT. AVEM3) .AND. (AVEY(J) .GE. AVEY(J+1))) THEN

C IS AVEY(J) LESS THAN THE MAX PEAK VALUE? AND IS IT GREATER THAN A
C THRESHOLD VALUE (ARBITRARILY GIVEN AS AVEM1/10 TO ELIMINATE NOISE)?

               IF ((AVEY(J) .LT. AVEM1) .AND. (AVEY(J) .GT. (AVEM1/10)))
     &            THEN

C IF THE NEW J-VALUE IS MORE THAN 1 UNIT AWAY FROM JM1
C THIS SHOULD ONLY FAIL IF THERE ARE 3 PEAKS OF EXACT SAME HEIGHT NEXT
C TO ONE ANOTHER

                  IF (ABS(JM1 - J) .GT. 1) THEN

C DEFINE NEW AVERAGE MAX VALUE AND J VALUE

                     AVEM3 = AVEY(J)
                     JM3 = J
                  ENDIF
               ENDIF
            ENDIF
   4     CONTINUE

C IF WE HAVE OBTAINED A NON-ZERO VALUE OF JM3 FROM THIS PROCEDURE THEN

         IF (JM3 .NE. 0) THEN

C REDEFINE IT AS JM2

            JM2 = JM3

C MAKE JM1 SMALLER THAN JM2

               IF (JM1 .GT. JM2) THEN
                  TEMP = JM1
                  JM1 = JM2
                  JM2 = TEMP
               ENDIF

C FIND PRECISE POSITION OF MAX NEAR JM1

               LIM1 = (JM1-1)*POINTS
               LIM2 = (JM1+1)*POINTS
               CALL MAXY(S, Y, LIM1, LIM2, SYMAX1, YMAX1, IMAX1)

C FIND PRECISE POSITION OF MAX NEAR JM2

               LIM1 = (JM2-1)*POINTS
               LIM2 = (JM2+1)*POINTS
               CALL MAXY(S, Y, LIM1, LIM2, SYMAX2, YMAX2, IMAX2)

C FIND PRECISE POSITION OF MINIMUM IN BETWEEN THESE

               LIM1 = IMAX1
               LIM2 = IMAX2
               CALL MINY(S, Y, LIM1, LIM2, SYMIN, YMIN, IMIN)
               WRITE(6,*) 'MAXIMUM 1 AT ', SYMAX1, ' HEIGHT ', YMAX1
               WRITE(6,*) 'MINIMUM AT ', SYMIN, ' HEIGHT ', YMIN
               WRITE(6,*) 'MAXIMUM 2 AT ', SYMAX2, ' HEIGHT ', YMAX2
               WRITE(8,*) 'MAXIMUM 1 AT ', SYMAX1, ' HEIGHT ', YMAX1
               WRITE(8,*) 'MINIMUM AT ', SYMIN, ' HEIGHT ', YMIN
```

```fortran
            WRITE(8,*) 'MAXIMUM 2 AT ', SYMAX2, ' HEIGHT ', YMAX2
         ELSE

C IF THE TWO MAXIMA ARE NEXT TO ONE ANOTHER AND THERE ARE NO OTHER
C PEAKS: MAKE JM1 SMALLER THAN JM2

            IF (JM1 .GT. JM2) THEN
               TEMP = JM1
               JM1 = JM2
               JM2 = TEMP
            ENDIF

C FIND MAXIMUM NEAR JM1 AND JM2

            LIM1 = (JM1-1)*POINTS
            LIM2 = (JM2+1)*POINTS
            CALL MAXY(S, Y, LIM1, LIM2, SYMAX1, YMAX1, IMAX1)

C PUT BOTH S-VALUES AT THIS POINT.

            SYMAX2 = SYMAX1
            YMAX2 = YMAX1
            IMAX2 = IMAX1
            IMIN = 0
            WRITE(6,*) 'SINGLE MAXIMUM AT ', SYMAX1, ' HEIGHT ', YMAX1
            WRITE(6,*) 'NO MINIMUM'
            WRITE(8,*) 'SINGLE MAXIMUM AT ', SYMAX1, ' HEIGHT ', YMAX1
            WRITE(8,*) 'NO MINIMUM'
         ENDIF
      ENDIF
      RETURN
      END

      SUBROUTINE TWOPEAK(S,Y,A1,A2,D1,D2,S1,S2,BL,AVSUM,NLINES,NB)

C TO FIT A TWO-PEAK MODEL BY ITERATING USING STARTING VALUES ALREADY
C OBTAINED.
C FORCED TO ITERATE AT LEAST 10 TIMES THROUGH WHOLE PROCEDURE

      IMPLICIT NONE
      REAL S(1000), Y(1000), A1, A2, D1, D2, S1, S2, AVSUM, NB, BL
      INTEGER NLINES, ITER
      REAL ERROR, OLDERROR

 9    WRITE(6,*) 'USING BEGINNING VALUES, ERROR = ',(AVSUM*100),' %'
      WRITE(8,*) 'USING BEGINNING VALUES, ERROR = ',(AVSUM*100),' %'
      CALL BESTA1(S, Y, A1, A2, D1, D2, S1, S2, BL, AVSUM, NLINES, NB)
      WRITE(6,*) 'NEW A1 = ', A1, ' ERROR = ',(AVSUM*100),' %'
      WRITE(8,*) 'NEW A1 = ', A1, ' ERROR = ',(AVSUM*100),' %'
      CALL BESTA2(S, Y, A1, A2, D1, D2, S1, S2, BL, AVSUM, NLINES, NB)
      WRITE(6,*) 'NEW A2 = ', A2, ' ERROR = ',(AVSUM*100),' %'
      WRITE(8,*) 'NEW A2 = ', A2, ' ERROR = ',(AVSUM*100),' %'
      CALL BESTD1(S, Y, A1, A2, D1, D2, S1, S2, BL, AVSUM, NLINES, NB)
      WRITE(6,*) 'NEW D1 = ', D1, ' ERROR = ',(AVSUM*100),' %'
      WRITE(8,*) 'NEW D1 = ', D1, ' ERROR = ',(AVSUM*100),' %'
      CALL BESTD2(S, Y, A1, A2, D1, D2, S1, S2, BL, AVSUM, NLINES, NB)
      WRITE(6,*) 'NEW D2 = ', D2, ' ERROR = ',(AVSUM*100),' %'
      WRITE(8,*) 'NEW D2 = ', D2, ' ERROR = ',(AVSUM*100),' %'
      CALL BESTS1(S, Y, A1, A2, D1, D2, S1, S2, BL, AVSUM, NLINES, NB)
      WRITE(6,*) 'NEW S1 = ', S1, ' ERROR = ',(AVSUM*100),' %'
      WRITE(8,*) 'NEW S1 = ', S1, ' ERROR = ',(AVSUM*100),' %'
      CALL BESTS2(S, Y, A1, A2, D1, D2, S1, S2, BL, AVSUM, NLINES, NB)
      WRITE(6,*) 'NEW S2 = ', S2, ' ERROR = ',(AVSUM*100),' %'
      WRITE(8,*) 'NEW S2 = ', S2, ' ERROR = ',(AVSUM*100),' %'
      CALL BESTBL(S, Y, A1, A2, D1, D2, S1, S2, BL, AVSUM, NLINES, NB)
      WRITE(6,*) 'NEW BL = ', BL, ' ERROR = ',(AVSUM*100),' %'
      WRITE(8,*) 'NEW BL = ', BL, ' ERROR = ',(AVSUM*100),' %'
```

```fortran
      OLDERROR = ERROR
      ERROR = AVSUM

      IF ((ERROR .LT. OLDERROR) .OR. (ITER .LE. 10)) THEN
         ITER = ITER + 1
         WRITE (6,*) 'OVERALL ITERATION NO. ', ITER
         WRITE (6,*) '*************************'
         WRITE (8,*) 'OVERALL ITERATION NO. ', ITER
         WRITE (8,*) '*************************'
         GOTO 9
      ENDIF
      RETURN
      END


      SUBROUTINE ADLOG(S,Y,A,D,SV,BL,AVSUM,LIM1,LIM2,NLINES,NB)

C TO OBTAIN STARTING VALUES OF A AND D GIVEN A VALUE OF S
C ONLY FITS WITHIN LIMIT SPECIFIED
C FORCED TO ITERATE AT LEAST 10 TIMES TO PREVENT SPURIOUS MINIMA

      IMPLICIT NONE
      INTEGER ITER
      REAL S(1000), Y(1000), A, D, SV, AVSUM, BL
      INTEGER NLINES, LIM1, LIM2
      REAL ERROR, NB
      REAL OLDERROR

      ITER = 0

      WRITE (6,*) 'CALCULATING STARTING VALUES'
      WRITE (8,*) 'CALCULATING STARTING VALUES'

    5 CALL ALOG(S, Y, A, D, SV, BL, AVSUM, LIM1, LIM2, NLINES, NB)
      CALL DLOG(S, Y, A, D, SV, BL, AVSUM, LIM1, LIM2, NLINES, NB)
      OLDERROR = ERROR
      ERROR = AVSUM
      IF ((ERROR .LT. OLDERROR) .OR. (ITER .LE. 10)) THEN
         ITER = ITER + 1
         GOTO 5
      ENDIF
      RETURN
      END


      SUBROUTINE ADLIN(S, Y, A, D, SV, AVSUM, LIM1, LIM2, NLINES, NB)

C TO OBTAIN STARTING VALUES OF A AND D GIVEN A VALUE OF S
C WITHIN LIMITS SPECIFIED
C FORCED TO ITERATE AT LEAST 10 TIMES TO PREVENT SPURIOUS MINIMA

      IMPLICIT NONE
      INTEGER ITER
      REAL S(1000), Y(1000), A, D, SV, AVSUM
      INTEGER NLINES, LIM1, LIM2
      REAL ERROR, NB
      REAL OLDERROR

      ITER = 0

      WRITE (6,*) 'CALCULATING STARTING VALUES'
      WRITE (8,*) 'CALCULATING STARTING VALUES'
    5 CALL ALIN(S, Y, A, D, SV, AVSUM, LIM1, LIM2, NLINES, NB)
      CALL DLIN(S, Y, A, D, SV, AVSUM, LIM1, LIM2, NLINES, NB)
      OLDERROR = ERROR
      ERROR = AVSUM
      IF ((ERROR .LT. OLDERROR) .OR. (ITER .LE. 10)) THEN
         ITER = ITER + 1
      ENDIF
      RETURN
```

```fortran
      END

      SUBROUTINE STARTS(S, Y, NLINES, SYMAX1, SYMAX2, IMIN)

C SUBROUTINE TO FIND STARTING VALUES OF S1 AND S2

      IMPLICIT NONE
      REAL S(1000), Y(1000)
      REAL SYMAX1, SYMAX2, YMAX1, YMAX2, TEMP
      INTEGER NLINES, IMIN

      WRITE (6,*) 'AUTOMATIC OPERATION'
      WRITE (8,*) 'AUTOMATIC OPERATION'
      CALL MAXY2(S, Y, NLINES, SYMAX1, SYMAX2, YMAX1, YMAX2, IMIN)
      IF (SYMAX2 .GT. SYMAX1) THEN
      ELSE
          TEMP = SYMAX2
          SYMAX2 = SYMAX1
          SYMAX1 = TEMP
      ENDIF
      WRITE (6,*) 'PEAK 1 AT ', SYMAX1, ' HEIGHT ', YMAX1
      WRITE (6,*) 'PEAK 2 AT ', SYMAX2, ' HEIGHT ', YMAX2
      WRITE (8,*) 'PEAK 1 AT ', SYMAX1, ' HEIGHT ', YMAX1
      WRITE (8,*) 'PEAK 2 AT ', SYMAX2, ' HEIGHT ', YMAX2
      RETURN
      END

      SUBROUTINE BESTA1(S,Y,A1,A2,D1,D2,S1,S2,BL,AVSUM,NLINES,NB)

C TO FIND THE BEST-FIT VALUE OF A1

      IMPLICIT NONE
      REAL S(1000), Y(1000)
      REAL A1, A2, D1, D2, S1, S2
      INTEGER NLINES, ITER
      REAL A1U, A1D, AVSUMU, AVSUMD, AVSUM, NB, BL

      ITER = 0

    4 CALL FITTWO(S,Y,A1,A2,D1,D2,S1,S2,BL,AVSUM,NLINES,NB)
      A1U = A1 + (A1/100)
      CALL FITTWO(S,Y,A1U,A2,D1,D2,S1,S2,BL,AVSUMU,NLINES,NB)
      A1D = A1 - (A1/100)
      CALL FITTWO(S,Y,A1D,A2,D1,D2,S1,S2,BL,AVSUMD,NLINES,NB)
      IF (ITER .LE. 10000) THEN
         IF ((AVSUMD .LT. AVSUM) .AND. (AVSUM .LT. AVSUMU)) THEN
            A1 = A1D
            ITER = ITER + 1
            GOTO 4
         ELSE IF ((AVSUMD .GT. AVSUM) .AND. (AVSUM .GT. AVSUMU)) THEN
            A1 = A1U
            ITER = ITER + 1
            GOTO 4
         ELSE
            WRITE (6,*) 'A1: DETECTED MINIMUM ', ITER, ' ITERATIONS'
            WRITE (8,*) 'A1: DETECTED MINIMUM ', ITER, ' ITERATIONS'
         ENDIF
      ELSE
            WRITE (6,*) 'A1: TOO MANY ITERATIONS; PROCESS FAILED'
            WRITE (8,*) 'A1: TOO MANY ITERATIONS; PROCESS FAILED'
      ENDIF
      RETURN
      END

      SUBROUTINE BESTA2(S,Y,A1,A2,D1,D2,S1,S2,BL,AVSUM,NLINES,NB)

C TO FIND THE BEST-FIT VALUE OF A2
```

```fortran
      IMPLICIT NONE
      REAL S(1000), Y(1000)
      REAL A1, A2, D1, D2, S1, S2
      INTEGER NLINES, ITER
      REAL A2U, A2D, AVSUMU, AVSUMD, AVSUM, NB, BL

      ITER = 0

    4 CALL FITTWO(S,Y,A1,A2,D1,D2,S1,S2,BL,AVSUM,NLINES,NB)
      A2U = A2 + (A2/100)
      CALL FITTWO(S,Y,A1,A2U,D1,D2,S1,S2,BL,AVSUMU,NLINES,NB)
      A2D = A2 - (A2/100)
      CALL FITTWO(S,Y,A1,A2D,D1,D2,S1,S2,BL,AVSUMD,NLINES,NB)
      IF (ITER .LE. 10000) THEN
         IF ((AVSUMD .LT. AVSUM) .AND. (AVSUM .LT. AVSUMU)) THEN
            A2 = A2D
            ITER = ITER + 1
            GOTO 4
         ELSE IF ((AVSUMD .GT. AVSUM) .AND. (AVSUM .GT. AVSUMU)) THEN
            A2 = A2U
            ITER = ITER + 1
            GOTO 4
         ELSE
            WRITE (6,*) 'A2: DETECTED MINIMUM ', ITER, ' ITERATIONS'
            WRITE (8,*) 'A2: DETECTED MINIMUM ', ITER, ' ITERATIONS'
         ENDIF
      ELSE
         WRITE (6,*) 'A2: TOO MANY ITERATIONS; PROCESS FAILED'
         WRITE (8,*) 'A2: TOO MANY ITERATIONS; PROCESS FAILED'
      ENDIF
      RETURN
      END

      SUBROUTINE BESTD1(S,Y,A1,A2,D1,D2,S1,S2,BL,AVSUM,NLINES,NB)

C TO FIND THE BEST-FIT VALUE OF D1

      IMPLICIT NONE
      REAL S(1000), Y(1000)
      REAL A1, A2, D1, D2, S1, S2
      INTEGER NLINES, ITER
      REAL D1U, D1D, AVSUMU, AVSUMD, AVSUM, NB, BL

      ITER = 0

    4 CALL FITTWO(S,Y,A1,A2,D1,D2,S1,S2,BL,AVSUM,NLINES,NB)
      D1U = D1 + (D1/100)
      CALL FITTWO(S,Y,A1,A2,D1U,D2,S1,S2,BL,AVSUMU,NLINES,NB)
      D1D = D1 - (D1/100)
      CALL FITTWO(S,Y,A1,A2,D1D,D2,S1,S2,BL,AVSUMD,NLINES,NB)
      IF (ITER .LE. 10000) THEN
         IF ((AVSUMD .LT. AVSUM) .AND. (AVSUM .LT. AVSUMU)) THEN
            D1 = D1D
            ITER = ITER + 1
            GOTO 4
         ELSE IF ((AVSUMD .GT. AVSUM) .AND. (AVSUM .GT. AVSUMU)) THEN
            D1 = D1U
            ITER = ITER + 1
            GOTO 4
         ELSE
            WRITE (6,*) 'D1: DETECTED MINIMUM ', ITER, ' ITERATIONS'
            WRITE (8,*) 'D1: DETECTED MINIMUM ', ITER, ' ITERATIONS'
         ENDIF
      ELSE
         WRITE (6,*) 'D1: TOO MANY ITERATIONS; PROCESS FAILED'
         WRITE (8,*) 'D1: TOO MANY ITERATIONS; PROCESS FAILED'
      ENDIF
      RETURN
```

```fortran
      END

      SUBROUTINE BESTD2(S,Y,A1,A2,D1,D2,S1,S2,BL,AVSUM,NLINES,NB)

C TO FIND THE BEST-FIT VALUE OF D2

      IMPLICIT NONE
      REAL S(1000), Y(1000)
      REAL A1, A2, D1, D2, S1, S2
      INTEGER NLINES, ITER
      REAL D2U, D2D, AVSUMU, AVSUMD, AVSUM, NB, BL

      ITER = 0

    4 CALL FITTWO(S,Y,A1,A2,D1,D2,S1,S2,BL,AVSUM,NLINES,NB)
      D2U = D2 + (D2/100)
      CALL FITTWO(S,Y,A1,A2,D1,D2U,S1,S2,BL,AVSUMU,NLINES,NB)
      D2D = D2 - (D2/100)
      CALL FITTWO(S,Y,A1,A2,D1,D2D,S1,S2,BL,AVSUMD,NLINES,NB)
      IF (ITER .LE. 10000) THEN
         IF ((AVSUMD .LT. AVSUM) .AND. (AVSUM .LT. AVSUMU)) THEN
            D2 = D2D
            ITER = ITER + 1
            GOTO 4
         ELSE IF ((AVSUMD .GT. AVSUM) .AND. (AVSUM .GT. AVSUMU)) THEN
            D2 = D2U
            ITER = ITER + 1
            GOTO 4
         ELSE
            WRITE (6,*) 'D2: DETECTED MINIMUM ', ITER, ' ITERATIONS'
            WRITE (8,*) 'D2: DETECTED MINIMUM ', ITER, ' ITERATIONS'
         ENDIF
      ELSE
         WRITE (6,*) 'D2: TOO MANY ITERATIONS; PROCESS FAILED'
         WRITE (8,*) 'D2: TOO MANY ITERATIONS; PROCESS FAILED'
      ENDIF
      RETURN
      END

      SUBROUTINE BESTS1(S,Y,A1,A2,D1,D2,S1,S2,BL,AVSUM,NLINES,NB)

C TO FIND THE BEST-FIT VALUE OF S1

      IMPLICIT NONE
      REAL S(1000), Y(1000)
      REAL A1, A2, D1, D2, S1, S2
      INTEGER NLINES, ITER
      REAL S1U, S1D, AVSUMU, AVSUMD, AVSUM, NB, BL

      ITER = 0

    4 CALL FITTWO(S,Y,A1,A2,D1,D2,S1,S2,BL,AVSUM,NLINES,NB)
      S1U = S1 + (S1/100)
      CALL FITTWO(S, Y, A1, A2, D1, D2, S1U, S2, BL, AVSUMU, NLINES, NB)
      S1D = S1 - (S1/100)
      CALL FITTWO(S, Y, A1, A2, D1, D2, S1D, S2, BL, AVSUMD, NLINES, NB)
      IF (ITER .LE. 10000) THEN
         IF ((AVSUMD .LT. AVSUM) .AND. (AVSUM .LT. AVSUMU)) THEN
            S1 = S1D
            ITER = ITER + 1
            GOTO 4
         ELSE IF ((AVSUMD .GT. AVSUM) .AND. (AVSUM .GT. AVSUMU)) THEN
            S1 = S1U
            ITER = ITER + 1
            GOTO 4
         ELSE
            WRITE (6,*) 'S1: DETECTED MINIMUM ', ITER, ' ITERATIONS'
            WRITE (8,*) 'S1: DETECTED MINIMUM ', ITER, ' ITERATIONS'
```

```fortran
         ENDIF
      ELSE
         WRITE (6,*) 'S1: TOO MANY ITERATIONS; PROCESS FAILED'
         WRITE (8,*) 'S1: TOO MANY ITERATIONS; PROCESS FAILED'
      ENDIF
      RETURN
      END

      SUBROUTINE BESTS2(S,Y,A1,A2,D1,D2,S1,S2,BL,AVSUM,NLINES,NB)

C TO FIND THE BEST-FIT VALUE OF S2

      IMPLICIT NONE
      REAL S(1000), Y(1000)
      REAL A1, A2, D1, D2, S1, S2
      INTEGER NLINES, ITER
      REAL S2U, S2D, AVSUMU, AVSUMD, AVSUM, NB, BL

      ITER = 0

    4 CALL FITTWO(S, Y, A1, A2, D1, D2, S1, S2, BL, AVSUM, NLINES, NB)
      S2U = S2 + (S2/100)
      CALL FITTWO(S, Y, A1, A2, D1, D2, S1, S2U, BL, AVSUMU, NLINES, NB)
      S2D = S2 - (S2/100)
      CALL FITTWO(S, Y, A1, A2, D1, D2, S1, S2D, BL, AVSUMD, NLINES, NB)
      IF (ITER .LE. 10000) THEN
         IF ((AVSUMD .LT. AVSUM) .AND. (AVSUM .LT. AVSUMU)) THEN
            S2 = S2D
            ITER = ITER + 1
            GOTO 4
         ELSE IF ((AVSUMD .GT. AVSUM) .AND. (AVSUM .GT. AVSUMU)) THEN
            S2 = S2U
            ITER = ITER + 1
            GOTO 4
         ELSE
            WRITE (6,*) 'S2: DETECTED MINIMUM ', ITER, ' ITERATIONS'
            WRITE (8,*) 'S2: DETECTED MINIMUM ', ITER, ' ITERATIONS'
         ENDIF
      ELSE
         WRITE (6,*) 'S2: TOO MANY ITERATIONS; PROCESS FAILED'
         WRITE (8,*) 'S2: TOO MANY ITERATIONS; PROCESS FAILED'
      ENDIF
      RETURN
      END

      SUBROUTINE BESTBL(S,Y,A1,A2,D1,D2,S1,S2,BL,AVSUM,NLINES,NB)

C TO CALCULATE THE BEST-FIT VALUE OF BL
      IMPLICIT NONE
      REAL S(1000), Y(1000)
      REAL A1, A2, D1, D2, S1, S2
      INTEGER NLINES, ITER
      REAL BLU, BLD, AVSUMU, AVSUMD, AVSUM, NB, BL

      ITER = 0

    4 CALL FITTWO(S, Y, A1, A2, D1, D2, S1, S2, BL, AVSUM, NLINES, NB)
      BLU = BL + (BL/100)
      CALL FITTWO(S, Y, A1, A2, D1, D2, S1, S2, BLU, AVSUMU, NLINES, NB)
      BLD = BL - (BL/100)
      CALL FITTWO(S, Y, A1, A2, D1, D2, S1, S2, BLD, AVSUMD, NLINES, NB)
      IF (ITER .LE. 10000) THEN
         IF ((AVSUMD .LT. AVSUM) .AND. (AVSUM .LT. AVSUMU)) THEN
            BL = BLD
            ITER = ITER + 1
            GOTO 4
         ELSE IF ((AVSUMD .GT. AVSUM) .AND. (AVSUM .GT. AVSUMU)) THEN
            BL = BLU
```

```fortran
            ITER = ITER + 1
            GOTO 4
         ELSE
            WRITE (6,*) 'BL: DETECTED MINIMUM ', ITER, ' ITERATIONS'
            WRITE (8,*) 'BL: DETECTED MINIMUM ', ITER, ' ITERATIONS'
         ENDIF
      ELSE
         WRITE (6,*) 'BL: TOO MANY ITERATIONS; PROCESS FAILED'
         WRITE (8,*) 'BL: TOO MANY ITERATIONS; PROCESS FAILED'
      ENDIF
      RETURN
      END


      SUBROUTINE FITTWO(S,Y,A1,A2,D1,D2,S1,S2,BL,AVSUM,NLINES,NB)

C TO CALCULATE TWO-PEAK MODEL USING SUPPLIED PARAMETERS

      IMPLICIT NONE
      REAL S(1000), Y(1000)
      REAL PI
      REAL NS1, NS2, NI1, NI2, NI, NS, MFP, HEIGHT(1000), SUM
      INTEGER I, NLINES
      REAL DELTAY, AVSUM, YSUM
      REAL S1, S2, BL
      REAL A1, D1, C1
      REAL A2, D2, C2
      REAL NB

      NS1 = 0.0
      NS2 = 0.0
      NI1 = 0.0
      NI2 = 0.0
      NI = 0.0
      NS = 0.0
      MFP = 0.0
      SUM = 0.0
      DELTAY = 0.0
      AVSUM = 0.0
      YSUM = 0.0

      PI = 3.14
      C1 = D1*SQRT((2*PI))
      C2 = D2*SQRT((2*PI))

      DO 8 I = 1, NLINES

C NO OF SITES OF STRENGTH S

         IF ((S(I)-BL) .GT. 0) THEN
            NS1 = (A1/(C1*(S(I)-BL)))*EXP((-1.0/2.0)*
     &         (((LOG(S(I)-BL)-S1)/D1)**2))
         ELSE
            NS1 = 0.0
         ENDIF
         NS2 = (A2/C2)*EXP((-1.0/2.0)*(((S(I)-S2)/D2)**2))
         NS = NS1 + NS2

C NO OF SITES OF STRENGTH GREATER OR EQUAL TO S

         IF ((S(I)-BL) .GT. 0) THEN
            NI1 = (A1/2.0)*ERFC((LOG(S(I)-BL)-S1)/(D1*SQRT(2.0)))
         ELSE
            NI1 = 0
         ENDIF
         NI2 =(A2/2.0)*ERFC((S(I)-S2)/(D2*SQRT(2.0)))
         NI = NI1 + NI2

C MEAN FREE PATH
```

```fortran
            IF (NI .NE. 0) THEN
               MFP = (1/NI)**(1.0/3.0)

C PEAK HEIGHT

               HEIGHT(I) = (NS*MFP) + NB
            ELSE
               HEIGHT(I) = NB
            ENDIF

C LEAST-SQUARES FIT

            DELTAY = HEIGHT(I) - Y(I)
            SUM = SUM + (DELTAY**2)
            YSUM = YSUM + Y(I)**2

            WRITE(1,*) S(I), Y(I), HEIGHT(I)
      8 CONTINUE
        REWIND(1)
        AVSUM = SQRT(SUM/YSUM)
        END

        SUBROUTINE ALIN(S, Y, A, D, SV, AVSUM, LIM1, LIM2, NLINES, NB)

C TO FIND BEST-FIT VALUE OF A FOR SINGLE PEAK - NORMAL DISTRIBUTION

        IMPLICIT NONE
        REAL S(1000), Y(1000)
        REAL A, D, SV, AVSUM
        INTEGER NLINES, ITER, LIM1, LIM2
        REAL AU, AD, AVSUMU, AVSUMD, NB

        ITER = 0

      4 CALL FITLIN(S, Y, A, D, SV, AVSUM, LIM1, LIM2, NLINES, NB)
        AU = A + (A/100)
        CALL FITLIN(S, Y, AU, D, SV, AVSUMU, LIM1, LIM2, NLINES, NB)
        AD = A - (A/100)
        CALL FITLIN(S, Y, AD, D, SV, AVSUMD, LIM1, LIM2, NLINES, NB)
        IF (ITER .LE. 10000) THEN
           IF ((AVSUMD .LT. AVSUM) .AND. (AVSUM .LT. AVSUMU)) THEN
              A = AD
              ITER = ITER + 1
              GOTO 4
           ELSE IF ((AVSUMD .GT. AVSUM) .AND. (AVSUM .GT. AVSUMU)) THEN
              A = AU
              ITER = ITER + 1
              GOTO 4
           ENDIF
        ELSE
           WRITE (6,*) 'TOO MANY ITERATIONS; PROCESS FAILED'
           WRITE (8,*) 'TOO MANY ITERATIONS; PROCESS FAILED'
        ENDIF
        RETURN
        END

        SUBROUTINE DLIN(S, Y, A, D, SV, AVSUM, LIM1, LIM2, NLINES, NB)

C TO FIND BEST-FIT VALUE OF D FOR SINGLE PEAK - NORMAL DISTRIBUTION

        IMPLICIT NONE
        REAL S(1000), Y(1000)
        REAL A, D, SV, AVSUM
        INTEGER NLINES, ITER, LIM1, LIM2
        REAL DU, DD, AVSUMU, AVSUMD, NB

        ITER = 0
```

```fortran
    4 CALL FITLIN(S, Y, A, D, SV, AVSUM, LIM1, LIM2, NLINES, NB)
      DU = D + (D/100)
      CALL FITLIN(S, Y, A, DU, SV, AVSUMU, LIM1, LIM2, NLINES, NB)
      DD = D - (D/100)
      CALL FITLIN(S, Y, A, DD, SV, AVSUMD, LIM1, LIM2, NLINES, NB)
      IF (ITER .LE. 10000) THEN
         IF ((AVSUMD .LT. AVSUM) .AND. (AVSUM .LT. AVSUMU)) THEN
            D = DD
            ITER = ITER + 1
            GOTO 4
         ELSE IF ((AVSUMD .GT. AVSUM) .AND. (AVSUM .GT. AVSUMU)) THEN
            D = DU
            ITER = ITER + 1
            GOTO 4
         ENDIF
      ELSE
         WRITE (6,*) 'TOO MANY ITERATIONS; PROCESS FAILED'
         WRITE (8,*) 'TOO MANY ITERATIONS; PROCESS FAILED'
      ENDIF
      RETURN
      END

      SUBROUTINE FITLIN(S, Y, A, D, SV, AVSUM, LIM1, LIM2, NLINES, NB)

C TO FIT MODEL TO A SINGLE, NORMAL-DISTRIBUTION PEAK

      IMPLICIT NONE
      REAL S(1000), Y(1000)
      REAL A, D, C, SV
      REAL NS, NI, MFP, HEIGHT(1000), DELTAY, SUM, PI
      INTEGER I, NLINES, LIM1, LIM2
      REAL AVSUM, NB, YSUM

      PI = 3.14
      C = D*SQRT((2*PI))

      NS = 0.0
      NI = 0.0
      MFP = 0.0
      DELTAY = 0.0
      SUM = 0.0
      AVSUM = 0.0
      YSUM = 0.0

    3 DO 2 I = LIM1, LIM2
         NS = (A/C)*EXP((-1.0/2.0)*(((S(I)-SV)/D)**2))
         NI =(A/2.0)*ERFC((S(I)-SV)/(D*SQRT(2.0)))
         MFP = (1/NI)**(1.0/3.0)
         HEIGHT(I) = (NS*MFP) + NB
         DELTAY = HEIGHT(I) - Y(I)
         SUM = SUM + (DELTAY**2)
         YSUM = YSUM + (Y(I)**2)
    2 CONTINUE
      REWIND(1)
      AVSUM = SQRT(SUM/YSUM)
      RETURN
      END

      SUBROUTINE ALOG(S, Y, A, D, SV, BL, AVSUM, LIM1, LIM2, NLINES, NB)

C TO FIND BEST-FIT VALUE OF A FOR SINGLE PEAK - LOG-NORMAL DISTRIBUTION

      IMPLICIT NONE
      REAL S(1000), Y(1000)
      REAL A, D, SV, AVSUM
      INTEGER NLINES, ITER, LIM1, LIM2
      REAL AU, AD, AVSUMU, AVSUMD, NB, BL
```

```fortran
      ITER = 0

    4 CALL FITLOG(S, Y, A, D, BL, SV, AVSUM, LIM1, LIM2, NLINES, NB)
      AU = A + (A/100)
      CALL FITLOG(S, Y, AU, D, BL, SV, AVSUMU, LIM1, LIM2, NLINES, NB)
      AD = A - (A/100)
      CALL FITLOG(S, Y, AD, D, BL, SV, AVSUMD, LIM1, LIM2, NLINES, NB)
      IF (ITER .LE. 10000) THEN
         IF ((AVSUMD .LT. AVSUM) .AND. (AVSUM .LT. AVSUMU)) THEN
            A = AD
            ITER = ITER + 1
            GOTO 4
         ELSE IF ((AVSUMD .GT. AVSUM) .AND. (AVSUM .GT. AVSUMU)) THEN
            A = AU
            ITER = ITER + 1
            GOTO 4
         ENDIF
      ELSE
         WRITE (6,*) 'TOO MANY ITERATIONS; PROCESS FAILED'
         WRITE (8,*) 'TOO MANY ITERATIONS; PROCESS FAILED'
      ENDIF
      RETURN
      END

      SUBROUTINE DLOG(S, Y, A, D, SV, BL, AVSUM, LIM1, LIM2, NLINES, NB)

C TO FIND BEST-FIT VALUE OF D FOR SINGLE PEAK - LOG-NORMAL DISTRIBUTION

      IMPLICIT NONE
      REAL S(1000), Y(1000)
      REAL A, D, SV, AVSUM
      INTEGER NLINES, ITER, LIM1, LIM2
      REAL DU, DD, AVSUMU, AVSUMD, NB, BL

      ITER = 0

    4 CALL FITLOG(S, Y, A, D, BL, SV, AVSUM, LIM1, LIM2, NLINES, NB)
      DU = D + (D/100)
      CALL FITLOG(S, Y, A, DU, BL, SV, AVSUMU, LIM1, LIM2, NLINES, NB)
      DD = D - (D/100)
      CALL FITLOG(S, Y, A, DD, BL, SV, AVSUMD, LIM1, LIM2, NLINES, NB)
      IF (ITER .LE. 10000) THEN
         IF ((AVSUMD .LT. AVSUM) .AND. (AVSUM .LT. AVSUMU)) THEN
            D = DD
            ITER = ITER + 1
            GOTO 4
         ELSE IF ((AVSUMD .GT. AVSUM) .AND. (AVSUM .GT. AVSUMU)) THEN
            D = DU
            ITER = ITER + 1
            GOTO 4
         ENDIF
      ELSE
         WRITE (6,*) 'TOO MANY ITERATIONS; PROCESS FAILED'
         WRITE (8,*) 'TOO MANY ITERATIONS; PROCESS FAILED'
      ENDIF
      RETURN
      END

      SUBROUTINE FITLOG(S,Y,A,D,BL,SV,AVSUM,LIM1,LIM2,NLINES,NB)

C TO FIT MODEL TO A SINGLE, NORMAL-DISTRIBUTION PEAK

      IMPLICIT NONE
      REAL S(1000), Y(1000)
      REAL A, D, C, SV
      REAL NS, NI, MFP, HEIGHT(1000), DELTAY, SUM, PI, BL
      INTEGER I, NLINES, LIM1, LIM2
```

```fortran
      REAL AVSUM, NB, YSUM

   PI = 3.14
   C = D*SQRT((2*PI))

   NS = 0.0
   NI = 0.0
   MFP = 0.0
   DELTAY = 0.0
   SUM = 0.0
   AVSUM = 0.0
   YSUM = 0.0

 3 DO 2 I = LIM1, LIM2
   IF ((S(I)-BL) .GT. 0) THEN
      NS = (A/(C*(S(I)-BL)))*EXP((-1.0/2.0)*
  &   (((LOG(S(I)-BL)-SV)/D)**2))
      NI =(A/2.0)*ERFC((LOG(S(I)-BL)-SV)/(D*SQRT(2.0)))
      MFP = (1/NI)**(1.0/3.0)
      HEIGHT(I) = (NS*MFP) + NB
      DELTAY = HEIGHT(I) - Y(I)
      SUM = SUM + (DELTAY**2)
      YSUM = YSUM + Y(I)**2
   ELSE
      HEIGHT(I) = NB
   ENDIF
 2 CONTINUE
   REWIND(1)
   AVSUM = SQRT(SUM/YSUM)
   RETURN
   END
```